Morphological and Structural Study of Ultrathin Lithium Fluoride Films on Organic Molecule Surfaces

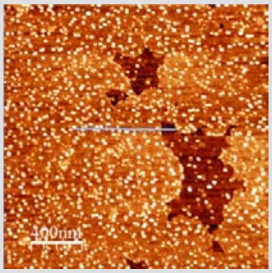

Felix Maye
March 2011

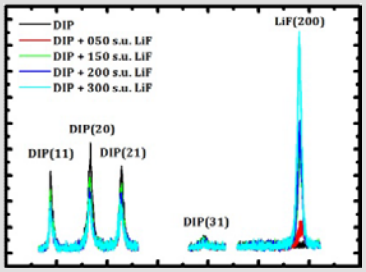

Directed by Prof. Dr. H. Dosch
Co-directed by Prof. Dr. J. Wrachtrup

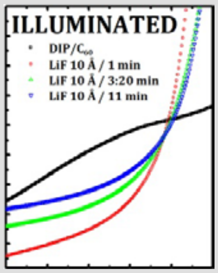

Max-Planck-Institut
für Metallforschung

MAX-PLANCK-GESELLSCHAFT

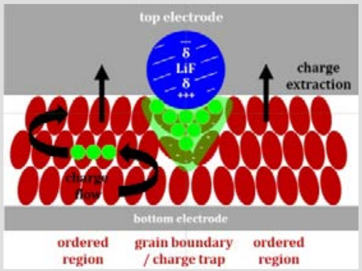

Institut für Theoretische
Und Angewandte Physik
der Universität Stuttgart

Morphological and Structural Study of Ultrathin Lithium Fluoride Films on Organic Molecule Surfaces

Von der Fakultät für Mathematik und Physik der
Universität Stuttgart zur Erlangung der Würde eines
Doktors der Naturwissenschaften (Dr. rer. nat.)
genehmigte Abhandlung

Vorgelegt von
FELIX MAYE
aus Chemnitz

Hauptberichter: Prof. Dr. Helmut Dosch
Mitberichter: Prof. Dr. Jörg Wrachtrup

Eingereicht am: 29.03.2011
Tag der mündlichen Prüfung: 27.05.2011

Institut für Theoretische und Angewandte Physik der
Universität Stuttgart

2011

Table of contents

ACRONYMS

AM	Amplitude modulation
ANKA	Angström Quelle Karlsruhe
AFM	Atomic force microscopy
CCD	Charge coupled device
C_{60}	Fullerene
DIP	Diindenoperylene
DOS	Density of states
EQE	external quantum efficiency
fcc	face centered cubic
FF	Fill factor
FM	Frequency modulation
GIXRD	Grazing incidence x-ray diffraction
HOMO	Highest occupied molecular orbital
hcp	hexagonal closed packed
HRTEM	High resolution transmission electron microscopy
ITO	Indium tin oxide
LiF	Lithium fluoride
LUMO	Lowest occupied molecular orbital
MBD	Molecular beam deposition
MBE	Molecular beam epitaxy
MIS	Metal insulator semiconductor
ML	Monolayer
MPI	Max-Planck-Institut
OLED	Organic light emitting diode
OPV	Organic photo voltaic
PTCDI-C_8	N,N’-dioctyl-3,4:9,10-perylene tetracarboxylic diimide
QCM	Quartz crystal microbalance
RMS	Root mean square
SPM	Scanning probe microscopy
SR	Spectral response
SiO_2	Silicon dioxide
TEM	Transmission electron microscopy
UHV	Ultra high vacuum
VdW	Van der Waals
XRD	X-ray diffraction
XRR	X-ray reflectivity

ZUSAMMENFASSUNG

1. Motivation

Durch den inflationären Gebrauch in Politik und Gesellschaft wurde das Wort „alternativlos“ zum Unwort des Jahres 2010 in Deutschland gewählt. Im Gegensatz dazu bekommt dieses Wort einen überaus berechtigten Sinn, wenn man vom Übergang von fossilen zu nachhaltigen Energiequellen spricht. Angesichts überbordenden Energieverbrauchs, endlichen fossilen Ressourcen und dem einsetzenden Klimawandel, muß dem Erreichen dieses Ziels höchste Priorität eingeräumt werden. Weiterentwicklung von bereits bestehenden Technologien hin zu konkurrenzfähigen Produkten und Erforschung neuartiger Methoden zur nachhaltigen Energiegewinnung werden einige der Herausforderungen für die Einleitung dieser Trendwende sein. Direkte Umwandlung von Sonnenlicht in elektrischen Strom ist ein vielversprechender Ansatz, umweltfreundliche Energieerzeugung zu realisieren. Photovoltaische Bauteile, die auf anorganischen Materialien basieren, haben ihr Potential bereits in den späten 60er Jahren des letzen Jahrhunderts gezeigt. Einer der ersten US Satelliten (Vanguard1), der mit Solarzellen basierend auf einkristallinem Silizium ausgestattet worden ist, konnte bereits annähernd sieben Jahre mit dieser Technik betrieben werden. Seit dieser Zeit sind viele Anstrengungen unternommen worden, um den Wirkungsgrad photovoltaischer Bauteile auf den aktuellen Weltrekord von 41,1 % zu steigern. Dieser wird derzeit von auf Gallium basierenden Mehrfachschicht Solarzellen gehalten.

Mit organischen Halbleitern steht seit den letzten Jahren eine neue Klasse von Materialien für den Einsatz in Halbleiterbauteilen im Brennpunkt der Forschung. Vor allem ihre einzigartigen Eigenschaften wie mechanische Flexibilität, angenommene niedrige Produktionskosten und ausreichende Verfügbarkeit machen sie für die Verwendung in der Halbleitertechnologie attraktiv. Organische Halbleiter werden mit einer Vielzahl von Anwendungen in Verbindung gebracht, sofern grundlegenden Fragen zu ihren physikalischen Eigenschaften geklärt und geeignete Herstellungsprozesse etabliert worden sind. Seitdem man den Einsatz von organischen Materialien im Bereich der Photovoltaik untersucht, sind bereits viele Ansätze für die Steigerung des Wirkungsgrades organischer Solarzellen bekannt. Bis dato werden dabei Werte von bis zu 8,3 % erreicht. Ein Meilenstein im Entwicklungsprozeß der organischen Photovoltaik ist die Einführung von planaren Hetero-Bindungen, die geeignete Grenzflächen für effektive Ladungstrennung schaffen. Zusätzlich hat die Weiterentwicklung zu sogenannten durchmischten Hetero-Bindungen die Leistungseigenschaften von organischen Solarzellen erheblich gesteigert. Derzeit stehen Dünnschichtsolarzellen, bestehend aus kurzkettigen organischen Molekülkombinationen unter Beobachtung. In diesen Zellen kann die strukturelle Anordnung der aktiven Materialien und damit der Ladungstransport innerhalb dieser Materialien gezielt beeinflußt werden.

Eine weitere Möglichkeit für die Steigerung organischer Solarzellen-eigenschaften ist die Verbesserung der Halbleiter-Metall-Kontaktflächen. Dies kann durch Einbringen geeigneter Zwischenschichten geschehen. Mit deren Hilfe sollen Injektions- und Extraktionsmechansimen der photogenerierten Ladungsträger am Kontakt verbessert werden. Speziell ionische Alkali-Fluorid-Verbunde scheinen geeignete Kandidaten für Grenzflächenlagen zu sein, obwohl die genauen Gründe für ihre positiven Einflüsse bis jetzt nicht aufgeklärt worden sind. Empirischen Studien mit Tests durch Versuch und Irrtum bescheinigen speziell Lithiumfluorid (LiF) ein vielversprechendes Potential, und führen bereits zu dessen häufiger Verwendung als Zwischenlagenmaterial. Interessanterweise wirkt sich LiF nur in sehr geringen Schichtdicken positiv aus, die typischerweise in Bereichen von weniger als einem Nanometer liegen. LiF ist ein weithin untersuchter Isolator mit großer Bandlücke und hat einige einzigartige Eigenschaften. Struktur, Gestalt und Zusammensetzung im Feststoffverbund aber auch in dünnen, auf anorganischen Substraten gewachsenen Schichten, sind vielfältig in der Literatur beschrieben. Dabei sind abweichende Ergebnisse je nach Ablagerungsmethode, nach anschließender Hitzebehandlung oder nach Wahl des Substrats erhalten worden.

Obwohl bereits einige Erklärungen für die Wirkungsweise dünner LiF-Schichten angegeben worden sind, sind direkte Kenntnisse der Gestalt und Struktur solcher Schichten auf organischen Oberflächen nicht bekannt. Einer der Gründe für den spekulativen Charakter zur Wirkungsweise von LiF ist die schwere Zugänglichkeit solcher Zwischenlagen in realen Systemen. Bisherige Untersuchungen in organischen Bauteilen sind dabei weitgehend mit indirekten Praktiken wie Spektroskopie-Methoden oder durch Analysen von elektrischen Stromspannungskennlinien durchgeführt worden. Um diesen Engpaß in der Beschreibung zu umgehen, werden die Eigenschaften ultradünner LiF-Schichten auf den Oberflächen von organischen Modellsystemen untersucht. Die Ergebnisse dieser Untersuchungen können zum Verständnis über die verantwortlichen physikalischen Mechanismen von Zwischenschichten an Kontaktflächen innerhalb organischer Solarzellen beitragen.

2. Experimentelle Ergebnisse

In dieser Arbeit werden im Wesentlichen experimentelle Ergebnisse über die Gestalt, Struktur sowie über die Stabilität von sehr dünnen LiF-Filmen auf organischen Oberflächen vorgestellt. Da die Eigenschaften dieser Filme in realen Systemen experimentell schwer zugänglich sind, wird auf organische Modellsysteme mit Einzellagenwachstum, bekannter Kristallstruktur, beeinflußbarer Oberflächengestalt und atomar flachen Oberflächen zurückgegriffen. Diese Systeme erlauben zum ersten Mal eine direkte Untersuchung der morphologischen und strukturellen Eigenschaften des abgelagerten anorganischen Materials. Dabei werden hochpräzisen Meßmethoden wie Rasterkraftmikroskopie (AFM), Transmissionselektronenmikroskopie (TEM) und Röntgenstreuung (XRD) eingesetzt. Es wird untersucht, ob eine strukturelle Wechselwirkung zwischen anorganischem und organischem Material stattfindet. Außerdem wird die Stabilität eines bestimmten Doppellagensystems beschrieben. Schlußendlich wird der Einfluß von LiF-Zwischenlagen auf die elektrischen Leistungseigenschaften in Solarzellen untersucht. Diese Solarzellen basieren auf denen, in dieser Studie verwendeten organischen Modellmolekülsystemen.

Morphologie (Kapitel V). In Schichtdicken von 10 Å, die typischerweise in organischen Bauteilen verwendet werden, bildet LiF räumlich getrennte Inseln. Inselbildung ist auf allen verwendeten organischen Oberflächen beobachtet worden, die sich durch Lagenwachstum auszeichnen. Die Inselbildung geschieht unabhängig vom elektronischen Charakter der Molekülfilme oder der, die Oberfläche definierenden chemischen Zusammensetzung. Die Höhen der direkt beobachteten Inseln bewegen sich durchgängig im Bereich von 40-60 Å und sind damit um ein Vielfaches größer als die angenommene Schichtdicke, die mit einer, an dicken LiF-Schichten kalibrierten Quartzwaage hergestellt worden sind. Eine Messung der Oberflächenbedeckung zeigt Werte, die für alle organischen Oberflächen um 1 % bei einer beabsichtigten Schichtdicke von 10 Å liegt. Zusätzliche Materialablagerung, die auf der Oberfläche einer bestimmten organischen Molekülschicht studiert worden ist, führt zu einem linearen Anwachsen der Anzahl an LiF Inseln. Die Größe der Inseln nimmt nur unwesentlich zu. Ein direkter Vergleich zwischen LiF-Anlagerung auf einer anorganischen und einer organischen Oberfläche offenbart variierende Inselhöhen auf der anorganischen Oberfläche, wohingegen die Inselhöhen auf der organischen Oberfläche eher einheitlich sind. Inselhöhen auf der organischen Oberfläche entsprechen dabei meist den maximalen Inselhöhen, die auf der anorganischen Oberfläche gemessen worden sind. Dieses Beobachtungen führen zu der Annahme, daß es sich bei den Inseln um LiF-Partikel handelt, die bereits beim Ablösungsprozeß an der Materialquelle oder im Gasstrom entstanden sind, anstatt sich durch Molekül Diffusionsprozeße auf der Oberfläche zu formieren. Dieser Prozeß würde zu einer Vergrößerung oder dem Zusammenfließen der Inseln führen, welche nicht beobachtet worden sind. Des Weiteren wird die Vermutung aufgestellt, daß einzig die Haftungseigenschaften der ankommenden Partikel auf den verwendeten Oberflächen die Morphologie sehr dünner LiF-Filme bestimmt. Eine Unabhängigkeit der Gestalt solcher Schichten von variierenden Wachstumsparametern, wie Substrattemperatur und Aufdampfrate bestätigen diese Annahme.

Die Verteilung der LiF-Partikel auf den organischen Oberflächen ist größtenteils zufällig. Es kann jedoch eine kettenartige Anordnung der Partikel an organischen Inselkanten und auf flachen organischen Oberflächenregionen beobachtet werden. Speziell ungeordnete Bereiche innerhalb der organischen Molekülfilme können als bevorzugte Adsorptionsplätze für LiF-Partikel identifiziert werden. Die kettenartige Anordnung der Partikel ist ebenfalls ausgeprägter wenn nur die erste Monolage des organischen Films sichtbar ist. Analysen der Inselhöhen innerhalb der auftretenden Kettenanordnung zeigen reduzierte Werte, wobei sich die Höhendifferenz im Rahmen einer organischen Monolage bewegt. Dies kann bedeuten, daß LiF-Partikel in das organische Netzwerk eindringen und bereits am Substrat haften. Da die kettenartige Anordnung mit zunehmender Schichtdicke des organischen Films verschwindet, kann eine Ursache dieses Verhaltens die Ausbildung von Rissen innerhalb der instabilen organischen Filme sein. Solche Risse können z.B. durch Wechselwirkung mit der Meß-Sonde oder nachträglicher Hitzebehandlung einfach erzeugt werden. Vielfache Probenpräparationen mit dem Ergebnis von nicht vollständig bedeckenden organischen Filmen im Verlauf dieser Arbeit bestätigen, daß Risse bereits während des organischen Wachstumsprozesses auftreten können. Dieses Verhalten ist speziell bei erhöhten Substrattemperaturen während des Wachstumsprozesses der organischen Schichten beobachtet worden.

Struktur (Kapitel VI). Querschnitt Aufnahmen ultradünner LiF-Schichten auf einer bestimmten organischen Moleküloberfläche mittels Transmissions-Elektronen-Mikroskopie offenbaren das Vorhandensein von Partikeln mit kugelförmiger Gestalt und Größen um 50 Å. Dies entspricht den gemessenen Inselhöhen der topographischen Aufnahmen von LiF auf dieser Moleküloberfläche. Innerhalb der Partikel sind Kristallebenen sichtbar, deren Abstände denen der LiF(111) Ebenenscharen entsprechen. Die winkelige

Orientierung dieser Ebenen ist konsistent mit der beobachteten Kristallstruktur von dickeren LiF-Schichten auf der Moleküloberfläche, bei der sich eine <100>-Orientierung parallel und senkrecht zur Oberfläche ausprägt. Weil die Partikel bereits eine kristalline Ordnung besitzen, kann angenommen werden, daß die Struktur von LiF-Schichten mit experimentell zugänglichen Dicken identisch mit der Struktur von LiF-Schichten ist, die nur unvollständige Bedeckung zeigen.

Ultradünne LiF-Schichten auf organischen Oberflächen mit Dicken im Bereich von 10 Å und damit einhergehender Inselbedeckung um 1 % zeigen nur schwache Röntgenstreusignale. Wenn die Schichtdicke auf einige Nanometer vergrößert wird, kann Röntgenstreuung bei Impulsüberträgen und damit Gitterebenenabständen, wie sie auch im Festkörperverbundstoff vorkommen, beobachtet werden. Unterschiedliche Raten zwischen den Streusignalen der LiF(111)- und der LiF(200)-Ebenen sind in der in-plane Orientierung auf verschieden organischen Oberflächen, und der out-of-plane Orientierung auf verschiedenen anorganischen Substraten beobachtet worden. Die Rauhigkeit der Oberfläche kann für das Auftreten einer erhöhten <111> Orientierung im Vergleich zur <100> Orientierung verantwortlich gemacht werden, da epitaktisches Wachstum nicht beobachtet worden ist. Die Anwesenheit einer lokal ausgeprägten in-plane Textur auf organischen Oberflächen ist in dieser Arbeit auf Grund des verwendeten Modelsubstrates experimentell nicht zugänglich. Das beobachtbare LiF-Streusignal interferiert dabei mit den Streusignalen des einkristallinen Siliziums unterhalb der SiO_2-Schicht.

Untersuchungen über die strukturellen Auswirkungen zunehmender LiF-Ablagerung auf die Kristallstruktur von zwei, jeweils im Lagenwachstum auftretenden organischen Molekülschichten zeigen keine dramatische Veränderung der zugänglichen strukturellen Information. Im Falle von Diindenoperylene (DIP) kann eine Kontraktion der Monolagendicke innerhalb des oberflächenabgewandten Lagenverbunds sowie eine leichte Expansion des in-plane Gitters beobachtet werden. Für N,N'-dioctyl-3,4:9,10-perylene tetracarboxylic diimide (PTCDI-C_8) zeigen die Auswertungen konstante Monolagendicken. Außerdem findet ebenfalls eine leichte Expansion der organischen triklinen Einheitszelle statt. Gitterparameteränderungen im beobachteten Größenbereich deuten auf Spannungseffekte innerhalb der organischen Schichten hin. Eine temperaturbedingte Gitterrelaxation innerhalb der organischen Molekülfilme in Folge der experimentellen Gegebenheiten wird als Ursache hierfür angenommen.

Der LiF-fcc-Gitterparameter expandiert mit zunehmender Materialablagerung auf beiden Moleküloberflächen und sättigt nach einer bestimmten abgelagerten Menge nahe dem Wert des Verbundfestkörperstoffs. Diese Gitterexpansion kann mit Anwesenheit von Nano-Partikeln erklärt werden, in denen verkürzte Gitterparameter aufgrund von internen Spannungen bereits beobachtet worden sind. Die Sättigung der Gitterparameterlänge kann dann mit der sich ausbildenden vollständigen LiF-Bedeckung erklärt werden. Vollständige Bedeckung ist durch die Veränderung der Schichtdicke des LiF/DIP Doppellagensystems direkt nachgewiesen worden. Konstante LiF-Korngrößen sind auf beiden Oberflächen innerhalb der gemessenen Schichtdicken beobachtet worden. Die absoluten Werte der Korngrößen weichen jedoch abhängig von der verwendeten Oberfläche voneinander ab, was im Widerspruch zu den gemessenen Inselhöhen der AFM Messung steht. Trotzdem kann behauptet werden, daß geschlossene LiF-Schichten aus kleinen Partikeln mit einheitlichen Größen aufgebaut werden. Poröse Strukturen speziell für geringe LiF-Schichtdicken und säulenartiges Wachstum bei steigender Schichtdicke werden bereits in der Literatur vorausgesagt.

Stabilität (Kapitel VII). LiF/DIP-Doppelschichtsysteme zeigen in Luft- und Helium-Umgebung eine Instabilität unter hochenergetischer Röntgenbestrahlung. Dieser Prozeß äußert sich durch Zerfließen der LiF-Partikel. Die Instabilität kann im Vakuum unterbunden werden. Röntgenreflektivität-Daten legen nahen, daß sich eine Zwischenlage von ungefähr 12 Å Dicke in beiden zerstörerischen Umgebungen ausbildet. Eine mögliche Erklärung für dieses Verhalten ist eine photochemische Reaktion zwischen hygroskopischem LiF und anwesendem Wasser.

Experimente mit parallelgewachsenen DIP- und LiF/DIP-Schichtsystemen unter Wärmeinfluß zeigen das Entnetzen der rein organischen Schicht. Das Entnetzen von DIP-Schichten läuft dabei in 2 Stufen ab. In der ersten Stufe reißt die organische Schicht auf, und es findet ein Zwischenlagentransport der organischen Moleküle von tieferliegenden Lagen zu den obersten Lagen statt. Dies führt zu lateralem Wachstum der jeweils obersten Lage. Die aufrecht stehende Anordnung der organischen Moleküle ist nach wie vor vorhanden, da die Filmoberfläche in der obersten Moleküllage atomar flach bleibt. In der zweiten Stufe werden durch das Zusammenfließen des organischen Materials Molekülinseln mit vielfach größeren Höhen beobachtet.

Das Entnetzen des DIP-Films kann durch das Aufbringen von LiF-Partikeln auf die organische Oberfläche verhindert werden. Die Gestalt des Schichtsystems wird dann durch nachfolgende Hitzebehandlung nur schwach verändert. Ein Eindringen der LiF-Partikel in die organische Schicht kann mittels Analyse der LiF-Inselhöhen beobachtet werden, welches bereits zu Beginn des Erhitzungsprozesses einsetzt. Die Eindringtiefe bewegt sich im Bereich einer organischen Monolage. Im Vergleich zur morphologischen Änderung speziell der rein organischen Oberfläche sind in der strukturellen Information des Schichtsystems nur leichte Änderungen zu sehen. Vermutlich tragen nur ungeordnete und dadurch mobile Bereiche innerhalb der organischen Molekülschicht zur Diffusion bei. Es kann angenommen werden, daß LiF-Partikel entweder diese ungeordneten Bereiche stabilisiert oder Adsorptionsplätze für die diffundierenden organischen Moleküle blockiert.

Leistungseigenschaften in organischen Solarzellen (Kapitel VIII). LiF-Zwischenschichten mit verschiedenen Dicken sind in Solarzellen mit organischen Hetero-Bindungen eingefügt worden. Die photovoltaischen Bauteile bestehen aus einer aktiven Donor-Acceptor Kombination (DIP/C_{60}) aus denjenigen organischen Materialien, die in dieser Arbeit hauptsächlich untersucht worden sind. Diese Materialien werden allgemein nicht für den Einsatz in leistungsstarker organischer Photovoltaik bevorzugt und zeigen deshalb auch nicht die besten Leistungseigenschaften. Wirkungsgrade von ungefähr 0.3 % sind für die rein organischen Solarzellen ohne den Einsatz von LiF erreicht worden. Diese Leistungseigenschaften sind allerdings ausreichend, um die wichtigsten Trends unter dem Einfluß von zunehmender LiF-Zwischenschichtdicke zu vergleichen. Es ist gezeigt worden, daß LiF-Zwischenlagen lediglich in sehr geringen Dicken die Klemmspannung der Solarzellen erhöhen, jedoch die Kurzschlußstromdichte verringern. Vergrößerte Ableitwiderstände bei geringen LiF-Bedeckungen können dabei die insgesamt reduzierten Stromflüsse erklären. Für den erhöhten Wirkungsgrad ist hauptsächlich der verbesserte Füllfaktor verantwortlich, der ein Indikator für verbesserte Leistungsauskopplung ist. LiF-Schichten in geringer Bedeckung führen zu einem Verschwinden der S-Form in den Strom-Spannungskurven und zu zunehmend diodenartigem Verhalten.

Eine weitere Serie von Solarzellen mit variierenden LiF Ablagerungsraten zeigt Wirkungsgrade von bis zu 1,2 %. Diese Werte sind dabei bis zu viermal größer als die Werte der effizientesten Solarzellen der vorherigen Serie, obwohl sie zum Teil identisch hergestellt worden sind. Die abweichenden Leistungseigenschaften innerhalb dieser Serie werden ebenfalls mit einer abweichenden Bedeckungsstärke der LiF-Schicht in Verbindung gebracht. Diese hat ihren Ursprung in der Verwendung einer Quarz-Kristall-Waage für die Herstellung der ultradünnen LiF-Schichten, die eine präzise Steuerung der Ablagerungsmenge in diesem Dickenbereich fast unmöglich macht. Die Messung zeigt, daß der positive Einfluß von LiF sehr stark von der Schichtdickenkontrolle während des Ablagerungsprozesses abhängt.

3. Über den positiven Einfluß von LiF in organischen Solarzellen

Das sehr robuste Wachstumsverhalten von sehr dünnen LiF-Schichten auf organischen Oberflächen ist vermutlich der Schlüssel zum Verständnis für die leistungssteigernden Eigenschaften bei Verwendung in organischen Solarzellen. Der Ausbildung von Nano-Partikeln mit kristallinen Eigenschaften, die direkt und indirekt auf allen untersuchten organischen Oberflächen bestätigt worden sind, wird dabei eine tragende Bedeutung zugewiesen. Diese Eigenschaft ist unabhängig von den zugänglichen Substrattemperaturen oder leichten Veränderungen der Ablagerungsgeschwindigkeit während des LiF-Wachstums. Geringe Änderungen der Kristallgitterparameter in den organischen Modellmolekülsystemen, die durch LiF-Abscheidung auftreten sind vermutlich nicht die verantwortlichen Mechanismen. Dieser Prozeß wäre von der jeweils verwendeten organischen Molekülschicht abhängig und ist damit eher unwahrscheinlich. Die Beeinflussung der organischen Kristallstruktur als den hauptsächlich verantwortlichen Prozeß anzusehen kann jedoch abschließend nicht geklärt werden.

Bevorzugtes Partikel-Haften auf ungeordneten Bereichen innerhalb der organischen Molekülschichten kann dafür verantwortlich sein, daß eine Verbesserung der elektrischen Eigenschaften nur für sehr geringe LiF-Bedeckungen um 1 % stattfindet. Sobald die ungeordneten Bereiche mit Partikeln besetzt worden sind, wirkt sich eine weitere Materialablagerung nur noch auf geordnete Bereiche innerhalb des organischen Netzwerks aus. Diese geordneten Bereiche sind jedoch für effizienten Ladungstransport und Ladungsextraktion notwendig. Der isolierende Effekt von LiF würde daraufhin dominieren.

In einem einfachen Szenario können die LiF-Partikel das Eindringen des Elektrodenmaterials in ungeordnete Bereiche innerhalb des organischen Netzwerks verhindern. Dabei würden die Ableitwiderstände vergrößert und parasitärer Ladungsfluß verhindert. Außerdem könnte sich das interne elektrische Feld verstärken, da der Abstand des Elektrodenmaterials zunimmt. In einem anspruchsvolleren Szenario können LiF Partikel die Potentiallandschaft an der Kontaktfläche durch ihre Wechselwirkung mit Deffektzuständen innerhalb der organischen Oberflächen verändern. Dies könnte durch induzierte Dipolmomente innerhalb der Partikel geschehen, die sich durch deren kristalline Eigenschaft bevorzugt einstellen. Da durch die LiF Partikel die Energiezustände von Defekten weniger zum gesamten elektronischen Verhalten an der Kontaktfläche beitragen, kann Fermi-Level-Pinnen an der Halbleiteroberfläche reduziert werden. Die isolierende Eigenschaft des Materials kann anschließend für die Ausbildung von selektiven Raumladungszonen innerhalb der ungeordneten Bereiche sorgen, die Ladungsfluß und zusätzliche Ladungseinfang innerhalb dieser Bereiche verhindern. Ladungsrekombination an der Kontaktfläche würde verbessert werden, weil nur noch geordnete Bereiche zur Ladungsextraktion beitragen.

MOTIVATION

The wording “without any alternative” has just won the election of the faux-pas-word in Germany 2010 due to its inflationary use in politics and society. In contrast, this wording is absolutely adequate regarding the changeover from fossil to sustainable energy sources in the next decades. Reasons are increasing energy consumption, finite nature of fossil fuel supply and the released climate change. A challenge of achieving this turnaround in the near future will be the development of already existent forms of renewable energy technologies towards a competitive state in the market but also the invention of new methods for clean energy supply. Direct conversion of sunlight into electrical power is one of the promising ways to realize non-polluting power generation. Photo voltaic devices based on inorganic materials showed their potential already in the late 1960th, when one of the first US satellites (Vanguard1), equipped with single crystalline silicon solar cells worked for almost seven years. By that time, many efforts have been achieved pushing light-to-power conversion efficiencies in Gallium based multi layer stack devices to an actual world record of 41.1 % [1].

A new class of materials for the use in semiconductor devices has reached the focus of research in the last years, namely organic semiconductors. Some of the unique features of organic molecules like their mechanical flexibility, their presumed cheap production costs and their availability are associated with an extensive area of applications, once the fundamental questions of the underlying physical mechanisms are answered and assembly processes are established. Many different approaches for increasing power conversion efficiency of organic photo voltaic devices have been proposed since the use of organic materials in solar cells is under investigation [2]. Up to now, values of 8.3 % [3] have been achieved. Milestones in this development are the invention of planar heterojunctions between donor and acceptor molecules [4] to create effective exciton-dissociation interfaces. In addition, the introduction of bulk heterojunctions from solution processed polymer-fullerene mixtures [5; 6] increased the device performance even more. The use of organic small molecule films with their ability of preparing well-defined multilayer structures [7] is currently under investigation. Structural properties in active organic materials and thus charge transport characteristics can be tuned with the use of such systems.

Another way of influencing power conversion efficiency of organic devices is the improvement of the contact and therefore the charge injection or extraction mechanisms by additional interlayers. Especially metal-fluoride ionic compounds seem to be good candidates for interfacial layers as described in more detail e.g. in [8; 9], even if the exact reason for the beneficial impact is still unknown. These empirical studies by testing in a trial and error process marked lithium fluoride (LiF) as a promising and already widely used material for improving device performance. Interestingly this is only valid for very low film thicknesses, typically in the range of less than one nanometer. LiF is a widely studied high band gap insulator and has some unique features. Structure, morphology and composition of LiF bulk material as well as in thin LiF films mostly on inorganic substrates are described in various publications but deviant results due to deposition techniques, post annealing processes and choice of substrates have been obtained.

In contrast, there is no exact knowledge about the morphology and structure of ultra thin LiF films grown on organic surfaces. Only speculations of the film growth have been proposed in the literature [10; 11]. Examinations on the positive impact of LiF interlayers in organic devices are mostly performed by indirect methods like spectroscopy techniques or analysis of the electrical IV-characteristics causing a speculative character of the suggested working mechanisms. To overcome this bottleneck, LiF films are grown on smooth amorphous substrates and organic molecules with layer-by-layer type growth modes, well known crystal structure, tunable surface morphology and atomically flat surfaces. This procedure allows decoupling the organic and inorganic morphological and structural features. Observation methods with nano resolution like atomic force microscopy (AFM), transmission electron microscopy (TEM) and x-ray diffraction (XRD) techniques allow the characterization of growth, dispersion and structure of ultrathin LiF films on these model systems. It may lead to a better understanding of the physical properties that are attributed to material incorporation at the contact area in organic devices.

I. BASICS OF ORGANIC SEMICONDUCTORS

First observation of photoconductivity in the organic compound anthracene ($C_{14}H_{10}$) by Pochettino in 1906 [12] and development of science in this field lead to the Nobel prize in chemistry (2000) for discovery and explanation of semiconducting properties of organic polyacetylen at ambient conditions for Heeger, Diarmid and Shirakawa [13; 14; 15]. Organic semi conductors are believed to be a low-cost and low energy consuming alternative to inorganic semiconductors, even if many of its physical and chemical properties like conductivity, charge carrier mobility or processing technology are not competitive so far.

1. Organic solid state bodies

A basic definition for the class of organic molecules is the presence of carbon as one of the main element constituents. Organic solids build up from these molecules can appear as organic single crystals, poly-crystal glasses or polymers. The main difference of organic compounds from inorganic solids is their internal bonding behavior leading to differences in their optical, electrical and mechanical properties. A comprehensive review is available e.g. in [16].

In summary, organic solids are formed by weak Van der Waals (VdW) forces between organic molecules. VdW linkage originates from the interaction between fluctuating multipole moments of neutral molecules with fully occupied molecular orbitals that do not allow the formation of ionic or covalent nor metallic bonding. The interaction is weak in comparison to covalent bonding and has very short range order. Binding energies of the VdW interaction are in the range of around 1-10 meV, which is a factor of thousand less than for covalent bonding interaction. The weak interaction between molecules in organic solids leads to properties of single molecules having much more influence on the whole than basic modules in other classes of solids. Due to the VdW binding, organic solids normally have lower melting and boiling points as well as lower dielectric constants, lower charge carrier mobility and higher compressibility in comparison to covalently-bonded inorganic solids. The short range of interaction forces between the molecules, however leads to the formation of high quality surfaces and interfaces with low defect and impurity concentrations. Organic solids are particular interesting because of their enormous variability. The physical properties such as band gaps can easily be tuned by minor chemical changes in the elementary composition. All these properties make them ideal candidates for future knowledge based material design and the development of cheap alternatives in various technological applications.

2. Delocalized π-bond systems

To understand the electronic properties of organic semiconductors, it is essential to elaborate the electronic configurations of Carbon that can be engaged in such molecule crystals. The electronic configuration of the ground state of an isolated carbon atom has four electrons in the outer electronic level, two paired s-electrons and two unpaired p-electrons in the configuration of $1s^2\,2s^2\,2p^2$ as demonstrated in [17]. One less stable electronic configuration, which is for example established in methane, the simplest representation of an organic compound, may be the mixing of the 2s- and the three 2p-orbitals

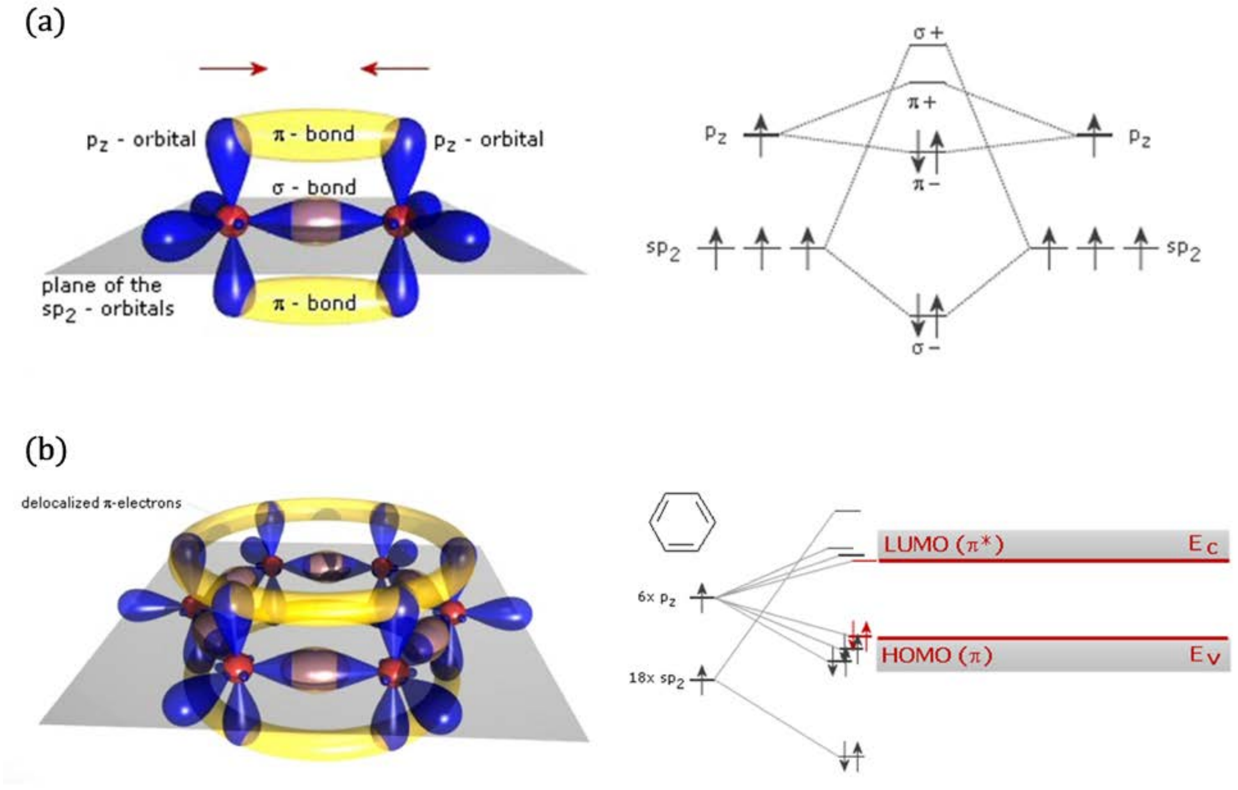

Figure I.1: Schematic view of sp_2*-hybridized electron orbitals of (a) ethen and (b) benzene. The double bond between carbon atoms is established by σ– and π-bonds with different binding energies respectively. The split in density of states for the valence electrons in comparison to the isolated atoms is shown beside. (From [18])*

creating a set of four equivalent degenerate orbitals denoted as sp^3 hybrid orbitals.

Another possible and often found configuration in organic semiconductors is the combination of the 2s orbital and two of the three originally orthogonal p orbitals to three sp_2 orbitals where the p_z orbital stays unaltered. The three sp^2 orbitals all lying in one plane and forming a triangle with angles of 120° between them while the p_z orbital is perpendicular to that plane, shown in Figure I.1(a) [18]. Bonds that are formed by overlapping sp^2 orbitals are so called σ-bonds. The energy gap between σ^- and σ^+ interdict excitation at room temperature. However, overlapping p_z orbitals can form additional binding sites denoted as π-bonds. Due to the low interaction between p_z-orbitals, the energy gap between the double occupied binding π^--orbital and the unoccupied non binding π^+-orbital is less pronounced in comparison to the energy gap of the σ-orbitals. π^{-}- π^{+} transitions from the filled to the unfilled levels can take place at moderate thermal energies and are responsible for optical absorption and semi conduction properties of most organic semiconductors. An important component of organic molecules where π-bond formation in sp^2 hybridized molecular orbitals occurs is the benzene molecule, shown in Figure I.1(b). This molecule is a prototype module for a system where σ-bonds, together with the nuclei, form a fixed potential in which the p_z-electrons can move. The p_z-electrons become delocalized and form a π -system with the extensions of the molecule. Due to the interaction of a large number of electrons, available states split up forming the highest occupied molecular orbitals (HOMO) and lowest unoccupied molecular orbitals (LUMO). Thus π- π^* transitions become available in such systems.

In organic semiconductors, the energy gap between occupied and empty states of HOMO and LUMO levels decreases with increasing delocalization and creation of additional excitation states. Energy gaps are usually in the range of 1-3 eV and correspond to the spectral range over the visible region from near infrared to near ultraviolet. The generation of optical excited states and dissociation to quasi free charge carriers become accessible. Again, the collective transport properties of the free charge carriers are dependent to the degree to which the π-electron system of one molecule is interacting with those of the neighbors. Finally charge carrier majorities in organic crystals are mostly intrinsic and created for example from shallow traps that are existent in the organic material. Nevertheless, doping in organic crystals is already in progress, see [19; 20].

II. SOLAR CELL PHYSICS

The efficient conversion of sunlight into electrical power needs detailed knowledge about the responsible physical mechanisms. To push the efficiency of photovoltaic device, all processes that contribute to the power conversion must be understood. The major processes in conventional solar cells are often realized in pn-junctions. Understanding the balance of flowing currents in this prototype junction helps to explain the experimentally accessible properties like current-voltage diagrams. In the description of organic solar cell operation, the concept of the pn-junction has to be exchanged by a model of heterojunctions between donor and acceptor materials. The process structure of organic photovoltaic devices has to be extended and will be discussed in more detail.

1. Micro- and macroscopic quantities in conventional semiconductors

In conventional semiconductor physics, well explained for example in [21] or [22], a material is called a semiconductor if the energy gap $E_{\mathrm{G}} = E_{\mathrm{C}} - E_{\mathrm{V}}$ between the valence and conduction band has typical numbers between 0.5-2.5 eV. An additional requirement is the full occupancy of the states in the valence band at $T = 0$. The number of available charge carriers for conduction is represented by the charge carrier density per energy and volume [eV^{-1}cm^{-3}] in the respective bands given as:

$$n^{\mathrm{e}}_{\mathrm{C}}(T) = \int_{E\mathrm{c}}^{\infty} D(E) f_{\mathrm{FD}}(E,T)dE, \tag{II.1}$$

$$n^{\mathrm{h}}_{\mathrm{V}}(T) = \int_{E\mathrm{c}}^{\infty} D(E)[1 - f_{\mathrm{FD}}(E,T)]dE. \tag{II.2}$$

The function $D(E)$ describes the available density of states (DOS) determined by solving the Schrödinger equation of the charge carriers in a given potential and for a considered energy. The split in two charge carrier concentrations for electrons and holes is a result of the energy gap of available states in k-space. It is caused by the periodic potential of the semiconductor crystal. The occupancy of available states in the valence and conduction bands, given by $D(E)$, is determined by the temperature and material dependent Fermi distribution:

$$f_{\mathrm{FD}}(E,T) = \frac{1}{\exp((E - E_F)/k_B T) + 1}. \tag{II.3}$$

The Fermi energy E_F is defined in general universality by $f_{\mathrm{FD}}(E = E_F) = 1/2$. For intrinsic semiconductors, E_F is placed in the middle of the energy gap. The behavior of semiconductors can be tuned by adjusting the two main quantities DOS and Fermi energy of the involved materials. Thermal and optical excitation processes are improved by an appropriate density of states $D(E)$ in the valence and conduction band regime. The Fermi energy E_F is positioned by implementation of defects, impurities, dopant atoms or guest molecules into the crystal compound. Doping will result in the creation of available states placed in the energy gap of the intrinsic semiconductor. These additional states are responsible for a shift of Fermi energy near the band edge of the valence band in case of a p-type or near the band edge of the conduction band in case of an n-type semiconductor at medium and low temperatures. The outcome of semiconductors with majority/minority charge carriers like electrons/holes in the n-type and holes/electrons in p-type configuration is achieved.

To link the microscopic quantities of a semi conducting material with the electrical behavior, one can imagine the situation where an external voltage is applied between two contacted sides of a semiconducting material. An electrical current will then flow due to the electrical field F:

$$j_{e,h} = \sigma_{\mathrm{el}} F \tag{II.4}$$

The proportionality factor σ_{el} is called electrical conductivity and is written as:

$$\sigma_{\mathrm{el}} = qn\mu. \tag{II.5}$$

This parameter is related to the specific resistivity by $\rho_{\mathrm{el}} = 1/\sigma_{\mathrm{el}}$. It depends on the charge q (+e for holes, −e for electrons) and the carrier density n_i of majority charge carriers, given in equation (II.1). Typical insulators have resistivity around 10^{10}-10^{20} Ωcm, conductors below 10^{-5} Ωcm and perfect semiconductor crystals 10^{4}-10^{8} Ωcm. The charge carrier mobility μ [$\mathrm{cm^2V^{-1}s^{-1}}$] in (II.5), is the fundamental (intrinsic) electronic transport quantity, which is specific for each semi conductor material. It also defined over the drift velocity in the field by:

$$v_{\mathrm{D}} = \mu F. \tag{II.6}$$

An explanation of experimentally observed values of $\mu(T, F)$ by various methods, described e.g in [23], is the key for understanding the conduction behavior and charge generation.

2. The pn-junction

Conventional solar cells are typically made of heterojunctions between p- and n-type semiconductors. The advantage of combining two materials with different band gaps in a heterojunction are as follows: In the first place the absorption range of light can be extended. Secondly, transport of excess charge carriers to their respective electrodes is improved by a potential difference established between the two materials. The principle of a pn-junction of identical but differently doped materials demonstrates already the essential parameters.

Figure II.1 shows the schematic energy alignment of p- and an n-type semiconductor in contact. According to [24] the pn-junction has a contact potential energy that is equal to the difference in energy of the two

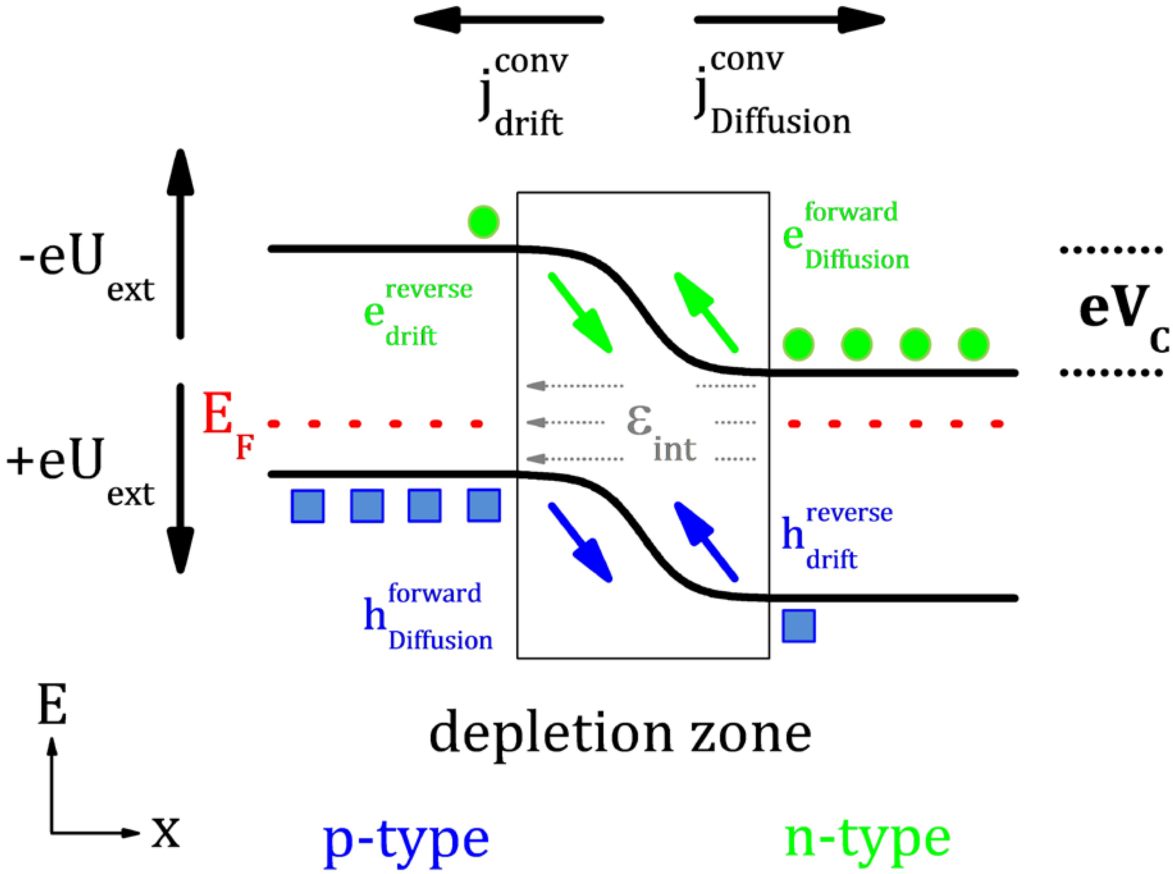

Figure II.1: Schematic charge and current flow for a pn-junction in equilibrium conditions. The balance between diffusion currents $j_{Diffusion}$ of majority- and drift currents j_{drift} of minority charge carriers can be varied by an applied external bias. Diffusion currents are dependent on the height of the energy barrier whereas drift currents are only proportional to the excess charge generation and recombination ratio. The arising internal field ε_{int} is dependent on the width of the depletion zone. It is sensitive to dopant concentrations and dopant energy levels (not drawn).(Reproduced from [21])

conductions bands:

$$eV_C = E_{\mathrm{C_p}} - E_{\mathrm{C}_n}. \tag{II.7}$$

The contact potential is also called built-in potential and is connected to the width of the depletion zone. This energy difference is related to the original Fermi energies as they are aligning towards a common energy level when the materials are brought in contact. Since n- and p-type materials are usually obtained by doping, the width of the depletion zone is dependent on the respective dopant donor or acceptor element concentrations. The derivation

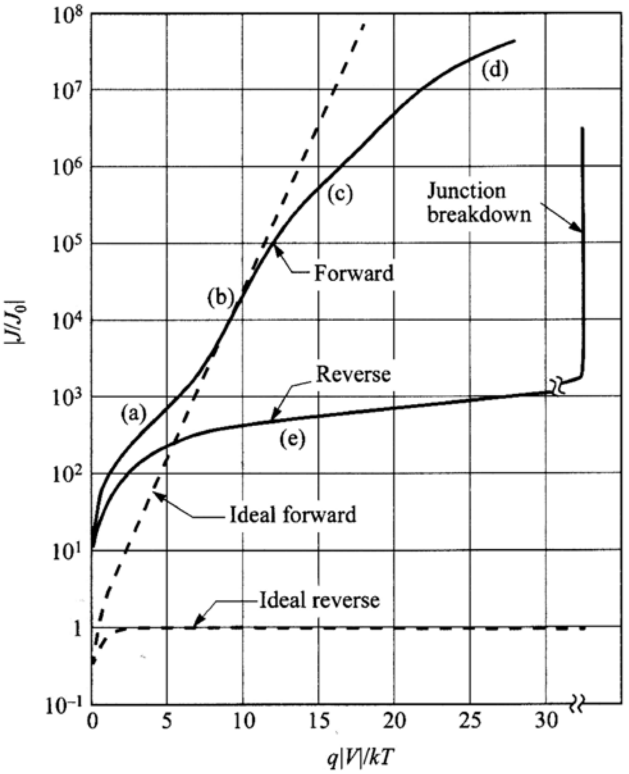

Figure II.2: Logarithmic current voltage characteristics of real vs. an ideal diode. Processes that are responsible of the displacement between real and ideal curve labeled in the figure are described in the text. (From [22])

of the contact potential in this way is valid only for conventional and ideal pn junctions.

The net flowing currents of the pn-junction under equilibrium conditions are zero, but internal current have to be considered. The internal currents are commonly termed forward and reverse currents. By convention, forward currents in a pn-junction are flowing due to a concentration gradient of majority charge carriers and are called diffusion currents. These currents are dependent on the barrier height between n- and p-type materials.

Diffusion currents are balanced by the so called drift currents which are dependent on the number of free excess charge carriers that exist in the system. This number is directly related to generation and recombination mechanisms and defined by material properties. Drift currents are flowing due to the energy gain of minority charge carriers when passing to the region where they become majorities.

When the pn-junction is contacted to an outer circuit, the current characteristics for applied potentials are described by the Shockley equation [25]:

$$j = j_0 \left[\exp\left(\frac{eU_{\text{ext}}}{nk_B T} \right) - 1 \right]. \tag{II.8}$$

In this equation, n is the ideality factor which indicates where recombination processes occur. This can either happen in the depletion region ($n = 1$) or in the neutral volume ($n = 2$). By convention a reverse bias tends to increase the energy barrier height at the junction and lowers the diffusion current. In this condition the saturation current j_s is flowing mediated only by drift currents. Saturation currents are electrically limited by generation- and recombination ratios of excess charge carriers and by their diffusion or drift lengths. Forward bias lowers the energy barrier at the interface and increases the diffusion currents.

Departures from the ideal behavior of a diode, shown in Figure II.2 are mainly caused by (a) generation and recombination of carriers in the depletion layer, (b) the high-injection condition that may occur even at relatively small forward bias, (c) parasitic current drop by series resistances, (d) tunneling of carriers between states in the band gap and (e) surface effects. In addition junction breakdown is expected under sufficiently large bias in the reverse direction.

3. Solar cells described in the diode model

The principle of an ideal solar can be understood as an illuminated diode where free excess charge carriers are generated by light increasing the drift current components of the diode. A conventional solar cell is realized by a pn-junction, contacted with two metals that have different workfunctions. One of the electrodes has to be transparent to allow excess charge carriers creation by optical absorption. The photo generated current j_{Ph} is limited by generation and recombination ratios of charge due to light absorption. Hence, the photovoltaic effect is observed in reverse bias conditions of a diode.

In a realistic model of an illuminated and contacted solar cell, the Shockley diode equation has to be expanded by resistances that appear in operation mode. The replacement circuit of a solar cell in Figure II.3(b) shows the arrangement of the additional resistivity. Due to losses in the contact or bulk, the series resistance R_S is introduced. The parallel shunt resistance R_P is attributed to charge conduction over the surfaces or to charge conduction through the junction via defects. Taking both resistances and the photo currents j_{Ph} into account, equation (II.8) has to be replaced by:

$$j = j_0 \left[\exp\left(\frac{eU_{\mathrm{ext}}}{nk_BT}\right) - 1\right] + \frac{V - jR_S}{R_P} - j_{\mathrm{Ph}}\,. \tag{II.9}$$

In ideal solar cells, parallel shunt resistances should be infinite while series resistance should be zero. In real solar cells, the resistances can be estimated by graphical methods. Since parallel shunt resistances are typically a few orders of magnitude larger than series resistances, the voltage drop at the series resistance at low voltages can be neglected. The value of the shunt resistance is estimated from the slope of the IV-curves at zero bias. When higher forward bias is applied, the diode becomes conductive and its resistance shrinks to zero. Currents are not limited by the parallel resistance anymore and only the series resistance determines the current-voltage relation. Thus the series resistance can be estimated by the slope of IV-curves at large positive bias.

To characterize a solar cell, a linear voltage sweep is applied to the device in the dark and under illumination. Resulting currents are measured and divided by the active area of the solar cell. This yields to the current density j. Key parameters for the light to power conversion process are indicated in Figure II.3(a). Following the conventional description, the short circuit current density $-j_{\mathrm{sc}}$ and the open circuit voltage V_{oc} are the intersections of the illuminated current-voltage curve with the j- and V-axis respectively. The power of the solar cell is extracted from the fourth quadrant of the illuminated IV- curve.

The generated maximum power density p_{MPP} results from the absolute value of the product of current j_{MPP} and voltage V_{MPP} at the maximum power point. The ratio between the maximum power and the product V_{OC} and j_{sc} is called the fill factor FF of the solarcell:

$$FF = \left|\frac{V_{\mathrm{MPP}}j_{\mathrm{MPP}}}{V_{\mathrm{oc}}j_{\mathrm{sc}}}\right|. \tag{II.10}$$

The fill factor illustrates the deviation of the generated power from the measured solar cell to the one that is theoretical possible in the particular system. With the introduction of the fill factor, the power conversion efficiency η of a solar cell is calculated as the ratio between the maximum generated power of the cell and the power density of the incident light p_{ill}:

$$\eta = \frac{p_{\mathrm{MPP}}}{P_{\mathrm{ill}}} = FF\,\frac{V_{\mathrm{oc}}j_{\mathrm{sc}}}{p_{\mathrm{ill}}}. \tag{II.11}$$

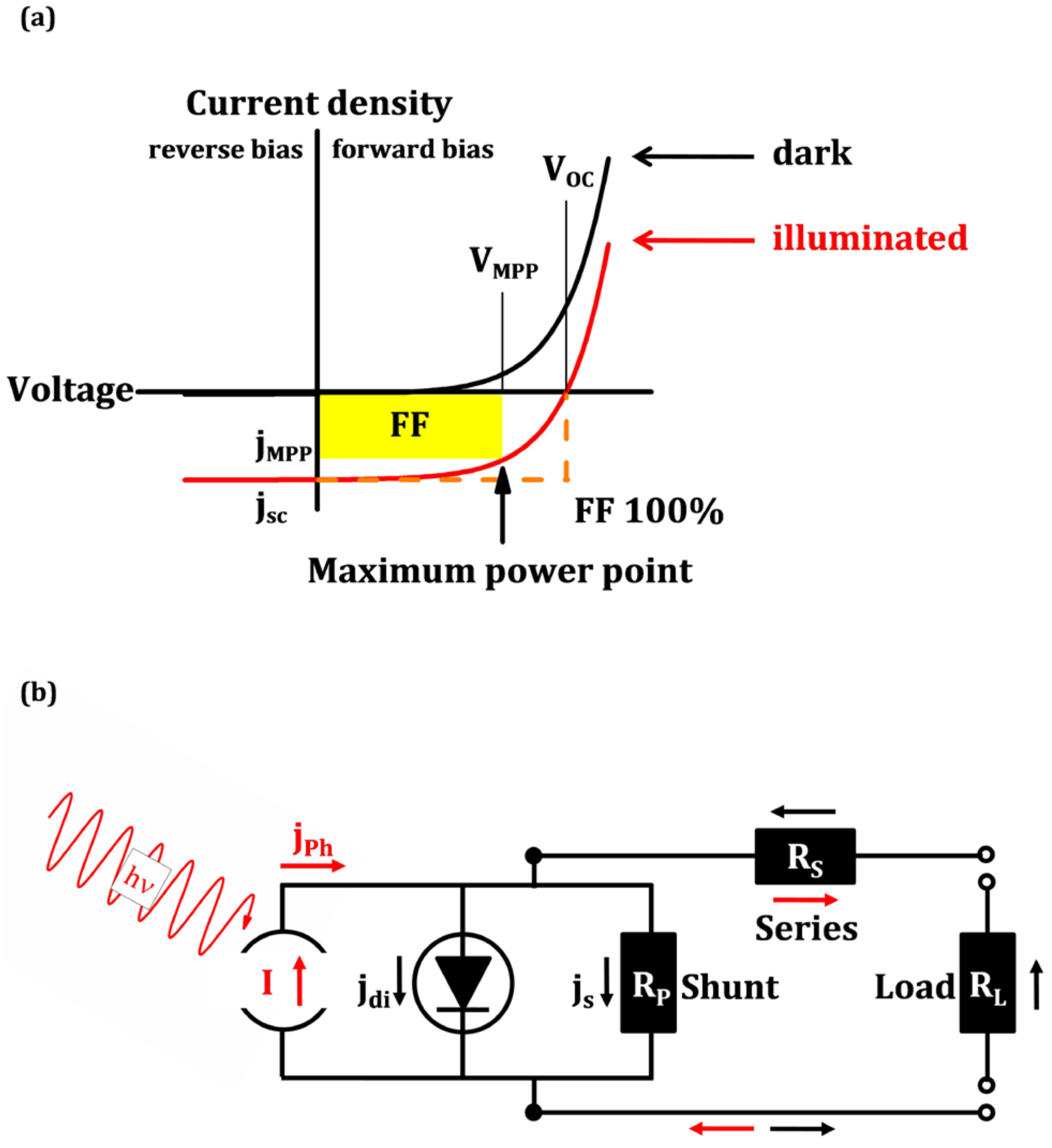

Figure II.3: (a) IV-characteristics of an ideal solar cell. The currents follow the realistic diode equation (II.9). Parameters for electrical characterization are indicated. (b) For the description of a realistic solar cell, resistances according to the replacement circuit have to be taken into account.

When the solar cell is illuminated with monochromatic light, insight into the excess charge carrier generation and charge transport processes is achieved. The spectral response $\mathrm{SR}(\lambda)$ is given by the ratio of the short circuit current density measured at a particular wavelength λ and the radiant flux of the incoming light at that wavelength:

$$\mathrm{SR}(\lambda) = \frac{j_{\mathrm{sc}}(\lambda)}{P_{\mathrm{ill}}(\lambda)}. \tag{II.12}$$

The wavelength dependent ratio of generated electrons per area and second in the external circuit to the number of the incoming photons per area and seconds, is denoted as the external quantum efficiency $\mathrm{EQE}(\lambda)$. It is derived with the help of the Planck-Einstein equation $E = hc/\lambda$ as as the fraction of current per area divided by charge of an electron and total light energy per area divided by the energy of a single photon:

$$\mathrm{EQE}(\lambda) = \frac{j_{\mathrm{sc}}(\lambda)/e}{P_{\mathrm{ill}}(\lambda)/(\lambda/hc)} = \mathrm{SR}(\lambda)\frac{hc}{\lambda e}. \tag{II.13}$$

In words, the EQE is a measure of how many of the incoming photons are converted into accessible charge carriers.

4. General mechanisms in organic solar cells

The general mechanisms in an organic solar cell are shown in Figure II.4. Instead of direct charge generation by light absorption like it appears in conventional solar cells, generation of free excess charge carriers is mediated by the formation of bound electron hole pairs which are treated as quasi particles and called excitons.

If the diffusion length of an exciton is sufficiently long, it travels through the material until it reaches a donor-acceptor interface. There it splits due to the internal field that is established in the depletion zone (see also figure Figure II.1). The relatively long lifetime of excitons in organic molecular crystals and thus long diffusion lengths in the range of several 10th of nanometers guaranties the conversion of light into electrical power in organic devices. Ultrafast charge transfer within the dissociation process, typically less than 100 fs, guaranties efficient organic photovoltaic devices performance. This transfer time is an order of magnitudes smaller than competing processes like radiative or non-radiative recombination occurring in the ns or sub ns time scale.

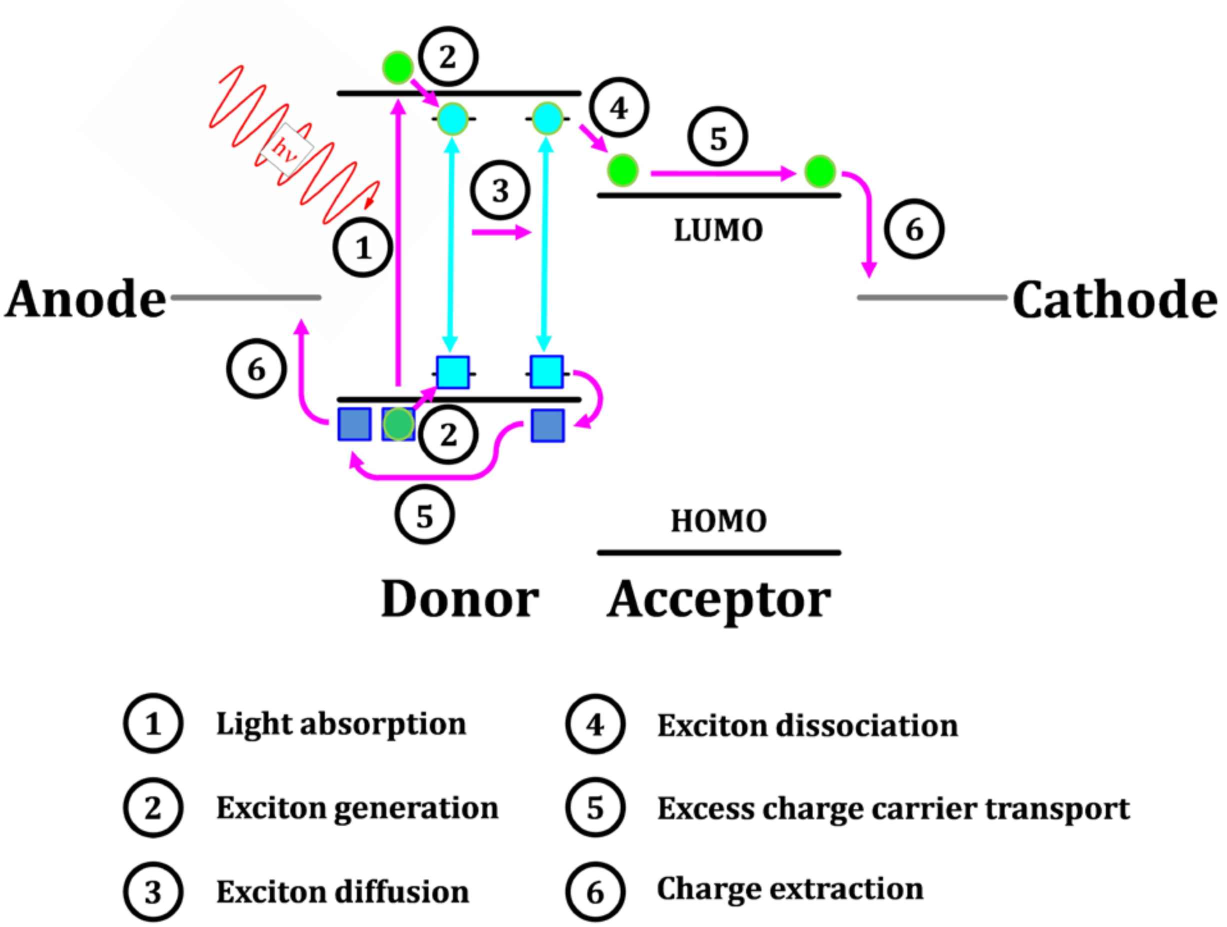

Figure II.4: Process structure of an organic donor-acceptor type organic solar cell. Each process contributes to the total efficiency of a photovoltaic device and has to be understood. Note that the process structure is indicated only at the donor side but occurs also in the acceptor material replacing holes with electrons. (Reproduced from [26]).

Once the excitons are split, free excess charge carriers can move, mostly by hopping transport mechanisms, to the respective electrodes. Finally, the charge is extracted to an external circuit where it can be used for applications. The overall efficiency of such a process is described by the product of all single processes:

$$\eta_{\text{total}} = \eta_{\text{Ab}} * \eta_{\text{Eg}} * \eta_{\text{Ediff}} * \eta_{\text{Ediss}} * \eta_{\text{Ct}} * \eta_{\text{Ce}} \,. \qquad \text{(II.14)}$$

Various reviews about the processes in organic solar cells are available, e.g. in [26; 27; 28; 29].

5. Excitons

The electronic alignment of the HOMO and LUMO levels in organic semiconductors mostly do not allow direct generation and separation of charge carriers at room temperature. Nevertheless, charge generation in such material is possible by photo excitation. The creation of electron hole pairs, so called excitons, bound by the Coulomb force takes place. Their dissociation at adequate interfaces leads to the formation of excess charge carriers. This happens either within a single homogenous layer or with much higher efficiency at interfaces of donor-acceptor systems.

Excitons can be understood as quasi particles described by additional energy states for electrons and holes with binding energies smaller than the band gap. According to [16], different forms of excitons are known namely Frenkel-type, Charge-transfer-type, Surface-type and Mott-Wannier-type. The separation into different types is attributed to the spatial localization of the excited electrons and holes from each other. For Frenkel excitons, the correlated electron-hole pair is localized on the same molecule and can move through the lattice in this form. Frenkel excitons are the typical form of excited states in organic crystals. Charge-transfer excitons have localization around the distance of two molecules between the correlated electron-hole pair. For Wannier excitons the distance between the excited electron and the hole which has been left can reach orders of magnitude of the crystal lattice units. This type of excitons is the usual form in inorganic semiconductors.

Due to the strong localization of Frenkel excitons, typically less than 5 Å, large Coulomb interaction and therefore strong exciton binding energies are observed. It follows a smaller optical gap than the excess charge carrier gap. Also thermal separation of excitons is unlikely because of their strong binding energy. Frenkel excitons have binding energies of 0.4 – 1.2 eV which are the lowest for the named types. Energy calculations show the creation of singlet and triplet states dependent on the spin states of the excited electrons ($S=0$ or $S=1$). Recombination processes take place via fluorescence of phosphorescence mechanisms serving for a long lifetime of excitons, see Figure II.5.

The motion of excitons is described by two different models. In resonance theory of Förster [30], energy transport is mediated by radiationless dipole-dipole interactions. The excited donor relaxes to its ground states, while a neighboring molecule is excited. The model involves only spin allowed transitions and energy transfer occurs over a distance in the range of 10 nm. It is the usual form of motion between singlet-singlet states.

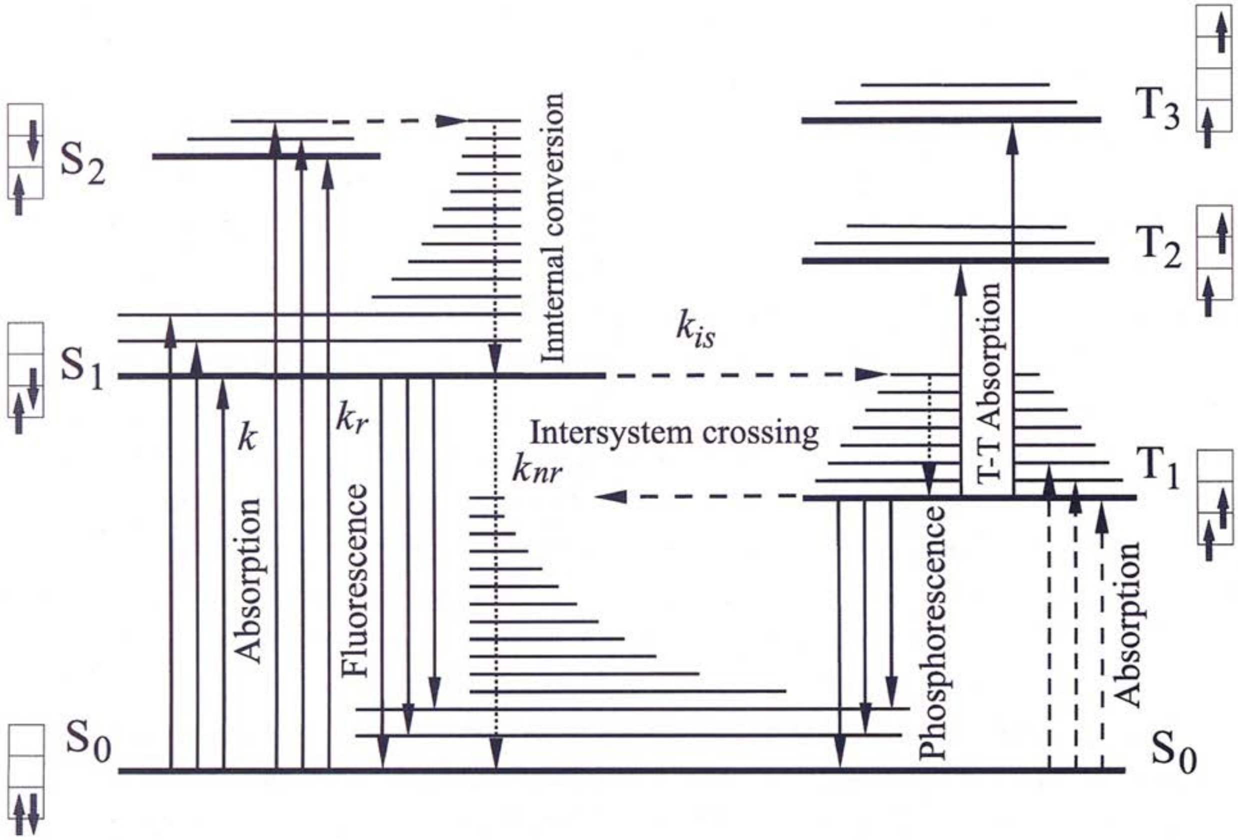

Figure II.5: Scheme of the energy terms of a molecule or molecular crystal. The electronic ground state S_0, the electronic singlet (S_1, S_2) and triplet (T_1, T_2, T_3) excited states as well as the vibronic states are shown. Triplet states have a total spin quantum number of S=1, while for singlet states, S=0. Light-induced transitions between singlet and triplet systems are therefore in general forbidden. Radiative transitions occur by absorption in the singlet and triplet systems, fluorescence and phosphorescence. Radiationless transitions take place as internal conversion from the higher to the lowest electronic excited states S_1 and T_1, as well as intersystem crossing. k is the rate constant for absorption, k_r for fluorescence and k_{nr} radiationless transfer (From [16]).

The Dexter mechanism [31] explains the transport by energy transfer mediated by exchanged electrons. It is referred as a radiationless transfer of energy by sensitized luminescence and is valid also for forbidden transitions. Dexter like transport occurs mostly for triplet-triplet transitions and over a range of up to 100 nm.

Exciton transport in general is modeled by the setup of a differential equation similar to Gaussian diffusion for the local exciton density $p(\boldsymbol{r})$:

$$D\frac{\mathrm{d}^2p(\boldsymbol{r})}{\mathrm{d}^2\boldsymbol{r}}+G(\boldsymbol{r})-\frac{1}{\tau_0}p(\boldsymbol{r})=0. \qquad \text{(II.15)}$$

The quantity $G(\boldsymbol{r})$ is the exciton generation rate. The diffusion coefficient D is a material specific parameter and is experimentally determined e.g. by measurements of sensitized fluorescence. The exciton is coupled with its lifetime τ_0 defining the exciton diffusion length:

$$L=\sqrt{D\tau_0} \qquad \text{(II.16)}$$

Exciton diffusion lengths are relatively long, even if the mobility of excitons is much lower than that of quasi free charge carriers. The crucial factor for this behavior is the long lifetime by reason of the strong internal binding energy of excitons.

6. Charge carrier transport

Charge carrier transport in semiconducting materials is one of the key features of understanding any device performance. It is generalized by the two scenarios: single crystals of organic molecules with delocalized π-electron systems show remarkable band like transport for a wide temperature range. Charge transport in polycrystalline or amorphous layers shows band like transport only for low temperatures whereas hopping transport with thermally activated charge carriers dominates for high temperatures. Experimentally observed temperature dependences of the charge carrier mobility are deviating from each other in both transport types.

According to [16], the question whether band or hopping transport mechanisms predominate in organic semiconductors can be tested by using a few clear cut criteria. For band conductivity, the mean scattering time τ_s of the charge carriers must be large in comparison to $\hbar/\Delta E_\mathrm{C}$, with ΔE_C as the band width of the conduction band. Also the mean free path length λ must be long in comparison to the lattice constant a_0 in the electrical field direction. In this case, charge carrier flow is described by Space-Charged Limited Current (SCLC) requiring no thermally-activated charge carriers.

Band like transport of quasi free charge carriers is realized only in an idealized situation of single crystals. The current is modeled by a plate capacitor thanks to a potential difference U and is also known as Child's law, namely:

$$j=f\varepsilon\varepsilon_0\mu(T)\frac{U^2}{d^3}. \qquad \text{(II.17)}$$

The relation is derived from the combination of equation (II.4) and (II.5). The density of free charge carriers n in equation (II.5) is quantified by charge and capacity of the configuration $n = Q/V = C * U/Ad = \varepsilon\varepsilon_0 A/d * U/Ad$ and the definition of the electrical field defined by $F = f\, U/d$. In the field independent case the numerical factor f is determined by the so called Mott-Gurney equation by $f = 9/8$ and the current is termed Trap Free Space-Charge Limited Current (TF-SCLC).

The weakness of the VdW interactions between the molecules in the crystal causes strongly localized wave functions of excess charge carriers. Hence the generation of excess charge carriers leads to an electrical polarization of the molecule in their next neighborhood. The relaxation time of this polarization is a factor 100 less than the time, needed for thermally assisted tunneling of charged carriers to neighboring molecules. It means that the polarization follows the charge motion nearly instantaneously and the excess charge carrier together with its polarized neighborhood is called a polaron. Model of band like transport of the emerging free charge carriers doesn't hold anymore for polaron transport so hopping mechanisms have to be deployed.

In contrast to band like transport, hopping mechanisms are actually discussed in various models, which are reviewed in [32]. The mobility for charge hopping transport is smaller by orders of magnitude than in crystals and the temperature dependencies are inverses over a large temperature interval compared to a conventional semiconductor. A model was first proposed by Abrahams and Miller [33] and is evaluated for the experimentally accessible quantities in polaron hopping transport [34]. The mechanism is also termed nearest neighbor hopping and depends on the difference between energies ΔE of the two states, the hopping probability ν_{Ph} attributed to the phonon spectrum and the factor α dependent on the overlap of the wave functions. The charger carrier current in case of electrons is then achieved by multiplying the electrical charge e, the hopping distance R, the number of electrons per unit cell $2N_e(E_F)k_BT$ and the difference of hopping probabilities in the two directions of the electrical field $\nu_{\mathrm{Ph}}e^{-2\alpha R-(\Delta E\pm eRF)/k_BT}$. It is thus:

$$j = 2eRN_e(E_F)k_BT\ \nu_{\mathrm{Ph}}\exp(-2\alpha R)\exp\left(-\frac{\Delta E}{k_BT}\right)\sinh\left(\frac{eRF}{k_BT}\right). \qquad \text{(II.18)}$$

The mobility that is derived from this model is obtained for weak fields $eRF \ll k_BT$ from the combination of equation (II.4) and (II.5) with:

$$\begin{aligned}\mu(T) &= \frac{j}{en_eF} = 2eR^2\,\nu_{\mathrm{Ph}}\exp(-2\alpha R)\exp\left(-\frac{\Delta E}{k_BT}\right)\\ &= \mu_0\exp\left(-\frac{\Delta E}{k_BT}\right).\end{aligned} \tag{II.19}$$

Even if various models were developed and proved on nicely ordered organic systems, the use of these models for disordered organic semiconductors is still controversial. Whether the charge carriers follow band or hopping transport has to be decided individually for each material system up to now.

7. Contact properties

7.1. Fermi level pinning

Real semiconductor surfaces as well as semiconductor metal interfaces have a different electronic alignment than the bulk material. In a simple view, the surface of a semiconductor can be understood as a specific material and is thus already a good model system for general contact behavior, see Figure II.6. By reason of the suboptimal saturation of bonding sites within the surface differing available states for majority charge carriers are expected. These states are created especially in the band gap of the semiconductor. It follows that the Fermi energy of the surface will be lowered, independently of the Fermi energy from the bulk material; in other words the Fermi energy is pinned inside the band gap of the semiconductor.

Studies on organic photovoltaic devices covered with metals of different workfunctions by Brabec et al. [35] turned out that the leading mechanism for charge extraction is not attributed to the electronic alignment of the metal

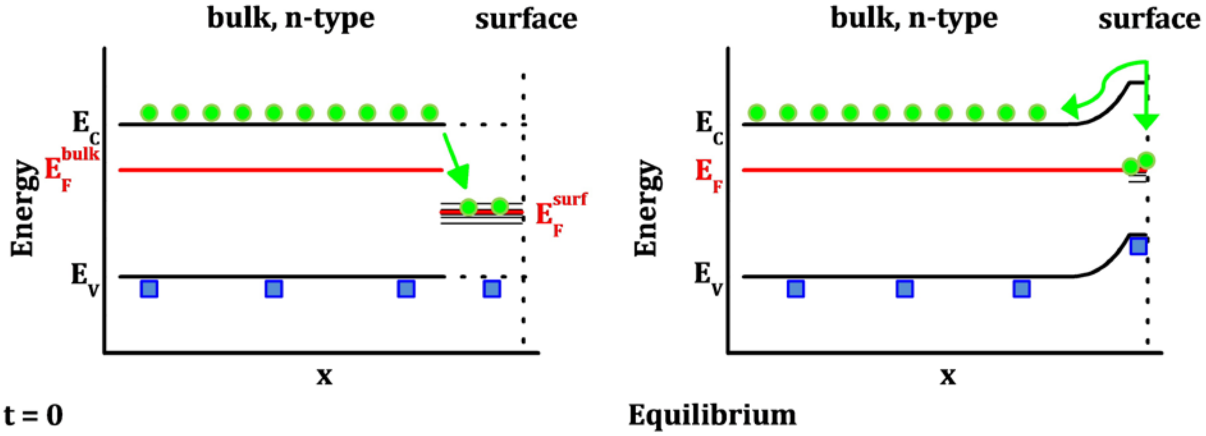

Figure II.6: Fermi level pinning in a semiconductor is attributed to the creation of additional states in the band gap due to energy alignment at the surface.

electrodes. Instead, Fermi level pinning due to defect states that contribute to interface barriers or midgap states are assumed to play a crucial role.

7.2. Contact types

When a semiconductor is in contact with metal, two major types of contacts can be distinguished. The classification of a specific contact is dependent on the work functions of the involved materials. The workfunction is the difference between the vacuum level and the Fermi level. The quantity is denoted as $q\Phi^{M}$ in case of the metal and $q\Phi^{SC}$ in case of the semiconductor. $q\chi$ is the electron affinity measured from the bottom of the conduction band to the vacuum level.

In a notional contact of surface and bulk, electrons (or holes) are travelling towards the surface expressed in the alignment of both Fermi energies. Depletion zones are created near the surface and band bending of conduction and valence bands will appear. The surface will be charged until an electrical field that is established in the depletion zone compensating more energy gain. This behavior serves for an energy barrier or sinks with the height of the difference between the workfunction of the metal and the electron affinity $q\chi$ of the semiconductor. Band bending at interfaces in general is a concept of conventional semiconductor materials that support band-like transport. Even if in organic semiconductors bands are replaced by the HOMO and LUMO levels of the molecular crystal, the concept of band bending for Fermi energy alignment within the metal-semiconductor interface is commonly used.

According to [21], two types of contacts are distinguished. In case of an n-type semiconductor, the contact is called a Schottky type contact when the workfunction of the metal is larger than that of the semiconductor. The contact is called an Ohmic contact when the workfunction of the metal is smaller compared to the one of the n-type semiconductor, see Figure II.7. This behavior is vice versa for p-type semiconductor. In case of a Schottky type contact the depletion zone is acting as an energetic barrier. The origin of the barrier is again explained by charge separation at the interface and an establishing internal electric field. Charge injection for these kinds of contacts can occur with a combination of three different processes which are described in detail in [22]. The processes are either thermionic emission (TE) over the barrier, field emission (FE) near the Fermi level or thermionic-field emission (TFE) at energies between TE and FE. While thermionic emission is a diffusion process, field emission is described as pure charge carrier tunneling. Therefore, TFE is a combination of both. In this case thermally excited charge carriers are tunneling through the barrier. The height and width of the energy

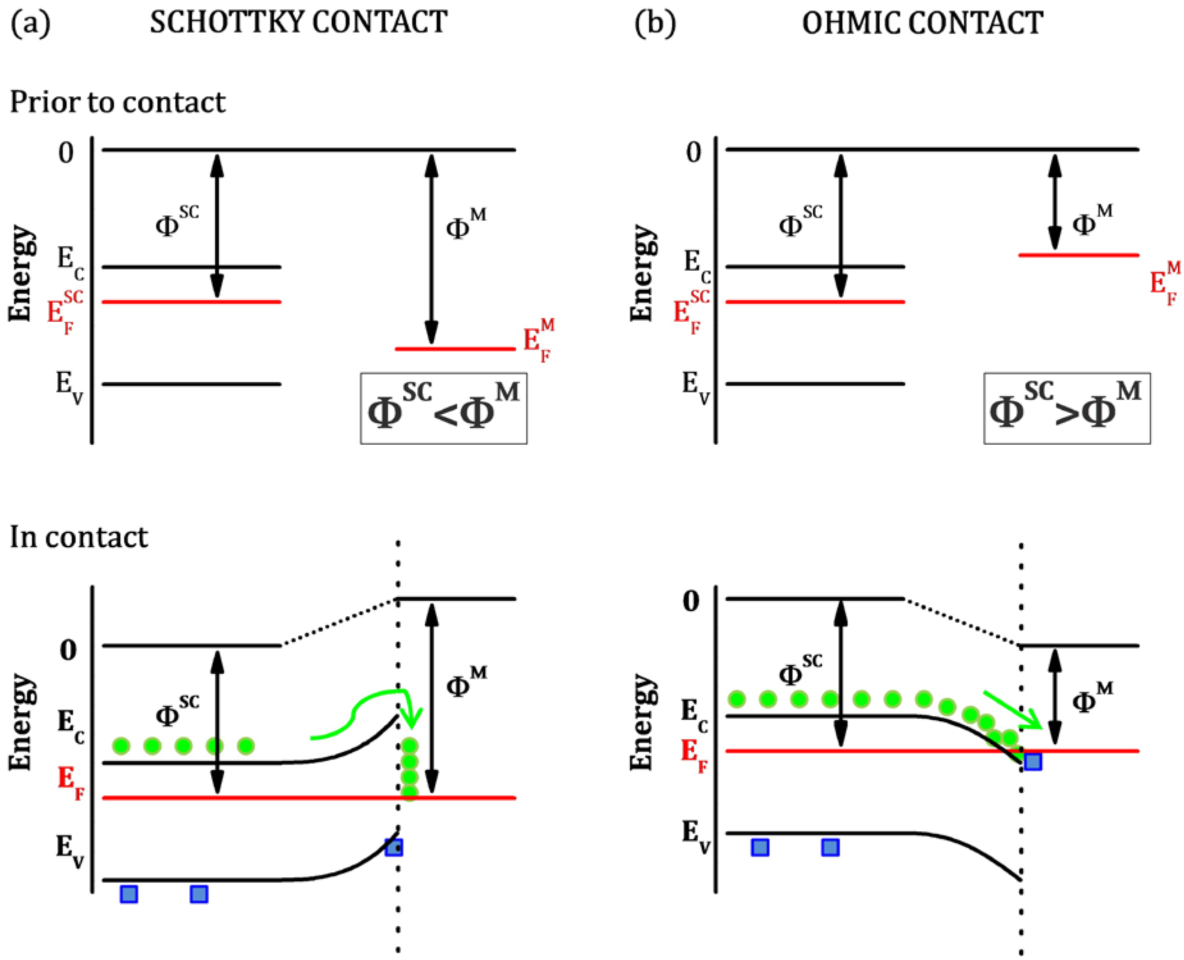

Figure II.7: Two different types of contact formation between an n-type semiconductor and a metal. (a) If the workfunction of the metal Φ^M *is larger than that of the semiconductor* Φ^{SC} *a Schottky contact is formed. (b) If the metal workfunction is lower, the contact is called an Ohmic contact. The contact type dependency with the workfunction difference between metal and semiconductor is vice versa for a p-type semiconductor. (Reproduced from [21])*

barrier is also influenced by image charges, arising at the metal side of the interface.

When an ohmic contact is formed, the energetic alignment, shown in Figure II.7(b) leads to accumulation of charge carriers in the semiconductor near the contact interface. The density of majority charge carriers is then locally increased and an accumulation zone is formed. The dimension of the accumulation zone is identical with the penetration depth of an external electrical field in the considered material. The width of the zone is called

Debye length. Charge flow from semiconductor to metal or metal to semiconductor is mainly unhindered. The current that flows through the contact is finally limited only by ohmic resistivity.

7.3. Metal-insulator-semiconductor (MIS) contacts

Metal-insulator-semiconductor structures, realized in the ideal conditions without existent charges in the insulating material and infinite resistivity in the insulator, are treated as ideal voltage controlled variable capacitor. Figure II.8 shows the energy alignment of such a structure for an n-type semiconductor with matching workfunctions of the metal and semiconductor for simplicity. When the MIS capacitor is biased with positive or negative voltages, three different cases can exist at the surface. For large negative bias voltages, the number of minority charge carriers at the surface, which are holes in n-type materials, is larger than the number of majority charge carriers (vice versa for p-type semiconductors). The surface is inverted and this is called inversion case. The depletion case occurs for small applied negative bias where only a depletion zone is created. Small applied positive bias lead to the accumulation case, where majority carriers are accumulated on the semiconductor surface.

Due to the concentration of charge an electrical field is established across the depletion zone. According to [22], the field *F(x)* is calculated by the potential Φ_p defined between the Fermi level of the intrinsic semiconductor E_i in the bulk and the after band bending, see Figure II.9:

$$F(x) = \frac{\sqrt{2}\mathrm{k_B}T}{qL_\mathrm{D}} f\left(\frac{q}{\mathrm{k_B}T}\Phi_p, \frac{n_0}{p_0}\right). \tag{II.20}$$

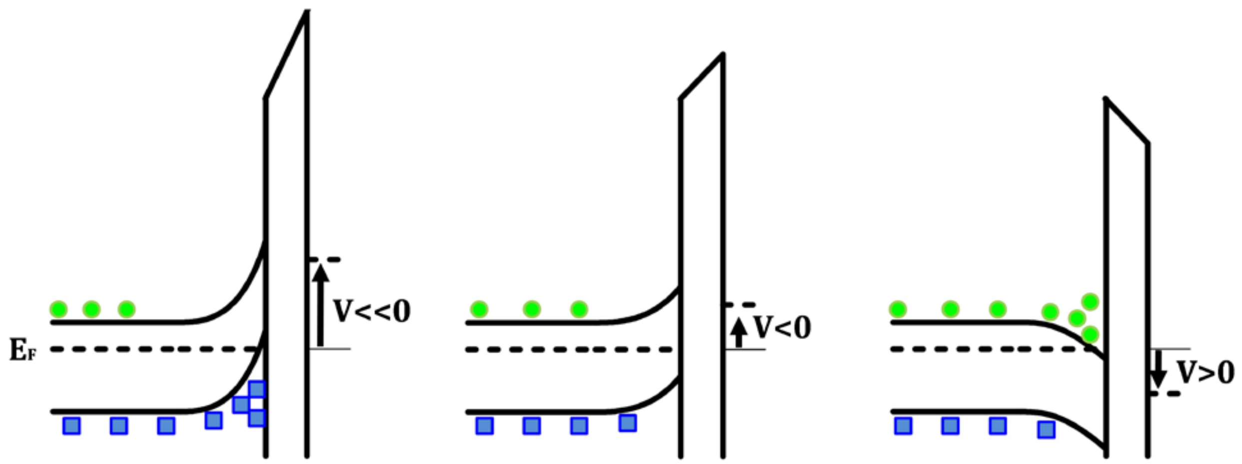

Figure II.8: (a) Inversion, (b) depletion and (c) accumulation case in a biased MIS(n-type) contact.

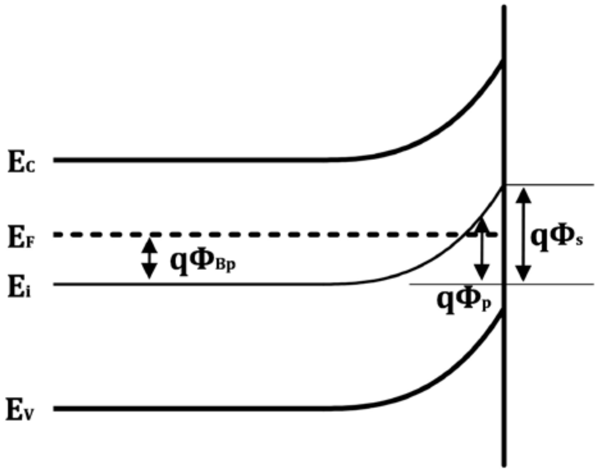

Figure II.9: Potential relations in MI(n-)S contact. The electrical field at the semiconductor surface can be described with the help of the surface potential that is related to the energy difference between the intrinsic Fermi level E_i *in the bulk and at the surface. Accumulation occurs when* $\Phi_S<0$*. Depletion occurs when* $\Phi_{Bp}>\Phi_S>0$*. Inversion occurs when* $\Phi_S>\Phi_{Bp}$ *(Reproduced from [22])*

In this equation, L_D is the extrinsic Debye length for holes, n_0 and p_0 are the densities of electrons and holes in the bulk of the semiconductor and f is a function that depends on the potential difference Φ_p. It is shown that under depletion and weak inversion conditions, f can be simplified using the surface potential Φ_S and setting $\Phi_p=\Phi_S$. Space charges caused by the electrical field *F(x)* at the semiconductor surface become proportional to the square root of the surface potential:

$$Q_S \sim \sqrt{\Phi S}. \qquad \text{(II.21)}$$

The space charge connected with the insulator dielectric constant ε_I and the thickness of the insulator d is responsible for potential V_i across the insulator expressed by its capacitance C_I:

$$V_I = \frac{|Q_S|d}{\varepsilon_I} = \frac{|Q_S|}{C_I}. \qquad \text{(II.22)}$$

The surface charge can also serve as a source for electrical polarization of the insulating material in the accumulation case.

III. EXPERIMENTAL

Description of physical properties in advanced material systems needs exact control over growth conditions as well as precise measurement methods for characterization. Sample production under ultra high vacuum (UHV) conditions provides high structural ordering during film growth and prevention of impurity incorporation, too. A combination of methods like atomic force microscopy, x-ray diffraction and transmission electron microscopy allows obtaining a deep insight into material systems in the sub-nanometer regime. These complementary techniques support each other as every method has its own disadvantages e.g. the need of extremely flat surfaces, the need of large enough regions with crystalline ordering and sophisticated specimen preparation. This chapter gives a short overview of the techniques that are mainly used in this study.

1. UHV sample preparation

1.1. Molecular beam deposition

All organic and inorganic films in this work have been produced by molecular beam deposition (MBD) techniques under UHV conditions. This technique is also known as molecular beam epitaxy (MBE) for deposition of inorganic materials on crystalline substrates, invented by Cho et al. [36]. Low pressures of less than 10^{-8} mbar and slow deposition rates around several Å /min as well as the variation of the substrate temperature during growth enable control over thickness, composition and structural ordering.

When molecules reach the surface, the leading mechanism in the growth of ordered nanostructures and thin films is the diffusion of the adsorbed species. According to Barth et al. [37], atoms or molecules have to overcome diffusion barriers along the surface when moving from one stable configuration to another. This implies that diffusion is mainly thermally activated. The key parameter that describes the growth kinetics in this model is the ratio D/F between the diffusivity D and the constant deposition rate F. D is the mean square distance travelled by an adsorbate per unit time and is described by an Arrhenius law of the form $D = D_0 \exp(-E_m/k_B T)$. E_m is the minimum energy difference between adsorption sides separated by an energy barrier. D_0 is a prefactor of the tracer diffusion [38]. If $D/F \gg 1$, adsorbed species have sufficient time to explore the potential energy surface. It gives the system the possibility to reach minimum energy configuration. Subsequently, the growth appears in equilibrium conditions. When $D/F \ll 1$, individual processes especially those leading to metastable structures are favored. In this case, the growth is determined mostly by kinetics.

For controlled evaporation of the materials, Knudsen-cells that use the principle of molecular effusion [39] are utilized in the MBD technique. The materials are heated by a surrounding ohmic resistive heater close to its sublimation temperature to provide suitable vapor pressure in an isothermal enclosure. Molecular effusion from a cylindrical crucible in the furnace with its open end face-to-face with the substrate gives rise to a cosine intensity distribution and low divergence of the vapor beam. Deposition rates are thus controlled by the cell temperature.

1.2. UHV equipment

Samples in this work have been mainly produced in a commercially available UHV system from *Omicron*, shown in Figure III.1(a). This system consists of three different chambers operated in atmospherically disconnected

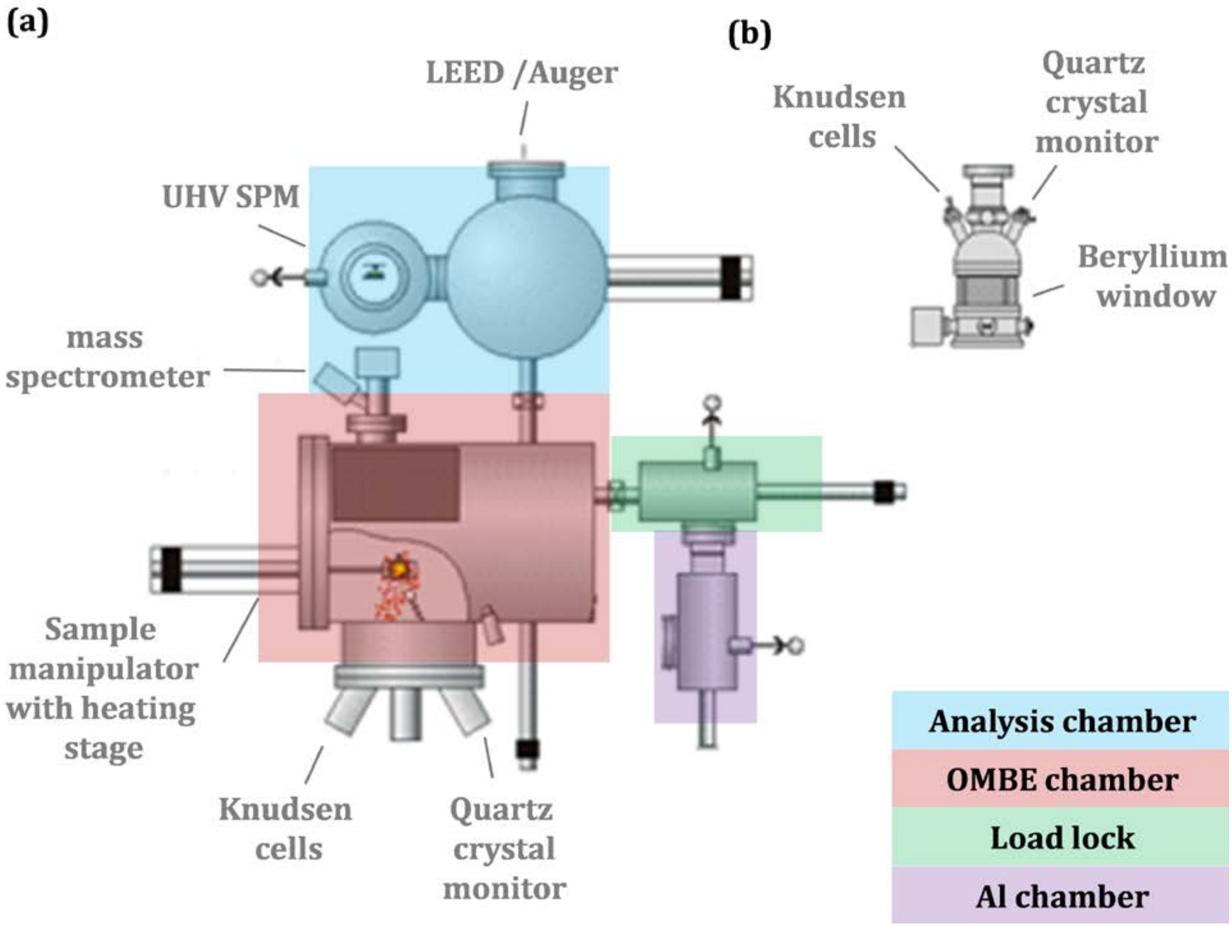

Figure III.1: (a) The Omicron UHV system consists of three different chambers and an attachable metal deposition chamber. Sample characterization is mainly performed outside the chamber. (b) For in-situ x-ray studies, a portable deposition chamber is used that contains all parts needed for molecular beam deposition.

conditions. Each chamber of the system is either pumped by a shared turbo molecular pump or have additional pumping systems attached. The use of ion-pumps as well as titanium sublimation pumps in the deposition and analysis chamber provides pressures below 10^{-9} mbar. Samples are moved from one chamber to another by a rod-transfer system while the load lock guarantees fast substrate insertion without changing the vacuum conditions in both other chambers.

The deposition chamber is equipped with up to four Knudsen cells for organic molecule deposition and one water cooled high temperature cell for LiF deposition. An attached quartz crystal monitor with variable position alignment is placed in the molecular vapor beam close to the sample.

Additionally, a mass spectrometer and a sputter gun are attached but have not been used in this work. The sample stage for molecule deposition contains a resistive heater and a nitrogen stream cooling system. Temperatures of the cells and the heater are monitored by *Eurotherm* controller with either C- or K-type thermocouples.

The analysis chamber is equipped with a UHV SPM as well as low electron energy diffraction (LEED) system and an Auger spectrometer. Due to the advanced lifetime of the *Omicron* system, these measurement systems didn't work properly and the analysis chamber has been mainly used as sample storage. Therefore characterization methods of the produced samples have been carried out ex-situ.

To avoid chamber contamination during preparation of photovoltaic devices, an additional chamber for deposition of the aluminum top electrode can be attached to the load lock. This chamber is also equipped with a high temperature Knudsen cell. The chamber can be replaced with a small transport chamber to limit device degradation during sample transport to the electrical characterization stage.

For in-situ x-ray experiments, a portable MBE system, shown in Figure III.1(b), provides connection sides for two organic deposition cells and the high temperature LiF cell. The chamber has a beryllium window allowing high transmission of x-ray radiation. A stationary quartz crystal monitor is attached. The chamber is pumped by a turbo molecular pump and pressures below 10^{-8} mbar are provided.

2. X-ray diffraction (XRD)

2.1. Elastic scattering

Current knowledge about nanoscopic structures would not have been developed so far without the invention of various scattering methods between radiation and matter. With the discovery of x-rays by Roentgen [40], radiation with wavelengths in the range of atomic distances has been accessible for technological and scientifically use. The use of x-ray scattering for determining crystal structures has been achieved for the first time by the Bragg's [41] in 1914. It is a powerful technique to resolve ordered atomic structures in a resolution of fractional amounts within the nanometer scale. The theory of x-ray scattering is well described in various textbooks; see e.g. [42; 43; 44; 45].

When scattering between electromagnetic waves with the form $\boldsymbol{E}(\boldsymbol{r}) = \boldsymbol{E}_0\exp(\mathrm{i}(\boldsymbol{kr} - \omega\boldsymbol{r}))$ and electrons occurs, momentum of the incoming electromagnetic wave $\boldsymbol{E}_\mathrm{i}$ and the scattered wave $\boldsymbol{E}_\mathrm{f}$ will be transferred to the scattering center and is calculated with the help of the wave vectors:

$$\boldsymbol{q} = \boldsymbol{k}_\mathrm{f} - \boldsymbol{k}_\mathrm{i}. \tag{III.1}$$

Referring to Als-Nielsen [43], the scattering amplitude mediated from an ordered material is written as:

$$S^{crystal}(\boldsymbol{q}) = -r_0 \sum_{\boldsymbol{r}_j} f_j(\boldsymbol{q}) \exp\left(\mathrm{i}\boldsymbol{q} \cdot \boldsymbol{r}_j\right) \sum_{\boldsymbol{R}_\mathrm{n}} \exp(\mathrm{i}\boldsymbol{q} \cdot \boldsymbol{R}_\mathrm{n}). \tag{III.2}$$

The classical electron radius is given by $r_0 = e^2/(4\pi\varepsilon_0 \mathrm{m}c^2)$ and the momentum transfer dependent quantity $f_j(\boldsymbol{q})$ is called the atomic form factor. The first sum in this equation is called the unit cell structure factor where the second is the sum over all lattice sites. The parameters $\boldsymbol{R}_\mathrm{n}$ are the lattice vectors that define the lattice of the crystal:

$$\boldsymbol{R}_\mathrm{n} = n_1\boldsymbol{a} + n_2\boldsymbol{b} + n_3\boldsymbol{c}. \tag{III.3}$$

The vectors $\boldsymbol{r}_j$ are the positions of the atoms with respect to any one particular lattice site. Thus the position of any atom in the crystal is given by $\boldsymbol{R}_\mathrm{n} + \boldsymbol{r}_j$.

In this work, the electron distribution of the material that is forming the lattice, expressed by the unit cell structure factor is of less interest. Regarding the appearance of scattering amplitudes, all terms in the lattice sum in equation (III.2) are phase factors located on the unit circle in the complex plane. The sum will be of the order of unity unless the scalar product of momentum transfer vector and scattering vector satisfy the following demand:

$$\boldsymbol{q} \cdot \boldsymbol{R}_\mathrm{n} = 2\pi \times \text{integer}. \tag{III.4}$$

This requirement is solved by introducing the concept of the reciprocal lattice that is spanned up by the reciprocal lattice basis:

$$\boldsymbol{a}^* = 2\pi \frac{\boldsymbol{b} \times \boldsymbol{c}}{v_c} \qquad \boldsymbol{b}^* = 2\pi \frac{\boldsymbol{c} \times \boldsymbol{a}}{v_c} \qquad \boldsymbol{c}^* = 2\pi \frac{\boldsymbol{a} \times \boldsymbol{b}}{v_c}. \tag{III.5}$$

The quantity $v_c = \boldsymbol{a} \cdot (\boldsymbol{b} \times \boldsymbol{c})$ is the volume of the unit cell and any lattice site in the reciprocal lattice is given by:

$$\boldsymbol{G} = h\boldsymbol{a}^* + k\boldsymbol{b}^* + l\boldsymbol{c}^*. \tag{III.6}$$

The so called Miller indices (h, k, l) in this equation are all integers by

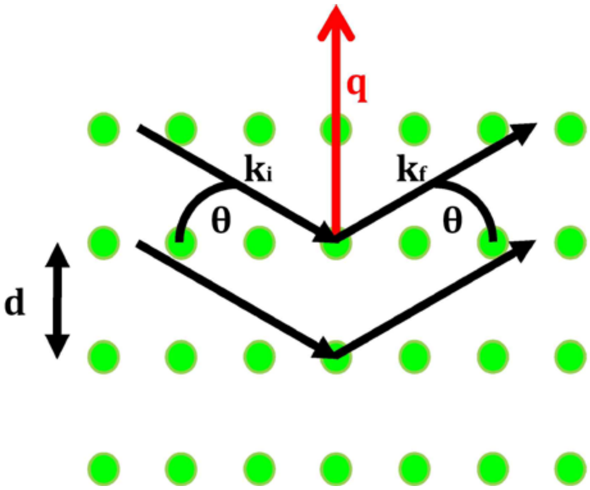

Figure III.2: Scattering geometry in real space according to Bragg's law.

definition. The product of a lattice vector in real and reciprocal is the searched quantity in equation (III.4):

$$\boldsymbol{R}_n \cdot \boldsymbol{G} = 2\pi(hn_1 + kn_2 + ln_3) = 2\pi \times \text{integer}. \tag{III.7}$$

It follows that non-vanishing scattering amplitudes only appear if the momentum transfer $\boldsymbol{q}$ coincides with a reciprocal lattice vector. It is also known as the Laue condition for the observation of diffraction signals from a crystalline lattice:

$$\boldsymbol{q} = \boldsymbol{G} \tag{III.8}$$

Also, it can be shown that the Laue condition is equivalent to Bragg's law [41]:

$$n\lambda = 2d\sin(\Theta). \tag{III.9}$$

This law expresses scattering by constructive interference of reflected electromagnetic waves out of geometrical considerations. Constructive interference only occurs if plane distances d in the crystal are multiples (integer n) of projections of the wavelength λ on the plane normals. This is expressed by the incident angle Θ relative to the observed plane set. The momentum transfer $\boldsymbol{q}$ is connected with the incident angle in the Bragg geometry. By conversion of equation (III.1) into $\boldsymbol{q} = |\boldsymbol{k}|(\boldsymbol{f} - \boldsymbol{i})$ and the relation $k = 2\pi/\lambda$ it follows:

$$|\boldsymbol{q}| = \frac{4\pi}{\lambda}\sin(\Theta). \tag{III.10}$$

This relation inserted into Bragg's law in equation (III.9) gives an easy to handle relation. It connects observable scattering signals at defined momentum transfer positions with distances of plane sets in the crystal:

$$|\boldsymbol{q}| = \frac{2\pi}{d}. \tag{III.11}$$

2.2. Index of refraction

The propagation of a plane electromagnetic wave is characterized in a classical approximation by the material dependent index of refraction. This parameter of material containing elements j is given by the following relation sometimes known as the optical theorem:

$$n = 1 - \frac{\lambda^2 r_0}{2\pi}\sum_{j=1}^{n} N_j f_j. \tag{III.12}$$

The quantities in this equation are the wavelength λ, the classical electron radius r_0, the average number density of atoms in the medium $N = (\rho_j/A_j)N_A$ (ρ: density; A: molar mass; N_A: Avogadro constant) and the atomic form factor f_j. If dispersion and absorption related effects are taken into account, the atomic form factor will get a complex quantity by energy dependent corrections f'_j and f''_j:

$$f_\mathrm{j} = f_{0,j} + f'_j - \mathrm{i}f''_j. \tag{III.13}$$

For this reason the complex atomic form factor leads to a complex refraction index for x-ray scattering:

$$n = 1 - \delta - \mathrm{i}\beta. \tag{III.14}$$

The quantities δ and β are positive real numbers and typically in the range of 10^{-5}-10^{-7} for x-ray wavelengths:

$$\delta = \frac{\lambda^2 r_0}{2\pi}\sum_{j=1}^{n} N_j\left(Z_j + f'_j\right) \approx \frac{N\lambda^2 r_0 Z}{2\pi}, \tag{III.15}$$

$$\beta = \frac{\lambda^2 r_0}{2\pi}\sum_{j=1}^{n} N_j f''_j \approx \lambda\frac{N\sigma_a}{4\pi}. \tag{III.16}$$

In these equations Z is the number of elementary charges of a scattering center and σ_a is the absorption cross section. The parameters are listed for a variety of elements in several databases, e.g. [46].

2.3. X-ray reflectivity (XRR)

In contrast to other x-ray scattering techniques, specular x-ray scattering is a method for investigating thin film structural ordering perpendicular to a substrate surface. For this purpose it has to be fulfilled that the observation of the signal response is in the plane of a polarized incoming x-ray beam. Additionally, equality between the incident-angle α_{i} and the exit-angle α_{f} of incoming and reflected x-rays is required.

When a polarized x-ray beam is passing an ideal flat interface between medium 1 and medium 2 with the polarization parallel to the x-z plane (x is the incident direction) of the beam (s-polarized), the electromagnetic wave split up into two parts. One describes the reflected electromagnetic wave in medium 1 and the other one the transmitted electromagnetic wave into medium 2:

$$E_{\mathrm{R}} = R * E_0 \exp(\mathrm{i}(\boldsymbol{k} \cdot \boldsymbol{r})), \tag{III.17}$$

$$E_{\mathrm{T}} = T * E_0 \, exp(i(\boldsymbol{k}' \cdot \boldsymbol{r}')). \tag{III.18}$$

The Fresnel coefficients R and T are calculated under the boundary conditions of continuity in tangential components of the electric vectors $\boldsymbol{k}$ and $\boldsymbol{k}'$ at the interface. The primed quantities describe the propagation in medium 2. The solution of this set of equations, nicely reviewed by Tolan [45], delivers the coefficients in the z-direction parallel to the surface normal:

$$R = \frac{k_z - k'_z}{k_z + k'_z}, \tag{III.19}$$

$$T = \frac{2k_z}{k_z + k'_z}. \tag{III.20}$$

The Fresnel coefficient R can be obtained with the help of Snell's law:

$$n \cos(\alpha_{\mathrm{i}}) = n' \cos(\alpha_{\mathrm{T}}) \tag{III.21}$$

Inserting the expression for the index of refraction by the ratio of the wave vectors $n'/n = |\boldsymbol{k}|/|\boldsymbol{k}'|$ in this equation and assuming that medium 1 is the vacuum (n = 1), the reflection coefficient R is derived by calculating it from the vector components of $\boldsymbol{k}$:

$$R = \frac{\sin(\alpha_{\mathrm{i}}) - \sqrt{n'^2 - \cos^2(\alpha_{\mathrm{i}})}}{\sin(\alpha_{\mathrm{i}}) + \sqrt{n'^2 - \cos^2(\alpha_{\mathrm{i}})}}. \tag{III.22}$$

The square of the reflection coefficient R^2 is a measurable quantity, also known as Fresnel reflectivity since it is the amplitude of the reflected wave in equation (III.17). As a consequence of the conservation of energy, the transmission coefficient is given by $T = 1 - R$.

Total external reflection occurs at small incident angles when an electromagnetic wave is passing an interface. The critical angle α_{c} of total reflection under which no transmission takes place is obtained by setting $\alpha_{\mathrm{T}} = 0$ in equation (III.21). By neglecting absorption and expanding the cosine with the Taylor formalism to $\cos(\alpha) = 1 - 1/2\alpha^2$ it follows:

$$\alpha_{\mathrm{c}} \approx \sqrt{2\delta}. \tag{III.23}$$

When the x-ray beam is scattered on a thin and atomically flat film, oscillations in the reflectivity curves can occur named as Kiessig fringes [47]. The oscillations are due to the interference of waves reflected from the top and bottom interfaces with different indices of refraction. Dips in the oscillations are caused by scattering of waves out of phase while peaks correspond to scattering in phase. The difference in momentum transfer for the arising peaks or dips allow estimating the total thickness D of the thin film. It is calculated by its difference in momentum transfer applying equation (III.10). The total thickness of the thin film is then:

$$D \approx \frac{2\pi}{\Delta q_z}. \tag{III.24}$$

When the thin film consists of a stack of N layers the situation is more complicated. In this case, the x-ray reflectivity is derived with the help of the Parratt algorithm [48]. In this formalism, the transmitted x-ray in the medium of the top-most layer serves as a new source for scattering at the next lower interface. With the ratio between reflection and transmission from the planes at the interfaces *j* and *j+1*, the resulting reflection coefficient is obtained by a recursion:

$$R_{F,j} = \frac{r_j}{t_j} = \frac{r_{j,j+1} + R_{F,j+1}\exp\left(2\mathrm{i}k_{\mathrm{z,j+1}}\mathrm{z_j}\right)}{1 + r_{j,j+1}R_{F,j+1}\exp\left(2\mathrm{i}k_{\mathrm{z,j+1}}\mathrm{z_j}\right)}. \tag{III.25}$$

In the recursion it is assumed that the region of $j = N + 1$ (usually the substrate) does not reflect any wave component. Therefore the recursion starts with $r_{N+1} = 0$ and is applied up to the topmost layer.

In a more realistic situation, roughness effects of the surface have to be taken into account. This is reached by adding an exponential term to the reflection obtained by a Gaussian height distribution of the reflecting interface:

$$R_\sigma = R\,\exp(-2k_z^2\sigma^2). \tag{III.26}$$

The quantity σ^2 in this equation is called the mean square roughness.

Especially in systems where each layer in the multilayer system has the same electron density Pseudo Bragg peaks are observed in the reflectivity. This is a consequence of constructive interference at the centers of mass of these repeating units, expected and predicted by Parratt's model. The momentum transfer positions of these maxima can be directly translated in layer thicknesses using equation (III.11).

2.4. Grazing incidence x-ray diffraction (GIXRD)

The technique of GIXRD is based on the fact that total reflection of x-rays occurs at the interface between vacuum and the less dense medium, if the incident angle is sufficiently small. Under the condition of total reflection, the transmitted electromagnetic wave is exponentially damped when passing the reflective interface. The material and angle dependent penetration depth reaches several nanometers. According to [42] it is given by:

$$\begin{aligned} l_i &= \frac{\lambda}{\sqrt{2}\pi}\left[\left(2\delta - \sin^2(\alpha_i)\right) - \sqrt{\left(\sin^2(\alpha_i) - 2\delta\right)^2 + 4\beta^2}\right]^{-1/2} \\ &\approx \frac{\lambda}{2\pi\alpha_c}. \end{aligned} \tag{III.27}$$

As a consequence of $\alpha_\mathrm{T} = 0$, a "distorted" also known as evanescent wave is propagating in the less dense medium with components only in the direction parallel to the surface. The evanescent wave is scattered at crystallographic planes, e.g. with their normal parallel to the surface, giving Bragg signals in the manner of equation (III.9).

In an argument of reciprocity, internal total refraction at the interface may also take place. If the surface would be an ideal flat surface and the propagating wave has still only parallel components after the scattering events at surface normal planes, the wave vector will never have a chance to be transmitted back in the vacuum. The reason is that the incident angle of the wave to the surface will always remain zero. Fortunately, real surfaces have a non-negligible roughness and a small portion of the scattered evanescent wave escapes from the material. In a simple view the angles of the scattered wave to the rough surface are above the critical angle of total internal reflection. With this argument the scattering depth is obtained by:

$$\Lambda = \frac{\lambda}{2\pi(l_{\mathrm{i}}+l_{\mathrm{f}})}. \tag{III.28}$$

Therefore, small angle in-plane scattering is extremely surface sensitive, whereas scattering contribution from the bulk is negligible in the grazing incidence geometry. Hence, observed x-ray signals are extremely weak. Observations of the depth profile with variation of the incident angle and fixed exit angles between 0 up to $4\alpha_{\mathrm{c}}$ by Dosch et al. [49] turned out a maximum signal response at the critical angle. This well described and understood mechanism [50] is used to find the optimum incident angle for reproducible application during measurement.

The GIXRD experiments in this work are mainly resolving the in-plane structure of thin organic molecule films. The influence of organic thin films on substrate signals cannot be applied due to the mostly non-epitaxial growth behavior of those films. Anyway, the in-plane structure of thin organic films, mostly attributed to intermolecular forces between the molecules, is experimentally accessible with the GIXRD technique. In these experiments the incident angle α_{i} as well as the detector angle α_{f} in the out-of-plane direction is set to the critical angle for total reflection shown in Figure III.3. Rotating the detector angle (2θ) around the surface normal serves for the variation of the observed momentum transfer.

As organic thin films consist of domains with different orientation but similar structural in-plane ordering, azimuthal orientation of the sample in respect to the incoming beam is without importance for the observation of Bragg scattering signals. Exact calculations of the electron density distributions out of the total distribution of the scattering intensity are limited by the unknown locally texture in these films.

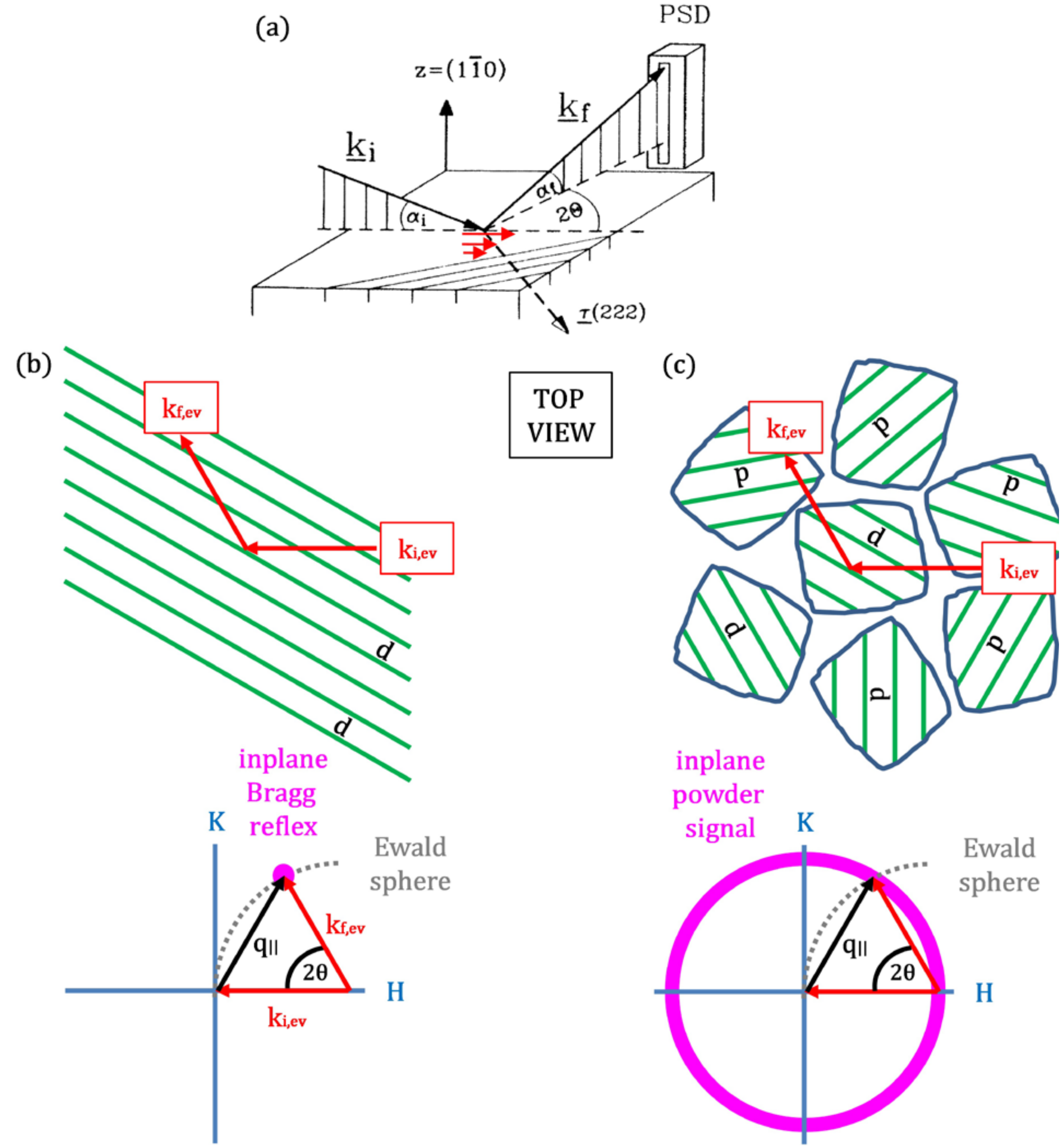

Figure III.3: (a) Scattering geometry for GIXRD measurements. The incident and detector angles α_i, α_f are at the critical angle α_c (from [49]). (b) For in-plane measurements the evanescent wave is scattered at planes perpendicular to the substrate surface. In case of a single crystalline film with only one orientation of the observed plane set, sharp Bragg peaks at defined azimuthal orientations are observed. (c) Randomly oriented crystalline grains result in an in-plane powder like signal.

3. Scanning probe microscopy (SPM)

3.1. Remarks

The powerful method for direct imaging atomic structures has been established by the experiments of Binnig and Rohrer when they reported their first successful tunneling experiment in 1982 [51]. The invention of the Scanning tunneling microscope (STM) leads to the Nobel Prize in physics in 1986 and releases the invention of several other techniques. In a general view, scanning probe microscopy is a tool where a short range interaction of a local probe that is scanned over the surface is monitored and the magnitude of interest is measured, recorded and processed. Principles of common used SPM techniques are nicely reviewed and visualized in [52] while a review about the variety of outstanding SPM methods is given e.g. by Loos in [53].

3.2. Atomic force microscopy

The development of atomic force microscopy (AFM), again by Binnig et al. [54], had an even more dramatic impact for the observation of surfaces as it is not only limited to conductive materials. This method allows measuring forces down to 10^{-18} N. It makes use of the effect that a macroscopic cantilever with an attached sufficient sharp tip is bended or twisted under the interaction with a sample surface, shown in Figure III.4. The spatially resolved displacement of the cantilever is monitored with the help of a reflected laser. The laser beam is projected from the cantilever to a photodiode mostly containing a matrix of 2×2 independent sectors. The position sensitive sensor allows measuring lateral and normal forces simultaneously, for the first time reported by Meyer et al. [55]. During measurement the sample is scanned underneath the tip line by line with one fast and one slow scan direction. The parameters that define present interactions between tip and sample are either measured directly or used as feedback to keep the vertical distance between tip and sample constant. Sub nanometer movements of the sample stage are performed with the help of piezo ceramic motors. The limiting factor for the vertical resolution in AFM is thus the accuracy of the motion process. The lateral resolution is obtained by geometrical considerations and is dependent on curvature R of the used tip as well as the vertical resolution of the instrument [52]:

$$\Delta l \approx \sqrt{8R\Delta z}. \qquad \text{(III.29)}$$

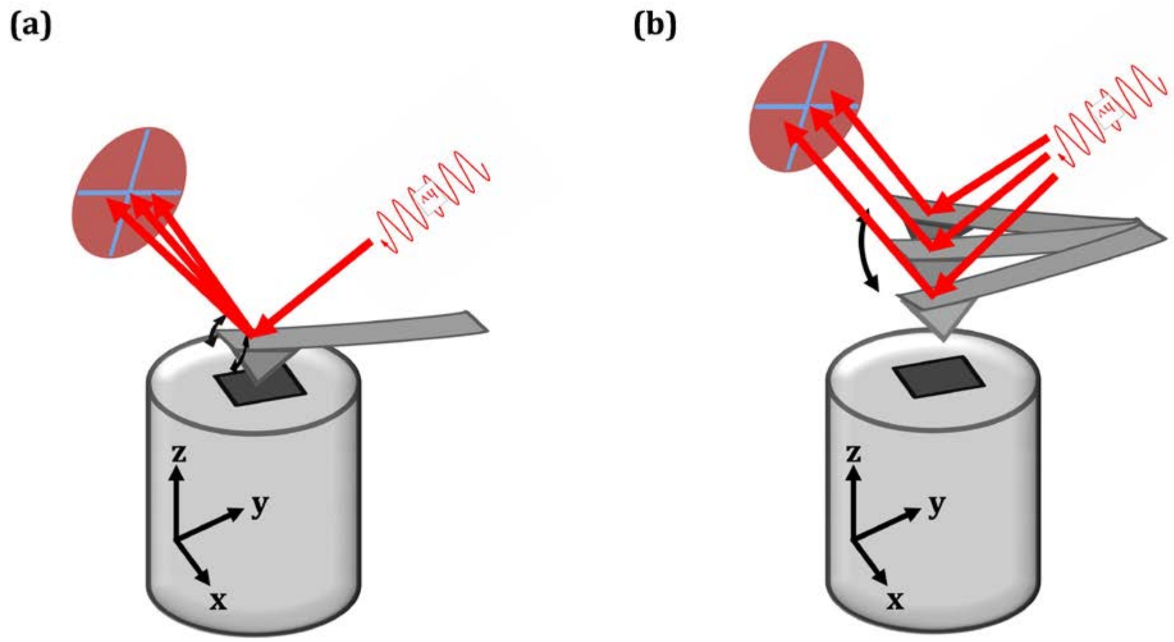

Figure III.4: (a) In contact AFM mode, the position of the deflected laser beam is kept constant by adjusting the height of the sample while it is scanned in x- and y-direction with an ultra precise piezo-ceramic motor. Additional torsion of the tip is detected to measure friction forces. (b) In dynamic FM or AM non-contact mode, the cantilever oscillates at its resonance frequency. Changes in the amplitude, frequency or phase due to surface features are used as feedback for z-movement while scanning the x- and y-direction.

Different types of operation modes for the AFM techniques have been developed, mostly depending on the type of interaction forces between tip and surface. The force distance curve in Figure III.5, assuming a Lennard-Jones potential, shows the three basic operational modes in AFM. In idealized vacuum conditions, electrostatic interactions between tip and surface are acting at small sample-tip distances in the range of few Å. These forces arise either from repulsion of the ion cores or from attraction by overlapping electron wave functions. The repulsive force on the tip in this regime can e.g. be calculated within the macroscopic model proposed by Hertz which solves the equation for the stresses and deformation in the contact zone for two bodies in contact [52; 56]:

$$F = -K\sqrt{R}h^{3/2}. \tag{III.30}$$

In this equation, K is the effective Young modulus of the given pair of materials

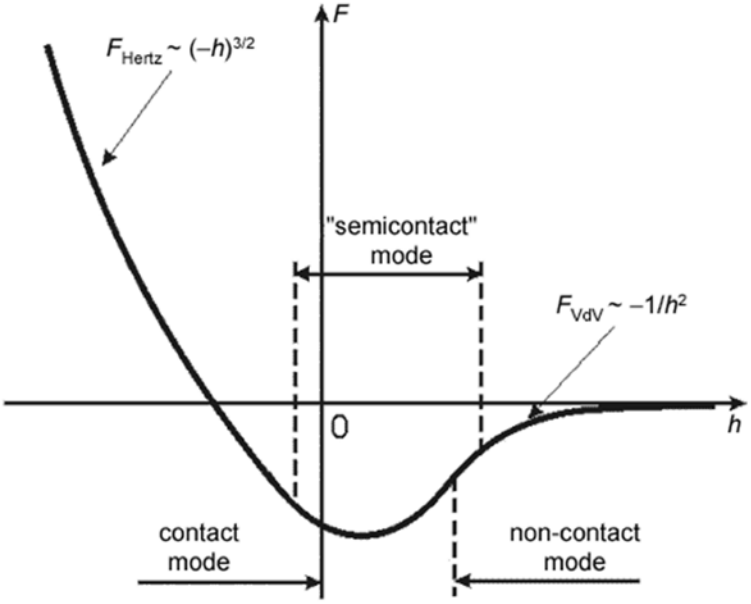

Figure III.5: Different force regimes for tip-sample interaction in atomic force microscopy. Positive forces are repulsive, whereas negative are attractive (From [52]).

and R the relative curvature of the indenter and the specimen with $1/R = 1/R_\mathrm{i} + 1/R_\mathrm{S}$ ($R_\mathrm{S} \rightarrow \infty$). h is the distance between the centers of mass of the two bodies.

Attractive adhesion forces are generally defined as the change in free energy when separating unit areas of two media. Capillary forces are due to mostly surface tension of water contamination that is always present when measuring under ambient conditions. In a work of Bradley [57], evaluated by Kendal [58], adhesion forces in the contact regime are described with according to Young-Dupré's equation for the work of adhesion $W = \gamma_1 + \gamma_2 - \gamma_{12}$ (γ as the free surface energy of identical particles) and spherical particles with diameter d by:

$$F = kWd. \tag{III.31}$$

Attractive Van der Waals forces are added, evaluated in the London theory for crossed cylinders with an equation:

$$F = \frac{-Ad}{12h^2}. \tag{III.32}$$

In this equation, d is the diameter of the cylinders, h is the distance between both and A the Hamaker constant in the range of 10^{-19} J. This law is refined for other geometries, see [58]. If the tip is retracted far enough from a surface, adhesion as a combination of capillary and long range Van der Waals forces acting as attractive forces.

The contact mode is shown in Figure III.4(a). In the absence of contamination e.g. by water films, measurements in the constant force mode allow extracting the lateral forces on the tip caused by friction between tip and sample. In the constant force mode, bending of the tip in the surface normal direction is kept constant by varying the absolute height position of the sample and scanning perpendicular to the longitudinal axis of the cantilever. Additional torsion besides the cantilever's reflection occurs and is proportional to the lateral force acting on the tip. Scanning each line in forward and back direction helps to distinguish between torsion caused by height steps and torsion caused by friction. The angle of cantilever twisting is the same when passing a topographical edge, but differently when caused by friction. The difference of the torsion angle measured in forward and backward scanning reveals signal contrast because of friction forces.

Organic thin films are mostly much softer than usually used AFM tip-materials like silicon or silicon nitride. The danger of complete removal of the film during measurement makes the contact mode unfavorable which works in the repulsive regime. Hence, the use of non-contact modes in the attractive force regime is preferred for such systems. Under weak attractive Van der Waals interaction in the constant force mode, the invention of dynamical non-contact modes first reported by Martin et al. [59] is denoted as a breakthrough. In the dynamic mode, the cantilever is mounted on a piezo actuator and the cantilever-tip unit is excited to oscillations at its resonance frequency as it is shown in Figure III.4(b).

The resonance frequency of such a free system is given with:

$$\omega = \sqrt{\frac{k_{\mathrm{eff}}}{m}}. \tag{III.33}$$

This equation includes the effective mass m of the cantilever and the effective spring constant $k_{\mathrm{eff}} = k_{\mathrm{L}} + \partial F/\partial z$ that is a sum of the lever spring constant and the force gradient due to tip sample interaction. According to Albrecht et al. [60], the system of tip-and sample in interaction is described by a damped harmonic oscillator with the quality factor Q. This factor is related to the damping characteristics of the tip. The following equation of motion can be applied:

$$m\ddot{z} + \frac{m\omega_0}{Q}\dot{z} + m\omega_0^2 z = F_0\cos(\omega_\mathrm{D} t). \tag{III.34}$$

The solution of this equation after a finite time step is a sum of the steady state solution and a transient term due to the change in $\partial F/\partial z$:

$$z(t) = A_0\cos(\omega_\mathrm{D} t + \varphi_0) + A_\mathrm{T}\exp\left(-\frac{\omega_0 t}{2\mathrm{Q}}\right)\cos(\omega_\mathrm{T} t + \varphi_\mathrm{T})\ . \tag{III.35}$$

In this equation, the phase shifts of the steady state solution $\varphi_0 = \tan^{-1}(\omega_0\omega_\mathrm{D}/[\mathrm{Q}(\omega_0^2 - \omega_\mathrm{D}^2)])$ and ω_T is the resonant frequency for free oscillation with $\omega_\mathrm{T} = \omega_0\sqrt{1-(1/4Q^2)}$. The amplitude A_0 of the steady-state term can be written as:

$$A_0 = \frac{F_0}{m\sqrt{\left(\omega_0^2 - \omega_\mathrm{D}^2\right)^2 + (\omega_0\omega_\mathrm{D}/Q)^2}}\ . \tag{III.36}$$

The solution in equation (III.35) offers two measurable quantities. In the amplitude modulation (AM) mode, the squared amplitude is used as the feedback parameter. It includes a constant term related to damping and free oscillation and the contribution from the transcend decay as well as a mixed term of both amplitudes. It turns out that the amplitude modulation mode is dependent on Q, as the exponential term is negligible for high Q values. Thus, the exponent $\omega_0 t/2Q$ determines the time, after which the steady state solution dominates. Therefore, the behavior of the system offers fast response but low sensitivity for low Q values while high sensitivity but low response for high Q values. To prevent contrary Q-behavior, frequency shifts with high Q cantilever are used as the feedback parameter in the frequency modulation (FM) mode. This mode provides slow response times in the range of $1/\omega_0$. Additionally, phase shifts that are usually compensated by applying an additional excitation frequency to insure maximum positive feedback are monitored. They offer a contrast between different materials.

3.3. Coverage determination method

To estimate the material coverage of one constituent in a bilayer system, most automated methods fail. Flooding to a specific height threshold and measuring the area above it is only sufficient, if the topography of the underlying surface feature large flat areas with an equal height distribution. If the underlying surface provides already areas with different heights, islands from the capping layer will be seized wrong or will be discounted. Supplementary, determining the right flooding parameter with a normalized method is impossible if the film roughness exceeds a certain limit.

Instead of that, a method of separating the impact of the underlying molecular film has to be applied that measures only the area coverage of the islands on top. It will give more meaningful coverage numbers for different ad-layer deposition amounts. For this purpose, Fourier subtraction developed by Turak et al. [61] has been used to deconvolute the two component topography. The method can be used even for systems where no direct image of the underlying surface is present. In this method, applied on an artificial grid in Figure III.6, the original image has been separated with its Gaussian smoothed facsimile by transforming both images in reciprocal frequency space:

$$\begin{aligned} \mathrm{F}\left(k_x, k_y\right) = \left(\frac{L}{N}\right) \sum_{\mathrm{x}=0}^{2\mathrm{N}-1} \sum_{\mathrm{y}=0}^{\mathrm{N}-1} z(x, y) \\ * \exp\left\{\left(\frac{-\mathrm{i}2\pi}{N}\right)\left(k_x x + k_y y\right)\right\}. \end{aligned} \tag{III.37}$$

The radial modulus of the real and imaginary spatial frequency Fourier components from both images are subtracted from each other. This method has the great advantage that amplitudes of every wave are separated without respect to their phase difference. It follows that amplification of wave components arising from the smoothed (substrate) image does not occur. The obtained real and imaginary part of the subtracted image has a preserved ratio from the phase of each spatial wave. Both subtracted complex parts are transformed back into real space using an inverse Fourier transform algorithm. With this procedure, the underlying surface is leveled to a common height which allows a more precise determination of the ad-layer coverage. Analyses of ad-layer coverage with automated particle analysis from converted binary images are carried out with the free available ImageJ software package [62]. It has to be mentioned that measured numbers for lateral distances by AFM methods depend upon some intrinsic systematic errors, e.g. the limited lateral resolution or changes of the tip size during measurement due to material agglomeration at the tip.

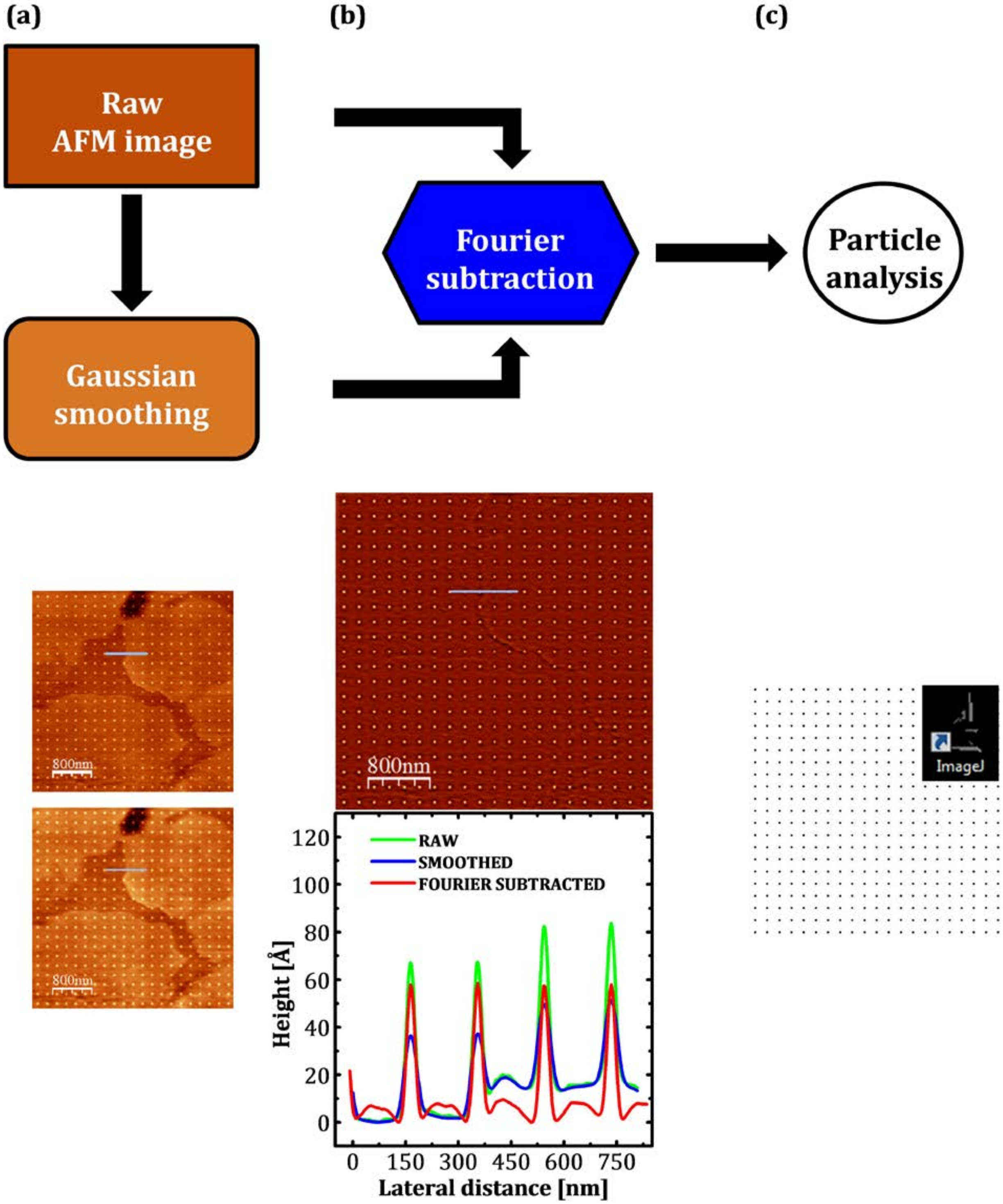

Figure III.6: (a) The reference sample was smoothed and subtracted from the original in reciprocal space. (b) The resulting image is a deconvolution of artificial island topography from the DIP topography. (c) Particle analysis has been performed after binary conversion.

Absolute numbers of island height distributions are also falsified by the Fourier subtraction process, indicated in Figure III.6(b). In case of artificial test grid, the simulated small islands show a height reduction of 14.6 %. Thus, the only reasonable value that is gained from particle analysis of the Fourier subtracted images is the number of hills/particles being left over. If the island dimensions are known from a complementary measurement technique, an estimation of the total coverage can be obtained. Note that island sizes from the ad-layer have to be uniform for a precise coverage determination.

4. High resolution transmission electron microscopy (HRTEM)

Electron microscopy is a powerful tool to investigate structures with dimensions in the Ångstrøm scale directly. Detailed information about the technique are given e.g. in [63; 64]. The technique is based on the wave like character of electrons described by the de Broglie wavelength. Free electrons are emitted by an electron gun, commonly equipped with a tungsten filament cathode as the electron source. The electrons are accelerated in an electrical field which strength defines their kinetic energy, typically between 40 and 400 keV. The electron beam is focused by electrostatic and electromagnetic lenses and transmitted through a specimen partially transparent to electrons. The kinetic energy is directly related to the material wavelength of the electrons. The dimensions of structures that the electrons can interfere with are adjusted by the biased voltage.

The incident parallel electron beam interacts elastically when passing through the specimen. As shown in Figure III.7, scattered electrons from the measured spot are forming a diffraction pattern on the back focal plane of the microscope. The objective aperture is a mechanical filter that just allows passing scattered electrons from specified plane sets of the sample. The signals are again focused together with the direct transmitted beam by an objective lens system. As a result of phase contrast, the interference of the scattered intensities from diffraction and direct transmission serves for optical reconstruction of the atomic structure from the sample. The focused beam is projected onto either a fluorescent viewing screen coated with phosphor or scintillator material such as zinc sulfide. Alternatively, the signal is photographically recorded by connecting the scintillator to a charge coupled device (CCD) camera via optical fibers.

Samples that are measured in cross-sectional transmission microscopy are limited to thicknesses around 100 nm due to complete absorption of the electrons. HRTEM ideally requires the preparation of specimens with very high quality. Prepared specimens should therefore have a uniform thickness

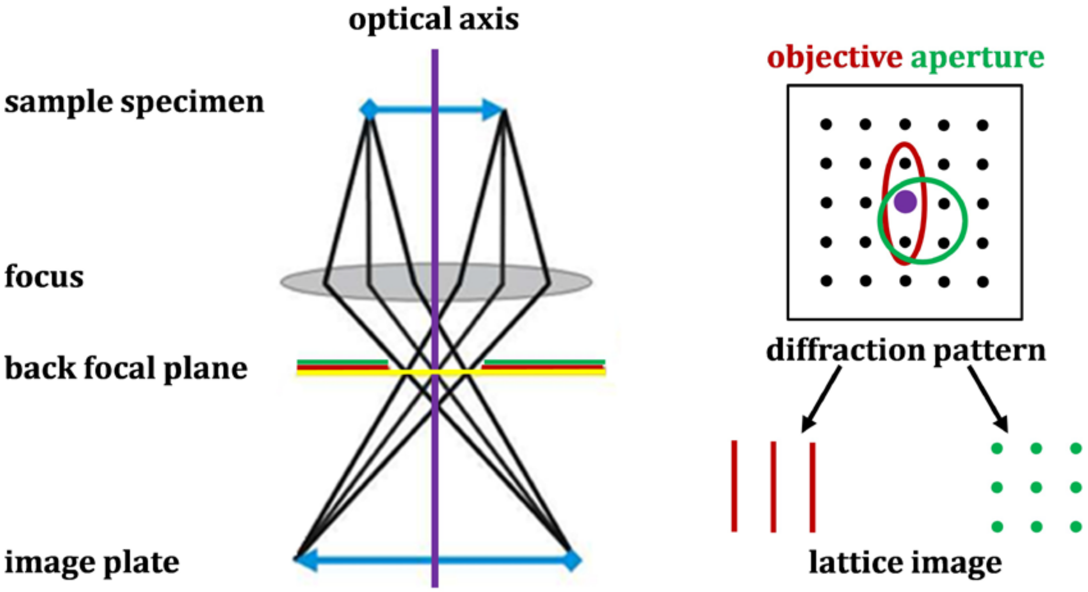

Figure III.7: Scheme of the HRTEM measurement system. Scattered electrons from the sample are focused to the back focal plan, forming a diffraction pattern. The objective aperture serves for a defined interference of scattered signals with the direct transmitted (T_0) beam. Thus, the phase contrast serves for atomic resolution of either plane sets or the atomic latter (Reproduced from [64]).

(ideally less than 30 nm) with relatively flat exit surfaces.

Soft organic films need special care during preparation of specimen [65]. For this purpose, the film/substrate sample is cut in two pieces and glued together on the film side in order to form a sandwich structure in advance. This procedure fixes and stabilizes the organic film in between the two parts of the substrate. Special epoxy glue with minimized stabilization time and temperature is used for that procedure. Subsequently, a slice of the sandwich structure with a thickness of several microns is mounted on special TEM grid.

Mechanical thinning from pre-cut specimen is achieved by grinding a concave impression or dimple, thinning the center to a disk to 3 mm in diameter and about several tens of microns thickness. Final thinning by Ar ion milling requires acceleration energies around 8 keV. The sample has to be in continuous rotation mode to minimize the redeposition of the sputtered atoms. After the thinning procedure, a hole in the slice is left over whereas its edges are in the right thickness for transmitting the electron beam.

IV. MATERIAL PROPERTIES

Different classes of organic semiconducting molecules are known. Molecule films from two perylene derivates, a polycyclic hydrocarbon and a fullerene are used to study the impact of inorganic LiF deposition. Layer-by-layer growth is featured by most of these organic materials, except the fullerene. This growth mode leads to very smooth organic surfaces, essential for studying ad-layer topography. Crystal structures in the organic thin film arrangement are known for all of the used organic molecules. Structural ordering is essential for charge as well as exciton transport and thus sufficient charge carrier mobility. The fullerene is an example of state-of-the art used molecule in photovoltaic devices but with a rough surface morphology. This chapter gives a short overview about the physical properties from materials and substrates used in this study.

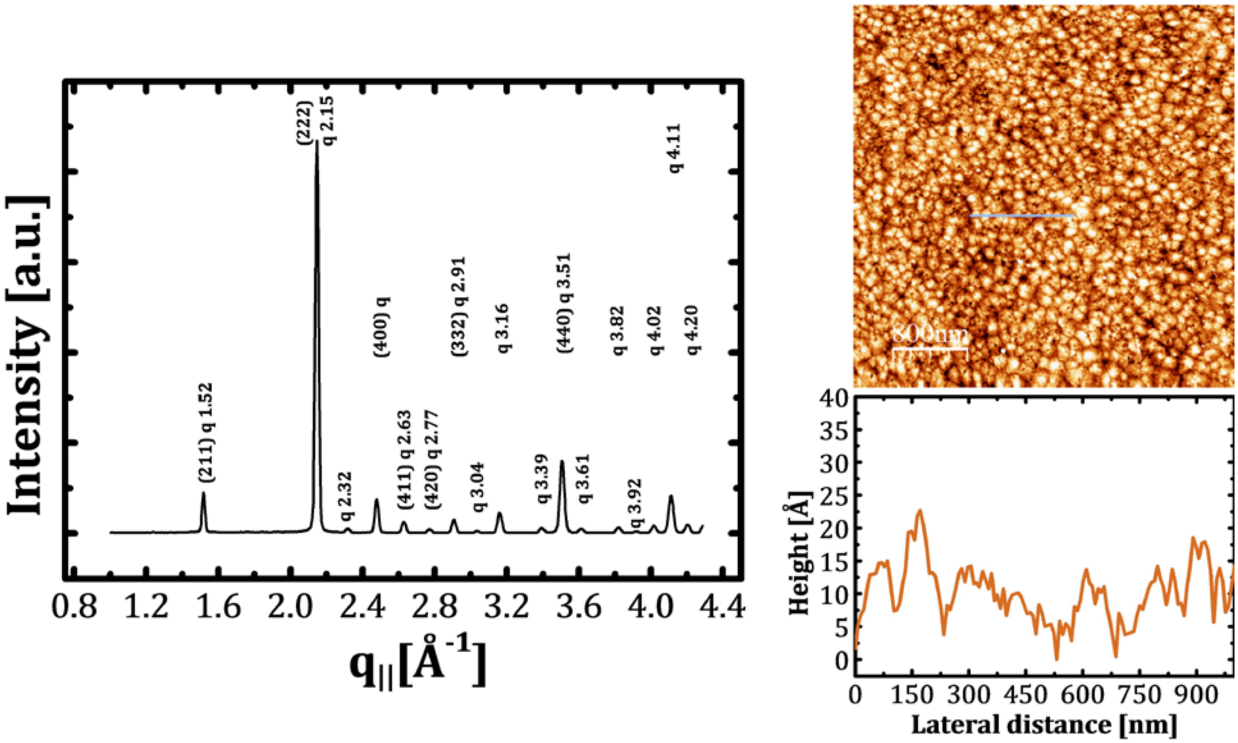

Figure IV.1: GIXRD in-plane response and surface morphology of an ITO substrate.

1. Substrates

Most optoelectronic organic devices use indium tin oxide (ITO) as one of the electrodes due to its optical transparency and electrical conductivity. These features are crucial for collecting light and transporting excess charge carrier to outer circuits. With its relatively high work function of 4.9 eV [66], ITO is mostly used as anode material in electrical circuitry. For improving device performance, many substrate treatments like plasma have been under investigation, e.g. in [67; 68]. Crystalline ITO can be viewed as an indium oxide cubic lattice with tin substitutions at cationic sites. A theoretical model for the surface configuration is given in [69]. When ITO is deposited on glass substrates it forms thin polycrystalline films, shown in Figure IV.1. Several observable in-plane Bragg reflections are interfering with expected organic thin film and inorganic LiF thin film x-ray response. This feature in combination with roughness values of commercial available ITO that do not undergo a limit of 5 Å, make ITO a less favorable candidate for studying ad-layer structure and surface morphology.

In this work (100) terminated silicon substrates capped by its native oxide layer with thicknesses around 12 Å are used in which the SiO_2 surfaces are treated as amorphous substrates. The structure of the underlying Si single crystal is well known [70]. It serves for a clear classification of structural response arising from the substrate or from the thin film of interest on top. Similar growth behavior of organic molecules on SiO_2 and on ITO substrates has been demonstrated by this group [71]. Also extremely flat surfaces with roughness values less than 1 Å legitimate the use of the SiO_2 surfaces as model substrates.

2. Organic molecules

2.1. DIP

Diindenoperylene (DIP) with the chemical formula $C_{32}H_{16}$ is a perylene-derivate with two indeno units, connected to a central perylene ($C_{20}H_{10}$) core. Its original name was periflanthene when it was first synthesized by pyrolysis of flouranthene ($C_{16}H_{10}$) [72]. Derivates of DIP are recently under investigation [73]. DIP has no polar groups and only weak solubility in most solvents. It has a relatively high decomposition temperature around 500° C and sublimation temperature between 200°-300° C. Sufficient stability against oxidation is

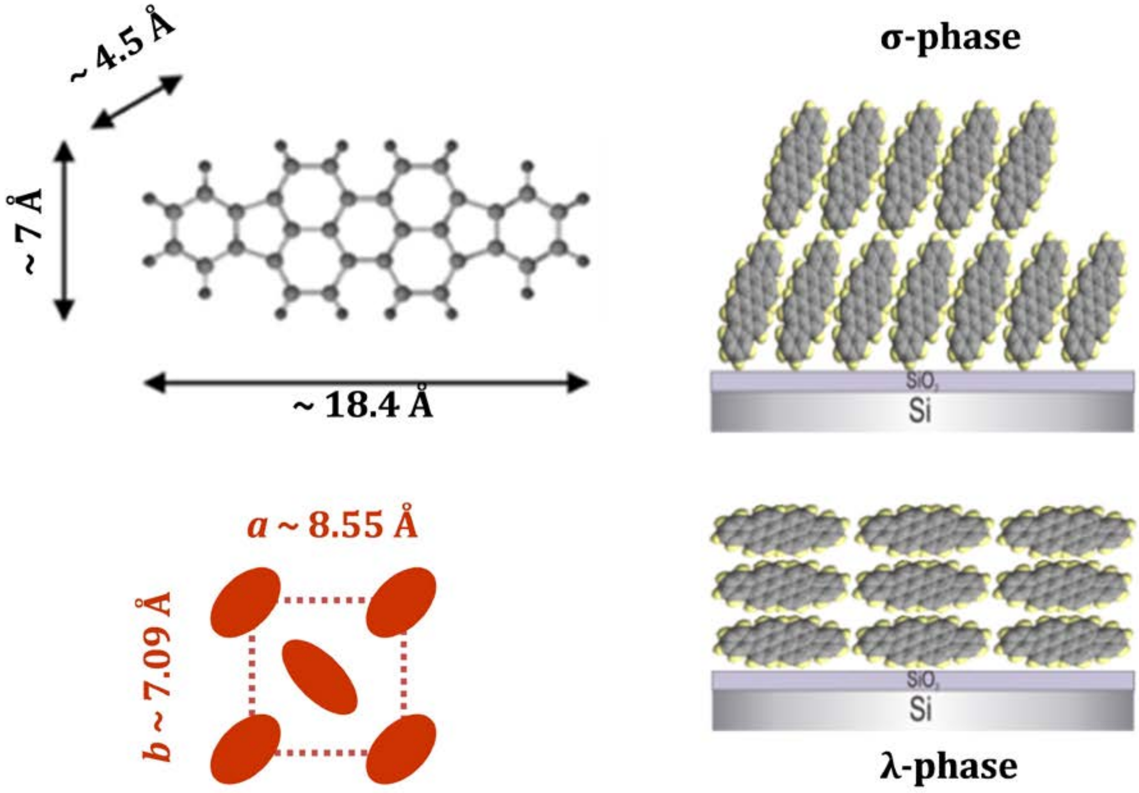

Figure IV.2: The diindenoperylene molecule and layer-by-layer growth modes on SiO_2 surfaces. DIP exhibits a polycrystalline in-plane arrangement in the σ-phase with a herringbone structure (from [80]).

attributed to the shape of the conjugated π-electron system. Molecule dimensions have been calculated with a molecule length of 18.4 Å, a width of around 7 Å and a depth of around 4.5 Å [74]. DIP has almost balanced transport characteristics of holes and electrons in the out-of-plane thin film growth direction [75] and can be used as donor systems in devices. Exciton diffusion lengths reach values up to 100 nm [76]. The DIP molecule film has an optical absorption maximum in the UV region around 300 nm [77]. The hole mobility of DIP has been measured with up to 0.1 $cm^2V^{-1}s^{-1}$ [23] parallel to the surface.

Thin film growth of DIP has been extensively studied on various inorganic surfaces [78; 79; 80; 81]. Two crystalline arrangements are known in the thin film structure when DIP is grown on amorphous SiO_2 with sufficient substrate temperature, namely the standing up σ-phase and the lying down λ-phase. The σ-phase that corresponds to the high temperature monoclinic bulk phase is the preferred arrangement. DIP in the λ-phase is observed after certain thickness and reduced substrate temperature during growth [82]. DIP in the σ-phase forms highly ordered polycrystalline thin films with a polycrystalline herringbone in-plane arrangement under suitable conditions with in-plane lattice parameters $a = 8.55$ Å and $b = 7.09$ Å. The roughness of such films rises with increasing film thickness denoted as rapid roughening phenomenon [83]. Layer-by-layer growth until the 10th monolayer in the σ-phase and initiation of rapid roughening has been observed [84; 85].

2.2. PTCDI-C_8

N,N'-dioctyl-3,4:9,10-perylene tetracarboxylic diimide (PTCDI-C_8) has the chemical formula $C_{40}H_{42}O_4N_2$. The molecule consists of a flat perylene diimide core with two 8-alkyl–substituted chains on opposite sides. Synthesis procedures are reported in [86]. Perylene bisimide derivates were initially applied for industrial purposes as red vat dyes. They are used as pigments due to their insolubility and migrational stability, light- and weather-fastness, thermal stability and chemical inertness [87]. Nowadays, perylene bisimide derivatives are promising candidates for organic semiconductor, especially as electron acceptor materials in heterojunctions. Studies of the electronic behavior have been performed by several groups [88; 89; 90] mainly for the use in transistor applications and turned out electron mobility up to 0.6 $cm^2V^{-1}s^{-1}$.

The molecule dimensions of PTCDI-C_n derivates have been investigated for different alkyl chain lengths between 30 and 70 Å [91]. The formation of a primitive triclinic unit-cell in the bulk material with lattice constants

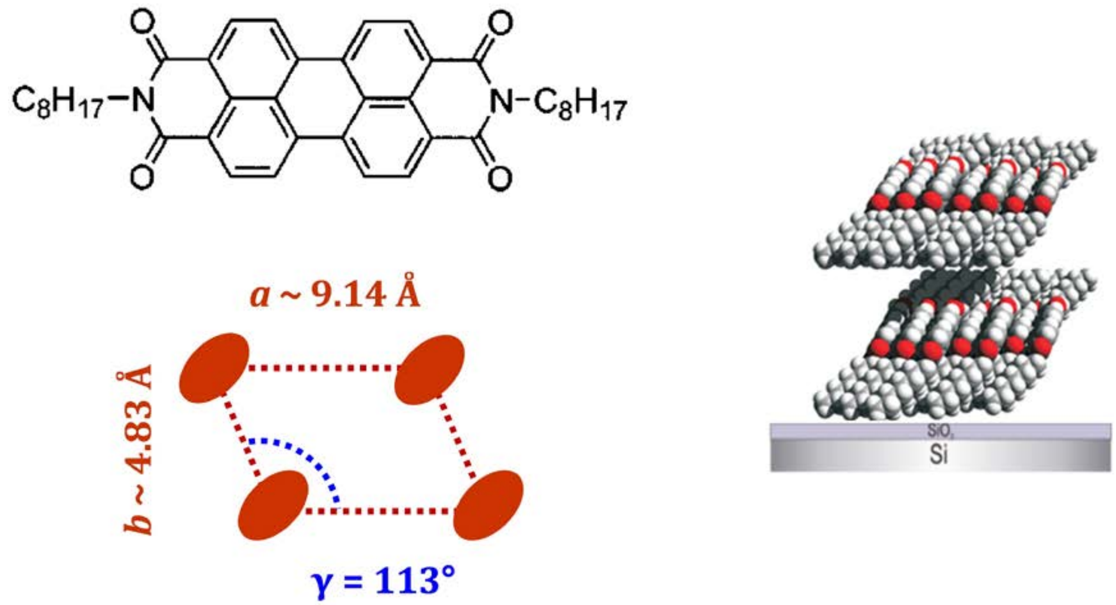

Figure IV.3: PTCDI-C_8 molecule with its layer-by-layer growth mode on SiO_2. An oblique in-plane unit cell structure has been reported (from [88], [93]).

$a = 4.68$ Å, $b = 8.50$ Å, $c = 19.72$ Å, $\alpha = 85.99°$, $\beta = 91.57°$ and $\gamma = 82.97°$ has been reported from the observation of nanowires [92].

PTCDI-C_8 forms atomic flat surfaces with large islands of a needle like morphology. Studies on the growth of PTCDI-C_8 on SiO_2 [93; 94] turned out layer-by-layer growth modes with layer-heights around 20 Å. Non-interdigitating growth behaviors of the alkyl chains and parallel alignment of the π-orbitals in the standing up phase have also been reported. An oblique primitive unit cell structure for the in-plane arrangement on SiO_2 was observed with lattice parameters $a = 9.14$ Å, $b = 4.83$ Å and an in-plane angle $\gamma = 113°$. The obtained triclinic crystal structure for PTCDI-C_8 thin film growth on Al_2O_3 differs again from the bulk structure [95]. It has been reported with $a = 8.50$ Å, $b = 4.68$ Å, $c = 21.65$ Å, $\alpha = 95.0°$, $\beta = 100.7°$ and $\gamma = 112.8°$; note that a and b are interchanged compared to the afore mentioned work. It turned out that the structural order on both substrates can be tuned by sufficient substrate temperatures.

2.3. Pentacene

Pentacene, an extensively studied linear polycyclic hydrocarbon with the chemical formula $C_{22}H_{14}$ is the next higher benzologue of in the naphthalene-antrahacene-tetracene series. It consists of five fused benzene rings and is a

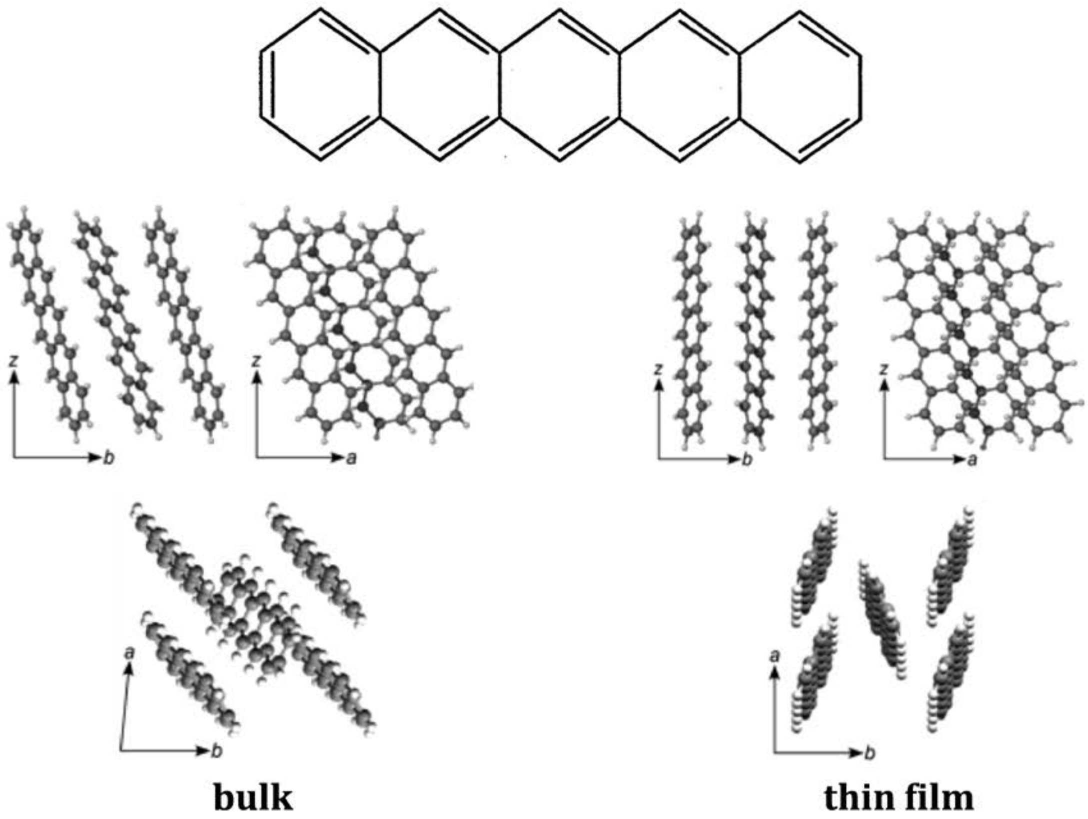

Figure IV.4: Pentacene bulk and monolayer structure. The monolayer structure has several polymorphs and shows herringbone inplane arrangement while the bulk structure has an oblique inplane unit cell (From [101]).

prototype donor molecule for organic electronic devices with hole mobility up to 0.7 $cm^2V^{-1}s^{-1}$ [96]. Pentacene is also one of the first organic molecules that could be directly imaged as a single object by AFM techniques [97]. It is a material that is already used in commercial applications [98].

A triclinic bulk crystal structure has been reported [99]. The growth of pentacene thin films shows several crystalline phases, so called polymorphs [100], dependent on the deposition conditions, substrate orientations and film thicknesses. Layer-by-layer growth with a fiber like structure has been demonstrated [101; 102]. A herring bone in-plane arrangement for sub-monolayer coverage on SiO_2 contrary to the bulk in-plane alignment has been reported in [99]. Out-of-plane herring bone arrangement for the stacked molecules has been reported for all phases [99; 103]. Evaporated thin films of pentacene undergo a phase transition from one of the polymorphs of the thin film structure with terrace like morphology to the bulk with a lamellar like structure beyond critical thicknesses. Thus, thin films offer large flat atomic islands [104].

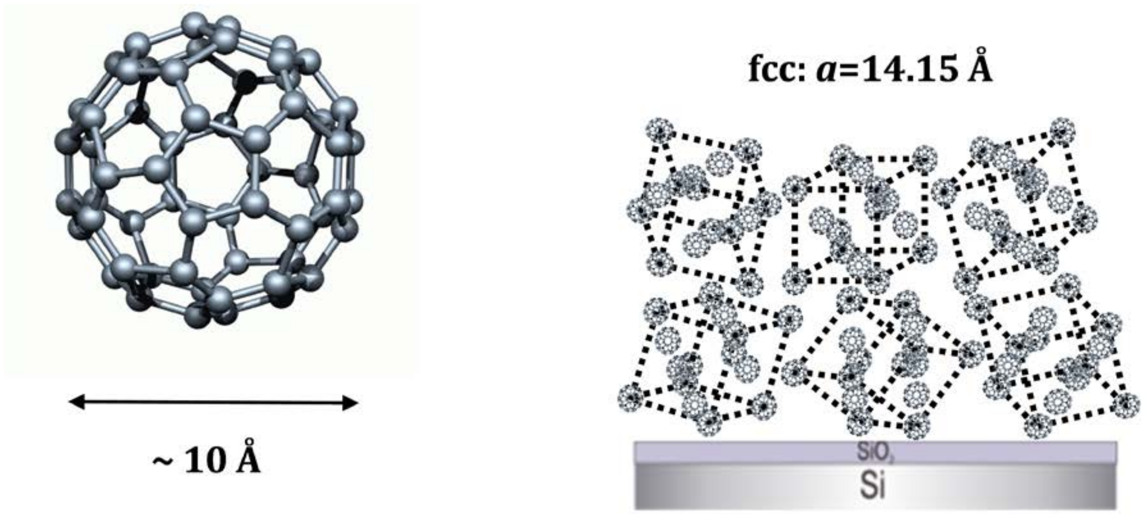

Figure IV.5: C_{60} molecule and polycrystalline fcc thin film structure.

2.4. C_{60}

Buckminster fullerene (C_{60}) was first synthesized by Kroto et al. [105]. It has icosahedra symmetry and consists mainly of pentagonal carbon units surrounded by benzene rings. The insufficient space coverage in that geometry leads to spherical concavity and cave like structure of the molecules with a VdW radius of 10 Å [106]. Since the discovery of C_{60} many other types of fullerenes are known. Fullerenes are promising candidates for organic electronic due to the large number of carbon sp^2 hybridization units and are often used as acceptor materials in organic devices [107; 108; 109; 110; 111]. The electron mobility of epitaxially grown C_{60} films has been measured with up to 1 cm^{2}V^{-1}s^{-1} [112] where hole mobility up to 1.7 cm^{2}V^{-1}s^{-1} has been reported for single crystals [113]. The optical absorption spectrum observed from a fullerene-oligophene-fullerene triad [114] shows absorption for wavelengths from the UV-range up to 550 nm with a local maximum at around 470 nm. Exciton diffusion lengths of C_{60} have been measured around 19 nm [115].

Hcp- and fcc single crystal structures of C_{60} is known with the fcc structure dominating at room temperature [116]. C_{60} thin films on SiO$_2$ have a polycrystalline fcc structure and lattice constant $a = 14.15$ Å [117].

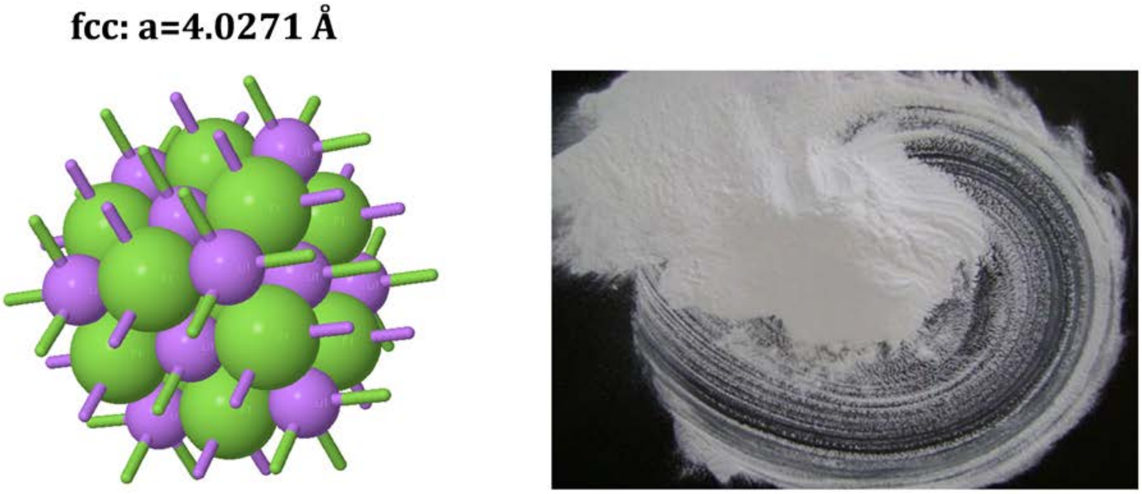

Figure IV.6: LiF forms ionic crystals in the NaCl fcc structure. It appears as white powder solid (From [70]).

3. Lithium fluoride

3.1. General properties

Lithium fluoride (LiF) belongs to the family of alkali halides and appears as white solid powder forming an ionic crystal with the cubic rock salt structure. The bulk lattice parameter of 4.0271 Å is reported by Thewlis [118]. The two involved elements lithium and fluoride have the smallest radius between alkali and halide ions. The cation-anion distance is with 1.5639 Å [119] the smallest for alkali halides which is caused by the fact that fluorine has the largest electron affinity amongst all elements. Single LiF molecules have dipole moments of 6.3 Debye (e.g. NaCl 8.5 D). It is also a very good electrical insulator due to its high band gap of 13.6 eV [120], one of the largest known for solids. In nature it also appears as very rare mineralogical form, called Griceite [121]. Lithium fluoride is of special technological and scientific interest because of some of its special features. It has already been shown, that thin coatings of LiF can reduce the work function of metal electrodes significantly enhancing electron injection and field emission in semiconductor devices [122]. Other studies have observed dipole layers in LiF thin films on diamond surfaces that lower the surface work function by inducing negative electron affinity [123]. Reversible hardening of lithium fluoride crystals by irradiation and post heating as well as the production of color centers has been reported [124]. The ability of forming color centers, induced by ionizing radiation, pushes LiF in the focus for applications in optoelectronics [125].

Table 1: Observable Bragg reflexes for the LiF fcc bulk structure with its lattice plane distances and momentum transfer.

(*hkl*)	***d* [Å]**	***q* [1/ Å]**
(111)	2.3250	2.7024
(200)	2.0136	3.1205

3.2. LiF in thin films

Thin films of LiF are mainly produced by vapor deposition techniques. The sublimation temperature of LiF is at 845° C [126]. Studies on the vacuum vaporization of LiF single crystals observed exponential rate dependence with temperature [127]. Additionally, the formation of different LiF vapor species has been reported [128]. Dimer and trimer formation has been directly observed and the existence of polymers in the vapor has been proposed. The formation of higher order LiF clusters was not excluded in this study.

The crystalline structure of LiF thin films on amorphous substrates has been described regarding the similarity between thin film and bulk structure. Early measurements by Montereali et al. [129] of LiF thin films on amorphous fused silica have shown a polycrystalline arrangement with the (111) planes nearly perpendicular to the substrate surface in the low temperature regime ($T < 200°C$). At higher substrate temperatures during growth ($T \geq 250°C$) the crystallites are arranged with their <100> orientation parallel to the substrate surface. Controversially, Kaiser et al. [130] reported a structure with the <100> orientation perpendicular and parallel to the amorphous substrate using borosilicate glass, vitreous carbon or carbon film surfaces. In their argumentation, the divergent result has been attributed to different film preparation conditions. Last but not least, Cosset et al. [131] observed both, (111) and (200) plane arrangement of the LiF crystallites parallel to a mono crystalline silicon substrate. Additionally, Di Nunzio et al. [132] reported two different LiF crystallite orientations on amorphous glass substrates, dependent on the substrate temperature during growth. For low substrate temperatures they discovered a $\langle 16\ 9\ 7\rangle$ texture in terms of crystallographic direction normal to the substrate plane, where $\langle 5\ 2\ 2\rangle$ texture has been proposed for high substrate temperatures during growth.

Morphological studies dependent on varying substrate temperatures during thin film growth are reported by Cosset et al. [131] as well as sample post annealing by Baldacchini et al. [133] and Golek et al. [134]. All studies observed granular and porous morphology and LiF film surfaces with large roughness. The influence of different deposition techniques on the morphology has been under investigation, like pulsed laser deposition by Perea et al. [135] and off-axis pulsed laser ablation by Henley et al. [136]. Transition of polycrystalline films to fully oriented single crystals have been demonstrated in both studies at substrate temperatures above 300° C. Quantitative analysis of thin film morphology was mostly hindered due the large roughness of LiF surface in such films.

V. MORPHOLOGY OF ULTRATHIN LiF FILMS

The growth of LiF on ultrathin films of organic molecules diindenoperylene, PTCDI-C_8, pentacene and C_{60} on atomically flat substrates is examined. All these molecules have well defined crystalline structures, and typically (except C_{60}) grow in a layer-by-layer mode for several monolayers. The tendency to form large atomically flat islands predestines them to ideal model systems for studying the interfacial morphology by decoupling the morphology of the active layers from that of the inorganic over-layer. In this chapter, the growth behavior of LiF on both donor and acceptor type molecules, which has previously been shown to have different chemical interactions with LiF, is examined by AFM techniques.

1. Experimental details

Thin films with different kinds of organic donor and acceptor molecules were prepared by organic molecular beam deposition. Amorphous and atomically flat SiO_2/Si(100) substrates were used for that purpose. The substrates were cleaned with acetone and ethanol in an ultrasonic bath for 15 min each, rinsed with deionized water for 1 min and dried in a N_2 stream. Prior to deposition, the silicon substrate was annealed under ultra high vacuum (UHV) up to 500° C for 30 min to remove adsorbed water and contaminants. The vacuum conditions during evaporation were typically in the range of 10^{-9} mbar. The organic molecules were either commercially purchased from *Alfa Aesar* (C_{60}) and *Sigma Aldrich* (pentacene) or acquired from the *Universität Stuttgart* (DIP) and *Universität Würzburg* (PTCDI-C_8). All molecules were purified twice by gradient sublimation before use.

The deposition process for ex-situ samples was performed by thermal evaporation from home built Knudsen cells. Several monolayers of organic molecules were deposited with deposition rates of 0.2 monolayers. Inorganic LiF films were also deposited by a commercially available water-cooled Knudsen cell with thicknesses around 10 Å and rates about 8 Å/min. The thickness was determined with a quartz crystal monitor (QCM) that is calibrated on a thick LiF film (~10000 Å). The evaporation temperature of the cell was set to 732° C in the comparative studies.

AFM measurements, processed with the free software *WSxM* [137] were done in air using a Nanotec AFM system in tapping mode with a phase locked loop (PLL) dynamic measurement board. The non contact silicon tips were PPP-FMR from *Nanosensors™* with a resonance frequency of 75 kHz, a force constant of 2.8 N/m and a tip radius of curvature and limiting lateral resolution of around 10 nm.

2. Morphology of ultrathin LiF films on organic surfaces

The morphology of LiF thin films on amorphous substrates has already been widely studied. Many researchers have used SiO_2 as model substrate to examine how the morphology and structure of LiF thin films changes, dependent on various sample treatment procedures. All these studies have used LiF films with thicknesses of several nanometers and deposition rates in the range of numerous nm/s. Contrarily, interlayer thicknesses around 10 Å are typically used, when LiF is introduced into organic devices (see e.g. [138; 139; 140; 141; 142; 143; 144; 145]). Previous studies of LiF growth on organic molecules have either used indirect methods for thin film characterization, e.g.

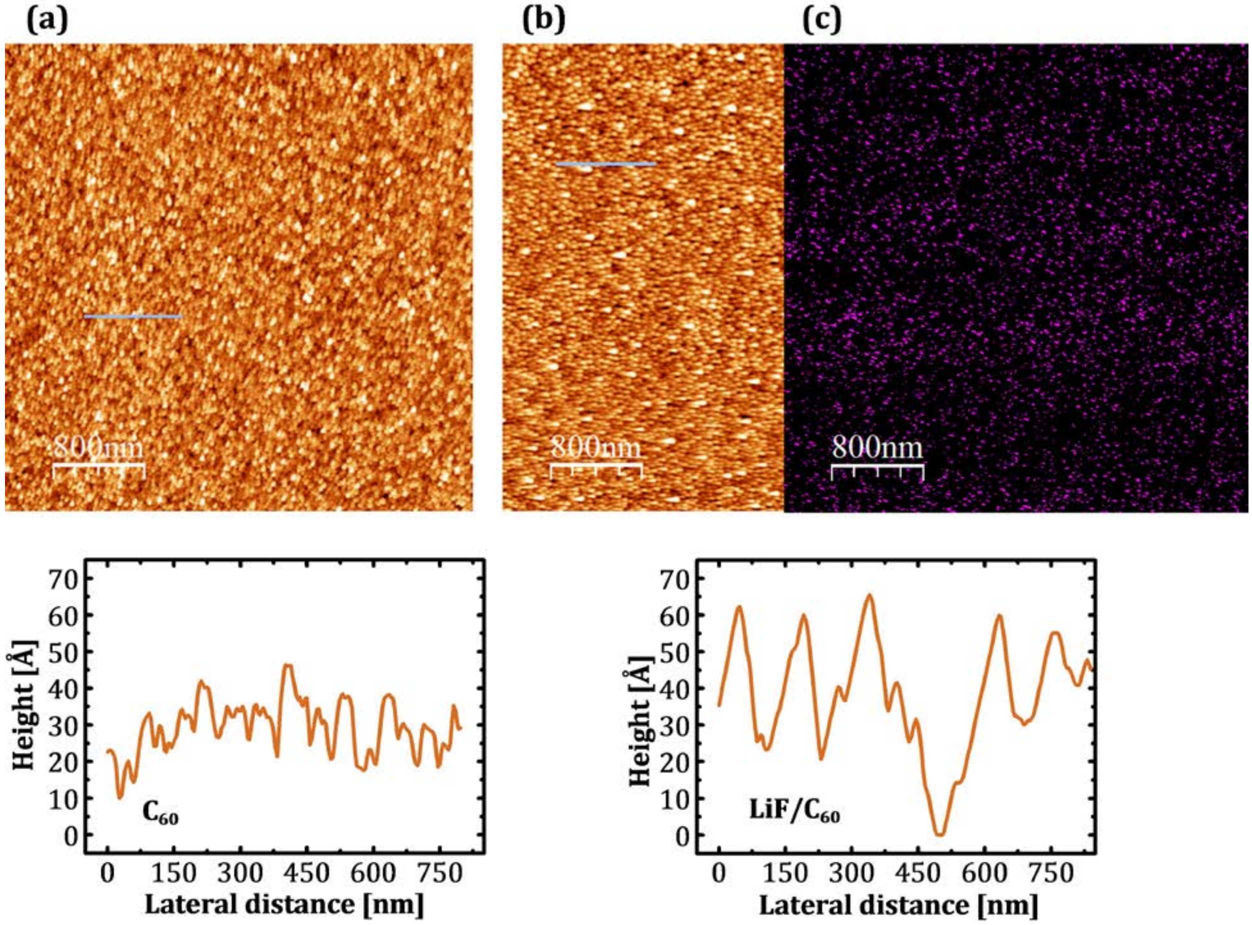

Figure V.1: (a) AFM topography from a thin film of C_{60} (~35 Å) deposited on SiO_2/Si(100). (b) Additional LiF on top of C_{60} cannot be clearly distinguished in the topography due to the rough morphology of the organic film. (c) Imaged material sensitive excitation frequency (for stabilization of the phase displacement in AFM tapping mode) of the LiF/C_{60} sample suggests LiF grains but does not allow quantifying LiF particle dimensions.

electron spectroscopy by Yokoyama et al. [146] or environmental scanning electron microscopy e.g. by Montereali et al. [147]. Other groups described LiF thin film morphology on rough organic surfaces by AFM techniques like Lee et al. [148], Shrotriya et al. [149] and Brown et al. [10]. It limits the ability to draw conclusions about the genuine LiF morphology. This is mainly caused by the roughness of typical molecular surfaces used in devices and it is generally difficult to decouple the LiF morphology and structure from that of the underlying organic layers.

An example of an ultrathin LiF film on C_{60} is shown in Figure V.1. C_{60} is an organic material that is commonly used in state-of-the-art organic photovoltaic devices, The rms roughness of the single organic in the $(4 \times 4)\ \mu m^2$ image in Figure V.1(a) is 5.6 Å which is almost half of rms roughness of the LiF/C_{60} bilayer configuration with 12.6 Å in Figure V.1(b). The organic and inorganic components can thus only be distinguished by material sensitive scanning parameters like the excitation frequency during switched on phase-locked-loop (PLL) of AFM tapping mode, see Figure V.1(c). The phase sensitive images suggest that the organic surface is not completely covered by the inorganic material.

In contrast, the growth of LiF on well described layer-by-layer grown small molecules with low surface roughness allows decoupling of the organic and inorganic morphology. Figure V.2 shows the morphology from a bilayer system of LiF on DIP, grown on amorphous SiO_2/Si(100). High crystallinity of the organic molecule film is achieved by sufficient SiO_2 substrate temperature (∼120°C) during material deposition, e.g. described by Zhang et al. [85].

Height steps in the range of 15-20 Å are observed in both topographies, the single organic layer in Figure V.2(a) as well as in the bilayer configuration in Figure V.2(b). The steps separate large flat organic regions with a common ground height. The steps fit to thickness of an organic monolayer formed by the upright standing DIP molecules. This suggests a layered growth of the DIP film in the so called σ-phase. The rms roughness measured on top of an organic island of DIP is less than 1 Å in the single and bi-layer configuration. The overall roughness of the organic film is dependent on the completeness of the full film and therefore the size and number of the emerging organic islands. The organic islands have lateral dimensions of several μm due to the incomplete monolayer coverage on top of the organic film.

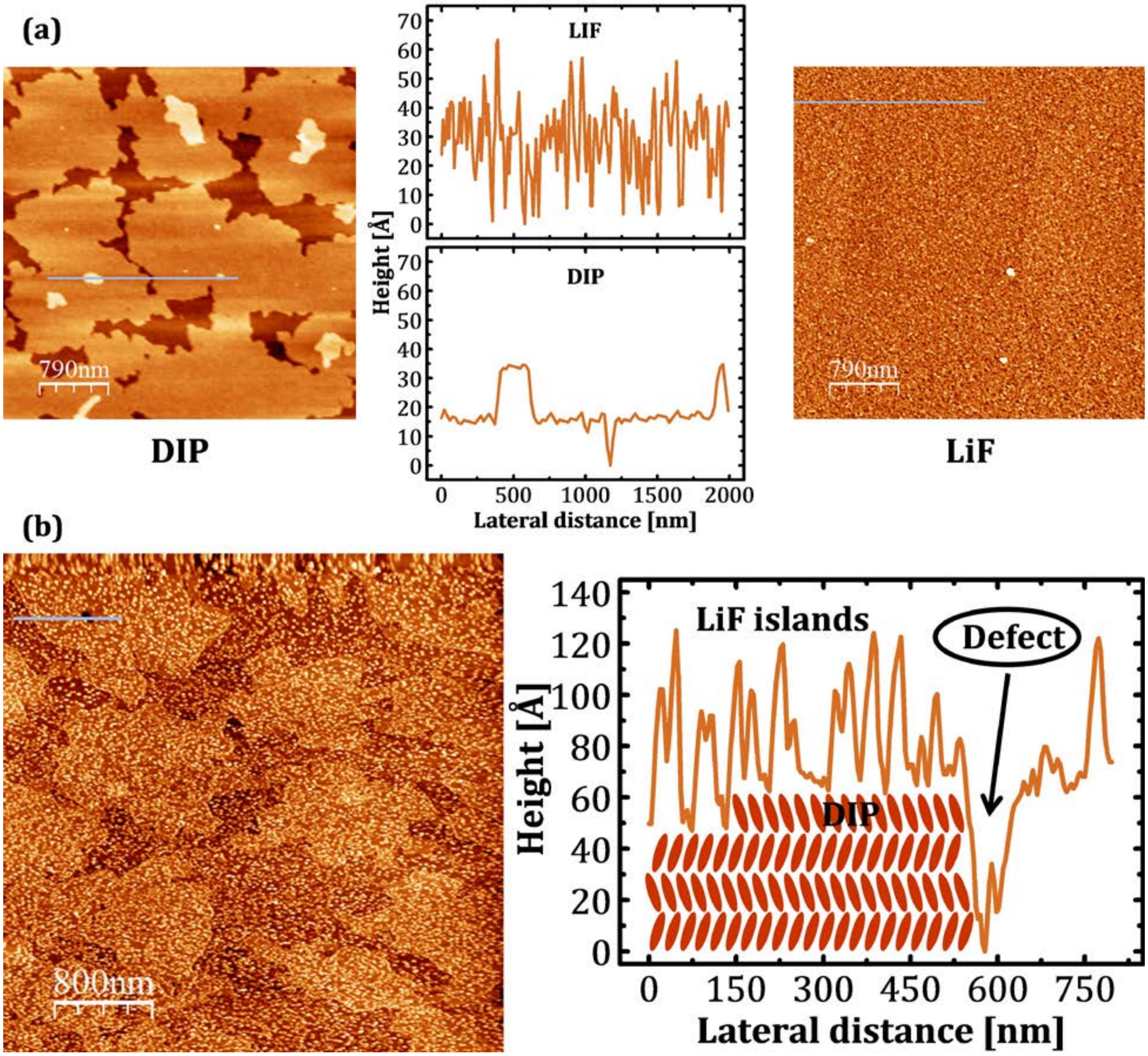

Figure V.2: (a) Topographical image from single films of organic molecule DIP and inorganic LiF on SiO_2/Si(100). (b) The bilayer configuration LiF/DIP/SiO_2 show much more disconnection of LiF islands in comparison to the single LiF film. Height steps between different DIP monolayers and peaked height fluctuations (20-60 Å) are discovered due to LiF . A defect site of the organic thin film is indicated showing the total thickness of the organic film (~62 Å, up to 4 monolayers with 15.5 Å).

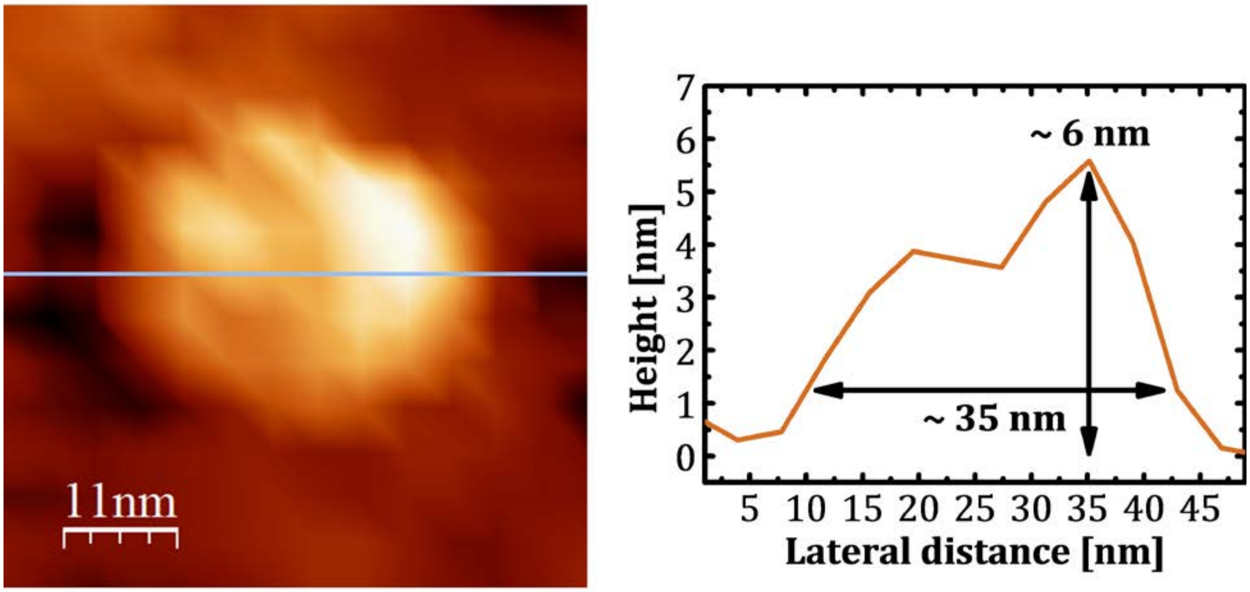

Figure V.3: The comparison of vertical and lateral sizes of an single LiF island show an obvious difference. This difference is attributed to the limited lateral resolution of the used AFM tip.

The organic molecule film with a total thickness of around 62 Å (up to four monolayers with a thickness of 15.5 Å) is covered by small and acute LiF islands in the bilayer configuration in Figure V.2(b). The inorganic islands are clearly disconnected and do not form a complete layer in the present LiF coverage. Increased accumulation at the edges of organic islands and on distinguished areas on top of flat surfaces appears. Note that monitored thicknesses of the LiF single film from Figure V.2(a) and the bilayer configuration in (b) are identical and again around 10 Å.

The height of the LiF islands has been measured in the range of 40-60 Å above the organic surface. The topography of LiF suggests circular shaped islands with lateral sizes up to 500 Å, shown in more detail in Figure V.3. This does not coincide with the measured LiF island height. There is a strong evidence that the limited lateral resolution of the used AFM tip (>10 nm) likely does not allow an accurate measurement of the lateral dimension of the LiF particles. Observations of changing lateral particle sizes already during the measurement of a single image (not shown) support this assumption. The problem has also been reported by Cremona et al. [150]. Nevertheless, symmetric spherical shape for LiF particles has been assumed which is in agreement with TEM measurements (see Chapter VI.1). Thus the particle area is calculated by using the height of the particles. Under these conditions, an

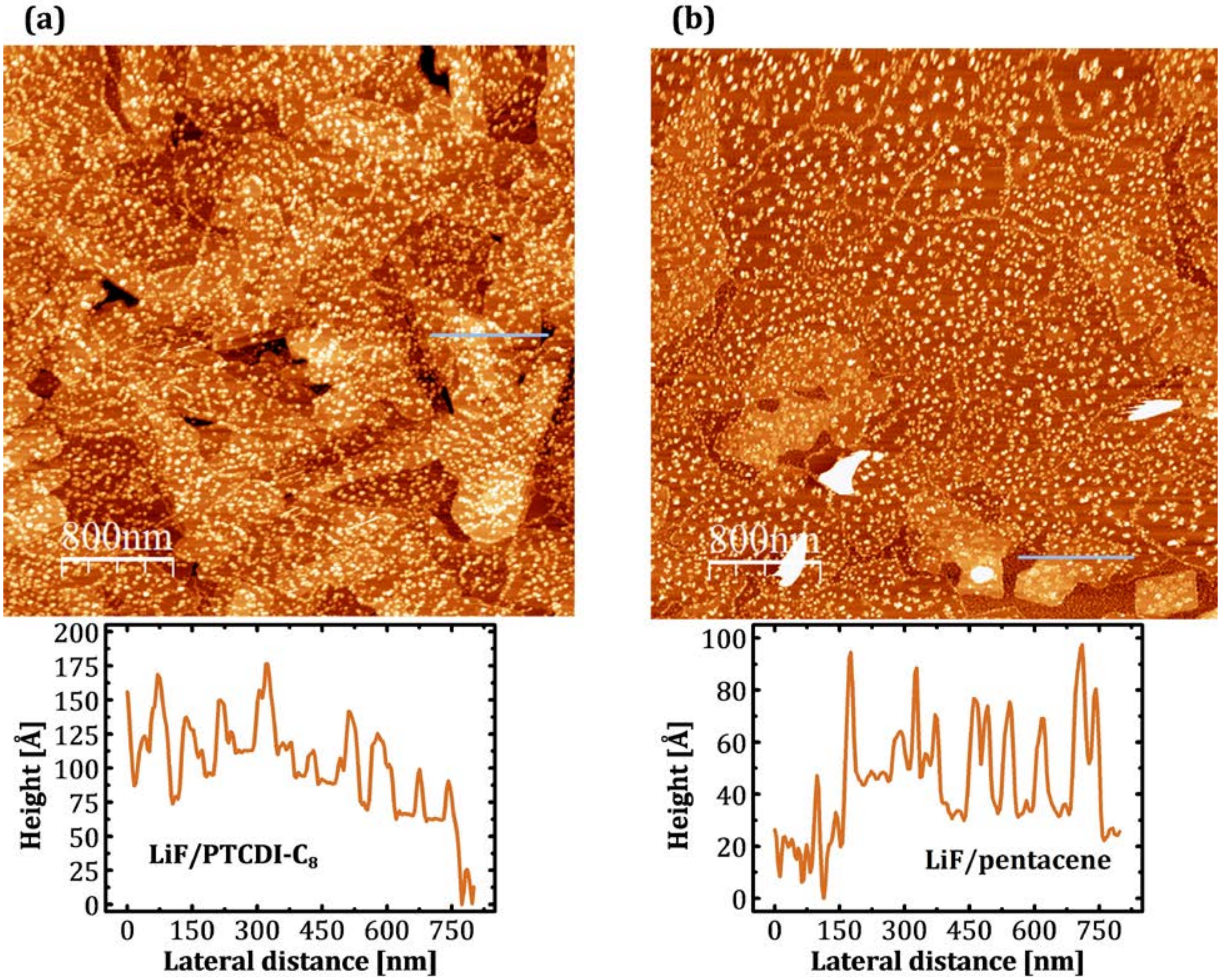

Figure V.4: (a) LiF island formation on organic acceptor molecules PTCDI-C_8 and (b) donor molecules pentacene. The islands are clearly disconnected in both cases. Chain like arrangement and dendritic agglomeration especially on the 1st monolayer of pentacene are observed.

estimation of the LiF coverage by multiplying the number of LiF islands with its area is applied and listed in Table 2.

Figure V.4 shows the growth of LiF with the same nominal thickness on two other layer-by-layer grown organic molecules PTCDI-C_8 and pentacene. Both donor (pentacene) and acceptor (PTCDI-C_8) type molecules have been deposited on SiO_2/Si(100) substrates. The total thickness of the underlying PTCDI-C_8 film in Figure V.4 is around 120 Å and around 45 Å for pentacene. Both organic molecules form large crystalline islands on the inorganic substrate with lateral sizes ranging from 0.1-4 µm. High crystallinity of the organic films has been achieved by sufficient substrate temperatures during growth (PTCDI-C_8 ~90° C, pentacene ~40° C). Surfaces on top of the organic islands have rms roughness around 1 Å in both cases.

Deposition of LiF on top of these flat organic surfaces leads again to the formation of disconnected islands with heights around 40-60 Å. This is independent of donor- or acceptor-like molecule surfaces, despite previous indications of differing charge transfer interactions with LiF [151]. The arrangement of the LiF islands on PTCDI-C_8 is mostly random but agglomeration on the edges of organic islands and even on top of a flat surface area has been observed.

LiF islands on top of pentacene have a more dendritic arrangement compared to the morphology on DIP and PTCDI-C_8. This behavior is especially observed on the 1st monolayer of pentacene and will be discussed in more detail in one of the next sections. The lateral sizes of the LiF islands are always larger than their respective heights. As it is stated above, this observation is due to the limited lateral resolution of the AFM tip and a spherical shape of the particles has been assumed.

Table 2: Thin film coverage on different organic molecules with equal deposition amounts of LiF. The minimum particle size for automated island counting was set to 0.3277 nm^2. A statistical square root error for the determined number of islands has been assumed.

10 Å LiF monitored by QCM	Image size [μm×μm]	LiF islands average height [Å]	Number of LiF islands	LiF coverage [%]
DIP	4×4	50 ± 10	8846 ± 94	1.08 ± 0.45
PTCDI-C_8	4×4	50 ± 10	5014 ± 71	0.61 ± 0.25
pentacene	4×4	50 ± 10	4690 ± 69	0.57 ± 0.24

As heights of the LiF islands do not deviate significantly from each other, the coverage has been determined from Fourier subtracted topographies with an assumption of equal particle dimensions on the observed organic surfaces.

A comparison of LiF coverage in Table 2 turns out different values on each organic molecule surface. The difference in coverage is neither related to the roughness nor incompleteness of the respective organic molecule surface. Additionally, a systematic effect in coverage behavior on donor- or acceptor-type surfaces has not been observed. Even if LiF has been deposited with the same monitored thickness it is not clear, if the divergent coverage values are dependent on the organic surface under study or due to slightly variations in the growth conditions. Simultaneous LiF growth on all organic molecule surfaces, which reduce this uncertainty, has not been successful because of experimental limitations. It is stated that all coverage numbers are around 1% for the monitored thickness of 10 Å. LiF has the largest coverage on DIP where the lowest is measured on PTCDI-C_8.

The observation shows that characterization of ultrathin LiF films depends extremely on the method of monitoring film heights. As LiF thin films are prepared by tracking the film thickness by means of a somehow calibrated quartz crystal monitor, the association of ultrathin films (<60 Å) with a specified thickness does not explain the true character of ultrathin LiF films.

3. LiF thin film morphology on inorganic vs. organic surfaces

Figure V.5 shows an example where LiF covers two different surfaces on one sample, the inorganic SiO_2/Si substrate as well as sub-monolayer coverage of DIP. The film thickness has been monitored again with a thickness of 10 Å and the film has been deposited with rate of around 8 Å/min. Parallel growth of LiF on both surfaces allows a direct comparison to differences in the morphology.

A granular structure of the LiF film is visible on SiO_2. The topography of the LiF film on the inorganic substrate indicates granular morphology as reported already for thick films. Yazicigil et al. [152] proposed already a porosity of LiF thin films. Contrary, vanishing porosity has been proposed for ultrathin LiF films (less than 300 Å) by Kaiser et al. [130]. In contrast, measured morphology in this examination suggests a porous structure from initial conditions due to the deposition of nanoscaled islands/particles. LiF agglomerates at random positions on inorganic surface. The observed LiF grains seem to be partly connected. The topography suggests also non-unique lateral sizes of the LiF grains. It is again not clear, if this is related to the limited resolution of the measurement technique. In contrast, much less LiF islands are visible on DIP and they are mostly disconnected. Increased accumulation at the edges of the organic island is also indicated.

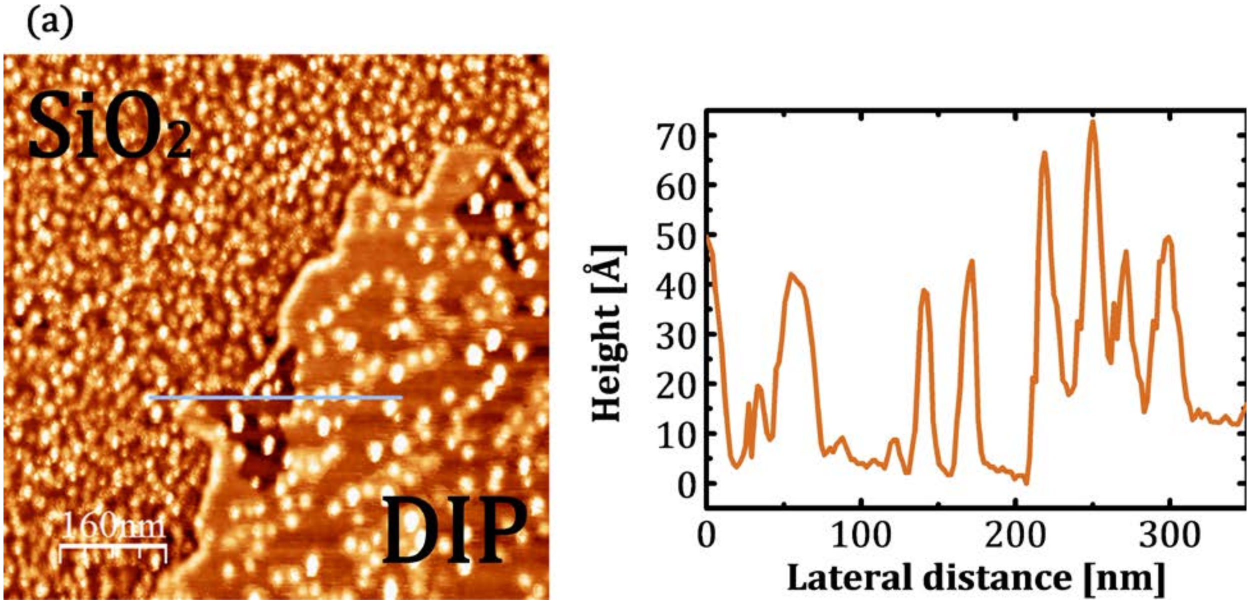

Figure V.5: (a) Topographic image of a LiF film grown on a SiO_2 substrate partially covered by one DIP island.

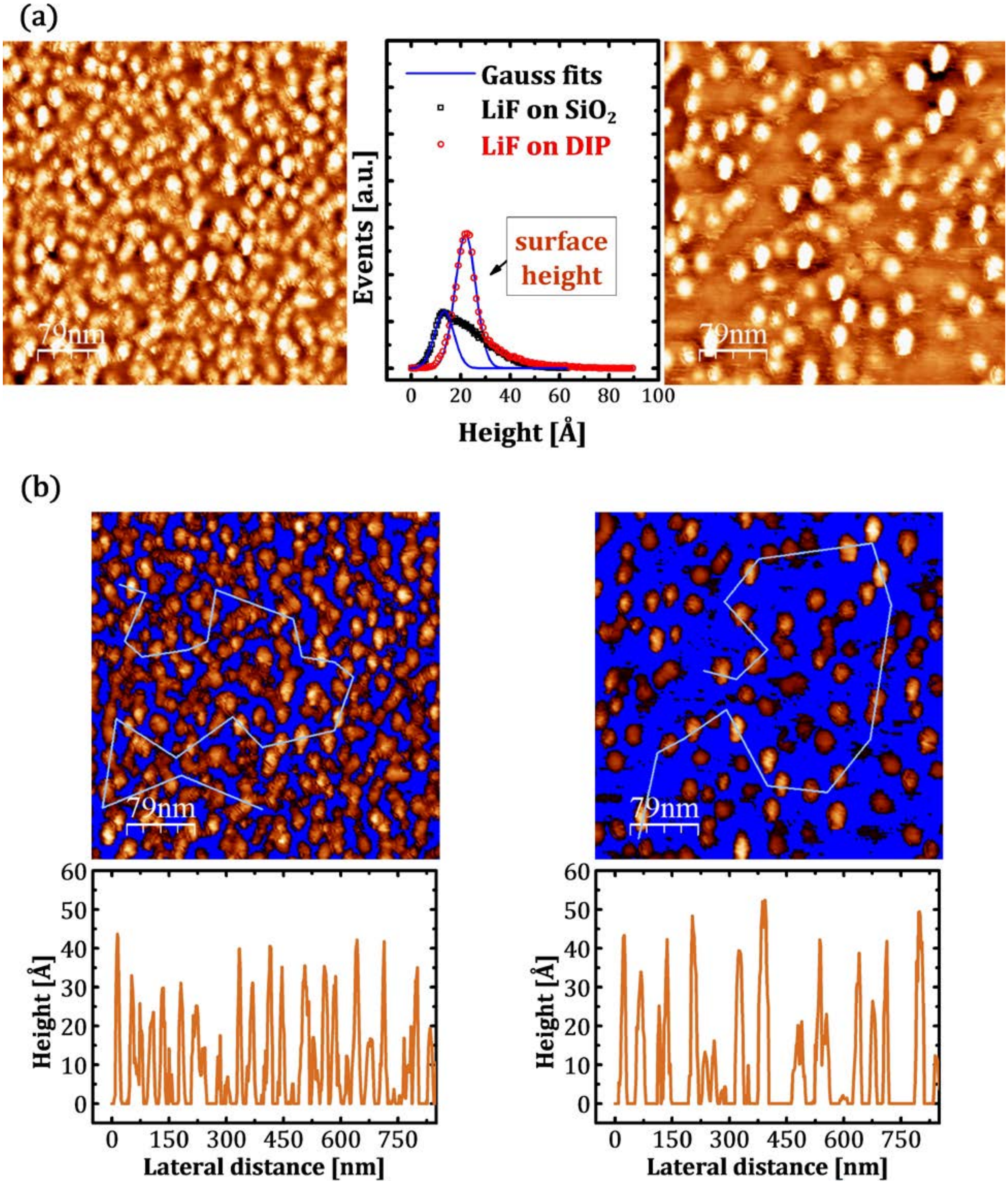

Figure V.6: (a) Fourier subtracted topographies of LiF, parallel grown a SiO_2 *(left) and DIP (right). Surface heights are expressed by Gaussian distributions in the height histogram. (b) The surface average height has been used as flooding threshold. Height profiles suggest slightly larger LiF particle heights on DIP.*

Fourier Subtraction has been applied to the sample topography for comparison to the particle sizes and estimation of the material coverage. Zoomed Fourier subtracted images from both surfaces are shown in Figure V.6. The measured height distributions from both images show strong peaks. These peaks have been attributed to the average height of the respective surface underneath.

This identification is justified since the underlying surfaces have Gaussian distributed heights caused by the Fourier subtraction procedure. Otherwise, heights of the LiF particles are expressed in the tail of the distributions and difficult to quantify. Nevertheless, the obtained surface height together with an added σ-error from the Gaussian fit has been used as a flooding threshold.

Resulting height profiles from the flooded images allow a comparison of LiF particles heights even if absolute numbers are falsified by the Fourier subtraction process. It turns out, that maximum LiF particle heights are slightly smaller on the SiO_2 surface compared to DIP. Particles have also varying vertical sizes on the inorganic surface whereas they have rather equal heights on the organic surface.

For an estimation of the LiF coverage, equal particle heights of around 50 Å and symmetric spherical particle shape have been assumed for both surfaces. The values for SiO_2, shown in Table 3, are only an upper limit as the particle height distributions do not suggest uniform particle heights on this particular surface. On this assumption, the LiF coverage on SiO_2 is up to four times larger than that on DIP.

Table 3: Determined coverage of direct compared LiF thin films on SiO_2 and DIP. The minimum particle size for automated island counting was set to 0.3277 nm^2. A statistical square root error for the determined number of islands has been assumed.

Substrate	Image size [μm×μm]	LiF islands average height [Å]	Number of LiF islands	LiF coverage [%]
SiO_2	0.4×0.4	50 ± 10	366 ± 20	4.57 ± 2.07
DIP	0.4×0.4	50 ± 10	100 ± 10	1.24 ± 0.62

The appearance of LiF particles with various heights and increased coverage on the inorganic surface compared to particles with more uniform heights and less coverage on the organic surface gives indication that sticking of already present LiF particles defines the morphology of the film. In this manner mere particles with sufficient mass and thus sufficient kinetic energy are able to disrupt the ordered organic surface and create adsorption sites. Reported negative U-center dangling bonds [153] in SiO_2 surfaces explain also that smaller LiF particles show sticking to this inorganic surface.

4. Morphology with increasing LiF film thicknesses

As the organic surfaces are not completely covered by LiF, it is interesting to see how the film evolves with increasing LiF deposition. To study this behavior, two different amounts of LiF have been grown on DIP/SiO_2. Because of the ex-situ character of the experiment the thickness of the organic film is up to 3 monolayers for the lower LiF coverage and up to 4 monolayers for larger LiF coverage. It is not important here as long as full coverage of the

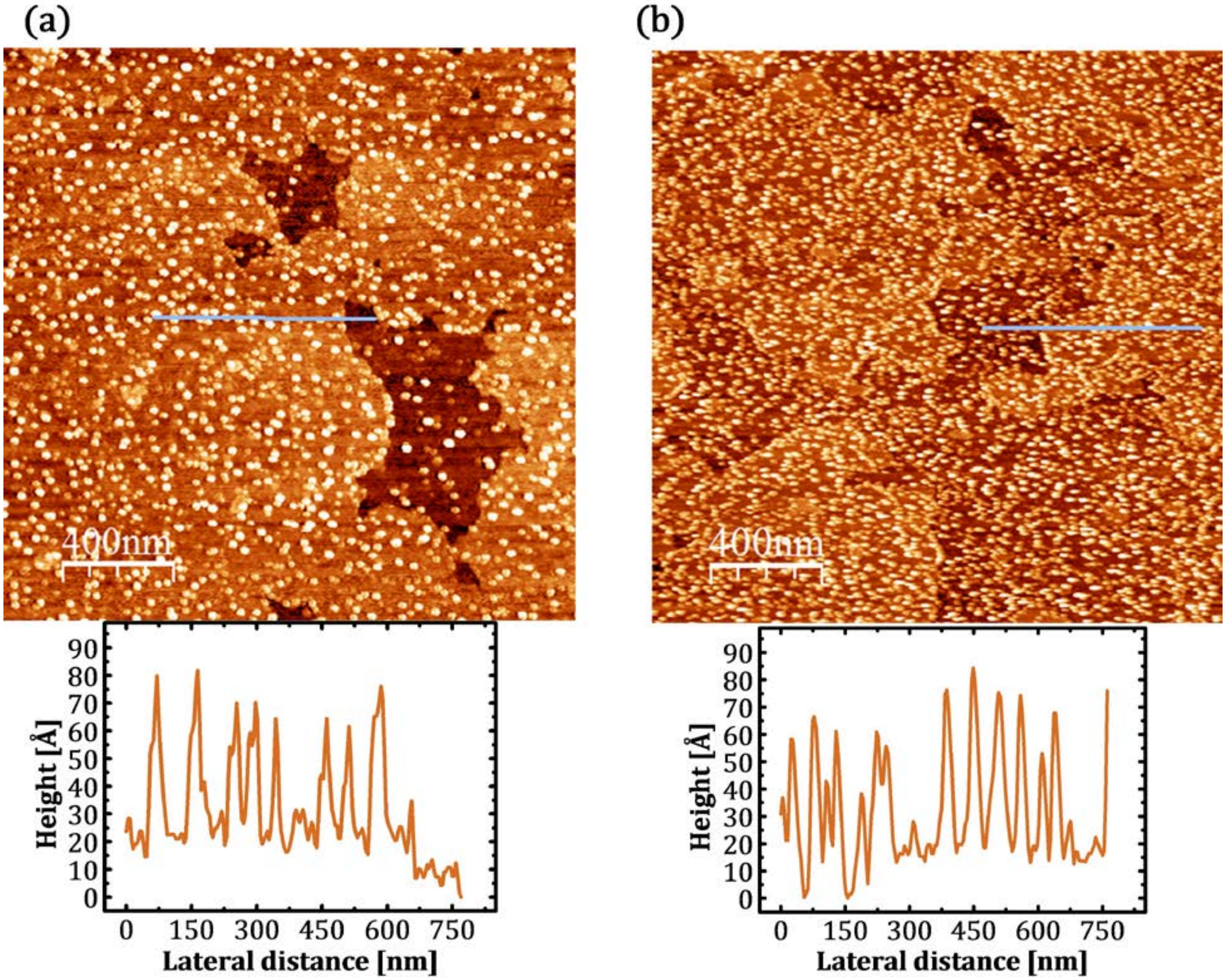

Figure V.7: Topographic images of nominally (a) 5 Å and (b) 10 Å LiF deposited on DIP/SiO_2.

organic film has been reached. Sufficient substrate temperature during organic molecule growth has been applied to create atomically flat surfaces on top of the organic film. The monitored thickness of the lower covered sample in Figure V.7 is half of the sample which shows a monitored thickness of 10 Å.

Zoomed regions of each sample have been Fourier subtracted to analyze the LiF particle heights in more detail. Height histograms of the Fourier subtracted images are shown in Figure V.8. Strong signal peaks at 18.6 Å for less LiF coverage and 21.4 Å for larger LiF coverage have been determined by Gaussian fitting. These values were again attributed to the remaining surface average height of the underlying and not completely subtracted surface morphology. The surface values with an added σ-error from the Gaussian distribution have been used as flooding threshold. As the particles do not show a completely uniform height, only a qualitative comparison can be discussed. Height profiles from the flooded images show no significant difference in the particle size between both deposition amounts. Just the number of LiF increases when more material is deposited.

Analyses of the coverage of these two systems with an assumed average particle height of 50 Å on both surfaces from Figure V.7, performed from Fourier subtracted images of both samples (not shown), are listed in Table 3. The obtained values indicate a linear mass to coverage relation below 100 percent LiF coverage.

Table 4: Determined coverage of two ultrathin LiF films on DIP/SiO$_2$ with two different monitored thicknesses. The minimum particle size for automated island counting was set to 0.3277 nm^2. A statistical square root error for the determined number of islands has been assumed.

LiF monitored by QCM	Image size [μm×μm]	LiF islands average height [Å]	Number of LiF islands	LiF coverage [%]
5 Å	2×2	50 ± 10	1368 ± 37	0.67 ± 0.29
10 Å	2×2	50 ± 10	2578 ± 51	1.26 ± 0.53

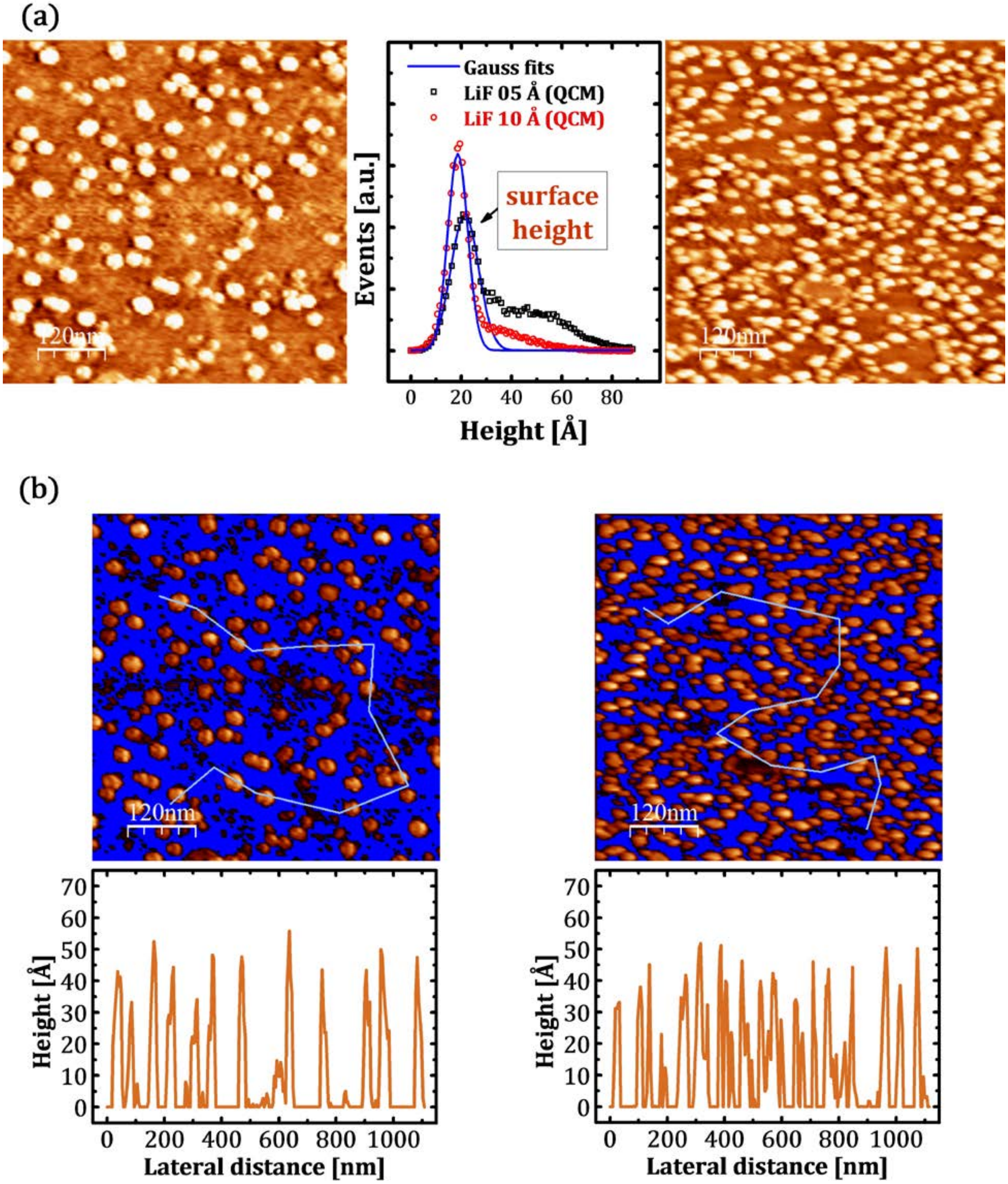

Figure V.8: (a) Fourier subtracted topographies of LiF on DIP nominally 5 Å (left)and 10 Å (right). Surface heights are expressed by Gaussian distributions in the height histogram. (b) The surface average height has been used as flooding threshold. Height profiles suggest equal LiF particle heights for both monitored thicknesses.

The formation of a complete layer build up from small LiF particles is proposed within an extrapolation of the observed behavior. Even if the coverage shows a linear mass behavior, a clear statement is difficult due to the uncertainty in particle height and coverage determination. Anyway direct particle growth on the organic surface is unlikely as the particle sizes would increase in size. Instead of that, sticking of already present particles at the organic surface is assumed

5. Variation of LiF growth parameter

The influence of varying LiF growth parameters like the substrate temperature during growth and the deposition rate has been investigated on DIP and PTCDI-C_8. Changing of the substrate temperature is very limited by reason of the soft character of the organic molecule films and destructive

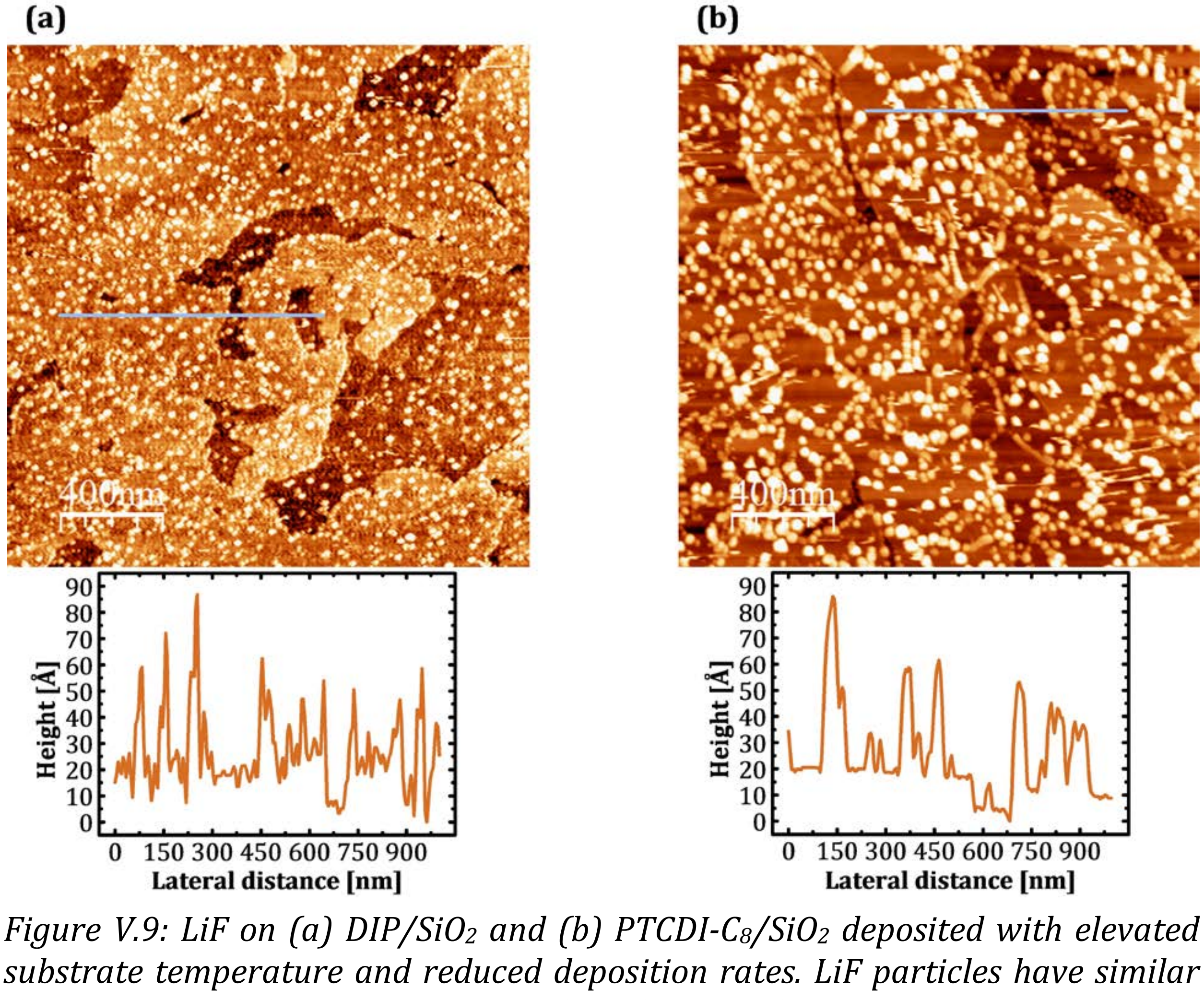

Figure V.9: LiF on (a) DIP/SiO_2 and (b) PTCDI-C_8/SiO_2 deposited with elevated substrate temperature and reduced deposition rates. LiF particles have similar dimensions and dispersion compared to the growth at room temperature and with fast rates.

influence of heat to the stability of the organic network. Elevated substrate temperatures around 97.5° C and 88° C during LiF growth have been tested. Changing deposition rates are achieved by reducing the cell temperature from 732° C to 650° C. This increases the deposition time by a factor of around 8.

No differences could be observed in the topographical images obtained from LiF/DIP and LiF/PTCDI-C_8 bilayer configurations in Figure V.9. LiF island heights are again in the range of 40-60 Å which does not indicate larger particle dimensions. Agglomeration at island edges and in the chain arrangement is visible but not different from samples with LiF grown at room temperature or with the fast rate, for example in Figure V.2 and Figure V.4.

6. Chain-like arrangement of LiF particles on organic surfaces

Preferred sticking of LiF particles at edges of flat organic islands and chain-like arrangement on top of the organic flat surfaces has been discovered on all layer-by-layer grown organic molecules used in this study. Figure V.10(a) points out the height profile across LiF particles on a single island of DIP with the height of one monolayer. According to the measured profile, heights of particles that are placed on the edge of one island (1) differ around 20 Å from the ones placed on top of the organic island (2). This number is just in the range of the size from an upright standing DIP molecule. The particle heights are comparable to the ones measured on the inorganic SiO_2 substrate (3) next beside, which suggests that these particles are sitting at the side of one island and not on top of it.

The same behavior appears also on fully covered organic surfaces. The chain-like arrangement of LiF is very pronounced especially on the first monolayer of the organic surfaces with an equal height distribution. Measured height profiles from LiF particles on top of a DIP monolayer and in the chain-like arrangement in Figure V.10(b) show again a height difference that is in the range of one monolayer of an upright standing organic molecule. The reason for this behavior can either be preferred sticking of the particles on the inorganic surface underneath or at the boundary of an ordered region in the organic network. As the chain arrangement vanishes for thicker organic films, but is still visible even on top of organic films with coverage of several monolayers, combinations of both described adsorption places are possible.

An argument for preferred sticking at organic island edges is shown in Figure V.11(a) and (b). The LiF/DIP bilayer configuration with chain-like arrangement of the LiF particles has been measured constantly during several hours.

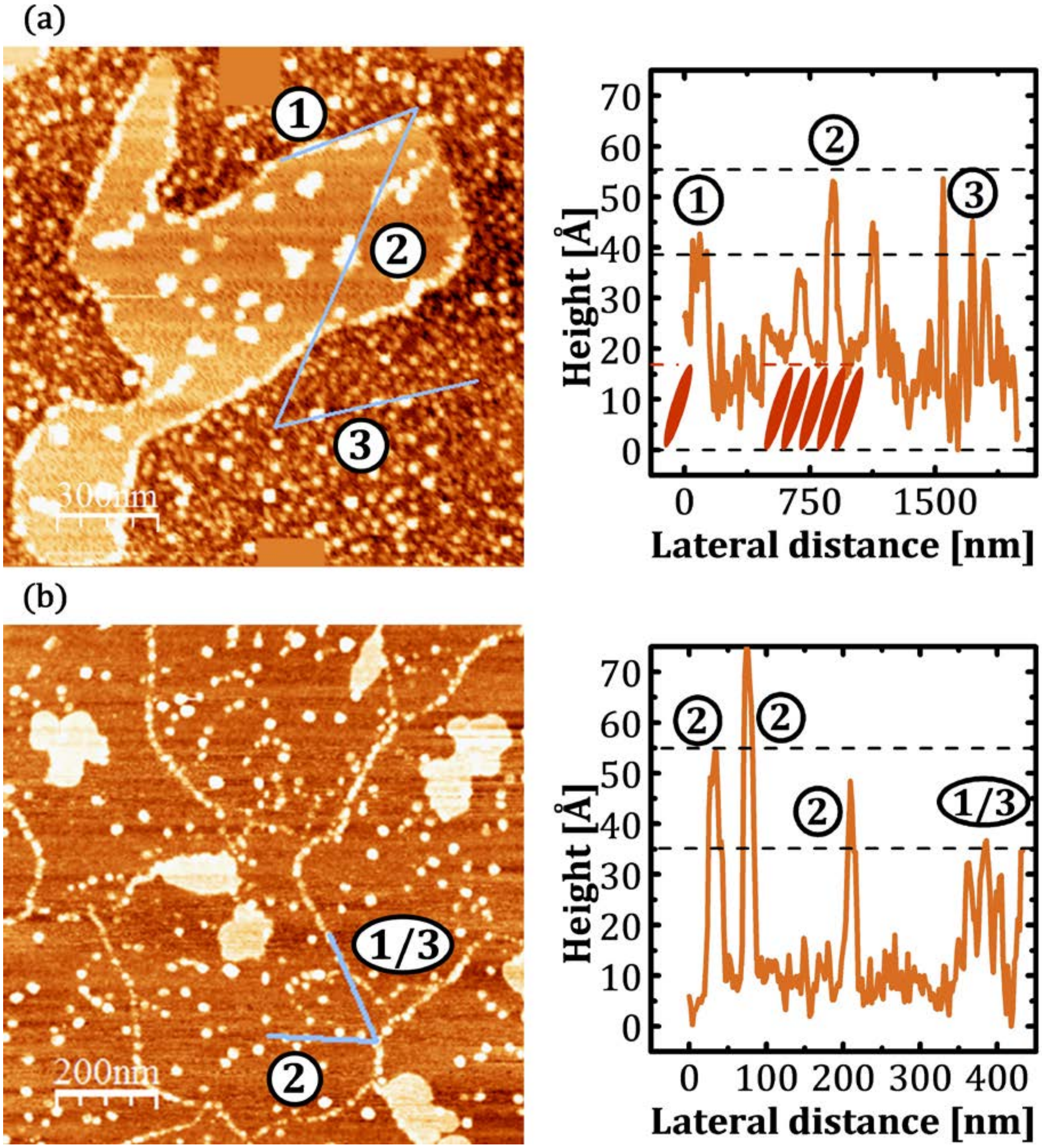

Figure V.10: (a) Topographic image (left) and corresponding height profile (right) of LiF particles on top of an organic DIP island (2) and on the edge of that island (1). The observed height difference is in the range of a DIP monolayer. Particle heights at the specified positions are comparable to the ones grown on SiO_2 (3). (b) Topographic image (left) and corresponding height profile (right) on top of one atomically flat DIP monolayer (2) and in the chain-like arrangement (1/3). This difference suggests that LiF particles in the chain-like arrangement stick to the inorganic SiO_2 surface already.

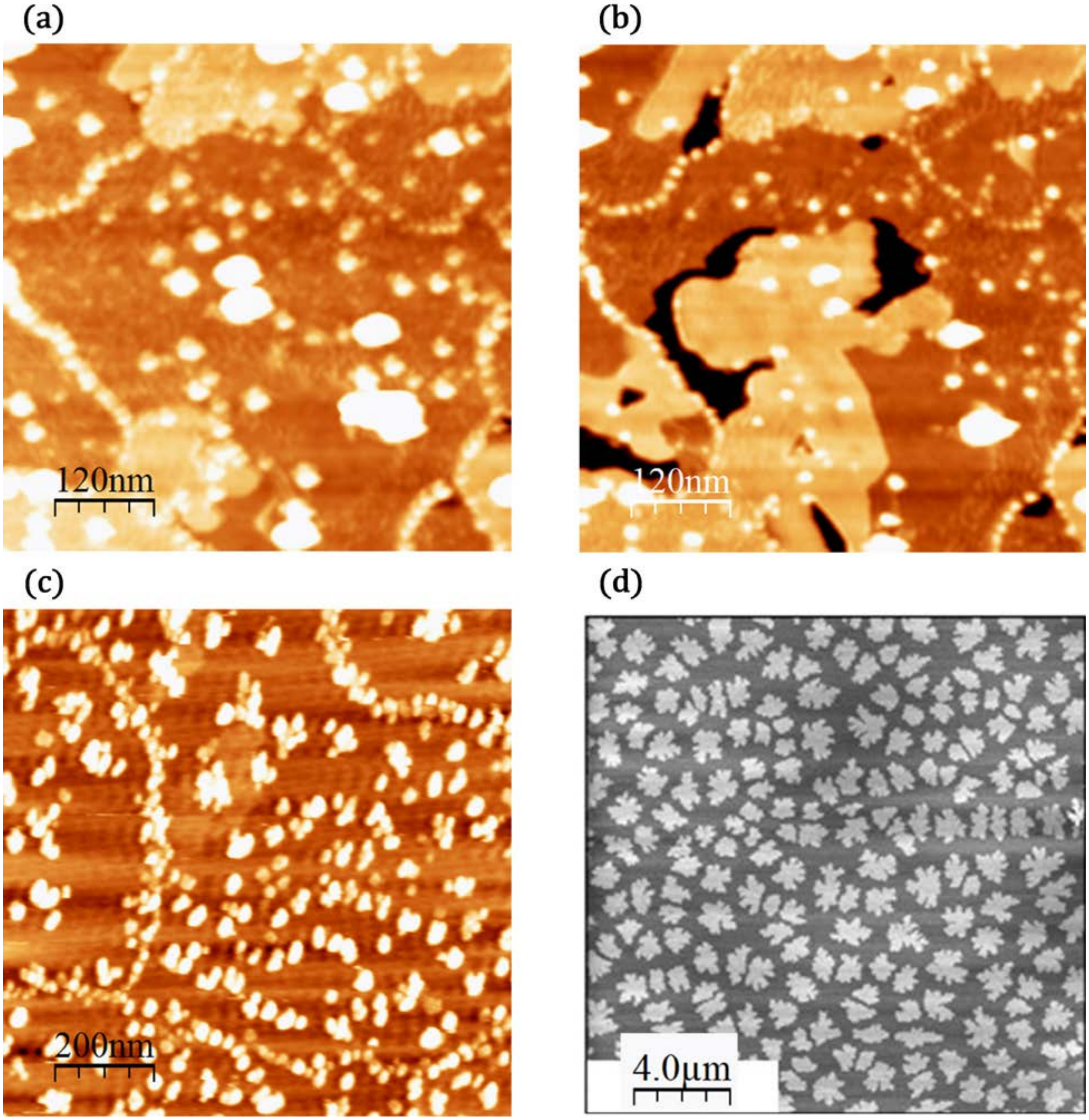

Figure V.11: (a) Topography of LiF particles on the first monolayer of DIP. (b) The same area after constant measurement for several hours. The organic film cracks up at positions where chain-like LiF particle arrangement takes place. (c) Dendritic shape of LiF particles on pentacene are related to the morphology of (d) the organic film, when LiF sticks again on the edges of ordered large organic islands (from [153]).

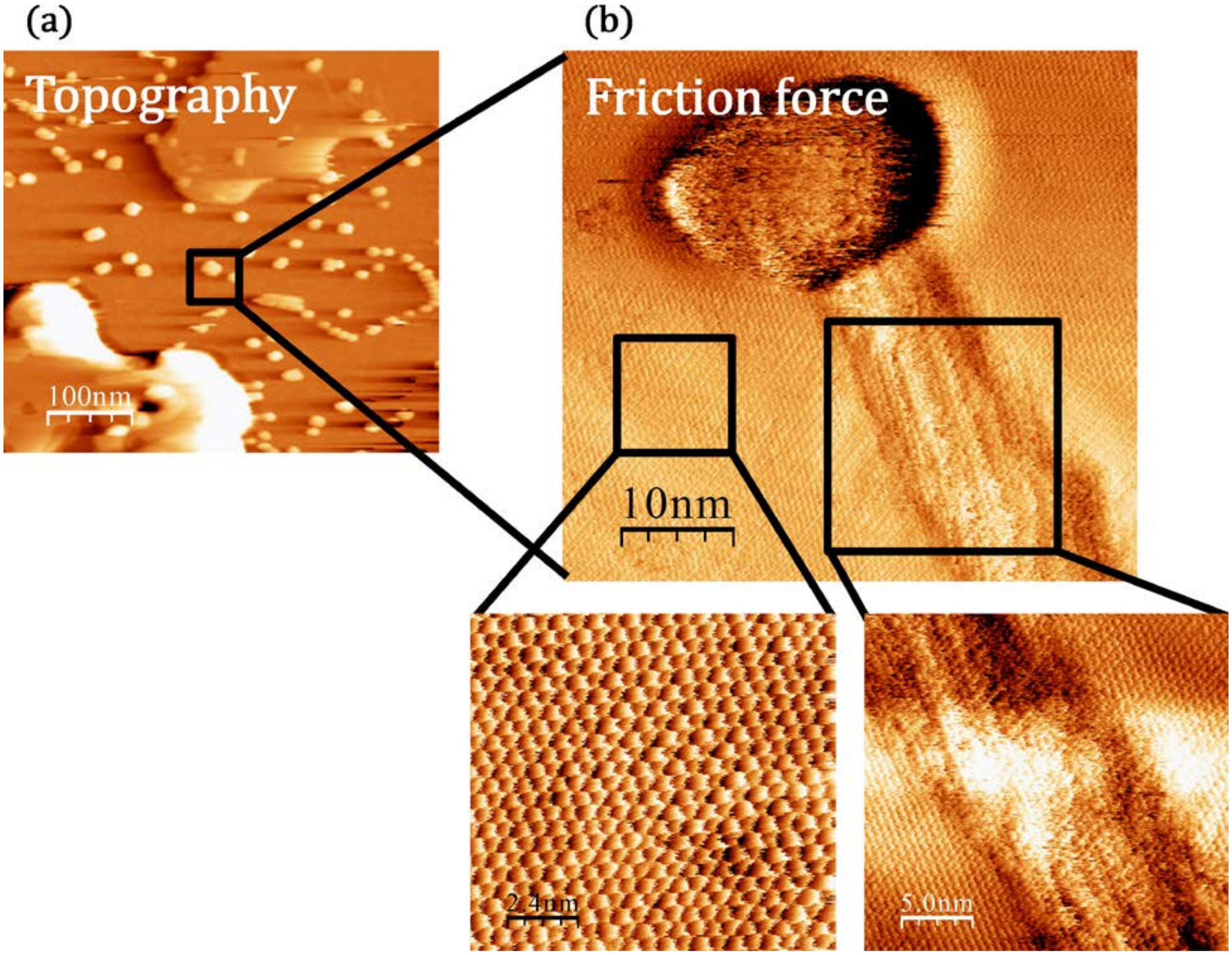

Figure V.12: (a) Topography of LiF particles on the atomically flat surface of a DIP monolayer (b) Friction force microscopy show disordered regions nearby a LiF particle where as herring bone ordering is observed on the flat organic surface.

It turns out that the organic film is not stable under the tip interaction during AFM measurement. Organic molecules have been removed from the first monolayer and begin to form a second monolayer on top of it. During this process, the positions of the LiF particles stay constant. Supplementary, the organic film cracks up at the regions, where LiF chain-like arrangement is observed.

A comparison to the arrangement of LiF particles on a monolayer of pentacene in Figure V.11(c) with the morphology of the underlying organic film in Figure V.11(d) (from [154]) for less than 100% coverage can explain why dendritic agglomeration of LiF particles takes place on this surface. It is assumed that particles are placed at the edges of connected areas and not fully ordered regions in the organic film. These particles stick either at preferred sides on the upright standing molecules or “feel” the inorganic substrate underneath. Preferred sticking on inorganic surfaces compared to the organic surface has already been observed in the previous section. Maybe an increased intermolecular dipole formation and thus stronger van der Waals interaction caused by the orientation of the π-orbitals between the inorganic particles and the organic molecules are responsible for this behavior.

Friction force measurements[1] in Figure V.12(b), performed under UHV conditions, show the structural composition of the atomically flat organic surface of a monolayer DIP at the surrounding of a LiF particle. The herring bone configuration of the organic molecules that is indicated in the zoomed region is destroyed nearby the particle. Two reasons for this observation are thinkable: either the particle sticks to the already disordered region or the impact of the particle creates this disordered region where preferred sticking due to unsaturated dangling bonds takes place. Probably both scenarios occur, dependent on the thickness of the organic layer.

7. Summary and discussion

LiF forms nano-sized islands with almost equal dimensions on different electron acceptor and donor type organic model surfaces. The islands are clearly disconnected. It turns out that films with a thickness of nominal 10 Å end up in an island like morphology with island heights of 40-60 Å. LiF material coverage has been determined around 1% at this nominal thickness when spherical particle shape and equal particle dimensions are assumed. Additionally, the material coverage varies on the different organic surfaces. It could not be clarified, if this difference is due to varying growth parameters, uncertainties in the coverage determination method or if this is a real effect.

Comparison of side by side grown LiF on inorganic and organic surfaces indicate deviant sticking of the material. Particles have various heights on the inorganic surface whereas particle heights are more uniform on the organic surface. The maximum particle height is the same in both cases. Measurements with varying masses of deposited LiF turned out an increase in the total island number but nearly constant island heights and therefore particle sizes. No coalescence of the particles occurs. Variations of growth parameters like substrate temperature and growth rate do not indicate a change in morphology of the grown LiF films. Neither the size, estimated from the island

---

[1] Measurements performed by the group of Roland Bennewitz (Liebniz-Institut für Neue Materialien, Saarbrücken)

heights, nor the dispersion of the particles shows much variation. A particle composition build up from diffusing LiF molecules is unlikely as the particles would grow in size [155].

The appearance of particles in a chain like arrangement especially on thin organic films, with observed height differences of around one organic monolayer, points to preferential sticking on the inorganic silicon dioxide surface. Increased agglomeration on disordered regions in the organic molecule film has directly been discovered by friction force measurements. It is explained with preferentially particle adsorption at trapping sites that are established by defects or dangling bonds in the organic network. The observed particle agglomeration at organic island edges supports this scenario.

A possible reason for the emergence of larger LiF clusters is the relatively low evaporation temperature of the material (around 730° C) as low temperatures are needed to have control over the film growth in the ultrathin regime. It is well below the sublimation temperature of LiF and can lead to the ablation of clusters that might be already existent in the basic material. Formation of LiF clusters with dimensions in the range of 5 to 8 nm has already been reported in the literature by Wang et al. [156] even if the clusters have been produced at much higher evaporation temperatures by the inert gas condensation method. As LiF is evaporated under UHV conditions in this study, the observed particle formation would imply that LiF particles are already present in the vapor beam. Most likely they are generated during the desorption process in material source. Desorption of larger clusters could originate in an increased electron affinity due to the number of constituent molecules like it has been reported by Fernandez-Lima et al. [157]. According to Alonso [158], the cohesion in ionic clusters is described by potentials composed of an attractive part because of electrostatic monopole forces and a repulsive part from quantum mechanical overlap of the electronic clouds of ions with filled electron shells. It leads to strong bonding between 2-4 eV per atom which serves for cluster stability at low evaporation temperatures.

Additionally, larger mass of the clusters and thus higher kinetic energy, when arriving at the surface, can be the origin of preferred sticking of the large LiF clusters compared to sticking of single LiF molecules. Especially at low deposition rates this increased kinetic energy by the larger mass of the clusters can be responsible for the destruction of the crystalline order in the organic film and creation of adsorption sites or additional dangling bonds.

VI. STRUCTURE OF ULTRATHIN LiF FILMS

An aim of this project is to determine if the beneficial impact of LiF in photovoltaic devices is coupled to the structural behavior of either the inorganic/organic interface or the structure of the inorganic material by itself. Therefore, the structural ordering of LiF on amorphous substrates like SiO_2/Si as well as on two prototype organic surfaces has been investigated in more detail. Structural modification of LiF and organic molecules in the bilayer configuration has been observed for increasing LiF deposition amounts.

1. Experimental details

In- and ex-situ x-ray measurements were performed at the MPI-MF beamline at the third-generation synchrotron *ANKA* (*Angstrømquelle Karlsruhe*) [159]. The beamline provides a focused x-ray beam with a high brilliance; in all experiments an energy of 10 keV and accordingly a wavelength of λ=1.239 Å was used. The reflected signals were monitored either by an avalanche photo diode or by a 2D CCD *Pilatus* detector from *Dectris™*. To limit beam damage, the ex-situ samples were probed in a dedicated vacuum chamber, equipped with an x-ray transparent beryllium dome with base pressure less than 10^{-6} mbar. In-situ experiments were also carried out in a vacuum chamber, consisting of three different slot positions for Knudsen cells, a quartz crystal monitor and a specially designed shutter system. The pressure condition in this particular chamber was less than 10^{-9} mbar.

The deposition process for in- and ex-situ samples was performed by thermal evaporation from home built Knudsen cells. Several monolayers of organic molecules were deposited with deposition rates of around 0.2 monolayers per minute. Inorganic LiF films were also deposited by a commercially available water-cooled Knudsen cell with rates less than 10 Å/min. The cell temperature for ex-situ samples was constantly at 732° C. For the in-situ x-ray experiment, the cell temperature was varied between 650 and 750° for obtaining constant rates. The thickness of the LiF films was determined from a quartz crystal monitor (QCM). The calibration of the QCM for the in-situ experiment was performed by analysis of the obtained reflectivity data on DIP afterwards.

Cross sectional TEM data was collected in collaboration with the *StEM* (*Stuttgarter Zentrum für Elektronenmikoskropie*) of *MPI-MF*. Preparation of TEM specimens was performed with the method, described in detail by Dürr et al. [65]. The films were measured by a CM200 microscope (*Philips*) operated at 200 keV with a point resolution of 2.7 Å. The sample remained stable in the electron beam only for 1-2 min but the features of the organic molecules vanish already after several seconds in the beam.

2. Crystalline character of single LiF particles

The lateral resolution of the measured AFM topography limits the ability to draw a conclusion about the exact shape of the LiF particles, as well as their interaction with the organic material. More precise probes testing the crystalline arrangement of LiF as well as that of the organic molecule film have to be applied.

For that purpose, transmission microscopy on one particular model system, with an established procedure of specimen preparation, has been carried out[2]. The experiments have been performed on a LiF/DIP bilayer grown on a SiO_2/Si(100) substrate. The thickness of the amorphous SiO_2 capping layer on top of the Si(100) surface has been determined as 12.5 Å. The thickness of the organic layer is around 230 Å in concession to the TEM specimen preparation procedure. Both the DIP film and the LiF nanoparticles are visible in the images in Figure VI.1 as marked. Length scales have been calibrated by the known plane distances of Si(111) that have been resolved in the images.

The vertical planar stacking of DIP molecules, represented by crystallographic planes between each organic monolayer, has been identified with a thickness of 14.6 Å. The weak contrast between organic monolayers in the image causes discrepancies to the monolayer distances of DIP measured in XRD (~17.5 Å). These value for the layer stacking suggests DIP occurs in the standing up phase (σ-phase), as also supported by XRD.

Of importance is that the LiF particles observed on top of the organic surface are single crystalline. The particles are clearly separated from each other and show a spherical shape. The size of a particle is measured around 50 Å in each dimension but with large uncertainty. There is no evidence of the particles penetrating into the organic film. Contrarily, diffusion of the particles into the glue used for TEM sample preparation has been observed. It suggests a weak sticking coefficient of LiF on DIP and hence a low interaction between LiF particles and the organic surface.

The crystalline character of LiF particles is confirmed by the visible crystallographic planes in Figure VI.1(b) that only show up inside the nanoparticles. Facets of the particles are not visible. However, the measured plane distances presented in Table 5 are related to the LiF(111) plane set distance which is known from the bulk with 2.3 Å.

The obtained angles between visible planes and the sample surface are consistent with the ones formed among body diagonal and peripheral faces of a cubic system. Taking both features into account, the result implies that LiF forms single crystal particles with <100> orientations of the cubic system are either perpendicular or parallel to the substrate surface which is in strong agreement to the observed x-ray response of such systems. It is assumed that LiF films in incomplete coverage have the same structural composition like thicker films showing complete coverage.

---

[2] TEM measurements performed by Marion Kelsch (StEM group MPI-MF Stuttgart)

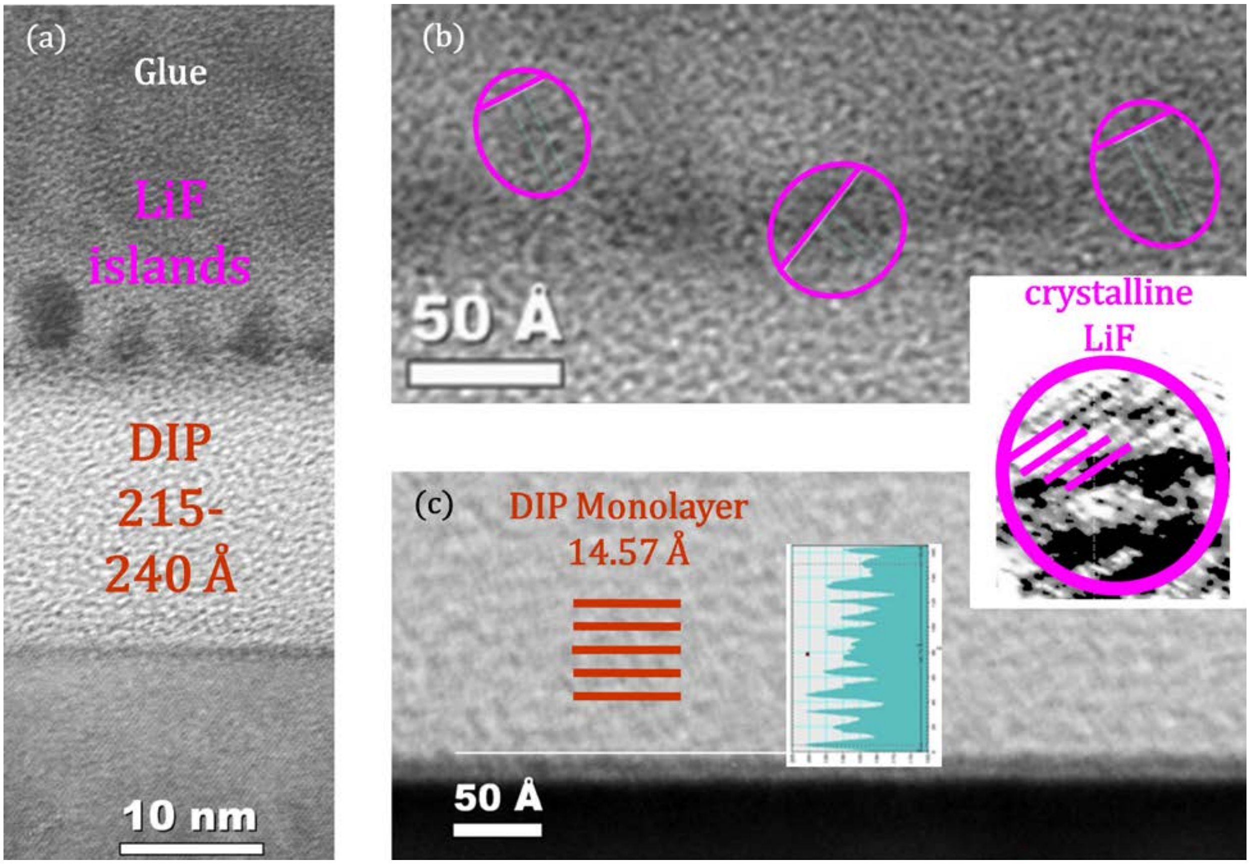

Figure VI.1: (a) Cross sectional transmission electron microscopy images of LiF/DIP bilayer on a $SiO_2/Si(100)$ surface. The sample is cut in two pieces and glued together in a sandwich to prevent damage during specimen preparation. (b) Single LiF particles with crystallographic planes are visible on top of the organic surface. (c) The planar stacking and also the thickness of the organic DIP monolayer is determined from the intensity profile in the inset.

Table 5: Crystallographic parameters of some selected LiF nanoparticles, measured from a bilayer system of LiF/DIP

	Particle 1	Particle 2	Particle 3
Plane distance [Å]	2.23	2.19	2.24
Orientation towards the surface [°]	27	52	27

3. Significance of structural information from ultrathin LiF films

In a first attempt, an ultrathin LiF with the nominal thickness of 10 Å deposited on the organic molecule DIP has been investigated by high energy synchrotron radiation. It has been confirmed by AFM measurements that this bilayer shows incomplete LiF coverage of around 1 %. For these initial x-ray experiments a point detector (avalanche photo diode) has been used. Ex-situ XRR data obtained from a bare DIP film with a thickness of around four monolayers and a LiF/DIP bilayer configuration with the same monitored organic film thickness is shown in Figure VI.2(a).

Only slight differences in the out-of-plane response from the bare organic film and the bilayer configuration are visible. It is not clear if the reflectivity variation occurs due to added LiF or is caused by the different organic layer thicknesses as this data is obtained in an ex-situ study of two different samples. Probably LiF contributes only to the total intensity as the observed XRR data in Figure VI.2(b) obtained from LiF directly deposited on the SiO_2 substrate shows already no features from the LiF film on top. Additionally, the incomplete coverage of such LiF films on organic surfaces with particle agglomeration on plateaus and different height values can cause an incoherent scattering contribution to the XRR signal.

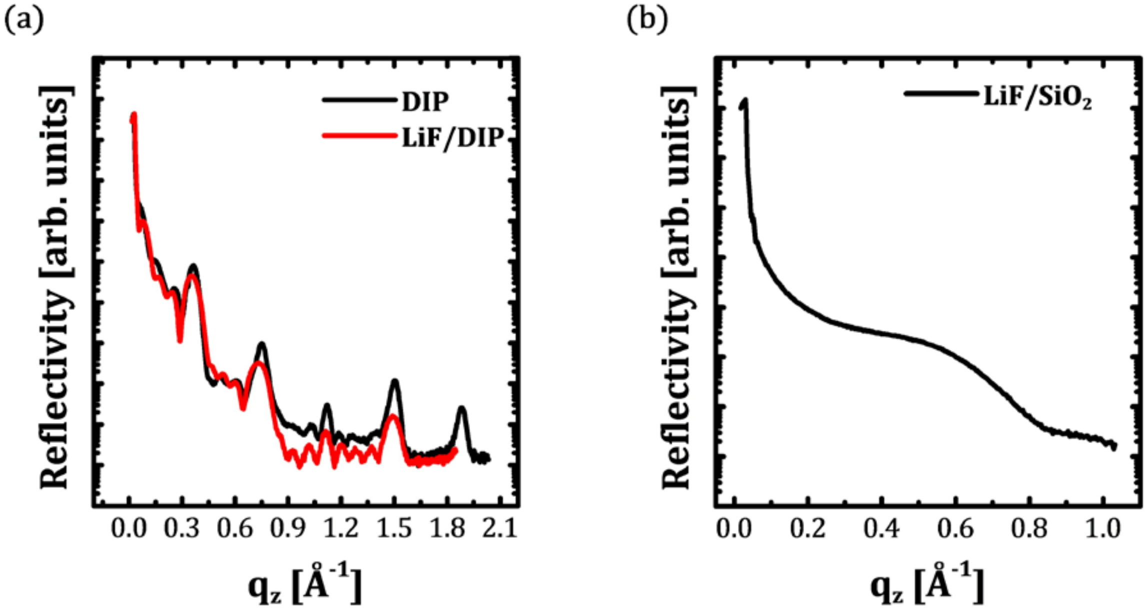

Figure VI.2: (a) Ex-situ XRR data from two samples, a single film of DIP/SiO_2 and a LiF/DIP/SiO_2 bilayer configuration. The LiF coverage on four monolayers DIP is around 1%. (b) XRR data of a LiF/SiO_2 sample for comparison.

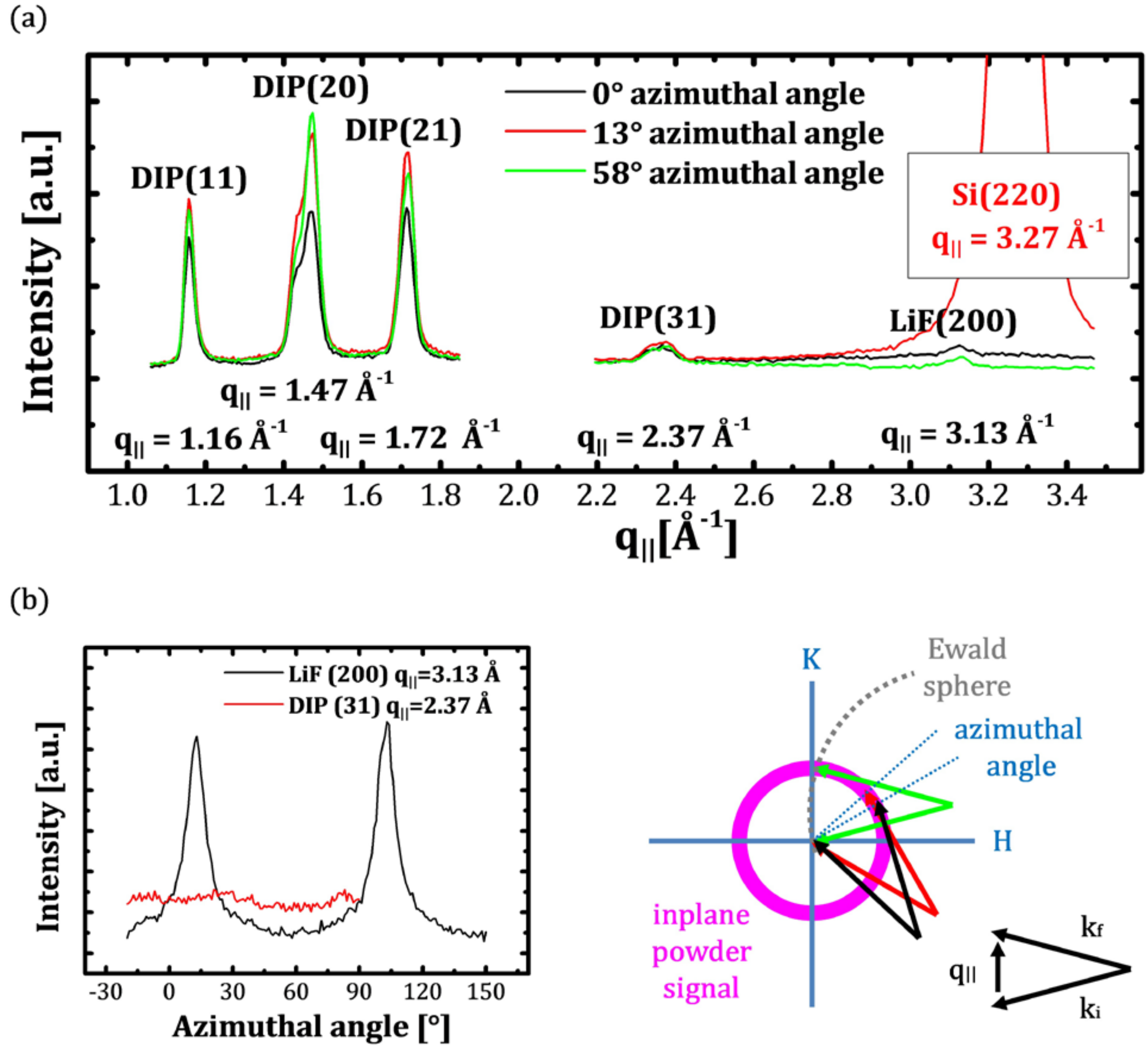

Figure VI.3: (a) GIXRD data of an ultrathin LiF film on DIP/SiO$_2$. (b) Substrate interference of the Si(220) response is clearly observed. (b) Azimuthal scans with fixed momentum transfer of the LiF(200) reflection shows periodicity but is attributed to the Si substrate interference.

Grazing incidence data from particular LiF/DIP sample at varying azimuthal is shown in Figure VI.3(a). Peak intensities caused by the DIP herringbone in-plane structure of the σ-phase show total signal height changes dependent on the azimuthal orientation and suggest a slight misalignment of the sample. The changing ratio between the integrated intensity of the DIP peaks measured at different fixed azimuthal angle is likely attributed to a locally established texture of the herring bone structured grains, i.e. the films are not totally isotropic. Anyway, overall random orientations of the DIP grains with respect to the substrate normal is assumed since no preferred texture of such films is reported in the literature. The weak peak at $q_{||}$ = 3.13 1/Å is identified as a reflection arising from the LiF(200) planes.

Azimuthal scans in Figure VI.3(b) with a fixed momentum transfer at the LiF(200) position show periodic modulation within 90°. For comparison an azimuthal scan of the DIP(31) response shows only slight modulation at different angles suggesting intrinsic errors in the sample alignment. The modulation of the LiF peak is attributed to the (220) reflex of the SiO_2/Si(100) substrate. The reflex overlays the region of expected LiF signals as it is shown in Figure VI.3(a). GIXRD data measured at two other azimuthal orientations show differing background signals at expected LiF positions. The increased noise is probably caused by the interfering tail of the substrate peak but in general only weak LiF response is visible.

In contrast to the weak scattering contribution from LiF deposited on the organic surface, LiF films on inorganic SiO_2 show clear x-ray scattering response in the in- and out-of plane geometry in Figure VI.4. Note that the thickness for out-of-plane texture examination in (c) has been increased to 100 nm to achieve sufficient signal. The samples have been prepared ex-situ and the substrates have been kept at room temperature during deposition. Only signals of fcc LiF(200) planes perpendicular and parallel to the substrate surface have been observed on the SiO_2 substrate. Weak or rather missing signals of LiF(111), expected at $q_{||}$ = 2.70 1/Å, are visible in both geometries. This signal distribution of the two in-plane peaks deviates from the reported LiF thin film structure [130; 131]. It is assumed that the reason for the structural ordering of LiF is likely independent on the crystallinity of the substrate underneath the native SiO_2. The amorphous layer on top of the Si(100) surface exceeds a thickness of around 12.5 Å and prevents a direct interaction with the single crystalline silicon.

As the in- and out-of-plane response of thin LiF films shows polycrystalline grain arrangement independent from the azimuthal orientation of the sample, an additional test of present texture has been performed. Rocking scans for both momentum transfer values around the surface normal are shown in Figure VI.4(c). A diffuse background is visible for both scattering positions but weak signal from LiF(111) expected at the angular position in respect to a <100> orientation parallel to the substrate surface is indicated. Azimuthal scans at this orientation of the momentum transfer vector suggest an azimuthal 90° periodicity but due to limitation in time, more detailed in formations about the texture are pending.

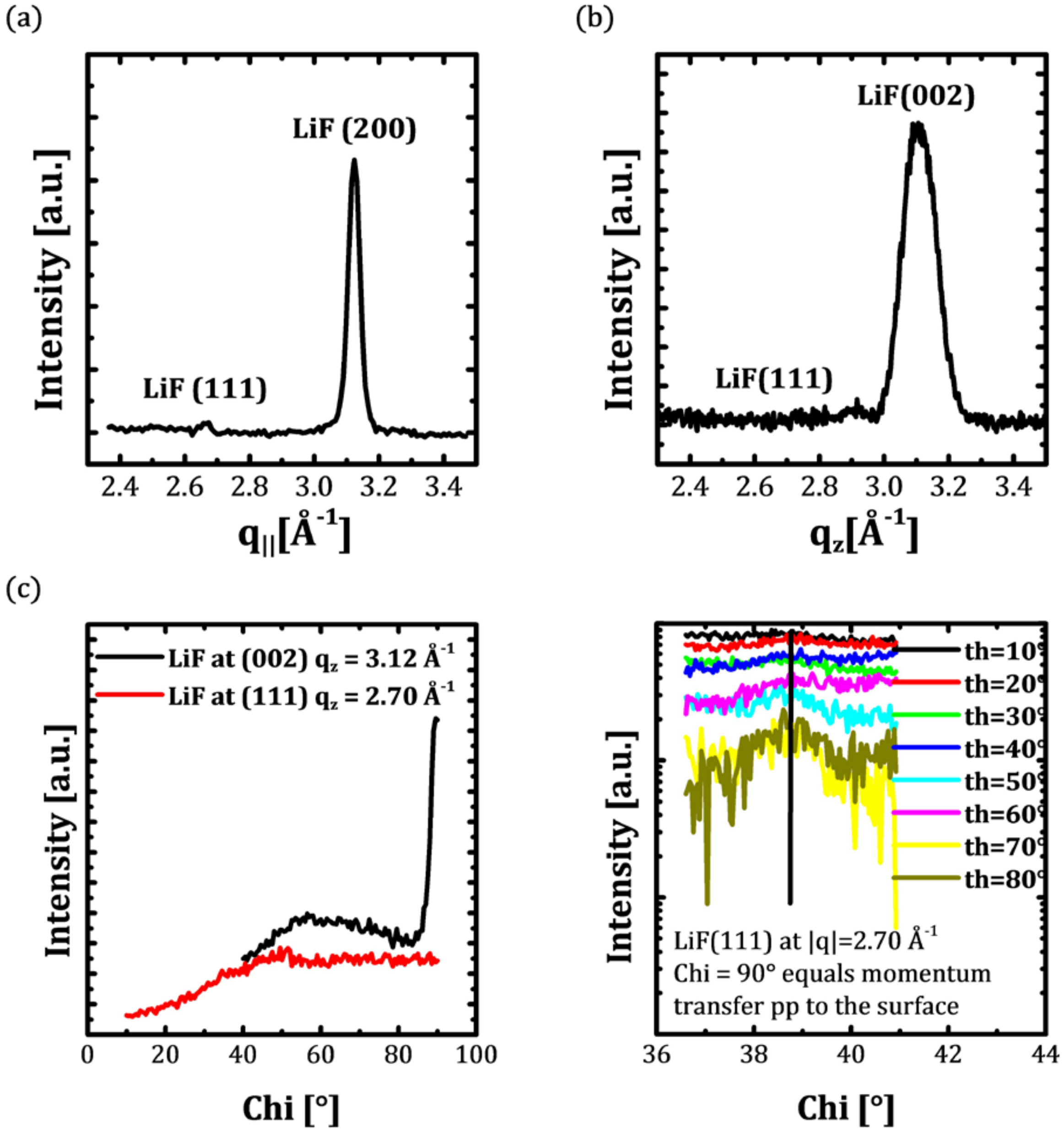

Figure VI.4: (a) In- and (b) out-of-plane XRD measurements of LiF deposited on amorphous SiO_2/Si(100). Strong (200) ordering perpendicular and parallel to the substrate is observed. (c) The data suggest weak 90° azimuthal texture when the LiF(111) is measured in respect to the surface normal.

To overcome the substrate interference of LiF and Si signals all following measurements have been carried out at azimuthal orientations far from the positions of detected substrate interference. In addition, the Si(220) substrate peak is used to obtain the transmission function for reproducible sample alignment to the optimal incident angle in comparative ex-situ GiXRD studies.

Furthermore, the use of a two-dimensional detector allows to cover a large regions in reciprocal space with only a view diffractometer steps during the measurement has been introduced. Long counting times are possible which are essential to detect diffraction signals of LiF with the extremely weak x-ray response described above.

4. Variation of LiF crystallite orientations

Figure VI.5 shows of a comparison of collected in-plane data from thick LiF films above full coverage on two different organic donor (DIP, pentacene) and two different acceptor molecules (PTCDI-C_8, C_{60}). The monitored thicknesses are in the same range for the plotted data sets. Signals from the expected bulk values for LiF in the rocksalt structure are observed in all cases. The appearance of LiF(111) and LiF(200) scattering signals is dependent on the organic molecule surface that is used for the bilayer configuration. Only

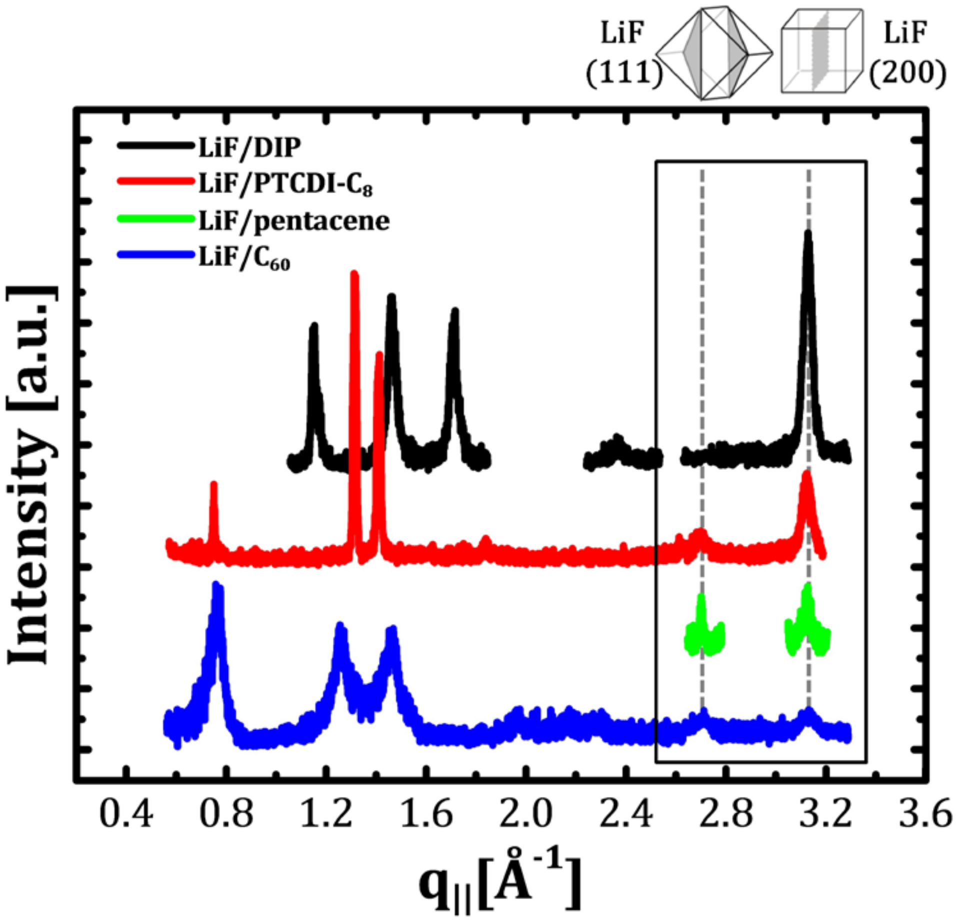

Figure VI.5: GiXRD data of LiF on four different organic molecules. Differences in LiF peak heights and ratios point to different orientations of the LiF scattering centers.

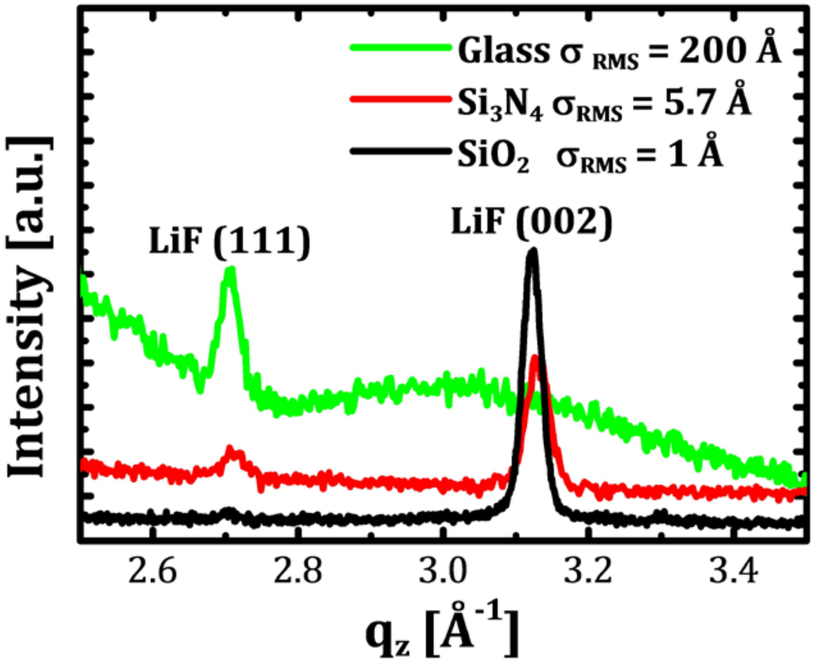

Figure VI.6: Specular out-of-plane XRD data from thick LiF films on three inorganic surfaces with different surface roughness σ.

reflected signals from LiF(200) planes are observed in case of DIP. The absolute intensity of the LiF scattering signal is also the largest on that surface and decreases for the other organic molecules. This feature is related to the height homogeneity of the respective organic surface which determines how many scattering centers contribute to the signal. In case of PTCDI-C_8, pentacene as well as C_{60} LiF(200) and LiF(111) signals are visible. The ratio between peak heights of LiF(111) and LiF(200) reflexes differs dependent on the particular organic surface underneath. Different crystallographic orientation of LiF can thus not be related to the electronic character of the organic semiconducting molecules as LiF(111) and LiF(200) signals show up simultaneously on both donor pentacene- or acceptor type molecules.

A comparison of the out-of-plane data of LiF films on SiO_2/Si(100) and two other inorganic amorphous substrates[3] in Figure VI.6 shows also different LiF crystallite orientations. This is most likely dependent on the roughness of the underlying substrates which can be the reason of the discrepancies in already reported crystal orientations in LiF thin films. It is assumed that varying LiF peak ratios in the in-plane x-ray response on organic surfaces are also related to the organic surface roughness.

---

[3] Measurements performed by Udo Welzel and Ralf Mayer (XRD service group MPI-MF Stuttgart)

5. In-situ study of LiF on DIP

To probe the crystallographic interaction between the inorganic LiF and the prototype donor molecule DIP, in-situ x-ray diffraction experiments with increasing LiF amounts have been performed. The organic film has a thickness of around 5 monolayers. LiF has been deposited stepwise on top of the organic molecules with a cell temperature of 732° C. The heat of the LiF deposition cell caused fluctuations in the monitored height due to the physical closeness of cell and the quartz monitor. Thus the monitored height values are only meaningful for relative comparison of the data within this particular experiment. This is expressed in the use of scaling units instead of thickness. In- and out-of plane x-ray data has been collected after each growth step. Measurements are carried out on the same sample area during the experiment and sample was only moved for height alignment.

Specular out-of-plane measurements of the system are presented in Figure VI.7. Kiessig fringes caused by the overall thickness of the bilayer configuration are present in the data. Oscillating features are smeared out due to increasing surface roughness with LiF deposition. Superimposed Bragg reflexes from the periodic variation of the electron density in the organic layer-by-layer stack are also recognized. The incomplete coverage of the LiF

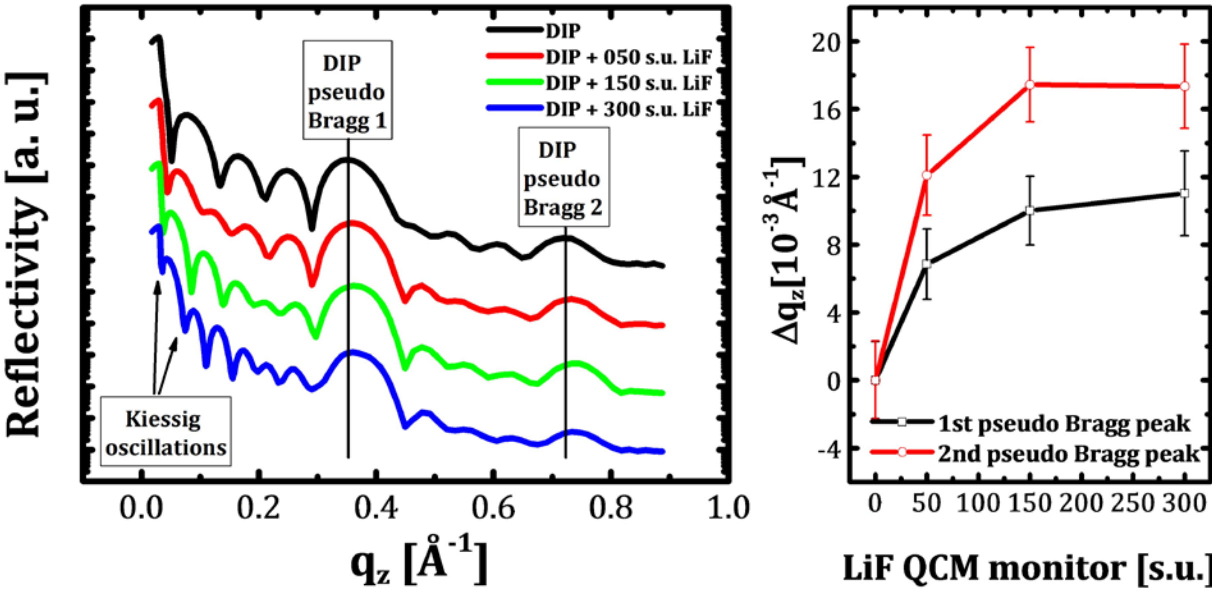

Figure VI.7: Specular x-ray reflectivity of LiF/DIP/SiO₂ bilayer configuration with different monitored thickness on top of ~5 monolayers of planar stacked DIP. The monolayer distance is expressed in the pronounced Bragg signal in the reflectivity. Kiessig fringes are used for bilayer height analysis films at low thicknesses probably causes an incoherent averaging of the LiF electron density signal and thus gives no detailed information about the LiF film on top of the organic molecules. An accurate model of the electron density of the underlying organic film itself which reproduces the observed data could not been repeated with the reported models. Simulation of the signal differences caused by the additional deposition of LiF with meaningful results was already limited by too many unknown parameters.

Nevertheless, the monolayer distance of the upright standing organic molecules have been deduced from analysis of the observed Bragg peaks in Figure VI.7. The momentum transfer values q_z of the first two Bragg peaks have been obtained with the help of a Voigt distribution fit. The given data error contains the sum of the experimental angular resolution and the fit mismatch of the center positions. For the calculation of the monolayer thickness $d = 2\pi/q_z$ a refinement has been used to take both reflections into account. It should be noted, that the position of the 2nd Bragg peak is more reliable because the reflectivity has less interference with the Kiessig fringes at that momentum transfer range.

In a geometrical consideration, the monolayer distance is connected with the tilt of the upright standing DIP molecules. This is only valid if the molecules are not interpenetrating when they grow layer by layer. Hence, the measured monolayer distance in Table 6 is a result of the tilted standing-up DIP molecules. For the bare organic DIP film, the thickness of a monolayer has been derived with 17.52 Å. Comparing this thickness to the length of the molecule that is assumed to be 18.4 Å [74], the molecule tilt is about an angle of 17.8° towards the surface normal. The DIP monolayer thickness decreases during LiF deposition. It is related to an angular change of the organic molecule tilt angle up to 21.8°, see Figure VI.8.

Analyses of the bilayer thickness in Table 7 by observation of shifting Kiessig fringes show the evolution from incomplete to a complete covered LiF film. The bilayer thickness in Figure VI.9 increases by initial LiF deposition and stays constant until a specific deposited material amount is reached. Subsequently, it increases linear with additional material deposition.

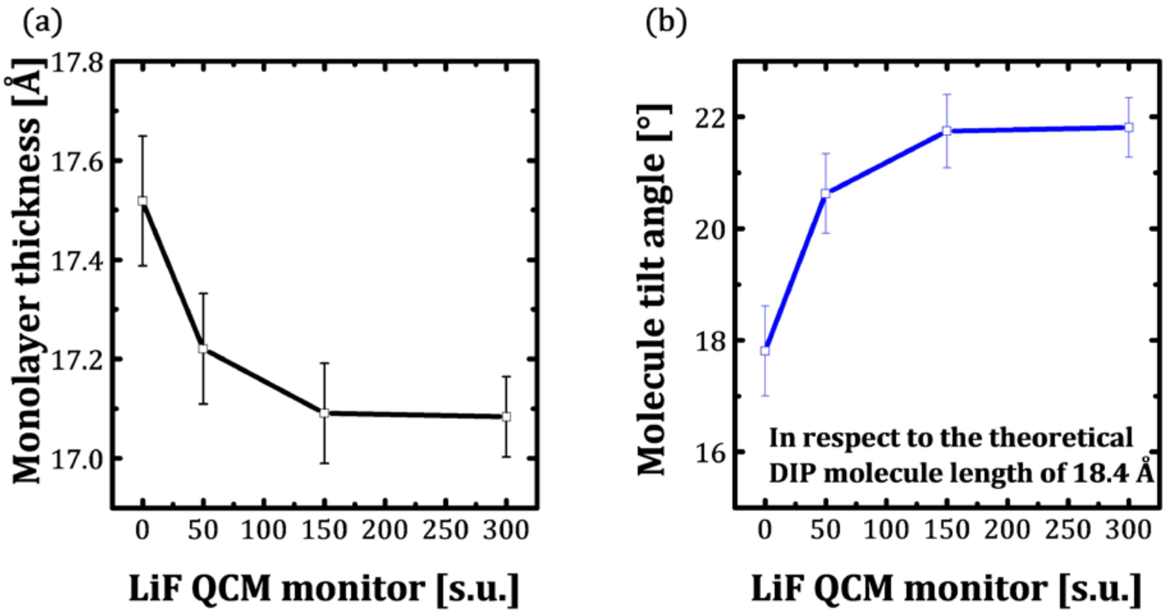

Figure VI.8: (a) Fitted DIP monolayer thickness and (b) according molecular tilt angle in respect to the full molecule length show trends.

Table 6: Relation of the measured monolayer distance to the molecular tilt angle of DIP molecules in a layer by layer configuration assumed for a dense packed organic film.

DIP	**Monolayer thickness [Å]**	**Tilt angle in respect to 18.4 Å molecule length [°]**
DIP ~5 monolayer	17.52	17.8
DIP + 050 s.u. LiF	17.22	20.6
DIP + 150 s.u. LiF	17.09	21.7
DIP + 300 s.u. LiF	17.08	21.8

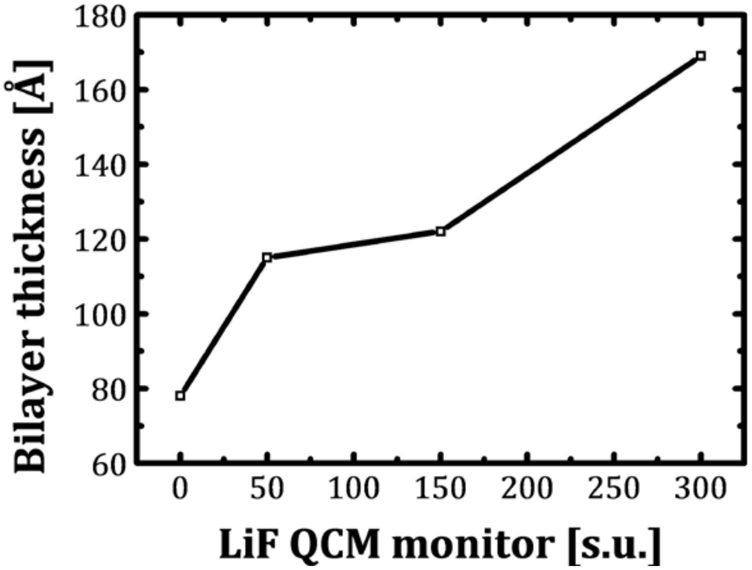

Figure VI.9: Evolution of the LiF/DIP bilayer thickness obtained from q_z *positions of Kiessig fringes.*

Table 7: LiF/DIP Bilayer thickness derived from the observed q_z *positions of Kiessig fringes in the specular x-ray data.*

LiF/DIP	**Bilayer thickness [Å]**	**LiF thickness [Å]**
DIP ~5 monolayer	78	---
DIP + 050 s.u. LiF	115	36
DIP + 150 s.u. LiF	122	44
DIP + 300 s.u. LiF	169	91

Grazing incidence data in Figure VI.10(a) shows peak signals from DIP for lower momentum transfers as well as a LiF signal response at a position expected from the bulk material. The observed signals from the organic film are again related to the reported herringbone structure of DIP with the assigned reflex positions. The observed peak for the LiF crystal structure is attributed to the LiF(200) lattice configuration.

The LiF signal is weak for low deposition amounts and increases with additional material deposition. At the same time the overall intensity of the organic response is decreased. It can be attributed to the decreased penetration depth of the x-ray beam into the organic molecule film caused by

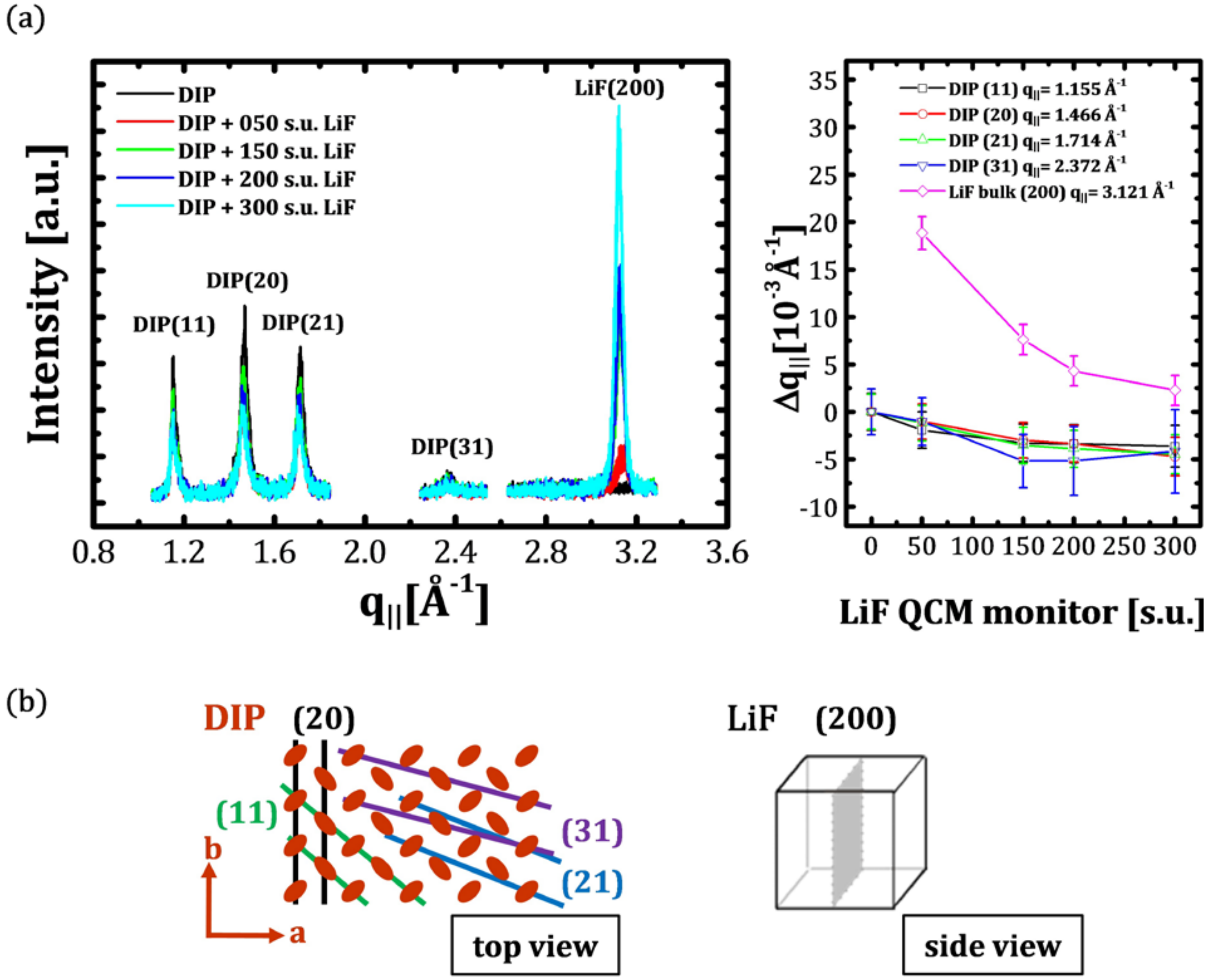

Figure VI.10: (a) In situ GiXRD data (left) of evolving LiF films on organic donor molecule DIP/SiO$_2$. Centre positions of the observed in-plane peaks were fitted with Lorentzian distribution functions (right). (b) Schematic arrangement in the observable crystallographic planes in real space for DIP herring bone structure and LiF fcc structure.

the increased density of the LiF film. The observed structural orientation of the LiF crystallites on DIP is comparable with the one measured on amorphous SiO_2/Si(100) in the previous section. A dramatic change in the in-plane response of the organic structure by vanishing or appearing reflex signals does not occur. Consequently, reordering of the organic structure is excluded.

Slight changes in the momentum transfer positions are used to evaluate the lattice parameter variation of organic and inorganic structures. As local established texture cannot be obviated, the atomic form factor has not been used for analysis of the structural configuration. Neither an area- nor Lorentzian correction has been applied to the integrated intensity of the measured films for comparing data for varying LiF thicknesses. The lattice parameters are only determined from a geometrical point of view considering a fixed momentum transfer range in q_z for observable in-plane Bragg reflections.

The observed scattering signals have been fitted with Lorentzian distribution functions to obtain the respective momentum transfer. High precision of the detector setup in this experiment allows resolving peak position changes with a resolution of $|\boldsymbol{\Delta q}| \sim 0.004\ 1/\text{Å}$. A rectangular in-plane unit cell is assumed for the organic lattice and justified by the observed equality of DIP (11) and (1-1) reflexes. The obtained values have been fitted by the spacing formula for the general triclinic crystal (e.g. Warren [44]):

$$q_{hkl} = 2\pi\sqrt{\frac{1}{d_{hkl}^2}} = \frac{2\pi}{(1+2\cos\alpha\cos\beta\cos\gamma-\cos\alpha^2-\cos\beta^2-\cos\gamma^2)^{1/2}} \times \begin{Bmatrix} \frac{h^2\sin\alpha^2}{a^2}+\frac{k^2\sin\beta^2}{b^2}+\frac{l^2\sin\gamma^2}{c^2}+\frac{2hk}{ab}(\cos\alpha\cos\beta-\cos\gamma) \\ +\frac{2kl}{bc}(\cos\beta\cos\gamma-\cos\alpha)+\frac{2lh}{ac}(\cos\gamma\cos\alpha-\cos\beta) \end{Bmatrix}^{1/2} \tag{VI.1}$$

Errors of the calculated lattice parameters were given using the maximum difference in respect to all calculated and measured $q_{||}$ values. With this assumed error, the error for the lattice parameter has been calculated with a Gaussian error propagation applied to the triclinic spacing formula. The misfit between calculated and measured reflex is therefore a convolution of experimental and intrinsic errors. It is sufficient for describing the trend of the lattice parameter variation. A total error including the limited resolution of the experimental setup has still to be considered when discussing absolute values of the determined lattice parameters, listed in Table 8 and Table 9.

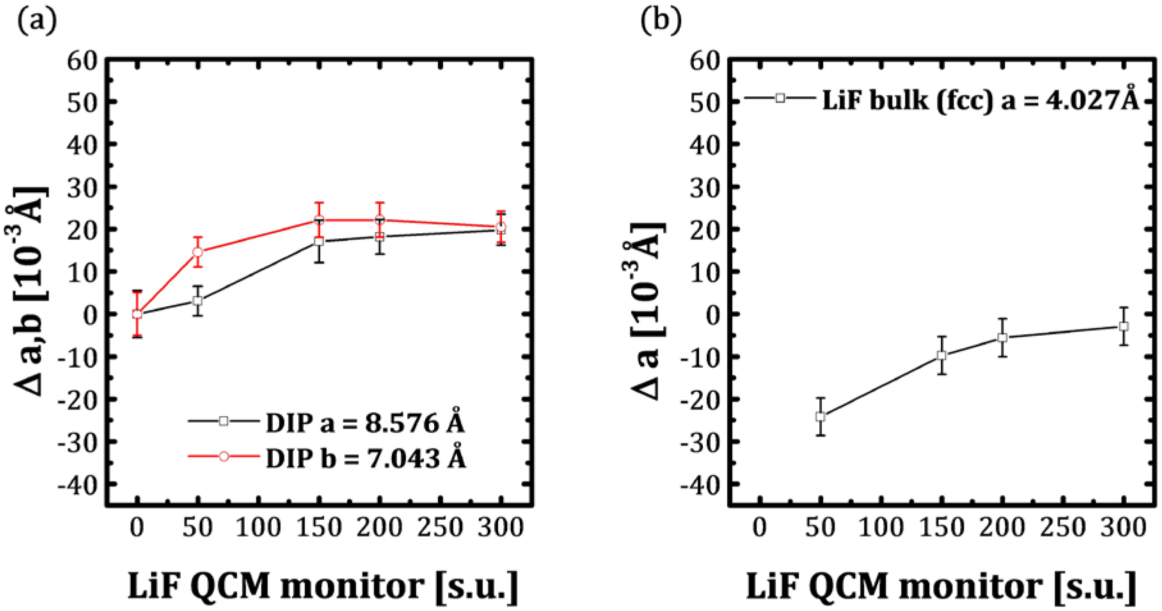

Figure VI.11: The the change in lattice parameters (a) for the DIP herringbone inplane structure normed to the neat organic film as well as (b) for the LiF fcc unit cell normed to the expected bulk value.

Table 8: Fitted in-plane lattice parameters of LiF fcc structure in LiF/DIP/SiO_2 bilayer configuration.

LiF (fcc)	|***a***| [Å]
DIP (~5 ML)	
050 s.u. LiF	4.0028
150 s.u. LiF	4.0172
200 s.u. LiF	4.0214
300 s.u. LiF	4.0241

Table 9: Fitted in-plane lattice parameters of DIP herring bone structure in LiF/DIP/SiO$_2$ bilayer configuration.

DIP (herringbone)	|***a***| [Å]	|***b***| [Å]
DIP (~5 ML)	8.576	7.044
050 s.u. LiF	8.579	7.059
150 s.u. LiF	8.593	7.066
200 s.u. LiF	8.594	7.066
300 s.u. LiF	8.595	7.065

Table 10: Measured & calculated reflex positions for DIP (inplane herring bone unit cell).

measured *calculated*	**DIP(11)** [Å^{-1}]	**DIP(20)** [Å^{-1}]	**DIP(21)** [Å^{-1}]	**DIP(31)** [Å^{-1}]
DIP (~5 ML)	1.1554	1.4663	1.7140	2.3719
	1.1543	*1.4654*	*1.7155*	*2.3721*
050 s.u. LiF	1.1535	1.4653	1.7128	2.3709
	1.1527	*1.4648*	*1.7141*	*2.3707*
150 s.u. LiF	1.1521	1.4633	1.7105	2.3667
	1.1512	*1.4625*	*1.7115*	*2.3670*
200 s.u. LiF	1.1520	1.4629	1.7102	2.3667
	1.1512	*1.4623*	*1.7114*	*2.3668*
300 s.u. LiF	1.1517	1.4616	1.7096	2.3677
	1.1512	*1.4620*	*1.7112*	*2.3665*

The crystallographic angles α between $\boldsymbol{a}$ and $\boldsymbol{c}$ as well as β between $\boldsymbol{b}$ and $\boldsymbol{c}$ are assumed to be 90° in the structure of DIP and the Miller index l equals zero. The sum of squared errors between calculated and measured momentum transfer positions has been minimized with the variation of the lattice parameter $|\boldsymbol{a}|$ and $|\boldsymbol{b}|$ in the organic herringbone structure. Resulting momentum transfer positions for DIP are listed in Table 10.

The parameters of the organic crystal lattice as well as the LiF lattice parameters are changing slightly as LiF is deposited on the organic surface. The derived lattice parameters for DIP are expanding compared to the initial value of a neat film. In the same time the LiF lattice relaxes from a contracted structure closer to the bulk configuration. The expansion saturates after a critical thickness of LiF deposition. This saturation is attributed to complete layer formation according to the observed out-of-plane data in Figure VI.9.

Analyses of the peak breadth by following the Scherrer equation [160] provide a tool for deriving the linear dimension L of the scattering crystallite grains in the full covered film. The parameter depends on the Bragg angle Θ, the wavelength λ of the x-ray beam and a numerical factor K as long as the scattering centers are symmetric:

$$w = \frac{K\lambda}{L\cos\Theta}. \qquad \text{(VI.2)}$$

With an assumed spherical shape of the inorganic crystallites in the in-plane direction, the numerical factor K was set to $2\sqrt{\ln 2/\pi} = 0.93$ following the argumentation in the reference. The derived size of LiF crystallites in Figure VI.12 shows values which deviate from the particle size, obtained from AFM topography and TEM measurements. A reason for this mismatch can be a non circular shape of the particles or a disruption of the peak breadth analysis by LiF scattering from grains, which are sitting on organic islands with different heights. Nevertheless the size does not increase with additional LiF deposition.

Lattice parameter variations in sub-Ångstrøm regime are mostly related to strain. As both structures are expanding the change is probably not related to an interaction and energy transfer between the organic and inorganic material. The expanded organic lattice parameters are probably related to an increasing substrate temperature of around 30° C, noticed in ongoing experiment. The elevated temperature arises from the physical closeness of the hot LiF cell in the relatively small experimental environment of the in-situ vacuum chamber. As organic thin films are very sensitive to heat, a relaxation of the whole organic structure due to thermal expansion is thinkable. The

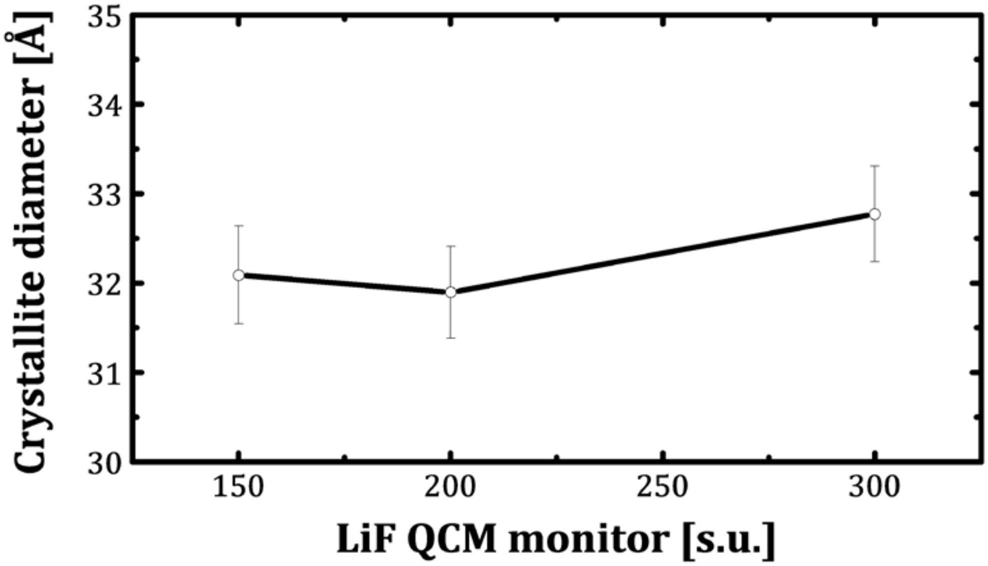

Figure VI.12: Obtained crystallite sizes of fully covered LiF films in LiF/DIP bilayer configuration.

relaxation of the LiF lattice parameters is explained by the formation of the complete layer, as this material is much more stable in the room temperature range. Especially nano particles are known to have compressed lattice parameters due large number of surface atoms compared to the atoms in the volume. Hence, the strain is released, when a full film is established and facets of the nanoparticles are close to each other.

Another interesting feature comes into focus, when the observed in-plane lattice relaxation of DIP is compared to the out-of-plane contraction of one DIP monolayer. The experimental data shows that the compression ratio of the monolayer thickness d_{mono} is equal to 0.1. This does not match to the reported compression ratio of a rectangular lattice vector $\boldsymbol{c}$ for organic thin films, derived by the postulation of a constant volume of the unit cell (usually between 0.3 and 0.4, see e.g. Tahk et al. [161]). If a periodic arrangement of the organic monolayers is present, a projection of the real lattice spacing $|\boldsymbol{c}|$ tilted with an angle toward the $\boldsymbol{a}$-$\boldsymbol{b}$ plane is established which is in principle not defined by the molecule tilt. The exact length of the **c**-axis and its orientation cannot be determined from this experiment as the q_z dependence of the in-plane reflexes has not been measured. The results presented here suggest that $|\boldsymbol{c}| \neq d_{\mathrm{mono}}$. This implies that the unit cell of thin films is more likely mono or even triclinic.

6. In-situ study of LiF on PTCDI-C_8

After observing a lattice parameter relaxation on the donor molecule DIP, the same experiment has been carried out on a PTCDI-C_8 surface, a prototype acceptor like organic network. The organic film has a thickness of around 10 ML. The deposition rate of LiF has been reduced by a cell temperature difference of around 100° C compared to the experiment on DIP. This has been done with the intention to have better control over the deposited amount of material. Less thermal fluctuations of the quartz monitor compared to the experiment on DIP have been recognized. Additionally, the cell has been refilled prior to the experiment.

Specular out-of-plane data from the bilayer system in Figure VI.13 shows no variation of the 1st order Bragg peak. For this system the momentum transfer position stays constant according to the assumed error. The specular response of the system gets smeared out due to the roughness of the surface when LiF is deposited on the organic surface. The second order minima of the Kiessig oscillation could not have been evaluated from the data, thus analyses of the total bilayer thicknesses do not provide sufficient accuracy.

The in-plane data of GIXRD measurements in Figure VI.14 shows signal response from the organic film as well as peak intensity from LiF that

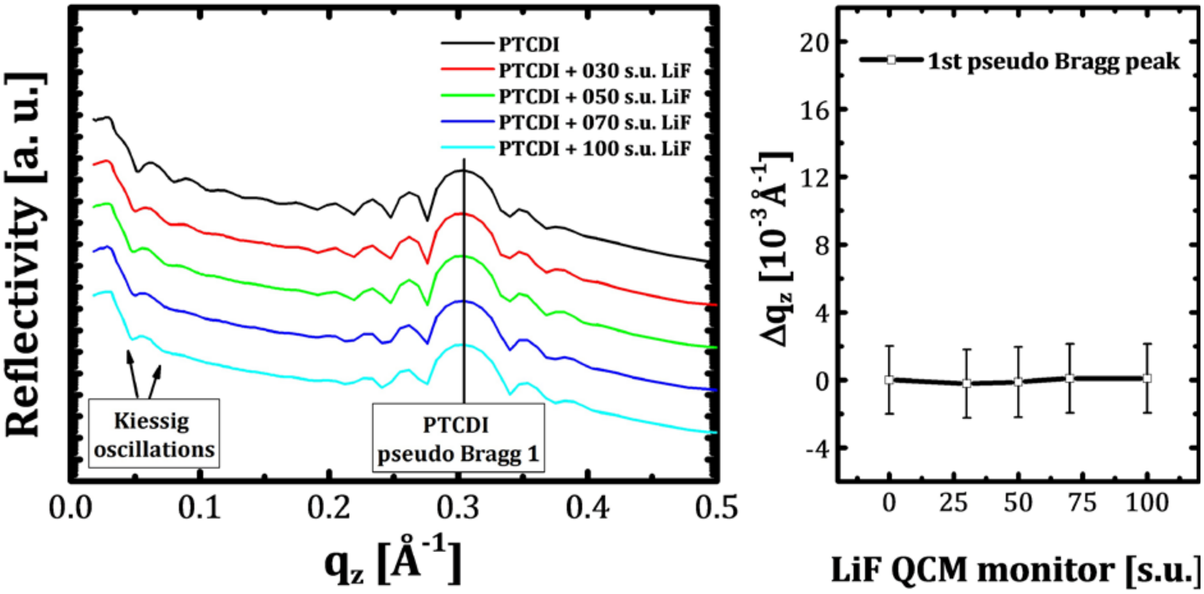

Figure VI.13: Specular x-ray reflectivity of LiF/PTCDI-C_8/SiO_2 bilayer configuration. The monolayer distance (20.71 Å) of the organic molecule does not change due to increased LiF deposition.

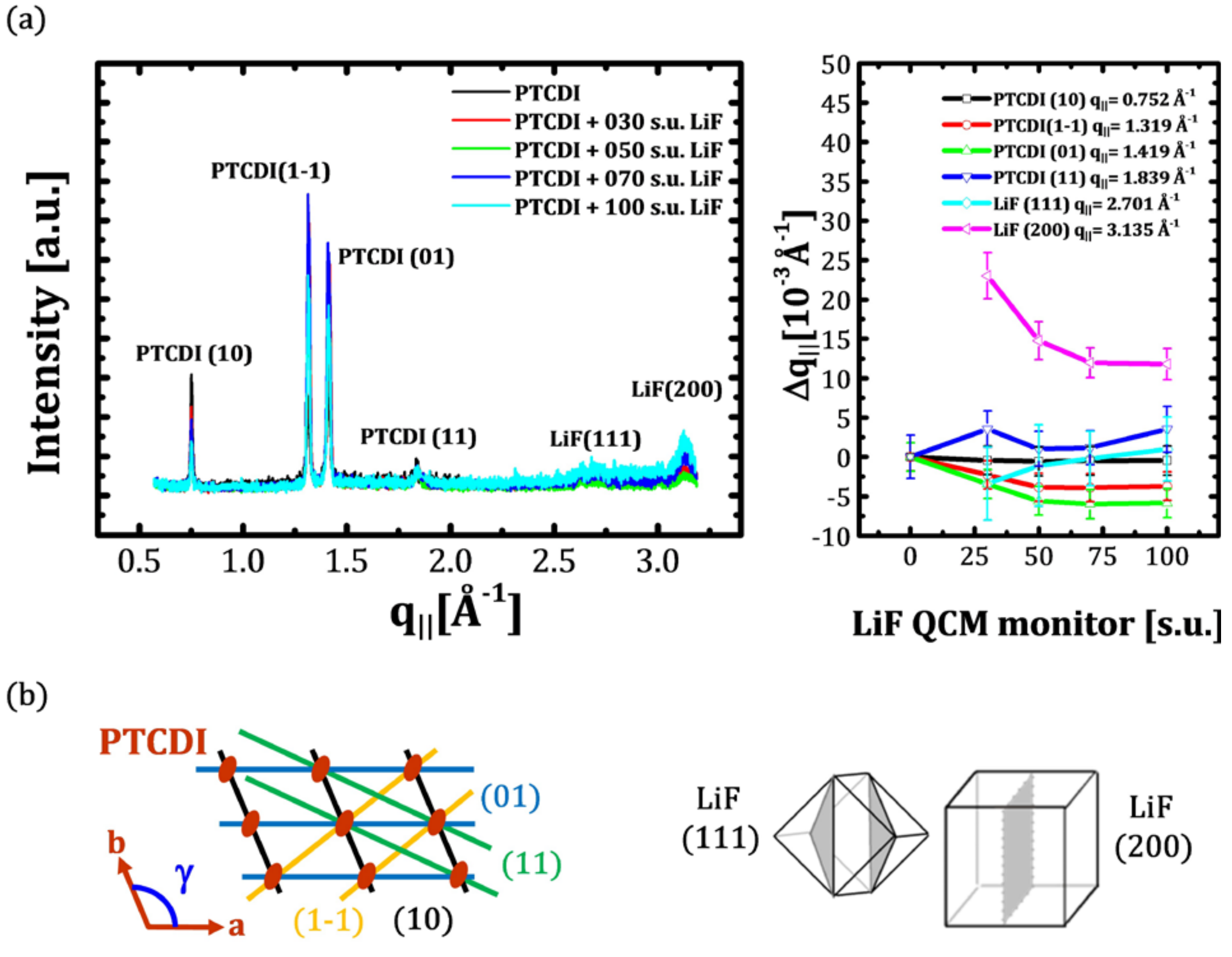

Figure VI.14: (a) In situ GiXRD data (left) of evolving LiF films on organic acceptor molecule PTCDI-C_8/SiO_2. Centre positions of the observed in-plane peaks were fitted with Lorentzian distribution functions (right) (b) Schematic arrangement in the observable crystallographic planes in real space for PTCDI oblique and LiF fcc structure.

increases with the rising LiF deposition amount. The formation of an oblique in-plane unit cell in the PTCDI-C_8 structure is expressed in the appearance of (11) and (1-1) reflection signals.

LiF shows up in the (200) configuration perpendicular to the surface with an observable LiF(111) reflex. The increased signal noise for larger amounts of LiF is probably related to the experimental deposition process. The overall intensity of the organic in-plane response decreases for additional LiF deposition. A variation of the momentum transfer of the organic in-plane response and a shift of LiF reflexes takes place due to increased LiF deposition.

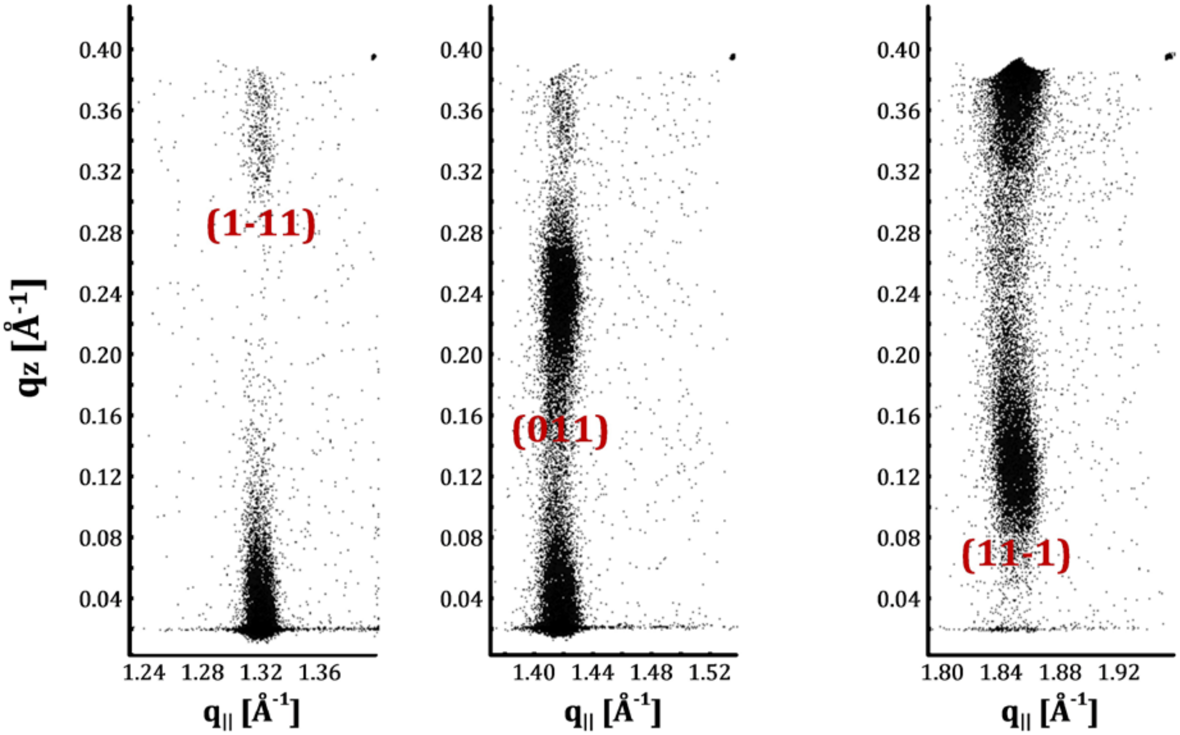

Figure VI.15: Observed PTCDI-C_8 out-of-plane reflexes with assigned positions for the structural model of a corresponding triclinic unit cell.

As the LiF(111) signal is very weak, only the LiF(200) signal has been fitted for analysis of the structural change in the LiF crystal structure. Three observable out-of-plane reflexes from PTCDI-C_8 in Figure VI.15 have been used for the reconstruction of the triclinic organic unit cell with a structural model proposed by Krauss et al. [95]. The momentum transfer positions $|q| = (q_{||}^2 + q_z^2)^{1/2}$ have been fitted together with the observed in-plane data (see Table 12) applying the triclinic master formula from equation (VI.1).

The obtained values for the lattice parameter of the organic film in Table 11 show an increased trend in the lattice parameters $|\boldsymbol{a}|$ and $|\boldsymbol{b}|$ and the angle γ between both in-plane lattice vectors. The value of $|\boldsymbol{c}|$ has been kept constant after fitting the single organic film argued by the constant monolayer thickness that has been observed in the specular data in Figure VI.13.

Table 11: Fitted lattice parameters of PTCDI-C$_8$ (triclinic unit cell) in LiF/PTCDI-C$_8$/SiO$_2$ bilayer configuration.

PTCDI-C$_8$ (triclinic)	|***a***| [Å]	|***b***| [Å]	γ [°]	|***c***| [Å]	α [°]	β [°]
PTCDI-C$_8$ (~10 ML)	9.108	4.816	112.84	23.282	88.16	94.51
030 s.u. LiF	9.142	4.835	113.09	23.282	87.46	96.80
050 s.u. LiF	9.153	4.842	113.12	23.282	87.07	97.29
070 s.u. LiF	9.139	4.842	113.07	23.282	87.45	96.76
100 s.u. LiF	9.137	4.842	113.18	23.282	87.15	96.59

Table 12: Measured & calculated reflex positions of PTCDI-C$_8$ with respect to triclinic unit cell.

measured *calculated*	**PTCDI (100)** [Å^{-1}]	**PTCDI (1-10)** [Å^{-1}]	**PTCDI (010)** [Å^{-1}]	**PTCDI (110)** [Å^{-1}]	**PTCDI (1-11)** [Å^{-1}]	**PTCDI (011)** [Å^{-1}]	**PTCDI (11-1)** [Å^{-1}]
PTCDI-C$_8$ (~10 ML)	0.7522	1.3194	1.4189	1.8392	1.3596	1.4409	1.8536
	0.7505	*1.3209*	*1.4157*	*1.8413*	*1.3596*	*1.4409*	*1.8536*
030 s.u. LiF	0.7518	1.3171	1.4154	1.8427	1.3588	1.4366	1.8466
	0.7517	*1.3161*	*1.4127*	*1.8410*	*1.3599*	*1.4392*	*1.8484*
050 s.u. LiF	0.7517	1.3156	1.4133	1.8402	1.3599	1.4344	1.8450
	0.7515	*1.3149*	*1.4109*	*1.8390*	*1.3607*	*1.4365*	*1.8465*
070 s.u. LiF	0.7517	1.3155	1.4129	1.8404	1.3572	1.4342	1.8445
	0.7517	*1.3145*	*1.4104*	*1.8386*	*1.3583*	*1.4368*	*1.8462*
100 s.u. LiF	0.7518	1.3157	1.4130	1.8427	1.3585	1.4340	1.8488
	0.7521	*1.3145*	*1.4116*	*1.8408*	*1.3594*	*1.4361*	*1.8503*

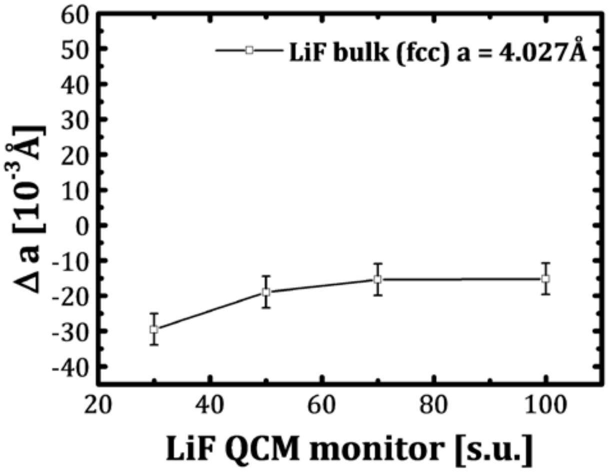

Figure VI.16: Lattice parameter shift of LiF deposited on PTCDI-C_8/SiO_2.

Table 13: Fitted in-plane lattice parameters of LiF fcc structure in LiF/PTCDI-C_8/SiO_2 bilayer configuration.

LiF (fcc)	**|*a*|** [Å]
DIP (~5 ML)	
030 s.u. LiF	3.998
050 s.u. LiF	4.008
070 s.u. LiF	4.012
100 s.u. LiF	4.012

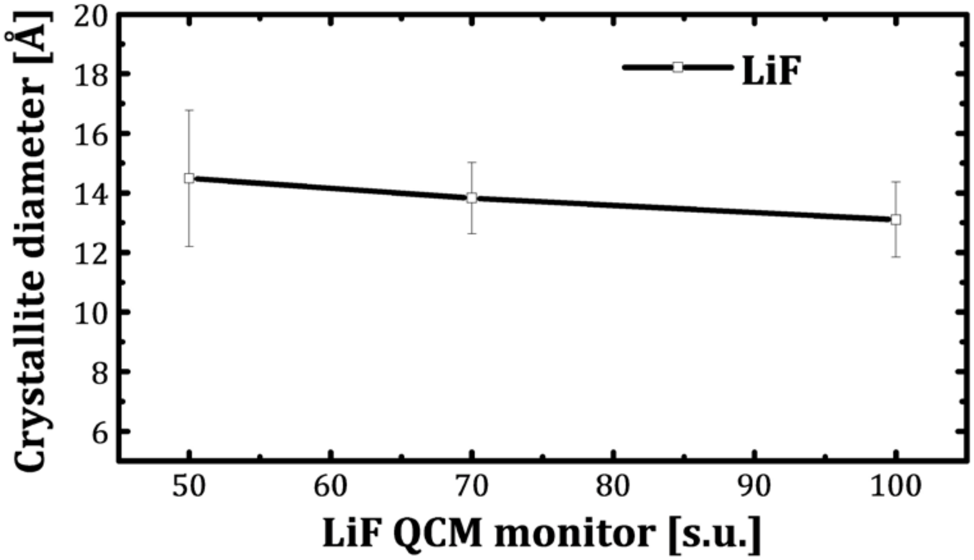

Figure VI.17: Analysis of the crystallite LiF from a LiF/PTCDI-C_8 bilayer system according to the Scherrer formula.

A change in the crystallographic angles α and β can be stated with this method. However, the large number of fit parameters compared to the available data set of different reflex positions does not allow further statements for lattice parameter variation of the complex triclinic structural model. In contrast to DIP, the variation of the organic in-plane lattice parameters, listed in Table 11, is rather dramatic in case of PTCDI-C_8. LiF shows again an increasing length of the lattice parameter $|\boldsymbol{a}|$ from the bulk value, listed in *Table 13*. The difference to the bulk value decreases for rising deposition amounts but saturates at much lower monitored thicknesses of the uncalibrated QCM. Probably less thermal fluctuations of the monitor or the use of fresh LiF are responsible for this behavior. In the saturation regime, the difference to the reported bulk value of 0.020 Å is much larger compared to LiF deposition on DIP.

LiF(200) peak breadth analyses in Figure VI.17 according to the Scherrer equation (VI.2) yield smaller LiF crystallite sizes compared to the result on DIP. This fact is probably related to the needle like topography, reported for PTCDI-C_8 surfaces from thicker layers. LiF films with complete coverage would not form a layer with uniform heights in this case. Another reason might be the lower cell temperature during deposition and thus smaller sizes of formed clusters in the vapor beam that stick to the organic surface. Contrarily, smaller particle dimensions at lower LiF deposition rates have not been verified in

AFM measurements. Nevertheless, the size of scattering centers is almost constant for increasing LiF deposition.

The changing lattice parameters of LiF as well as the saturation are again related to strain effects of nano particles in the low coverage regime. Formation of a LiF film with complete coverage is assumed in the saturation regime. The film is also formed by grains with almost equal sizes. The variation of the organic lattice is again related to thermal expansion due to the increasing substrate temperature recognized during the experiment.

7. Summary and discussion

Cross-sectional images from LiF in the incomplete coverage regime on organic DIP layers show formation of spherical and crystalline LiF particles with sizes of around 50 Å in each dimension. Observable lattice planes, measured with distances of the bulk fcc structure, suggest an orientation of the crystalline particles with <100> ordering parallel to the DIP surface. The particles are disconnected from each other and no penetration inside the organic film is visible. Weak sticking on the organic surface is assumed as the particles are diffusing into the glue used for TEM specimen preparation.

X-ray scattering signals for LiF film thicknesses that are typically used in organic devices are in general weak. Changes in the specular reflectivity are attributed to increasing roughness as well as changes in the total bilayer thickness caused by LiF deposition. Not completely covered surfaces lead to incoherent scattering of x-rays in the specular out-of-plane response of the added material. The accessible structural information gained from ultrathin LiF films is thus very limited. Examinations on the structure of ultrathin films of LiF on amorphous SiO_2/Si(100) have shown stronger scattering signals. This is related to the uniform height of the LiF film when deposited on the atomically flat inorganic surface and also to the better sticking of LiF particles on these surfaces. The observed scattering response differs from the orientations of the fcc lattice compared to reported structures on other amorphous substrates. Only weak texture is indicated.

Different peak ratios of the in-plane response related to LiF films in the full coverage regime have been observed. DIP is the only organic surface in this study that show only LiF(200) signals. On all other surfaces, LiF(200) and LiF(111) reflexes are visible but with different intensity ratios. Comparison with the growth on different inorganic surfaces suggests the surface roughness as one of the influencing parameter. Since non-epitaxial growth is assumed this is understood in a simple view of rolling dyes on a surface. Flat faces coming to lie parallel to a flat surface while the edges point towards the surface when the surfaces exceed a certain roughness.

In-situ x-ray studies on one donor type and one acceptor type organic molecule with layer-by-layer growth mode show variations in the lattice parameters in the sub-Ångstrøm regime of both organic and inorganic species. Re-ordering of the organic and the inorganic crystal structure does not occur. A correlation between any of the organic lattice constants with the LiF lattice constant has not been identified.

The lattice constant of LiF increases on both organic surfaces and saturates close to the reported bulk value after specific amounts of LiF are deposited. The discrepancy to the bulk value is smaller on DIP surfaces than on PTCDI-C_8 surfaces. Expansion of the organic lattice occurs in both organic model systems. Most likely this is not related to an energy transfer between the inorganic and organic constituents in the bilayer. A relaxation or expansion of the organic lattices due to thermal energy is more reasonable as increased substrate temperatures have been recognized during both in-situ experiments.

Lattice contraction is a well known behavior of nanoparticles due to induced strain [162]. Differences between surface and cohesive energies that originate in the uncoordinated bonds in the surface shell of nano particles yield to smaller lattice constants the smaller the particle size gets. A relation between the size of the particles and the contraction has also been reported [163]. As the LiF lattice constant does not reach the bulk value, it is assumed that full coverage is established by a porous arrangement of agglomerated particles. The constant grain sizes obtained by peak breadth analysis on both organic molecules do also fit in this scenario. The formation of LiF with complete coverage could be directly observed on DIP regarding the trend of total bilayer thickness.

VII. LiF STABILIZATION EFFECTS

Degradation is an important issue especially from a commercialization point of view regarding the lifetime of organic devices. Degradation is attributed to the strong impact of atmosphere (oxygen and water) as well as to the interaction with light in particular in the blue and even higher energetic range. Thermal instability is also reported in various aging experiments on organic small molecule systems. This chapter deals with the stability of the LiF/DIP bilayer configuration under strong x-ray illumination and examination of the thermal stability by a post heating procedure in ambient conditions.

1. Experimental details

The samples for this study were produced ex-situ by molecular deposition techniques. SiO_2/Si(100) substrates were used. The substrates were cleaned in Ethanol and Acetone 15 min each. SiO_2 substrates were heated to 500° C for 30 min prior deposition to remove moisture. The rate during deposition of organic molecules was set to 0.2 monolayers/min. The LiF coverage is around 1% for all samples (around 10 Å monitored by QCM) and rates around 8 Å/min were used. Half covered LiF samples were produced with a small tantalum sheet that was mounted on the sample holder and could be moved to shadow half of the sample during LiF deposition.

Beam damage experiments were carried out in air and either in a helium flooded chamber or a pumped UHV chamber both equipped with a beryllium dome. The fast aging process was realized with a heating plate inside an aluminum coated box to achieve dark environmentally condition with constant humidity. X-ray measurements were carried out at the synchrotron radiation source (ANKA) at 10keV beam energy. AFM measurements were performed with the AFM nanotech system (*Dulcinea*) and processed with WSxM software [137].

2. Radiation damage

Degradation by light induced chemical reactions like oxidation or damage due to thermally activated material diffusion are limiting factors for the lifetime of thin film based organic devices. Especially in this project, structural stability of the prepared films at least during experiments is essential for achieving meaningful results in comparative ex-situ x-ray studies. As changing scattering signals have been recognized during x-ray measurements, the question of probe-sample interaction emerged for the investigated inorganic/organic thin films. To study this behavior in more detail, observations of the specular out-of-plane response under strong x-ray beam illumination with defined exposure time have been carried out.

Figure VII.1 shows the reflectivity data obtained from three different LiF/DIP bilayer systems in (a) air, (b) helium and (c) vacuum. The samples have been measured after beam illumination with duration of 1 h and consequently on the same spot. Stable reflectivity curves have only been observed in the vacuum condition.

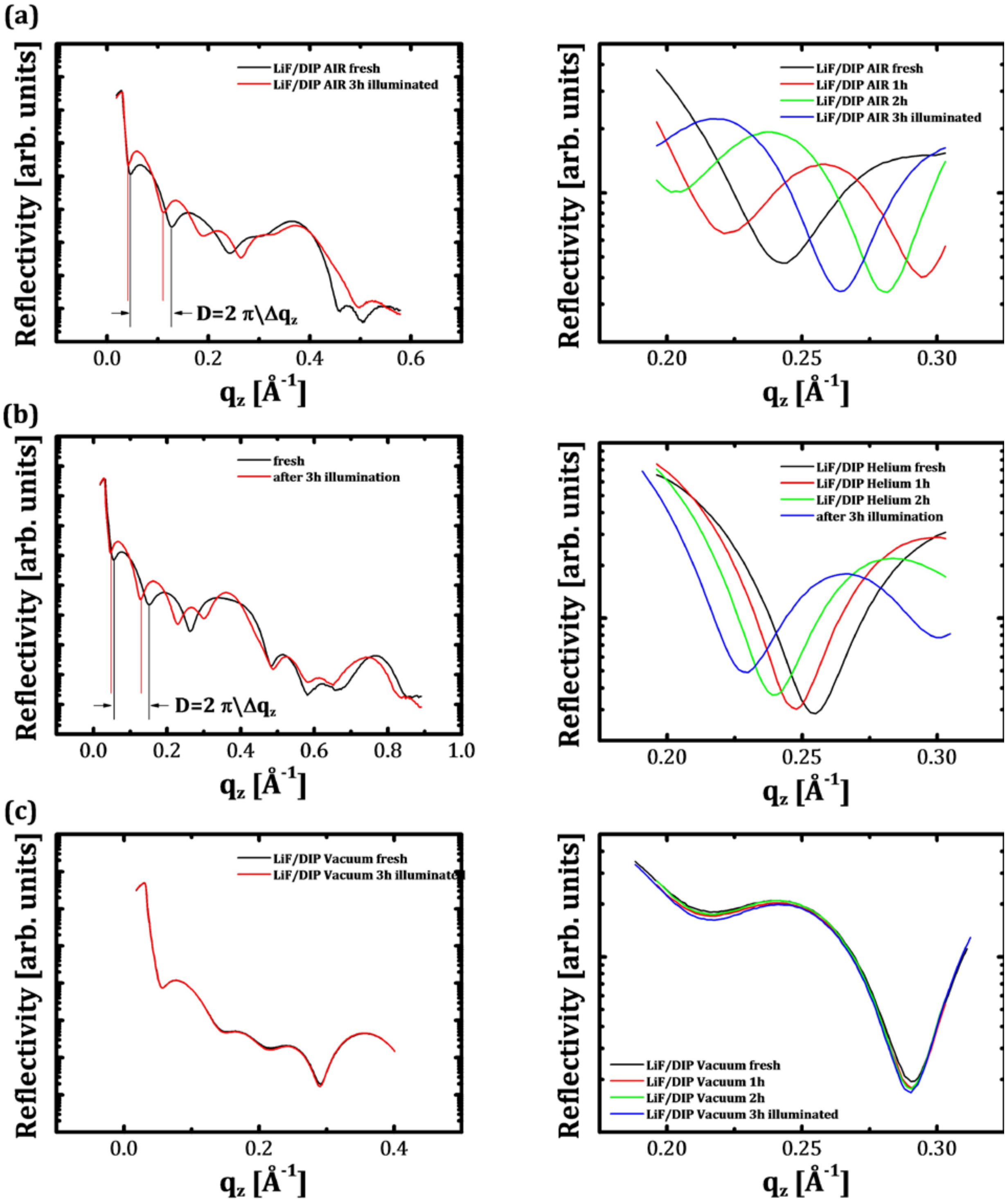

Figure VII.1: X-ray reflectivity of three different LiF/DIP bilayer systems under (a) air, (b) helium and (c) vacuum conditions before and after illumination (left). Each sample has been measured at Kiessig oscillation minima four times each with 1 h under 10keV x-ray illumination (right). Stable signals are only obtained under vacuum conditions.

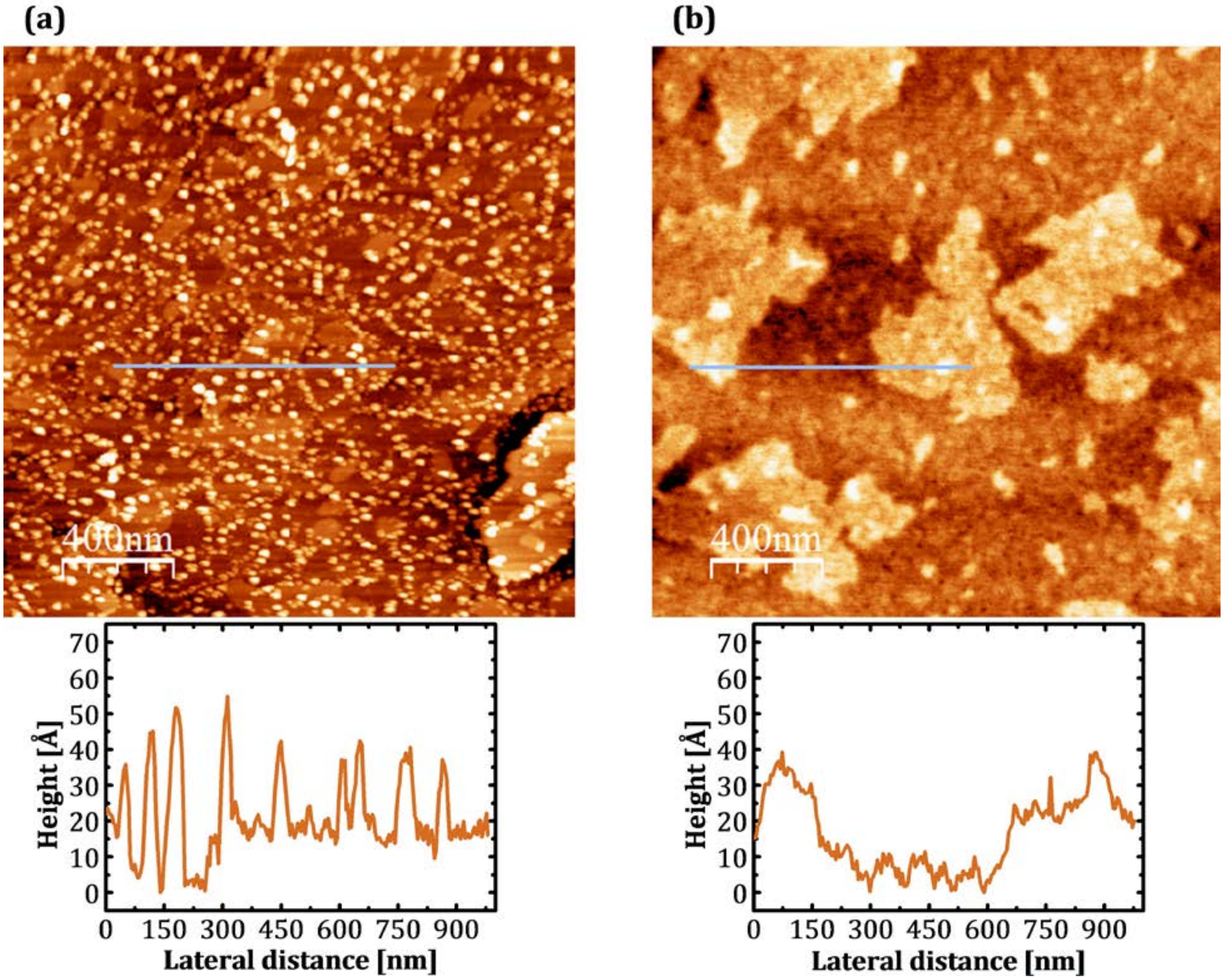

Figure VII.2: Surface morphology of LiF/DIP bilayer configuration before and after radiation damage in air and helium atmosphere.

Shifts in the Kiessig oscillations are visible under helium and air environment while the signal change is more pronounced in air. Analysis from the positions of the first two oscillation minima suggests an increased bilayer thickness in both cases. The differences in thickness for the as-prepared and illuminated samples are 12.04 Å in air respectively 11.34 Å in helium atmosphere and thus close to each other.

Topographical images before and after sample damage in Figure VII.2 indicate a drastic change in the surface morphology. It is not clear, if the damaged spot caused by beam illumination has exactly been hit during AFM measurement. However, vanishing LiF islands and decreasing LiF island heights as well as increasing noise on areas without visible LiF islands can be seen. Smaller periodic fluctuations in the height profile point to a deliquescence of the LiF particles. In parallel, increased lateral dimensions of the remaining particles is indicated. Height steps of organic islands are slightly larger in the damaged sample topography and can be caused by the smaller LiF particles on top of the organic surface.

Since damage happens in air and helium environment, oxidization of surface is excluded. A thermal effect is also unlikely as this would also cause sample damage in the vacuum environment. A more likely reason is the presence of water even if the dry helium atmosphere should prevent water infiltration. An explanation of the mechanism that is responsible for the instability under radiation and the reason for the increased bilayer thickness has to be answered in future studies.

3. Dewetting protection

The phenomenon of dewetting describes a breakup of thin films into droplets and is usually observed in liquids. Anyway, it does also occur in solid thin films. Dewetting is often a limiting factor for technological applications reducing their life time and performance. The process is mainly due to the weak intra molecular van der Waals forces causing diffusion already at moderate temperatures. It is thus a thermally activated process. Theoretical models are already developed [164] but exact knowledge of the particular material system and high throughput characterization methods are needed for detailed analysis. Dewetting of ultrathin DIP films with thicknesses of less than two monolayers has recently been reported by Kowarik et al. [165].

Dewetting of DIP films with even larger thicknesses has been observed in this work by studying the influence of sample degradation by post heat treatment. Stepwise heating in ambient condition with controlled humidity of around 60% has been performed on split samples. The samples consist of a DIP film of around four ML deposited with an $SiO_2/Si(100)$ at room temperature and an additional ultrathin LiF film that is deposited on one half of the sample. Figure VII.3 shows the morphology of the organic and inorganic/organic surfaces in a series of heating steps with 9 h between (a) and (b) and 4.5 h between (b) and (c) at a temperature of 90° C. The initial organic surfaces are similar on both areas of the substrate with lateral organic islands dimensions of around 150 nm. The LiF coverage is indeterminate in this case because the DIP surface has a non uniform height distribution like expected for room temperature deposition. Defects in the organic film are already observed on both sides in the initial morphology. LiF forms randomly arranged islands on the organic surface. Heights of the LiF islands are measured in a range of 40-60 Å in initial conditions.

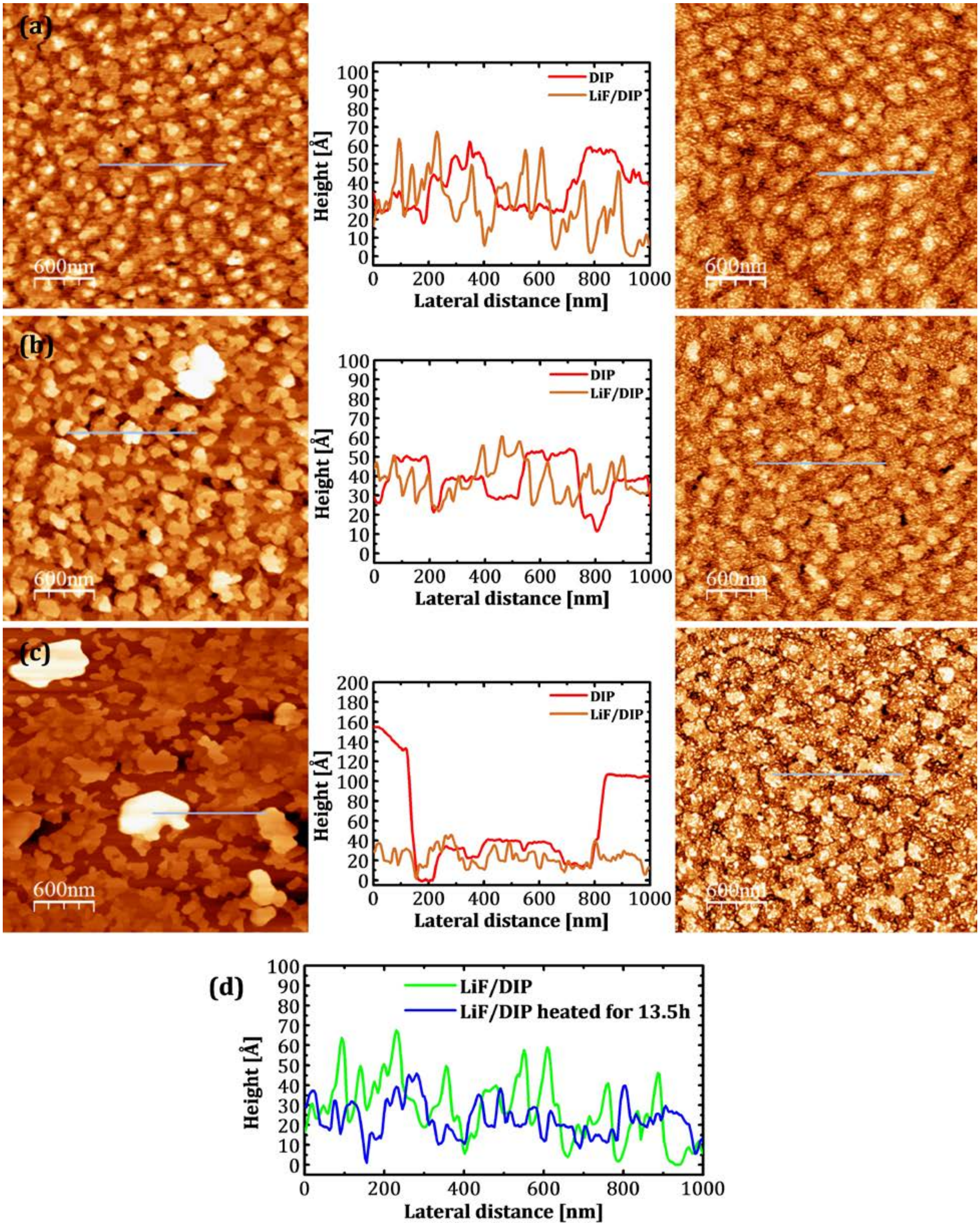

Figure VII.3: (a) Initial surfaces, (b) surfaces after 9 h heating and (c) after 13.5 h heating at 90° C of parallel grown DIP (left) and LiF/DIP (right). (d) Comparison of LiF island heights.

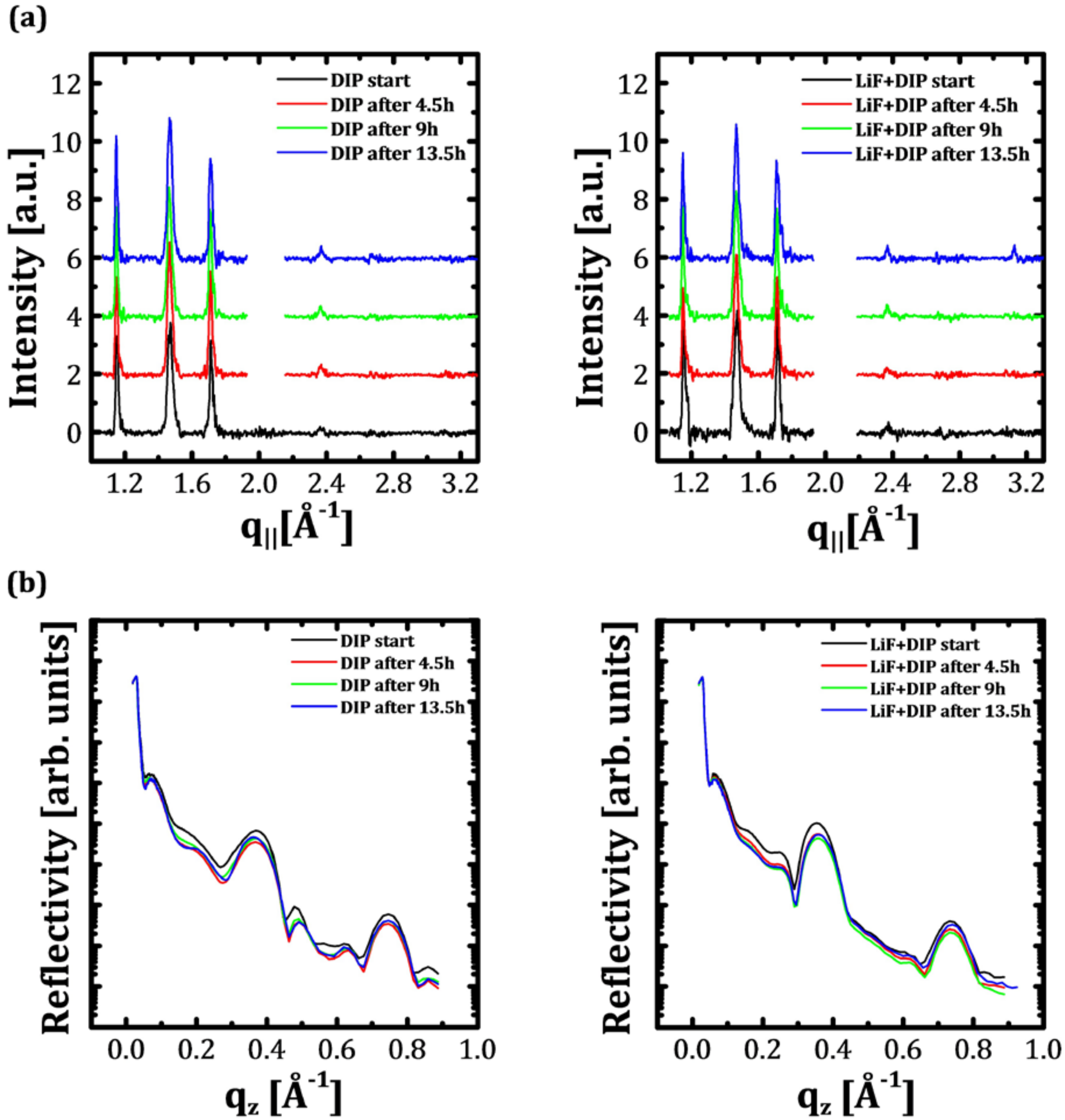

Figure VII.4: (a) In-plane and (b) specular XRD data of DIP (left) and LiF/DIP (right) split sample. Samples have been heated for the labeled time at 90° C.

Modifications of the DIP-only surface morphologies have been observed after both aging steps. The organic film starts dewetting the substrate surface where material agglomerates at the top most organic islands. Since the amount of material on the surface is consumed, an interlayer transport from the bottom to the top has to take place. The islands of the topmost layer increase in lateral size forming an atomic flat organic surface. It is assumed that the layer-by-layer stack arrangement is still conserved. In the end stage, formation of thick mostly circular shaped DIP islands occurs. The overall process might be described as Ostwaldt ripening due to minimization of surface energy in 3 dimensional expanded clusters, already reported for DIP growth modes by Zhang [166]. It is followed by coalescence. As temperature is responsible for this behavior, the dewetting process is driven by thermally activated diffusion of the organic molecules.

In contrast to the bare organic surface, the morphology of the LiF covered DIP film does not evolve by dewetting. Lateral changes of DIP as well as crack formation have not been observed. LiF island heights in initial conditions and already after the first heating step show height differences of approximately 20 Å. This difference stays almost constant even for further heating. LiF particles are probably penetrating into the organic film. The observed height difference suggests a constant penetration depth of one organic monolayer. The stabilization mechanism can thus be explained either by a saturation of adsorption sites which are unsaturated π-orbitals as the dewetting of DIP suggests. Pinning of the molecules is also thinkable, which hinders the organic molecule diffusion process by creation of energy barriers.

The dewetting process has surprisingly no dramatic effect on the structural ordering of the artificially aged samples in both systems. XRD studies in Figure VII.4 have been performed ex-situ due to the heating procedure in ambient conditions. Quantitative analyses of the organic signal response are ambiguous due to the unknown local texture of the organic films. Nevertheless, LiF scattering reflexes are almost not observed for the initial and early aged samples, although a LiF(200) in-plane scattering signal shows up after 13.5 h heating time. The signal might be caused by LiF crystallites that have penetrated through the organic layer and reach the SiO_2 surface. Only slight changes of the Kiessig oscillations in the specular data suggest that the averaged total film thickness is kept constant. Increase in the total layer thickness like observed in the AFM data is not indicated. Bragg signals from the multilayer stack do not change significantly what implies still present layer-by-layer arrangement even after dewetting.

4. Summary and discussion

LiF/DIP bilayer systems are unstable under high energy radiation when measured in ambient conditions or under helium atmosphere. A transition of the specular out-of-plane response in these environments has been observed. Shifts of the Kiessig oscillations caused by a variation of the bilayer thickness point to the formation of additional layers with the same thickness in both atmospheres. Sharp and acute LiF islands that are present in the initial morphology vanish after radiation influence. Deliquescence of the LiF particle as well as a lateral coalescence of the remaining particles is indicated. The total thickness observed in the reflectivity experiment increases and is explained by the formation of layer with more uniform electron density distribution. This layer serves for coherent out-of-plane scattering. As the damage does not appear in vacuum condition, a photochemical reaction of hygroscopic LiF due to present water contamination in both non vacuum conditions is thinkable.

Post heating in ambient conditions and under controlled humidity show dewetting of bare organic DIP films. Thermally activated diffusion is most likely responsible for this process which is accompanied by coalescence of the organic molecules and formation of huge islands. In contrast, LiF covered organic surfaces do not show changes in the organic morphology. A decrease of inorganic particle heights has been observed that correspond to a thickness of an organic monolayer. Penetration of LiF particles is assumed. Beginning crack formation via diffusion at already disordered regions in the organic film might cause the penetration of LiF particles. Blocking of adsorption sites especially at the edges of the organic islands is possible. Also stabilization of the organic film and hindering of thermally activated organic molecule diffusion might be a reason for the stabilization effect.

The in-plane structure of the organic film is not disturbed by the dewetting process. Nearly unchanged signals from the herringbone arrangement are visible in all post heating stages. Differences in the out-of-plane stacking that would be expected by the dramatic evolution in case of the bare organic surface morphology do not occur. Slight variations in the overall intensity in the specular out-of-plane data show no systematic behavior. This implies that only molecules of already disordered regions in the film contribute to the dewetting process or that the signal response is not affected due to the measurement of averaged electron density distributions in the film.

VIII. LiF IN PHOTOVOLTAIC DEVICES

Ultrathin films of LiF are widely used in organic photovoltaic devices especially in combination with an aluminum top electrode. Increased power conversion efficiencies have been already reported but only if the film thickness does not exceed 1 nm. As proof of principle, LiF has been added to the best performing donor acceptor combinations from organic molecules used in this study. Thicknesses and deposition rates of the LiF films have been varied. LiF film thicknesses are comparable to the low coverage regime in the morphology chapter as they are monitored with the same calibrated QCM. Equal growth behavior on smooth and rough organic surfaces has to be assumed as the organic surface previous to LiF deposition consists of fullerene molecules with rough surface morphology.

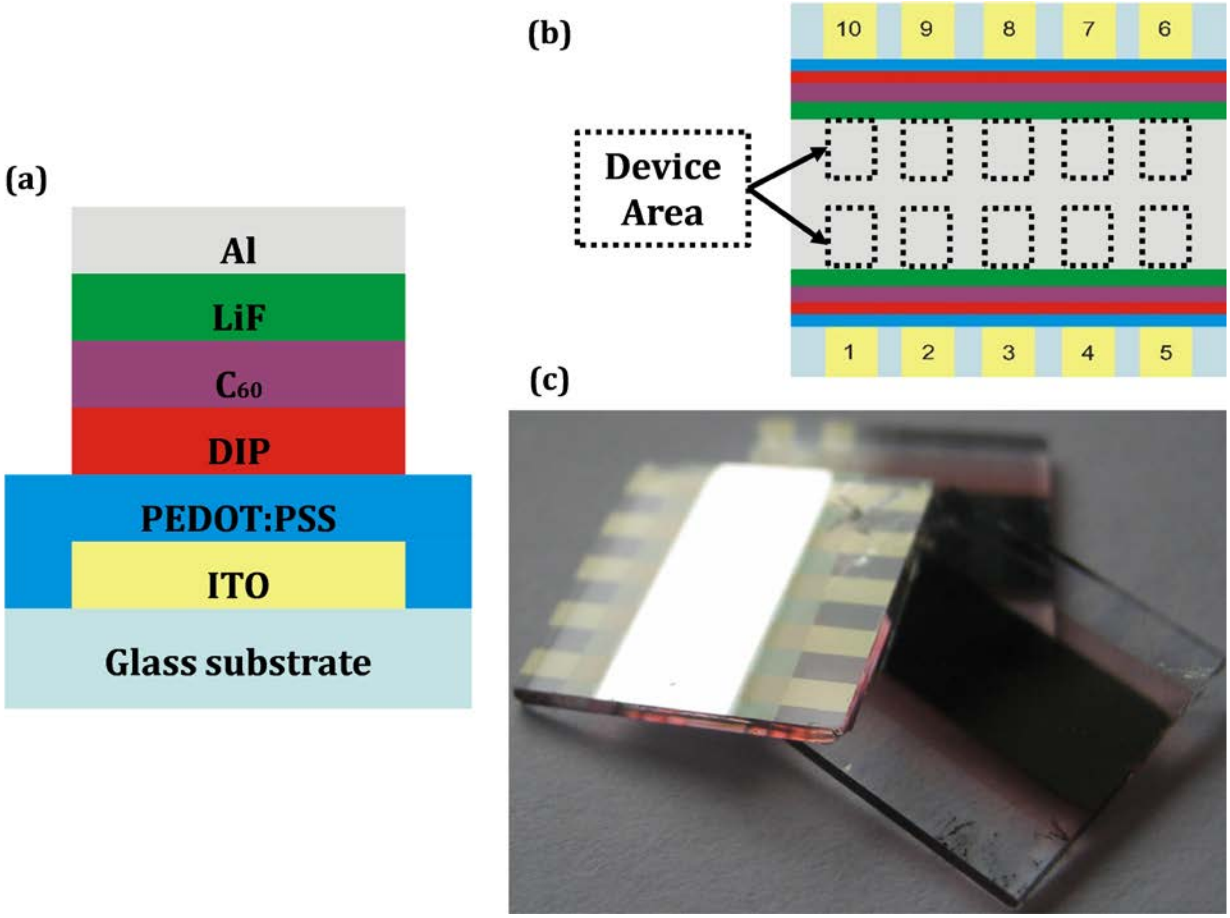

Figure VIII.1: (a) Sketch of the vertical layer stacking for the fabricated devices. (b) The ITO/glass substrate was patterned to achieve 10 independent devices per substrate and thin film combination. (c) Image of a set of tested devices.

5. Experimental details

The organic devices consists of a bilayer configuration (Figure VIII.1) of two semiconducting molecules DIP (donor) and C_{60} (acceptor), thermally evaporated in the OMBD chamber at pressures less than 10^{-8} mbar. Glass-ITO substrates (*Thin film devices Inc.*) were chemically etched to maintain 10 devices on one single substrate, see Figure VIII.1. Subsequently they were cleaned in acetone and ethanol 15 min each. Pedot:PSS (Baytran 8000; *H.C. Stark*) was spin coated at 6000 rpm for 3 min, resulting in a thin layer of around 20 Å thickness. The substrates were degassed at 120° C for 30 min at pressures less than 10^{-8} mbar afterwards. The active materials (600 Å DIP/500 Å C_{60}) were deposited with a rate of around 10 Å/min with the substrate held at room temperature. LiF was deposited at various thicknesses with pressures less than 10^{-8} mbar and cell temperatures between 650° C and 732° C. The Al electrode of 500 Å was grown in a separate UHV chamber at a pressure less

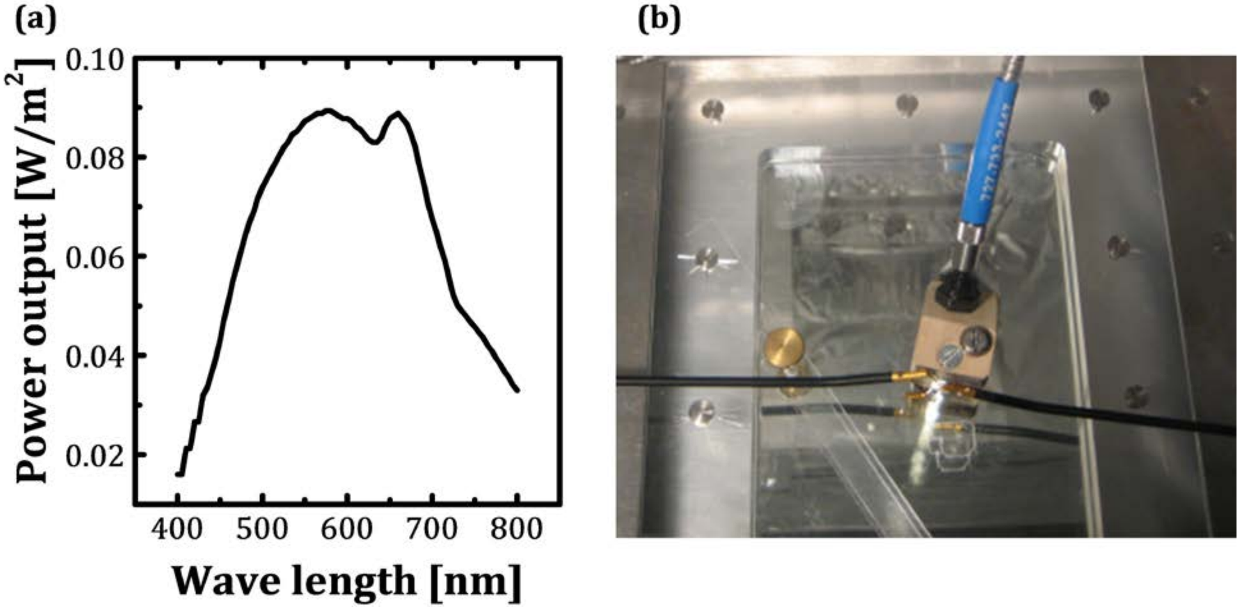

Figure VIII.2: (a) Power spectrum of the illumination spot with an area of 18.8 mm². (b) The light from the source has passed an optical fiber, a collimator lens and has been reflected from a mirror before arriving at the position for device characterization.

than 10^{-6} mbar. Once all the layers were deposited, the devices were transferred to a nitrogen filled glove box (O_2 conc. < 0.1%, humidity <1%) using a vacuum transfer chamber. All electrical characterization was done in the glove box under a nitrogen atmosphere with an HP 4155C Semiconductor Parameter Analyzer (*Agilent Technologies*), measured by coaxial probes PH 100 (Süss MicroTec Inc). Note that the organic devices were never exposed to air subsequent to production.

For probing solar cell performance, a tungsten halogen white light source HL-2000 (*Ocean Optics*) with an incident power flux of 66.15 W/m² measured by a thermopile sensor was used. The devices were characterized in back light reflection condition with an additional collimator lens between the optical fiber and the reflecting mirror. The power spectrum of the light spot at the sample position and the characterization stage is shown in Figure VIII.2. The EQE measurement was performed with a monochromator (Monoscan 2000, *Ocean Optics*) in addition. The device areas were measured after electrical characterization with a digital camera attached to an optical light microscope using appropriate measurement software (*Zeiss*).

6. LiF coverage dependent device performance

For probing the influence of ultrathin LiF films on photovoltaic devices, a set of samples with different LiF deposition amounts has been fabricated. The amount of LiF has been controlled with the same calibrated QCM that was used for investigations of the LiF morphology. This implies LiF coverage in the range of 1-3% for deposition on the planar molecules. Previous studies by this group [167] have identified a combination based on DIP as donor and C_{60} as acceptor - both deposited with the substrate at room temperature - as best operational devices from organic molecules used in this work. Devices with these kinds of molecule combinations reach power conversion efficiencies up to 4% recently described by Wagner et al. [168]. The introduction of a thin film of PEDOT:PSS between the transparent ITO electrode and the DIP layer in this devices serves for a well-defined workfunction larger than that of ITO, a smoother surface compared to the rough one of ITO, protection of the active layer from indium or oxygen penetration and prevention of short circuit currents. A more detailed description of the influence of PEDOT:PSS interlayers is given elsewhere [169; 170; 171; 172; 173].

HOMO levels of DIP are reported around -5.3 eV [168]. The energy gap of DIP on Au(111) which has a similar workfunction like ITO, has been observed with 1.44 eV [80] and calculated with 1.47 eV from first principles DFT [174].

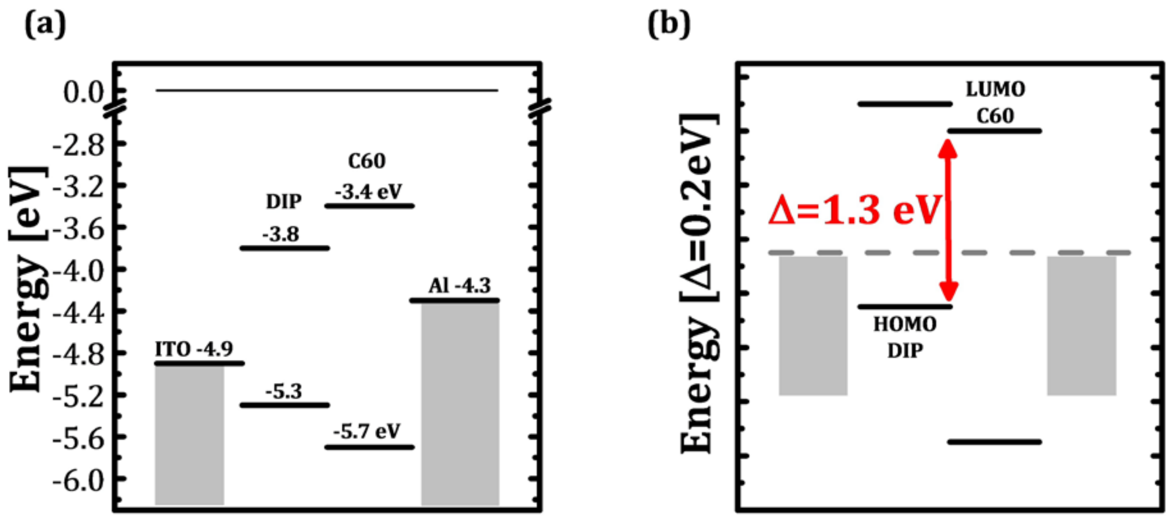

Figure VIII.3: Roughly estimated energy level scheme of the DIP/C_{60} donor-acceptor interface (a) under open circuit and (b) under short circuit condition. Obtained values are reported in [167; 79] (DIP) and [174; 175] (C_{60}).

Investigations on the energy levels for solid C_{60} films on aluminum turned out a HOMO position of around -5.7 eV for low C_{60} coverage on Al surfaces, taking a vacuum level shift of the metallic workfunction due to interface dipole formation into account [175]. The energy gap of C_{60} is reported in the range of 2.3 eV [176].

The reported features of the electronic alignment from the two active materials allow drawing a rough scheme of the energy levels existing in the stacked device, shown in Figure VIII.3. The achievable open circuit voltage (1.3 V) of such a device is estimated by the difference in the HOMO level of the donor and the LUMO level of the acceptor [35; 177]. A more reliable set of values can only be achieved by measuring the according energetic features for each combination of materials individually which is beyond the scope of this work.

Measurements of the diode like IV-curves of the fabricated organic devices are shown in Figure VIII.4. Only the best of the 10 devices on each substrate has been chosen in the presented data. A linear region in the semi-logarithmic plot in Figure VIII.4(a) that points to single diode like exponential current voltage characteristic is only indicated in the device with low LiF deposition amount. The same behavior has been observed for the illuminated devices in Figure VIII.4(b), even if all samples show photogenerated current and open circuit voltage under illumination. It is not clear if the produced solar cells apart from the low covered one are working properly.

Anyway, the performance of the cells calculated from the observed key parameter show power conversion efficiencies up to 0.3%. The relatively poor performance of these devices is attributed to several mostly experimental reasons. The absorption spectrum of the used white light source (Figure VIII.2) does not match the reported absorption spectrum of both organic molecules. Furthermore, the devices have not been encapsulated to reduce degradation. In addition, measurements in the back reflection geometry cause a divergence in the light spot. The estimation of the incident light power which is measured in a larger distance to the spot is therefore afflicted by large insecurities. Last but not least a poorly conceived sample probing stage as a result of the initial photovoltaic device characterization leads to difficulties in exact sample alignment.

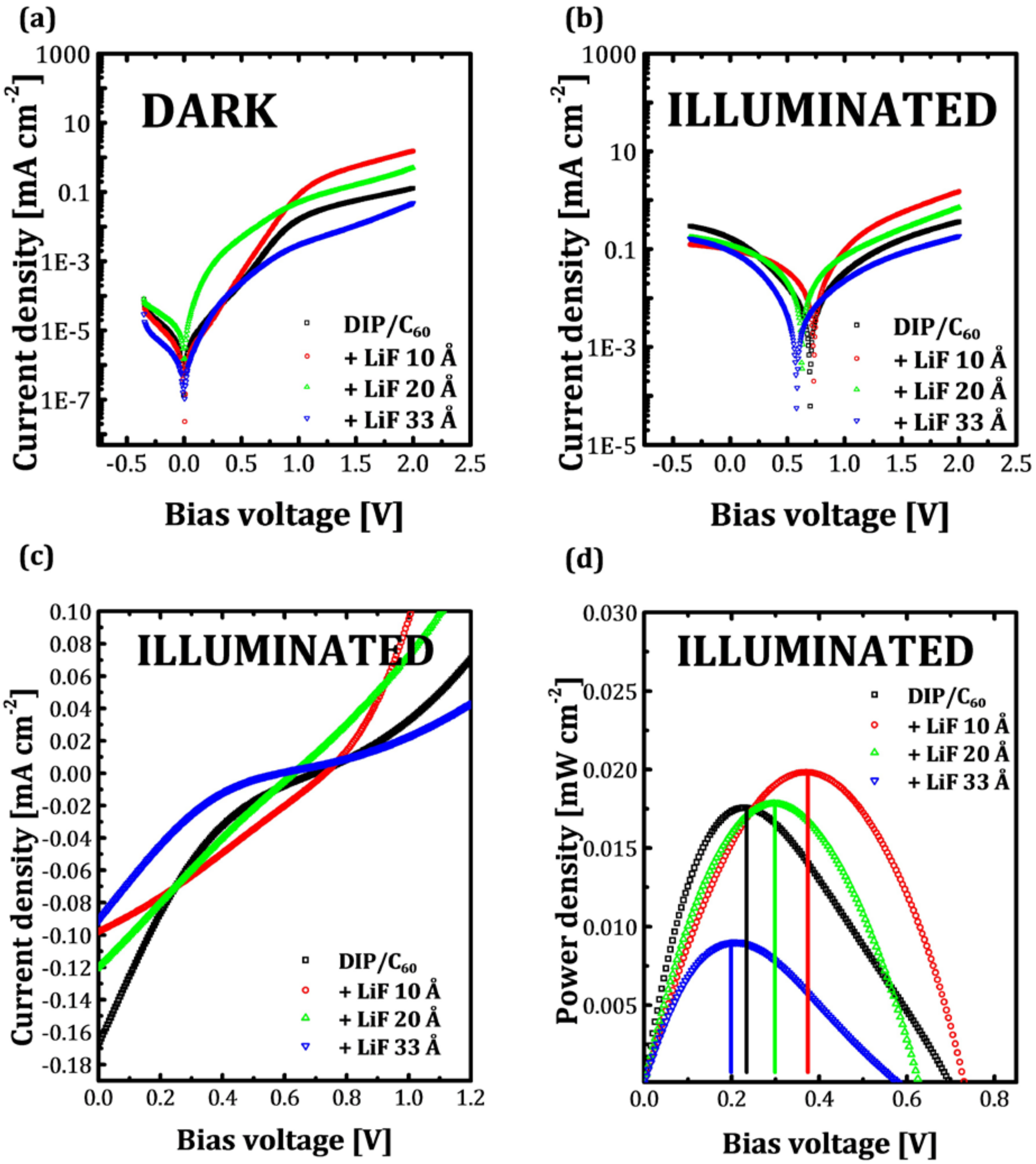

Figure VIII.4: (a) IV-curves of under dark conditions for different LiF amounts on C_{60}/DIP photovoltaic devices. Only the low covered device shows an acceptable diode behavior. (b) Open circuit voltages around 0.59-0.74 V have been observed for the illuminated devices. (c) The low covered device is the only one that does not show a strong s-shape in the power generation quadrant. (d) The maximum power output shifts to larger bias voltages and the absolute value increases for the low LiF deposition amount device.

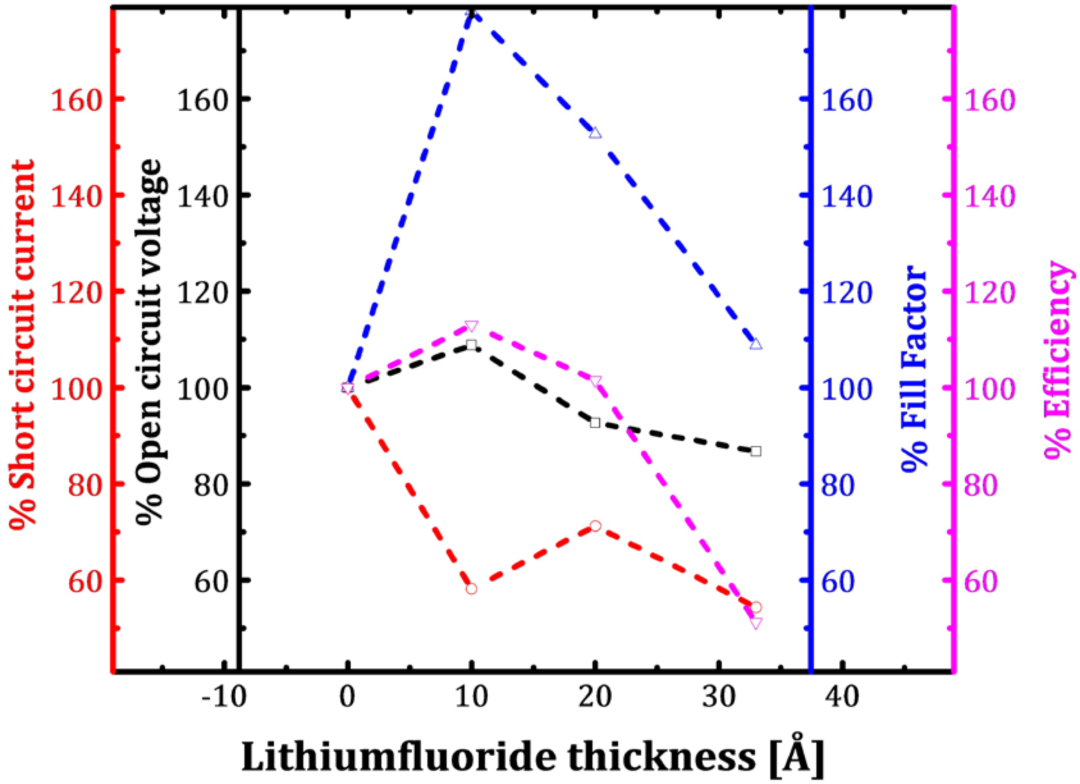

Figure VIII.5: Performance C_{60}/DIP devices with different LiF coverage normed to the bare organic device. The graphs are coded with the same color like the respective axis.

Table 14: Measured solar cell parameters of C_{60}/DIP devices with different LiF coverage.

LiF amount	**Area** [10^{-6} m^2]	V_{OC} [V]	j_{sc} [mA cm^{-2}]	p_{mpp} [mW cm^{-2}]	FF	η [%]
0	2.28	0.68	0.168	0.018	0.15	0.265
10 Å	1.51	0.74	0.098	0.020	0.28	0.300
20 Å	2.09	0.63	0.120	0.018	0.24	0.269
33 Å	2.42	0.59	0.091	0.009	0.17	0.136

As interest of this study focuses in the relative changes of electrical parameters for implementation of LiF, measured solar cell efficiencies are sufficient to investigate the predominant trends. The LiF coverage dependent changes of the interesting parameters listed in Table 14 are as expected: LiF improves the efficiency and power density of the device but only for low coverage. Degrading performance with increased material deposition is indicated. The best power conversion efficiency for the low covered LiF device is mainly attributed to the large fill factor and thus the best curve shape compared to an ideal device. This fact is also expressed in the highest power conversion as depicted in Figure VIII.4(d). Not only has the total value of the maximum power point increased but also the corresponding bias voltage in the power conversion quadrant.

The linear decreasing trend of the short circuit current density between the bare organic device and the devices with higher coverage in Figure VIII.5 is broken for the low LiF coverage device. A drastically decrease of the short circuit current density but increase of open circuit voltage has been observed for this device. The overall performance which is represented in the power conversion efficiency η shows no linearity. This is mainly caused by the better fill factors for all LiF covered devices. An interesting feature in the comparative study is the vanishing s-shape for the low covered LiF device, depicted in Figure VIII.4(c). S-shapes observed in the linear IV-curves of organic voltaic devices are still controversial and mainly attributed to the strength of the internal field in the device that might be established and influenced by interface dipoles.

Table 15: Shunt (R_p) and series (R_s) resistances obtained from the slope of the illuminated IV-curves at zero bias voltage (R_p) and largest measured bias voltage (R_s).

LiF amount	R_p [Ω cm^2]	R_s [Ω cm^2]
0	2344	2065
10 Å	10225	341
20 Å	5241	717
33 Å	4305	3908

Equivalent resistances within the realistic solar cell model described by equation (II.9) are listed in Table 15. They have been obtained by fitting the slopes of the IV curves of the illuminated devices at zero bias and larger positive bias. A dramatic increase of the shunt resistance and decrease of the series resistance for the best working device with low LiF coverage is indicated. Additional deposition of LiF enlarge the series resistance and both parameters stabilize but at larger absolute values. The small value of the shunt resistance for the bare organic device is also responsible for the highest measured short circuit current if the current is as sum of photo generated and shunt currents. However, modeling of the IV curves with the obtained values according to the realistic diode model failed (see next section).

7. LiF deposition rate dependent device performance

Another set of devices has been fabricated where the monitored thickness of LiF has been kept constant. The deposition rated and thus the deposition times have been changed by varying the temperature of the LiF cell. The amount of LiF that has been used is equal to the one monitored for the best working device in the previous section. The measured dark and illuminated IV-curves from this set of devices are shown in Figure VIII.6(a) and (b). The plotted data of the bare organic device is comparable with the one from the previous section. In contrast to the LiF covered devices, the bare organic sample does not show a clear diode behavior at all. Even if non zero values for short circuit current and open circuit voltage is obtained for this device under illumination, constant saturation currents for the dark series measurement at reverse bias conditions have not been observed. A vanishing s-shape of the linear plotted IV-curves for all LiF containing samples is clearly identified.

Performance parameter, listed in Table 16, shows the difficulty in the exact control of the LiF interlayer growth and devices fabrication processes. On the one hand, the bare organic device in this series has nearly the same performance like the one in the previous section even if the open circuit voltage and the fill factor are slightly increased. Contrarily, the device containing the LiF film, deposited with a monitored thickness of 10 Å in one minute (T_{cell} at 732° C) with all growth parameters identical to the low LiF covered device in the previous section, shows a four times larger total power conversion efficiency. A possible reason for the dramatically increased performance can be the use of LiF which has just been refilled before the growth process and has not been heated to the evaporation temperature as many times as the material used for the previous studies. It has been observed by eye that the material in the crucible is forming a compact solid block after extended time at elevated temperatures in the UHV environment compared to the powder form in initial conditions. Cluster formation may be enhanced in the powder form due to the larger material surface area

According to the data, fill factors and open circuit voltages of the LiF covered devices stay nearly constant when the LiF growth process slows down. The short circuit current decreases drastically when the LiF deposition rate has been reduced.

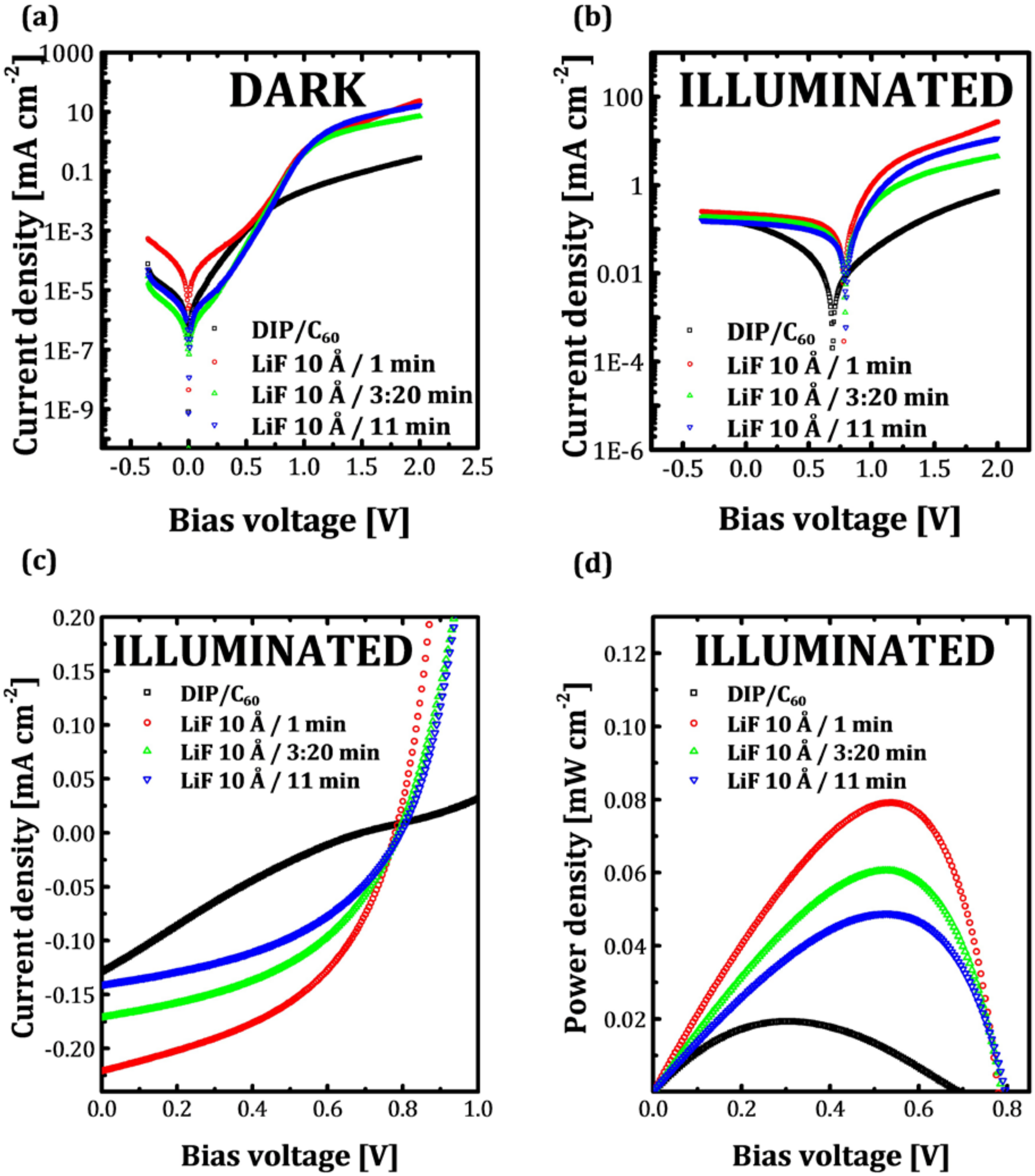

Figure VIII.6: (a) Dark and (b) illuminated semi logarithmic plots from a set of devices with the same monitored amount of LiF but different LiF deposition rates. (c) Linear plotted IV-curves show a strong s-shape for the bare organic but clearly diode like behavior of all LiF interlayer containing devices. (d) The absolute value of the maximum power point is reduced for slower deposition rates, but the corresponding value of the bias voltage stays nearly constant.

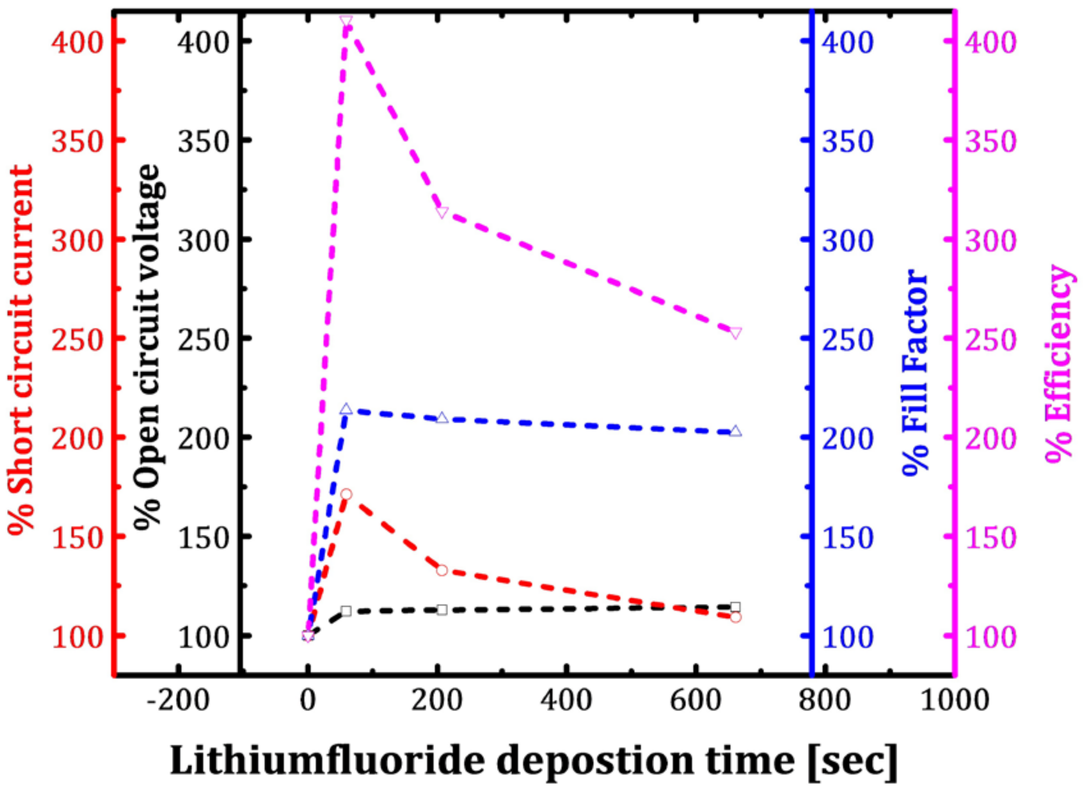

Figure VIII.7: Relative performance of C_{60}/DIP devices with same monitored amount of LiF deposited but different rates. The graphs are coded with the same color like the respective axis.

Table 16: Measured solar cell parameters of C_{60}/DIP devices with varying LiF deposition rates but the same monitored deposition amount.

10 Å LiF deposition time [min]	**Area** [10^{-6} m^2]	V_{OC} [V]	j_{sc} [mA cm^{-2}]	p_{mpp} [mW cm^{-2}]	***FF***	η [%]
---	1.46	0.70	0.129	0.019	0.22	0.292
1	1.21	0.78	0.221	0.079	0.46	1.197
3:20	2.09	0.79	0.171	0.061	0.45	0.915
11	1.79	0.80	0.141	0.049	0.44	0.738

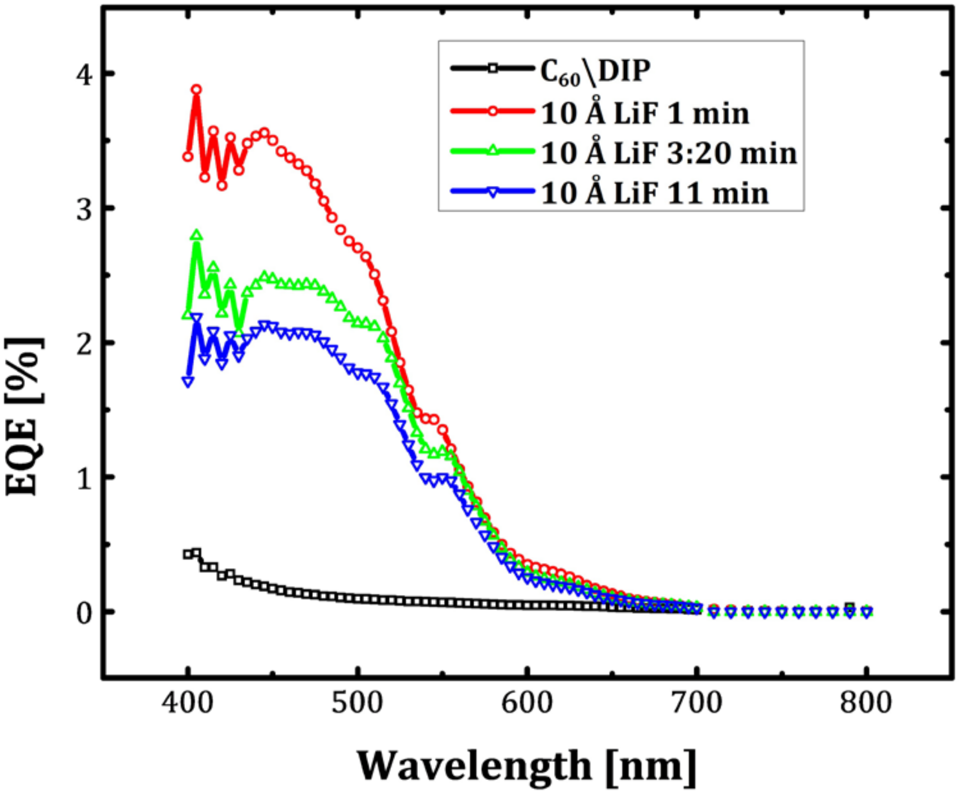

Figure VIII.8: External quantum efficiency (EQE) of the rate dependent device series. The shape of the curves obtained for the LiF devices does not change. The bare organic device has already been degraded between IV characterization and EQE measurement.

The power output of the LiF covered devices shown in Figure VIII.6(d) increases much more dramatically in comparison to the bare organic devices than it has been observed in the previous section. In contrast to the thickness dependent measurement, a shift in the corresponding bias voltage is not visible when LiF growth conditions are changed. It implies that the mechanism of charge generation in the bilayer system is unchanged while the current flow in the devices is reduced, probably due to limiting charge extraction. Comparison of the external quantum efficiency in Figure VIII.8 does also not indicate a drastic change in the working mechanism of the devices due to a changing rate of LiF deposition. Nevertheless, increased EQE at larger photon energies is visible for the best working device. The strong discrepancy in the EQE of all LiF covered devices to the bare organic one has its origin in the degradation of that particular sample when it has been measured.

The changing device performance caused by the reduced short circuit current is most likely attributed to a LiF coverage variation. A decreasing rate of the monitored thickness has been observed after deposition of the first 10 scaling units measured for each chosen cell temperature. The origin of this behavior is a temperature dependent fluctuation of the monitor due to the initiation of the material stream and the close distance or the cell and the monitor. This effect has more consequences when the deposition cell has been heated up to the highest temperature for deposition. It would mean that the best working device with the fast rate in the series has the lowest LiF coverage and the deposition amount for longer deposition times has increased.

Table 17: Shunt (R_p) and series (R_s) resistances obtained from the slope of the illuminated IV-curves at zero bias voltage (R_p) and largest measured bias voltage (R_s).

10 Å LiF deposition time [min]	R_p [Ω cm^2]	R_s [Ω cm^2]
1	12556	16
3:20	17188	197
11	14478	64

The obtained resistances for this series, listed in Table 17, do not show a clear trend. It is stated that all devices have large shunt resistances compared to the series resistance. When the assumption is made that the series resistance increases with additional material deposition, a situation where the best best working device grown with the fast rate has coverage just between the middle and slow grown device is conceivable.

Attempts of fitting the IV-curves with the realistic diode model in Figure VIII.9 have applied. Shunt and series resistances from the slope analyses have been used for the fit. It turned out that the obtained ideality factor of 10.9 indicates a non diode like behavior even for the best working devices which should have a value of 1-2. As parameters for the application of other models for the particular C_{60}/DIP device neither known nor measured, attempts of replicating of the measured data have not been successful so far.

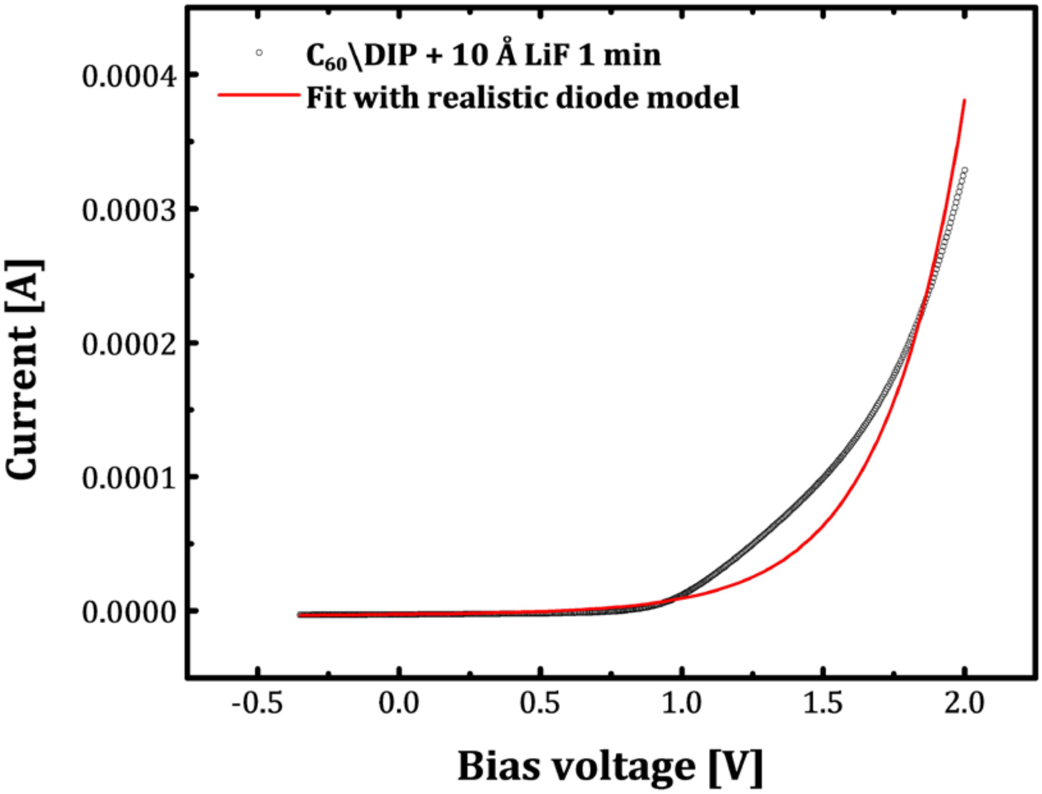

Figure VIII.9: The IV-curve from the fast deposited LiF device has been fitted with the realistic diode model from equation (II.9). An ideality factor n = 10.9 *has been obtained.*

8. Summary and discussion

The influence of LiF interlayers has been tested on organic photovoltaic devices that are made from combination of DIP as donor and C_{60} as acceptor molecules. The poor performance of the bare organic devices with power conversion efficiencies of 0.265 % is mainly attributed to the low fill factor of 0.15 which should be close to one for an ideal diode like behavior. Devices with LiF interlayers showed better performance only for very low thickness that is coupled with LiF coverage of around 1% assuming the same growth mode for LiF on C_{60} like on the planar molecules. An increased fill factor, increased open circuit voltage but less short circuit current has only been determined for this device with lowest coverage. The characteristics of the devices with thicker LiF interlayers, assumed to have doubled coverage, are already worse than the bare organic one. Analysis of the equivalent resistances revealed a five times larger shunt resistance and a ten times lower series resistance for the best working device. The shunt resistance is again lowered for additional material deposition but not linearly. Series resistances show a minimum for the low LiF covered device and is again increasing by additional material deposition. Especially the series resistances which might be connected to the insulating properties of a LiF interlayer are still much lower for all LiF covered devices compared to the bare organic one.

A vanishing s-shape in the IV-curve for the low covered device indicates that LiF has an impact on the internal electric field established between the donor and acceptor or rather on the charge recombination mechanism at the metal-organic interface. Kumar et al. [178] related the origin of the s-shape to interface dipoles. The resulting internal field that is responsible for the charge separation between donor and acceptor can overlap with the so called diffusion field that is present due to the workfunction difference of the electrodes. The sum of both can higher or lower the external field, established by the applied bias and serve for a current flow already at lower bias voltages, dependent on the orientation of the interface dipole. Wagenpfahl et al. [179] assigned space charges as origin of the characteristic deformation. These charges are created by surface defects and cause reduced surface recombination velocity of majority charge carriers. A reduction of the open circuit voltage by finite surface recombination velocities is derived in that model. The authors concluded a transit from Ohmic conductivity to space charge limited currents takes place expressed by the appearance of the s-shape characteristics.

A series of devices with the low LiF coverage and varying deposition rates showed a much better performance of all LiF covered devices in comparison to the thickness dependent series as well as in comparison to the bare organic devices. A reason for this behavior might be the reload of the LiF cell and thus a more powder like form of the material when heated for evaporation. Power conversion efficiencies are obtained between 0.74 % and 1.2 %. As the individual LiF covered devices in this series have nearly the same open circuit voltage as well as fill factors in the range of 0.45, the decreasing trend in the short circuit current densities are responsible for the drop in efficiencies. A clear trend of the equivalent resistances in the solar cell model has not been observed. The best working device has the lowest series resistance but all devices showed varying but quite high shunt resistances compared to the bare organic device. Changes in absolute numbers of the measured external quantum efficiency have been observed, but no change in the curve shape and thus in the absorption behavior of the devices is visible. Attempts to fit the IV-curves with the real diode model failed in a sense that ideality factors are far off a diode modeled like behavior.

Changing performance due to the varying deposition rate is most likely attributed to a variation of the deposited LiF amount due to thermal fluctuations of the quartz monitor during evaporation. It turned out that the fluctuation is larger when the deposition is performed at higher evaporation temperature and thus faster rates. In this assumption less material is deposited at high cell temperatures as actually deposited when compared to lower cell temperatures and slower deposition rates.

Altogether, LiF has a beneficial impact only at very low coverage around 1%. It improves the device performance dramatically with up to four times larger power conversion efficiencies. The most significant effect is the vanishing s-shape and thus improved fill factors. Control of the amount that is actually deposited on the organic surface is very poor in this coverage regime and stable and reproducible results are hard to achieve with the used experimental setup.

IX. SUMMARY AND OUTLOOK

1. Summary

This work describes the structure and morphology of ultrathin LiF films on organic model surfaces. LiF particles with crystalline features are directly observed for the first time on top of organic surfaces. Incomplete LiF coverage in the low thickness regime and quantification of particle dimensions lead to the assumption that the sticking behavior of already formed particles is responsible for the ultrathin film morphology. In addition, grain boundaries and defect sites are indentified as preferred particle adsorption sites. The particles are able to prevent thermally activated diffusion of organic molecules. An epitaxial relation between the LiF structure and the organic structure underneath has not been detected. LiF inserted into electrical devices shows only a beneficial effect on the performance when the coverage is very low. It is assumed that LiF particle adsorption on disordered regions in the organic films contributes to improved charge extraction at the contact areas when it is implemented in organic solar cells.

In the following, the results of this work are summarized in more detail:

Morphology (Chapter V). At thicknesses typical for organic devices LiF forms disconnected islands on all investigated layer-by-layer grown organic molecules (DIP, PTCDI-C_8 and pentacene), independent of the electronic character or the chemical composition terminating at the organic surfaces. The observed islands have mostly heights in the range of 40-60 Å which is much larger than the film thickness, tracked by a quartz crystal monitor and calibrated on thick LiF films. Direct observation of the material coverage from analyzing the area coverage is limited by the small size of the islands which is believed to be less than the lateral resolution of the AFM system (> 100 Å). By counting the number of islands and assuming a spherical shape, LiF coverage of around 1 % could be obtained on all organic surfaces at the monitored thickness of 10 Å. Additional material depositions studied on the surface of one particular organic molecule film, leads to linear increase in number of LiF islands but only very small increase in size. Direct comparison between LiF agglomeration on inorganic SiO_2 and DIP turned out larger variation of the particle sizes on the inorganic substrate and more uniform particle dimensions on the organic substrate. Furthermore, it seems that only the largest particles from the ones observed on the inorganic surface stick to the organic surface. The increased island number density and material coverage points to different sticking of particles dependent on the underlying surface. Thus the formation of islands/particles is believed to happen already in the desorption process at the material source or in the vapor beam. Diffusion processes on the surface would cause increased island dimensions or would show particle coalescence. It is proposed, that only the sticking behavior of the arriving particles on the underlying surfaces control the morphology of ultrathin LiF films. An independency of the LiF morphology by variation of growth parameters like substrate temperature or slightly elevated deposition cell temperatures assists this assumption.

The dispersion of LiF islands on the organic surface is mostly random but chain like arrangement at organic island edges and on flat regions of the organic surfaces has been observed. Friction force microscopy indicates disordered regions in the organic films as preferred LiF particle adsorption sides. The chain like arrangement is much more pronounced when only the first monolayer of the organic film is visible. Analysis of island heights in the chain formation show reduced heights of the islands in the range of an organic monolayer. This implies a penetration of LiF particles inside the organic network down to the inorganic substrate where preferred adsorption has been confirmed. Dendritic LiF island arrangement that follows the dendritic island morphology of the underlying organic molecule film supports this assumption. As the chain formation vanishes when the thickness of the organic films increases the predominant factor for this behavior may be the formation of cracks in the unstable organic films. Crack formation can be easily induced under interaction with an AFM tip or by post exposure to sufficient temperatures. Multiple undesired fabrications of incompletely covered organic films in the progress of this work, especially at elevated substrate temperatures, indicate that crack formation already appears during the organic molecule growth process.

Structure (Chapter VI). Cross sectional TEM images of ultrathin LiF films on DIP suggest particle formation on the organic surface with spherical dimensions of around 50 Å. That corresponds well to island heights measured from the topographical morphology of LiF on DIP. Crystal planes are visible inside the particles with a plane spacing that is consistent with LiF(111) plane distances. The angular orientation of the planes in relation to the DIP surface equals the observed crystal structure of thicker LiF films on DIP in x-ray experiments which shows up with <100> orientation parallel and perpendicular to the substrate surface. As the particles show already structural ordering, it is assumed that the crystal structures of LiF films on organic surfaces with experimentally accessible thicknesses are almost equal to the structure of the incomplete coverage regime.

Ultrathin LiF films on organic surfaces with thicknesses in the range of 10 Å and thus island coverage of around 1% show only weak scattering response. When the thicknesses is increased to several nanometers, the films show x-ray scattering at momentum transfer positions and therefore lattice plane distances that are expected from the bulk material. Different peak to peak ratios in the scattering signal between LiF(111) and LiF(200) planes have been observed in the in-plane direction on various organic surfaces and out-of-plane direction on various inorganic amorphous substrates. A more pronounced <111> orientation in comparison to the <100> orientation is caused by the roughness of the underlying surfaces as epitaxial growth of LiF has not been observed. The existence of locally established in-plane texture on SiO_2 substrates is experimentally not accessible. This is caused by interference of the LiF signal response with scattering signals from the Si(220) planes arising from the single crystalline silicon underneath the oxide layer.

Examinations on the structural impact of increasing LiF deposition on the crystal structure of two layer-by-layer grown organic molecule films show no dramatic variation of the accessible structural information. In case of DIP a contraction of the monolayer thickness in the out of plane layer stack as well as a slight expansion of the in-plane lattice is obtained by fitting the XRD data with an appropriate model. In case of PTCDI-C_8, the monolayer thickness in the out-of-plane direction stays constant within the error but also a slight expansion of the triclinic lattice has been derived by a geometrical fit. The small variation of the organic unit cells are attributed to strain inside the organic films. Since an increase in the substrate temperature has been noticed during the experiment, a lattice relaxation due to heat effects is thinkable.

The fcc lattice parameter of LiF shows expansion on both molecule surfaces, which saturates close to the reported bulk value after a specific amount of inorganic material deposition is reached. This lattice expansion is connected to the presence of nanoparticles for low monitored LiF thicknesses. The saturation of the lattice constant is coupled with the achievement of complete coverage, which has been directly confirmed by analysis of the total bilayer thickness evolution in the LiF/DIP configuration. LiF grain sizes show constant values on both surfaces for increasing deposition amounts. Even if the dimensions of the LiF scattering centers are deviating between DIP and PTCDI-C_8 , it is stated that the fully dense film is mostly composed of the small particles with constant sizes. Porous structures especially in the low thickness and columnar growth for increasing thicknesses are already predicted in the literature [130].

Stability (Chapter VII). LiF/DIP bilayer systems show instability under high energy x-ray illumination in air and helium atmosphere that is prevented under vacuum conditions. Deliquescence of LiF particles on the organic surface seems to appear. Specular out-of-plane data suggest the formation of an interlayer with nearly the same thickness of around 12 Å in both destructive environmental conditions. A possible explanation for this behavior is a photochemical reaction between hygroscopic LiF and present water which destroys the LiF nanoparticles.

Post heating experiments of parallel grown DIP and LiF/DIP surfaces show dewetting of the bare organic surface. Dewetting of the DIP layer appears in two stages. In the first stage, the organic film cracks up and interlayer transport of organic molecules from the bottom to the top layer takes place. This increases the lateral size of the topmost organic islands. As atomically flat surfaces have been observed on the enlarged topmost islands, the upright standing configuration of the organic molecules is still present. In the second stage, coalescence of the organic molecules occurs and large conglomerates of organic molecules could be observed in the organic film morphology.

Dewetting of the DIP film is prevented by adding LiF particles to the surface. The film morphology is then only slightly affected by the heat treatment. Penetration of the particles is indicated by analysis of the LiF particle heights and takes place already in the beginning of the post heating procedure. The penetration depth saturates in the range of one organic monolayer. Only slight changes in structural in- and out-of-plane data are visible on both surfaces compared to the transition of the layer morphology especially on the bare organic surface. Already disordered and high mobile regions in the DIP film are probably responsible for the diffusion of organic molecules. It is assumed that LiF particles either stabilize the disordered regions in the organic film or block adsorption sides for the diffusing organic molecules.

Device performance (Chapter VIII). LiF interlayers with different thicknesses have been implemented into organic hetero junction devices. The photovoltaic devices consist of active donor-acceptor (DIP/C_{60}) combinations from organic molecules mainly used in this study. These materials are not commonly favored for high performing organic photovoltaics and thus do not show the best device performance. Power conversion efficiencies around 0.3 % have been achieved for the bare organic material combination without the introduction of LiF interlayers. This performance is still sufficient to compare the main trends under the influence of LiF incorporation. It has been shown, that LiF increases open circuit voltage and reduces the short circuit current density but only at very low thicknesses. Increased shunt resistances in the low covered regime are responsible for the reduced overall currents. The main effect that serves for increased power conversion efficiency is the improved fill factor which is an indicator for enhanced power conversion. LiF films in the low coverage regime yield to more diode-like characteristics in the IV-curves of the device and vanishing s-shape.

Another set of devices has been produced with varying deposition rates of LiF. LiF covered devices show with 1.2 % up to four times more power conversion efficiency for the similar growth conditions like the best working device in the thickness series. Probably the use of recently reloaded material prior to deposition might be responsible for this behavior. The deviating performance of the devices in this series has been attributed to varying LiF coverage due to the bad control of the low film thickness by monitoring the growth with the quartz crystal.

2. About the beneficial impact of LiF in organic photovoltaic devices

Several reasons about the physical mechanisms attributed to LiF interlayers in organic devices are proposed in the literature. Le et al. [180] speculated about dissociated Li that reacts with the organic material to form radical ions, which has been justified by additionally observed states in the energy gap of the organic material. Turak et al. [181] proposed a modification of the chemical reactivity between electrodes and organic layers and therefore influences on the oxidation of the metal electrodes by creation of passivation layers. Shaheen et al. [182] suggested that the large dipole moment of LiF decreases the surface potential of the used electrode.

The formation of a dipole layer in organic/LiF/metal systems, which is already present for low LiF thicknesses of 5 Å has also been observed by Watkins et al. [183] by a measured vacuum level shift in the organic material. Nevertheless, an asymmetry of the dipole has been proposed if the results were compared with a work about metal/LiF/organic systems by Mori et al. [184]. All these studies have been performed on diverse organic molecules with diverse metal electrodes. It seems that the underlying physical property is rather a very general feature that might be connected to the growth of LiF itself - especially when referred to the fact that LiF is only used in devices as an interlayer between the already grown active organic material stack and the top contact. No reports about an improvement of device performance of LiF interlayers directly deposited on the bottom electrode are reported so far to the author's knowledge.

The very robust growth behavior of ultrathin LiF films on organic molecules is most-likely the key for understanding the improvement of these interlayers.

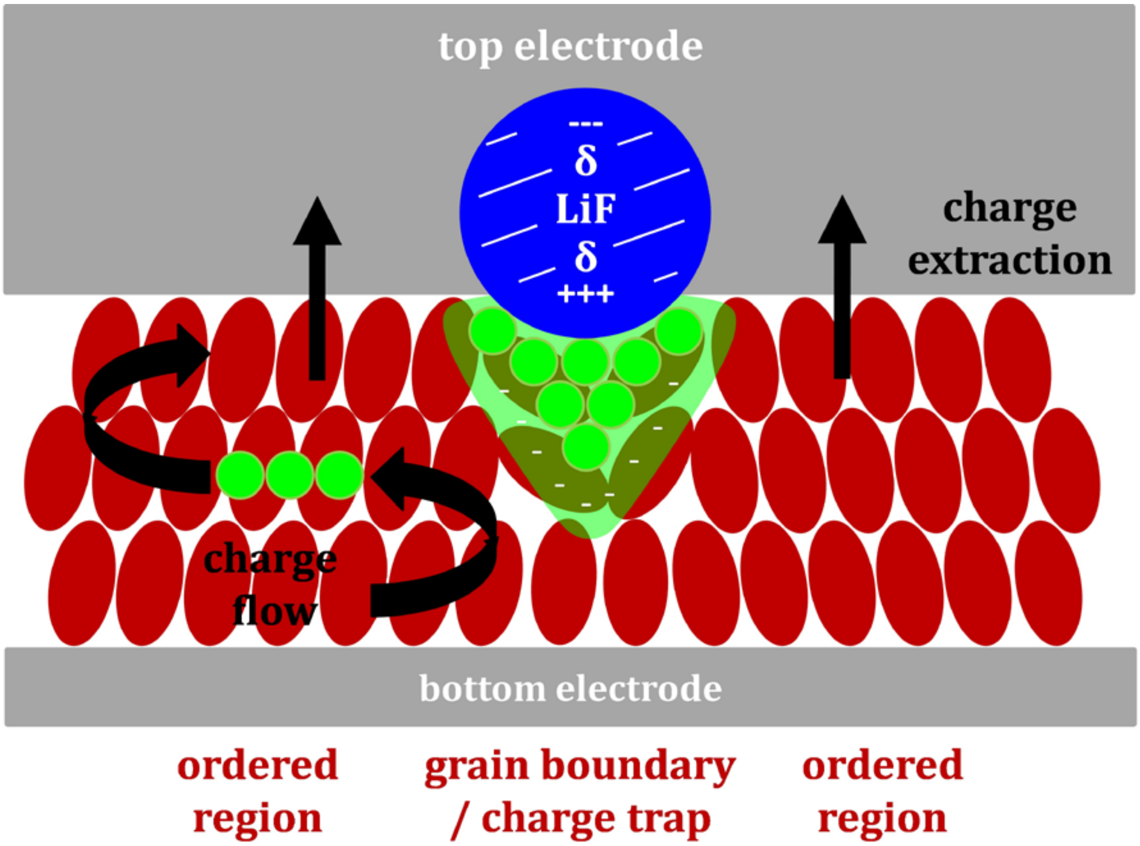

Figure IX.1: Speculative scheme about the positive impact of ultrathin LiF films in organic devices which adds up the proposed mechanisms with the observed LiF particle formation and preferred sticking on disordered regions. The formation of induced electric dipole moments can be improved by the crystalline nature of the particles and thus can affect the electronic alignment of the organic molecule network at the contact interface.

The formation of nano sized particles with crystalline features directly or indirectly confirmed on all investigated organic surfaces can contribute to an explanation of the improving mechanism. This formation is independently from an accessible substrate temperature variation or slightly varying deposition rates during growth. It is unlikely that the slight lattice variations of the organic model systems due to increased LiF deposition, which have been observed in this study, are the responsible mechanisms. Tailoring of the organic crystal structure as responsible process is not excluded, but would be dependent on the organic surface under investigation.

Preferential sticking of particles on disordered regions in the organic network would therefore be responsible for the improvement in device performance in the very low coverage regime (around 1%). Once the disordered regions are occupied by particles, additional LiF deposition will affect exclusively ordered regions that are essential for charge transport and extraction. In this case the insulating effect of LiF would dominate.

In a simple scenario, LiF particles just hinder the penetration of the electrode material into the disordered regions of the organic network. This would increase the shunt resistance of the device and decrease parasitic charge flow. Hence, the build in electrical field responsible for exciton dissociation is enforced as the distance between the electrode-materials would increase. In a more sophisticated scenario, like it is shown in Figure IX.1, the particles change the potential landscape of the contact area by interaction with surface defects. A reduction of Fermi level pinning at the contact area is then also reasonable since surface defect states contribute less to the energetic alignment at the contacts. This might be mediated by induced electric dipole moments established due to the crystalline nature of the LiF particles. The insulating properties of the material itself might serve for the formation of selective space charge regions which avoid charge flow and trapping of additional excess charge carriers in the disordered regions. Charge recombination at the contact area would also be improved as only ordered regions will contribute to the charge extraction mechanism.

3. Outlook

One of the main results of this study is the qualitative observation of LiF nano particles on several organic surfaces in ultrathin films with thicknesses around 1 nm. A more quantitative description of the system is mainly hindered by the poor control with the growth parameters when these low amounts of material are deposited. Already a definition of a “thickness” in the regime of incomplete coverage describes this problem as the monitored thickness is calibrated on very thick films. An exchange of the quartz-crystal monitor with more reliable tracking techniques, e.g. cavity ring down spectroscopy would be a first step to gain more quantitative knowledge about the morphology and sticking behavior of these films dependent on varying growth parameters.

It would be interesting to examine LiF directly in the vapor that originates from the evaporation source for proofing, where particle formation exactly takes place. A direct investigation of the LiF vapor especially at low evaporation temperatures could possibly clarify if particles are already ablated from the source material. A study of the powder like source material while constantly exposed to heating and cooling processes during a longer time period can reveal, if changes in structural composition due to thermal effects occur and if this influences the particle growth behavior.

A morphological investigation of other alkali halides deposited on the used organic model systems can show if the particle formation of LiF is a unique feature of this material or if particle formation can be attributed to a class of different materials. A more reliable and well understood system of active organic materials would help to understand the physical mechanism of LiF interlayers in devices. Theoretical modeling of current voltage characteristics would be possible due to better understanding of the determining parameters. With a better control of LiF film under exactly reproducible conditions, the best performing thickness of LiF films and their impact on devices can be investigated in more detail. This should be compared with observed coverage on layer-by-layer grown molecules. For that purpose, a more sophisticated electrical measurement stage as well as light source that fit to the solar spectrum is needed.

Testing the influence of LiF crystallite orientations in relation to the surface by varying the contact area roughness with different acceptor molecules might clarify if the crystallite orientation of the particles has an impact to the device performance e.g. by lowering or enlargement of induced dipole moments.

BIBLIOGRAPHY

1. **ISE-Fraunhofer.** [Online] http://www.ise.fraunhofer.de/press-and-media/press-releases/press-releases-2009/world-record-41.1-efficiency-reached-for-multi-junction-solar-cells-at-fraunhofer-ise.

2. **Kallmann, H.** Photovoltaic Effect in Organic Crystals. *The Journal of Chemical Physics.* 1959, Vol. 30, 2.

3. **Heliatek .** [Online] http://www.heliatek.com/news-19.

4. **Tang, W. C.** Two-layer organic photovoltaic cell. *Applied Physics Letters.* 1986, Vol. 48, 2, pp. 183-185.

5. **Yu, G.** Polymer Photovoltaic Cells: Enhanced Efficiencies via a Network of Internal Donor-Acceptor Heterojunctions. *Science.* 1995, Vol. 270, 5243, pp. 1789-1791.

6. **Halls, J. J. M., et al.** Efficient photodiodes from interpenetrating polymer networks. *Nature.* 1995, Vol. 376, 498.

7. **Peumans, P., Uchida, S. and Forrest, S. R.** Efficient bulk heterojunction photovoltaic cells using small-molecular-weight organic thin films. *Nature.* 2003, Vol. 425, pp. 158-162.

8. **Ahlswede, E., Hanisch, J. and Powalla, M.l.** Comparative study of the influence of LiF, NaF, and KF on the performance of polymer bulk heterojunction solar cells. *Applied Physics Letters.* 2007, Vol. 90, 163504.

9. **Reese, M. O., White, M. S. and Rumbles, G.** Optimal negative electrodes for poly(3-hexylthiophene):[6,6]-phenyl C61-butyric acid methyl ester bulk heterojunction photovoltaic devices. *Applied Physics Letters.* 2008, Vol. 92, 053307.

10. **Brown, T. M. and Friend, R. H.** Electronic line-up in light-emitting diodes with alkali-halide/metal cathodes. *Journal of Applied Physics.* 2003, Vol. 93, 10, p. 6159.

11. **Brabec, C. J., et al.** Effect of LiF/metal electrodes on the performance of plastic solar cells. *Applied Physics Letters.* 2002, Vol. 80, 7.

12. **Pochettino, A.** *Academia Lincei Rendiconti.* 1906, Vol. 15, p. 355.

13. **Chiang, C.K., et al.** Electrical Conductivity in Doped Polyacetylene. *Physical Review Letters.* October 24, 1977, Vol. 29.

14. **Shirakawa, H., et al.** Synthesis of electrically conducting organic polymers: halogen derivatives of polyacetylene, (CH)x. *Journal of the Chemical*

Society Chemical Communications. 1977, Vol. 16, pp. 578-580.

15. **Nordén, B.** The Nobel Prize in Chemistry, 2000: Conductive polymers (advanced information). *The Royal Swedish Academy of Science.*

16. **Schwoerer, Markus and Wolf, Hans Christof.** *Organic Molecular Solids.* s.l. : Wiley-VCH, 2007. ISBN 978-3-527-40540-4.

17. **Pope, Martin and Swenberg, Charles E.** *Electronic Processes in Organic Crystals and Polymers.* s.l. : Oxford University Press, 1982. ISBN 0-19-512963-6.

18. Organic semiconductor world. [Online] http://www.orgworld.de/.

19. **Simon, J. and André, J. J.** *Molecular Semiconductors.* s.l. : Springer, 1985.

20. **Brinkmann, M., et al.** Electronic and Structural Evidences for Charge Transfer and Localization in Iodine-Doped Pentacene. *Journal of Physical Chemistry A.* 2004, Vol. 108, pp. 8170-8179.

21. **Föll, Helmut.** Allgemeine Materialwissenschaft. *Hyperskripte .* [Online] 2010. http://www.tf.uni-kiel.de/matwis/amat/.

22. **Sze, S. M. and Ng, Kwok K.** *Physics of Semiconductor Devices.* 3. s.l. : Wiley , 2007. 978-0-471-14323-9.

23. **Karl, N.** Charge carrier transport in organic semiconductors. 2003, Vols. 133–134, pp. 649–657.

24. **Coleman, Charles C.** *Modern Physics for Semiconductor.* s.l. : Wiley-VCH, 2008. 978-527-40701-9.

25. **Shockley, W.** The theory of pn-junctions in semiconductors an pn-junction transitors. *Bell Systems Technical Journal .* 1949, Vol. 28, 3, p. 435.

26. **Moliton, A. and Nunzi, J.-M.** How to model the behaviour of organic photovoltaic cells. *Polymer International.* 2006, Vol. 55, pp. 583-600.

27. **Peumans, P.r, Yakimov, A. and Forrest, S. R.** Small molecular weight organic thin-film photodetectors and solar cells. *Journal of Applied Physics.* 2003, Vol. 93, 7, pp. 3693-3723.

28. **Bernède, J. C.** Organic Photovoltaic Cells: History, Principle and Techniques. *Journal on Chilean Chemical Society.* 2008, Vol. 53, 3, pp. 1549-1564.

29. **Spanggaard, H. and Krebs, F. C.** A brief history of the development of organic and polymeric photovoltaics. *Solar Energy Materials & Solar Cells.* 2004, Vol. 83, pp. 125-146.

30. **Foerster, Th.** Zwischenmolekulare Energiewanderung und Fluoreszenz.

Annalen der Physik. 437, 1948, 1-2, pp. 55-76.

31. **Dexter, D. L.** A Theory of Sensitized Luminescence in Solids. *The Journal of Chemical Physics.* 1953, Vol. 21, 5, pp. 836-850.

32. **Bässler, H.** Charge Transport in Disordered Organic Photoconductors. *physica status solidi (b).* 1993, Vol. 175, p. 15.

33. **Miller, A. and Abrahams, E.** Impurity Conduction at Low Concentrations. *Physical Review.* 1960, Vol. 120, 3, pp. 745-755.

34. **Mott, N. F. and Davis, E. A.** *Electronic Processes in Non-Crystalline Materials.* 2. Oxford : Clarendon Press, 1979. 0-19-851288-0.

35. **Brabec, C. J., et al.** Origin of the Open Circuit Voltage of Plastic Solar Cells. *Advanced Funtional Materials.* 2001, Vol. 11, 5, pp. 374-380.

36. **Cho, A. Y. and Arthur, J. R.** Molecular Beam Epitaxy. *Progress in Solid-State Chemistry.* 1975, Vol. 10, 3, pp. 157-191.

37. **Barth, J. V., Costantini, G. and Kern, K.** Engineering atomic and molecular nanostructures at surfaces. *Nature.* 2005, Vol. 437, pp. 671-679.

38. **Barth, J. V.** Transport of adsorbates at metal surfaces: From thermal migration to hot precursors. *Surface Science Reports.* 2000, Vol. 40, pp. 75-149.

39. **Knudsen, M.** Experimentelle Bestimmung des Druckes gesättigter Quecksilberdämpfe bei 0° und höheren Temperaturen. *Annalen der Physik.* 1909, Vol. 334, 6, pp. 179-193.

40. **Roentgen, W. C.** ON A NEW KIND OF RAYS. *Nature.* 1896, Vol. 53, 1369, pp. 274-277.

41. **Bragg, W. L.** The analysis of crystals by the X-ray spectrometer. *Proceedings of the Royal Society A.* 1914, Vol. 89, pp. 468-489.

42. **Dosch, Helmut.** *Critical Phenomena at Surfaces and Interfaces.* München : Springer-Verlag, 1992. 3-540-54534-4.

43. **Als-Nielsen, Jens and McMorrow, Des.** *Elements of Modern X-Ray Physics.* s.l. : Wiley, 2001. 0-471-49857-2.

44. **Warren, B. E.** *X-RAY DIFFRACTION.* s.l. : Dover edition, 1990. 0-486-66317-5.

45. **Tolan, M.** *X-Ray Scattering from Soft-Matter Thin Films.* Berlin : Spinger-Verlag, 1999. 3540651829.

46. **Gullikson, Eric.** CXRO. *THE CENTER FOR X-RAY OPTICS.* [Online] 2010. http://henke.lbl.gov/optical_constants/pert_form.html.

47. **Kiessig, H.** Untersuchung zur Totalreflexion von Röntgenstrahlen. *Annalen*

der Physik. 1931, Vol. 402, 6, pp. 715-769.

48. **Parratt, L. G.** Surface Studies of Solids by Total Reflection of X-Rays. *Physical Review.* 1954, Vol. 95, 2.

49. **Dosch, Helmut, Batterman, B. W. and Wack, D. C.** Depth-Controlled Grazing-Incidence Diffraction of Synchtron Radiation. *Physical Review letters.* 1986, Vol. 56, 11, pp. 1144-1147.

50. **Dosch, Helmut.** Evanescent absorption in kinematic surface Bragg diffraction. *Physical Review B.* 1987, Vol. 35, 5, pp. 2137-2143.

51. **Binnig, G., et al.** Tunneling through a controllable vacuum gap. *Applied Physical Letters.* 1982, Vol. 40, 2, pp. 178-180.

52. NT-MDT Integrated Solutions for Nanotechnology. [Online] http://www.ntmdt.com/spm-principles.

53. **Loos, J.** The Art of SPM: Scanning Probe Microscopy in Materials Science. *Advanced Materials.* 2005, Vol. 17, 15, pp. 1821-1833.

54. **Binnig, G. and Quate, C. F.** Atomic Force Microscope. *Physical Review Letters.* 1986, Vol. 56, 9, pp. 930-934.

55. **Meyer, G. and Amer, N. M.** Simultaneous measurement of lateral and normal forces with an optical-beam-deflection atomic force microscope. *Applied Physics Letters.* 1990, Vol. 57, 20, pp. 2089-2091.

56. **Fischer-Cripps, A. C.** The Hertzian contact surface. *Journal of Material Science.* 1999, Vol. 34, pp. 129-137.

57. **Bradley, R. S.** The cohesive force between solid surfaces and the surface energy of solids. *Philosophical Magazine.* 1932, Vol. 13, 86, pp. 7-17.

58. **Kendall, K.** Adhesion: Molecules and Mechanics. *Science.* 1994, Vol. 263, pp. 1720-1725.

59. **Martin, Y., Williams, C. C. and Wickramasinghe, H. K.** Atomic force microscope-force mapping and profiling on a sub 100-A scale. *Journal of Applied Physics.* 1987, Vol. 61, 10, pp. 4723-4729.

60. **Albrecht, T. R., et al.** Frequency modulation detection using high-Q cantilevers for enhanced force microscope sensitivity. *Journal of Applied Physics.* 1991, Vol. 69, 2, pp. 668-673.

61. **Turak, A., Heidkamp, J. and Dosch, H.** Molecular heterojunction morphology on rough substrate surfaces: component separation by Fourier subtraction. *Nanotechnology.* 2010, Vol. 21.

62. ImageJ, Image Processing and Analysis in Java. *http://rsbweb.nih.gov/ij/index.html.* [Online]

63. **Williams, D. B. and Carter, B. C.** *Transmission Electron Microscopy 2nd ed.* s.l. : Springer, 2009. 978-0-387-76500-6.

64. ETH Zürich. *electron microscopy.* [Online] http://www.microscopy.ethz.ch/elmi-home.htm.

65. **Dürr, A. C., et al.** Optimized preparation of coss-sectionl TEM specimens of organic thin films. *Ultramicroscopy.* 2003, Vol. 98, pp. 51-55.

66. **Huang, Z. H., et al.** Influence of plasma treatment of ITO surface on the growth and properties of hole transport layer and the device performance. *Organic Electronics.* 2008, Vol. 9, pp. 51-62.

67. **Li, L., et al.** Surface modification and characterization of indium-tin oxide for organic light emitting devices. *Journal of Material Science: Mater Electron.* 2008, Vol. 19, pp. 1214-1221.

68. **Banerjee, R.i, et al.** Degradation of tin-doped Indium-oxide film in hydrogen and argon plasma. *Journal of Applied Physics.* 1987, Vol. 62, 3, pp. 912-916.

69. **Paramov, P. B., et al.** Theoretical Characterization of the Indium Tin Oxide Surface and of Its Binding Sites for Adsorption of Phosphonic Acid Monolayers. *Chemistry of Materials.* 2008, Vol. 20, 16, pp. 5131-5133.

70. http://icsd.fkf.mpg.de/index.php. *Inorganic Crystal Sturcture Database.* [Online] 2011.

71. **Heidkamp, Jonathan.** Diploma thesis. Stuttgart : s.n., 2009.

72. **von Braun, J. and Manz, G.** *Verfahren zur Herstellung von Kondensationsprodukten des Fluoranthens. 595024* [ed.] Berlin Deutsches Reichspatentamt. 1934.

73. **Meiss, J., et al.** Tetrabutyl-tetraphenyl-diindenoperylene derivates as aternative green donor in bulk heterojunction organic solar cells. *Solar Energy Materials & Solar Cells.* Vol. 95, pp. 630-635.

74. **Münch, M.** PhD Thesis. Stuttgart : s.n., 2001.

75. **Tripathi, A. K. and Pflaum, J.** Correlation between ambipolar transport and structural phase transition in diindenoperylene single crystals. *Applied Physics Letters.* 2006, Vol. 89, 082103.

76. **Kurrle, D. and Pflaum, J.** Exciton diffusion length in the organic semiconductor diindenoperylene. *Applied Physics Letters.* 2008, Vol. 92, 133306.

77. **Huang, Y. L., et al.** Ultrathin Films of Diindenoperylene on Graphite and SiO2. *Journal of Physical Chemistry C.* 2009, Vol. 113, pp. 9251-9255.

78. **Ossó, Josep Oriol.** Growth, Sturcture, and Optical Properties of Highly Ordered Organic Thin Films of Phtalocyanine. *PHD thesis.* Institut de Ciència de Materials de Barcelona, Max-Planck-Institut für Metallforschung : s.n., 2004.

79. **Dürr, A. C., et al.** High structural order in thin films of the organic semiconductor diindenoperylene. *Applied Physics Letters.* 2002, Vol. 81, 12.

80. **de Oteyza, D. G., et al.** Crystallographic and Electronic Structure of Self-Assembled DIP Monolayers on Au(111) Substrates. *Journal of Physical Chemistry C.* 2008, Vol. 112, pp. 7168-7172.

81. **Dürr, A. C., et al.** Interplay between morphology, structure, and electronic properties at diindenoperylene-gold interfaces. *Physical Review B.* 2003, Vol. 68, 115428.

82. **Dürr, A. C., et al.** Observation of competing modes in the growth of diindenoperylene on SiO2. *Thin Solid Films.* 2006, Vol. 503, pp. 127-132.

83. **Dürr, A. C., et al.** Rapid Roughening in Thin Film Growth of an Organic Semiconductor (Diindenoperylene). *Physical Review Letters.* 2003, Vol. 90, 016104.

84. **Kowarik, S., et al.** Real-Time Observation of Structural and Orientational Transitions during Growth of Organic Thin Films. *Physical Review Letters.* 2006, Vol. 96, 125504.

85. **Zhang, X. N., et al.** Transition from layer-by-layer to rapid roughening in the growth of DIP on SiO2. *Surface Science.* 2007, Vol. 601, 12.

86. **Graser, F. and Hädicke, E.** Kristallstruktur und Farbe bei Perylen-3,4:9,10-bis(dicarboximid)-Pigmenten. *Liebigs Annalen der Chemie.* 1980, Vol. 1980, 12, pp. 1994-2011.

87. **Würthner, F.** Perylene bisimide dyes as versatile building blocks for functional supramolecular architetures. *Chemical Communication.* 2004, pp. 1564-1579.

88. **Struijk, C. W., et al.** Liquid Crystalline Perylene Diimides: Architecture and Charge Carrier Mobilities. *Journal of the American Chemical Society.* 2000, Vol. 122, pp. 11057-11066.

89. **Malenfant, P. R. L., et al.** N-type organic thin-film transistor with high field-effect mobility based on a N,N'-dialkyl-3,4,9,10-perylene tetracarboxylic diimide derivative. *Applied Physics Letters.* Vol. 80, 14, pp. 2517-2519.

90. **Chesterfield, R. J., et al.** Organic Thin Film Transistors Based on N-Alkyl Perylene Diimides: Charge Transport Kinetics as a Function of Gate Voltage and Temperature. *Journal of Physical Chemistry B.* 2004, Vol. 108, pp. 19281-

19292.

91. **Hädicke, E. and Graser, F.** Structures of Eleven Perylene-3,4:9,10-bis(dicarboximide) Pigments. *Acta Crystallographica C.* Vol. 42, pp. 189-195.

92. **Briseno, A. L., et al.** Perylenediimide Nanowires and Their Use in Fabricating Field-Effect Transistors and Complementary Inverters. *Nano Letters.* 2007, Vol. 7, 9, pp. 2847-2853.

93. **Krauss, T. N., et al.** X-ray/Atomic Force Microscopy Study of the Temperature-Dependent Multilayer Structure of PTCDI-C8 Films on SiO2. *Journal of Physical Chemistry C.* 2009, Vol. 113, 11, pp. 4502-4506.

94. **Krauss, Tobias N.** *Diploma thesis.* Universität Stuttgart : s.n., 2006.

95. **Krauss, T. N., et al.** Three-dimensional molecular packing of thin organic films of PTCDI-C8 determined by surface X-ray diffraction. *Langmuir.* 2008, Vol. 24, 22.

96. **Lin, Y.-Y., et al.** High-mobility pentacene-based organic thin film transistor. *Electron Devices, IEEE Transactions.* Vol. 44, 8, pp. 1325-1331.

97. **Gross, L., et al.** The Chemical Structure of a Molecule Resolved by Atomic Force Microscopy. *Science.* 2009, Vol. 325, pp. 1110-1114.

98. **Jang, Jin.** Displays develop a new flexibility. *Materials Today.* 2006, Vol. 9, 4.

99. **Campell, R. B., Robertson, J. M. and Trotter, J.** The Crystal and Molecular Structure of Pentacene. *Acta Crystallographica.* 1961, Vol. 14, pp. 705-711.

100. **Mattheus, C. C., et al.** Indentification of polymorphs of pentacene. *Synthetic Metals.* 2003, Vol. 138, pp. 475-481.

101. **Dimitrakopoulos, C. D., Brown, A. R. and Pomp, A.** Molecular beam deposited thin films of pentacene for organic field effect transistor applications. *Journal of Applied Physics.* 1996, Vol. 80, 4, pp. 2501-2508.

102. **Fritz, S. E., et al.** Structural Characterization of a Pentacene Monolayer on an Amorphous SiO2 Substrate with Grazing Incidence X-ray Diffraction. *Journal of the American Chemical Society.* 2004, Vol. 126, pp. 4084-4085.

103. **Schiefer, S., et al.** Determination of the Crystal Structure of Substrate-Induced Pentacene Polymorphs in Fiber Structured Thin Films. *Journal of the American Chemical Society.* 2007, Vol. 129, pp. 10316-10317.

104. **Chen, F.-C., et al.** Morphological study on pentacene thin-film transistors: the influence of grain boundary on the electrical properties. *Journal of Physics D: Applied Physics.* 2010, Vol. 43, 405103.

105. **Kroto, H. W., et al.** C60: Buckminsterfullerene. *Nature.* Vol. 318, pp. 162-

163.

106. **Wragg, J. L., et al.** Scanning tunneling microscopy of solid C60/C70. *Letters to nature.* 1990, Vol. 348, pp. 623-624.

107. **Stübinger, T. and Brütting, W.** Exciton diffusion and optical interference in organic donor-acceptor photovoltaic cells. *Journal of Applied Physics.* 2001, Vol. 90, 7.

108. **Gebeyehu, D., et al.** Bulk-heterojunction photovoltaic devices based on donor-acceptor organic small molecule blends. *Solar Energy Materials & Solar Cells.* 2003, Vol. 79, pp. 81-92.

109. **Colsmann, A., et al.** Organic tandem solar cells compormising polymer and small-molecule subcells. *Applied Physics Letters.* 2006, Vol. 89, 203506.

110. **Padinger, F., et al.** The Interconnection between Efficiency and Morphology of two component Systems in Plastic Solar Cells. *Materials Research Society Symposium Proceedings.* 2000, Vol. 598, pp. BB9.3/1-6.

111. **Kazukauskas, V., et al.** Charge Carrier Mobility and Ageing of ZnPc/C60 Solar Cells. *Molecular Crystals and Liquid Crystals.* 2010, Vol. 522, pp. 61-74.

112. **Singh, T. B., et al.** High-mobility n-channel organic field-effect transistors based on epitaxially grown C60 films. *Organic Electronics.* 2005, Vol. 6, pp. 105-110.

113. **Frankevich, E., Maruyama, Y. and Ogata, H.** Mobility of charge carriers in vapor-phase grown C60 single crystal. *Chemical Physics Letters.* 1993, Vol. 214, 1, pp. 39-44.

114. **van Hal, P. A., et al.** Full temporal resolution of the two-step photoinduced energy-electron transfer in a fullerene-oligo-fullerene triad using sub-10fs pump-probe spectroscopy. *Chemical Physics Letters.* 2001, Vol. 345, pp. 33-38.

115. **Monestier, F., et al.** Optical modeling of organic solar cells based on CuPc and C60. *Applied Optics.* 2008, Vol. 47, 13, pp. 251-256.

116. **Kitamoto, T., et al.** Single-Crystal Structural Study of fcc and hcp C60 from 107 to 298 K Using Synchrotron X-Rays. *Japanese Journal of Applied Physics.* 1993, Vol. 32, pp. 424-427.

117. **Kobayashi, S., et al.** C60 thin-film transistors with high field-effect mobility, fabricated by molecular beam deposition. *Science and Technology of Advanced materials.* 2003, Vol. 4, pp. 371-375.

118. **Thewlis, J.** Unit-Cell Dimensions of Lithium Fluoride made from Li6 and Li7. *Acta Crystallographica.* 1955, Vol. 8, 36, pp. 36-38.

119. **Wharton, L., et al.** Microwave Spectrum, Spectroscopic Constants, and Electric Dipolemoment of Li6F19. *The Journal of Chemical Physics.* 1963, Vol. 38, 5, pp. 1203-1210.

120. **Klocek, P.** *Handbook of Infrared Optical Materials.* New York : Marcel Dekker, 1991. p. 291.

121. **van Velthuizen, J. and Chao, G. Y.** Griceite, LiF, a new mineral species from Mont Saint-Hilaire, Quebec. *The Canadian Mineralogist.* 1989, Vol. 27, pp. 125-127.

122. **Schlaf, R., et al.** Photoemission spectroscopy of LiF coated Al and Pt electrodes. *Journal of Applied Physics.* 1998, Vol. 84, 12, pp. 6729-6736.

123. **Wang, Y. M., et al.** Recent studies on diamond surfaces. *Diamond and Related Materials.* 2000, Vol. 9, pp. 1582-1590.

124. **Nadeau, J. S. and Johnston, W. G.** Hardening of Lithium Fluoride Crystals by Irradiation. *Journal of Applied Physics.* 1961, Vol. 32, 12.

125. **Montereali, R. M., et al.** Lithium fluoride thin-film detectors for soft X-ray imaging at high spatial resolution. *Nuclear Instruments and Methods in Physics Research A.* 2010, Vol. 623, pp. 758-762.

126. **Kojima, H., Whiteway, S. G. and Masson, C. R.** Melting points of inorganic fluorides. *Canadian Journal of Chemistry.* 1968, Vol. 46, pp. 2968-2971.

127. **Howlett, D. L., Lester, J. E. and Somorjai, G. A.** Vacuum Vaporization Studies of Lithium Fluoride Single Crystals. *The Journal of Physical Chemistry.* 1971, Vol. 75, 26.

128. **Snelson, A.** Heats of Vaporization of the Lithium Fluoride Vapor Species by the Matrix Isolation Techniques. *Journal of Physical Chemistry.* 1969, Vol. 73, 6, pp. 1919-1928.

129. **Montereali, R. M., et al.** LiF Films: Production and Characterization. *Thin Solid Films.* 1991, Vol. 196, pp. 75-83.

130. **Kaiser, U., et al.** Structure of thin fluoride films deposited on amorphous substrates. *Thin solid films.* 1992, Vol. 217, pp. 7-16.

131. **Cosset, F., et al.** Thin reactive LiF films for nuclear sensors. *Thin Solid Films.* 1997, Vol. 303, pp. 191-195.

132. **Di Nunzio, P. E., et al.** Texture Analysis of LiF Thin Films Evaporated onto Amorphous Substrates at Different Temperatures. *physica status solidi (a).* 1997, Vol. 164, 747.

133. **Baldacchini, G., et al.** Cystalline Transitions of Thin LiF Films Evaporated

on Amorphous Substrates. *physica status solidi (a).* 1995, Vol. 151, pp. 319-327.

134. **Golek, F. and Mazur, P.** LiF thin layers on Si(100) studied by ESD, LEED, AES, and AFM. *Surface Science.* 2003, Vol. 541, pp. 173-181.

135. **Perea, A., et al.** On the growth of LiF films by Pulsed Laser Deposition. *Applied Surface Science.* 1999, Vols. 138-139, pp. 533-537.

136. **Henley, S. J., Ashfold, M. N. R. and Pearce, S. R. J.** The structure and composition of lithium fluoride films grown by of-axis pulsed laser ablation. *Applied Surface Science.* 2003, Vol. 217, pp. 68-77.

137. **Horcas, I., et al.** WSxM: A software for scanning probe microscopy and a tool for nanotechnology. *Review of Scientific Instruments.* 2007, Vol. 78.

138. **Hung, L. S., Tang, C. W. and Mason, M. G.** Enhanced electron injection in organic electroluminescence devices using Al/LiF electrode. *Applied Physics Letters.* 1996, Vol. 70, 2, pp. 152-154.

139. **Jabbour, G. E., et al.** Highly efficient and bright organic electroluminescent devices with an aluminium cathode. *Applied Physics Letters.* 1997, Vol. 71, 13, pp. 1762-1764.

140. **Lee, J., et al.** High efficiency organic light-emitting devices with Al/NaF cathode. *Applied Physics Letters.* 2003, Vol. 82, 2.

141. **Reyes-Reyes, M., Kim, K. and Carroll, D. L.** High-efficiency photovoltaic devices based on annealed poly(3-hexylthiophene) and 1-(3-methoxycarbonyl)-propyl-2-phenyl-(6,6)C61 blends. *Applied Physics Letters.* 2005, Vol. 87, 083506.

142. **Wen, F. S., et al.** Effect of electrode modification on organic photovoltaic devices. *Materials Chemistry and Physics.* 2006, Vol. 95, pp. 94-98.

143. **Kim, M.-S., et al.** Choice of electrode geometry for accurate measurement of organic photovoltaic cell performance. *Applied Physics Letters.* 2008, Vol. 92, 133301.

144. **Zhao, Y., et al.** Effects of thermal annealing on polymer photovoltaic cells with buffer layers and in situ formation of interfacial layer for enhancing power conversion efficieny. *Synthetic Metals.* 2008, Vol. 158, pp. 908-911.

145. **Gao, D., et al.** C60:LiF Blocking Layer for Environmentally Stable Bulk Heterojunction Solar cells. *Advanced Materials Communication.* 2010, Vol. XX, pp. 1-5.

146. **Yokoyama, Takahiro, et al.** Energy Level Alignment at Alq3/LiF/Al Interfaces Studied by Electron Spectroscopies: Island Growth and of liF and

Size Dependence of the Electronic Structures. *Japanese Journal of Applied Physics.* 2003, Vol. 42, Part 1, No. 6A.

147. **Montereali, R. M., et al.** Morphological, electrical and optical properties of organic light-emitting diodes with a LiF/Al cathode and an Al-hydroxyquinoline/diamine junction. *Synthetic Metals.* 2004, Vol. 143, 2.

148. **Lee, Y. J., et al.** Surface morphology and interdiffusion of LiF in Alq3-based organic light-emitting devices. *Ultramicroscopy.* 2008, Vol. 108, 10.

149. **Shrotriya, V., et al.** Efficient light harvesting in multiple-device stacked structure for polymer solar cells. *Applied Physics Letters.* 2006, Vol. 88, 6, p. 064104.

150. **Cremona, M., et al.** Grain size distribution analysis in polycrystalline LiF thin films by mathematical morphology techniques on AFM images and X-ray diffraction data. *Journal of Microscopy.* 2000, Vol. 197 Pt3, pp. 260-267.

151. **Yuan, Y., et al.** Interaction between organic semiconductors and LiF dopant. *Applied Physics Letters.* 2004, Vol. 85, 21.

152. **Yazicigil, O. G., et al.** Sturctural Control of Lithium Fluoride Thin Films. *Material Researc Society Symposium Proceedings.* 2005, Vol. 875, O12.9.1.

153. **Gitlin, D., Karp, J. and Moyzhes, B.** Dangling bonds with "negative Hubbard U": Physical model for degradation of SiO2 gate dielectric under voltage stress. *Journal of Applied Physics.* 2002, Vol. 92, 12, pp. 7257-7260.

154. **Ruiz, R., et al.** Dynamic Scaling, Island Size Distribution, and Morphology in the Aggregation Regime of Submonolayer Pentacene Films. *Physical Review Letters.* 2003, Vol. 91, 13, pp. 136102-1 - 136102-4.

155. **Jensen, P.** Growth of nanostructures by cluster deposition: Experiments and simple models. *Reviews of Modern Physics.* 1999, Vol. 71, 5, pp. 1695-1735.

156. **Wang, G. and Liu, F.** Structures and properties of LiF Cluster-assembled Nanofilms. *Journal of Material Science Technology.* 1997, Vol. 13, pp. 274-279.

157. **Fernandez-Lima, F. A., et al.** Theoretical and Experimental Study of Negative LiF Clusters Produced by Fast Ion Impact on a Polycrystalline 7LiF Target. *Journal of Physical Chemistry A.* 2009, Vol. 113, pp. 15031-15040.

158. **Alonso, J. A.** *Structure and Properties of Atomic Nanoclusters.* s.l. : Imperial College Press, 2005. 978-86094-551-9.

159. **Stierle, A., et al.** Dedicated Max-Planck beamline for the in situ investigation of interfaces and thin films. *Review of scientific instruments.* 2004, Vol. 75, pp. 5302-5307.

160. **Patterson, A. L.** The Scherrer formula for X-ray Particle Size

Determination. *Physical Review.* 1939, Vol. 56, pp. 978-982.

161. **Thak, D., Lee, H. H. and Khang, D.-Y.** Elastic Moduli of Organic Electronic Materials by the Buckling Method. *Macromolecules.* 2009, Vol. 42, pp. 7079-7083.

162. **Ouyang, G., et al.** Atomistic origin of lattice strain on stiffness of nanoparticles. *Physical Chemistry Chemical Physics.* 2010, Vol. 12, pp. 1543-1549.

163. **Solliard, C. and Flueli, M.** Surface Stress and Size Effects on the Lattice Parameter in Small Particles of Gold and Platinum. *Surface Science.* 1985, Vol. 156, pp. 487-494.

164. **Chattopadhyay, S. and Meredith, J. C.** Combinatorial screening of organic electronic materials: thin film stability. *Measurement Science and Technology.* 2005, Vol. 16, pp. 128-136.

165. **Kowarik, S., et al.** Dewetting of an Organic Semiconductor Thin Film Observed in Real-time. *Advanced Engineering Materials.* 2009, Vol. 11, 4.

166. **Zhang, Xue Na.** PhD Thesis. Universität Stuttgart : s.n., 2008.

167. **Nguyen, Minh.** Diploma Thesis. Universität Stuttgart : s.n., 2010.

168. **Wagner, J., et al.** High Fill Factor and Open Circuit Voltage in Organic Photovoltaic Cells with Diindenoperylene as Donor Material. *Advanced Functional Materials.* 2010, Vol. 20, pp. 4295-4303.

169. **Greczynski, G., et al.** Photoelectron spectroscopy of thin films PEDOT-PSS conjugated polymer blend: a mini-review and some new results. 2001, Vol. 121, pp. 1-17.

170. **Kim, W. H., et al.** Effect of Annealing on the Electrical Properties and Morphology of a Conductive Polymer used as an Anode in Organic Light-Emitting devices. *Journal of Polymer Science: Part B: Polymer Physics.* 2003, Vol. 41, pp. 2522-2528.

171. **Fan, B., Mei, X. and Ouyang, J.** Significant Conductivity Enhancement of Conductive Poly(3,4-ethylendioxythiophene):Poly(styrenesulfonate) Films by Adding Anionic Surfactants into Polymer Solution. *Macromolecules.* 2008, Vol. 41, pp. 5971-5973.

172. **Pingree, L. S. C., MacLeod, B. A. and Ginger, D. S.** The Changing Face of PEDOT:PSS Films: Substrate, Bias, and Processing Effects on Vertical Charge Transport. *Journal of Physical Chemistry C.* 2008, Vol. 112, pp. 7922-7927.

173. **Friedel, B., et al.** Effects of Layer Thickness and Annealing of PEDOT:PSS Layers in Organic Photodetectors. *Macromolecules.* 2009, Vol. 42, pp. 6741-

6747.

174. **Ramaniah, L. M. and Boero, M.** Sturctural, elelctronic, and optical properties of the diindenoperylene molecule from first-principles density-functional theory. *Physical Review A.* 2006, Vol. 74, 042505.

175. **Seo, J. H., et al.** Energy level alignment between C60 and Al using ultraviolet photoelectron spectroscopy. *Applied Surface Science.* 2006, Vol. 252, pp. 8015-8017.

176. **Lof, R. W., et al.** Band gap, Exitons, and Coulomb Interaction in Solid C60. *Physical Review Letters.* 1992, Vol. 68, 26, pp. 3924-3927.

177. **Uhrich, C., et al.** Origin of open circuit voltage in planar and bulk heterojunction organic thin-film photovoltaics depending on doped transport layers. *Journal of Applied Physics.* 2008, Vol. 104, 043107.

178. **Kumar, A., Sista, S. and Yang, Y.** Dipole induced anomalous S-shape in I-V curves in polymer solar cells. *Journal of Applied Physics.* 2009, Vol. 105, 094512.

179. **Wagenpfahl, A., et al.** S-shaped current-voltage characteristics of organic solar devices. *Physical Review B.* 2010, Vol. 82, 115306, pp. 1-7.

180. **Le, Q. T., et al.** Photo emission study of aluminum-(8-hydoxyquinoline) aluminum and aluminum/LiF/tris-(8-hydroxyquinoline) aluminum interfaces. *Journal of Applied Physics.* 2000, Vol. 87, 1, pp. 375-379.

181. **Turak, A., et al.** Oxidation of LiF-Coated Metal Surfaces. *Journal of The Electrochemical Society.* 2007, Vol. 154, 8, pp. H691-H697.

182. **Shaheen, S. E., et al.** Bright blue organic light emitting diode with improved color purity using a LiF/Al cathode. *Journal of Applied Physics.* 1998, Vol. 84, 4, pp. 2324-2327.

183. **Watkins, N. J. and Gao, Y.** Vacuum level alignment of pentacene on LiF/Au. *Journal of Applied Physics.* 2003, Vol. 94, 2, pp. 1289-1291.

184. **Mori, T., et al.** Electronic structure of 8-hydroxyquinoline aluminum/LiF/Al interface for organic electroluminescent device studied by ultraviolet photoelectron spectroscopy. *Applied Physics Letters.* 1998, Vol. 73, 19, pp. 2763-2765.

DANKSAGUNG

Ich möchte mich an dieser Stelle bei denjenigen Personen bedanken, die zum Gelingen dieser Arbeit beigetragen haben.

Besonders danke ich Herrn **Prof. Dr. Helmut Dosch** für die Überlassung des Themas dieser Dissertation und für die freundliche Aufnahme in seine Abteilung. Ohne seine Motivationsfähigkeit, seinen Einsatz und seine Geduld wäre diese Arbeit niemals zustande gekommen. Ich danke Herrn **Prof. Dr. Jörg Wrachtrup** für die Übernahme der Mitberichterstattung. Außerdem möchte ich mich bei Herrn **Prof. Dr. Günter Wunner** für die Übernahme des Prüfungsvorsitzes bedanken. Ich danke **Prof. Dr. Manfred Rühle** für Möglichkeit, diese Arbeit zu einem Abschluß zu bringen

Weiterhin bedanke ich mich bei **Dr. Ayse Turak** für die persönliche Betreuung dieser Arbeit, der Strukturierung des Projekts und der Unterstützung bei zahlreichen Meßzeiten. Ich möchte mich außerdem sehr herzlich bei **Dr. Janos Major** bedanken, der immer ein offenes Ohr hatte und sich für die Korrektur dieser Arbeit bereit erklärt hat.

Zusätzlich möchte ich mich sowohl bei **Marion Kelsch** (StEM MPI-MF) wie auch der Gruppe um **Prof. Dr. Roland Bennewitz** (INM Saarbrücken) und der Gruppe um **Dr. Udo Welzel** (XRD Service Group MPI-MF) für die experimentelle Zusammenarbeit bedanken.

Ich danke **Dr. Carmen Munuera** für zahlreiche Erklärungen zur AFM-Technik. Ebenfalls danke ich **Peter Lienerth**, **Jonathan Heidkamp, Deniz Ergyun** und vor allem **Minh Nguyen** für die vielen Vorarbeiten, für die Unterstützung bei der täglichen Laborarbeit und für die hilfreichen Diskussionen. Ich danke den ehemaligen Mitgliedern der Organic-Gruppe innerhalb der Abteilung Dosch für die fachliche Hilfe und die gute Arbeitsatmosphäre: **Dr. Esther Barrena**, **Dr. Tobias Krauss**, **Monamie Sanyal**, **Dr. Xue Na Zhang** und **Dr. Yi Zhang**.

Herzlich möchte ich mich auch bei **Peter Schützendübe**, **Taufan Zimmer**, **Ralf Weigel**, **Frank Adams, Annette Weißhardt** und **Michael Schäfer** für die Unterstützung bei zahlreichen technischen Herausforderungen bedanken. Außerdem bedanke ich mich bei **Claudia Sussdorff** für die organisatorische Zusammenarbeit.

Ich danke **Burak Ozdol** und **Dr. Moritz Becker** für die Hilfe bei der Datenanalyse. Weiterhin danke ich **Dr. Max Nülle** und **Dr. Navid Kohrshidi** für die Hilfe bei der Gestaltung dieser Arbeit. Ich möchte mich bei **Dr. Steffen Sonntag** für die freundschaftliche Unterstützung bedanken.

Ich danke allen Mitgliedern der **Abteilung Dosch** für die hilfreichen Erklärungen und die gute Zusammenarbeit. Ich möchte ebenfalls allen Mitarbeitern des **Max-Planck-Instituts für Metallforschung** danken, die positiv an dieser Arbeit mitgewirkt haben. Des Weiteren danke ich den Mitarbeitern der **Universität Stuttgart** für die zur Verfügung gestellten organischen Materialien. Verzeiht mir, daß ich eure Namen nicht einzeln aufzähle, es würde den Rahmen sprengen.

Liebe **Katrin**, lieber **Fred** und liebe Familie, ich danke Euch aus tiefstem Herzen für Eure mentale Unterstützung während meiner Lehrjahre. Ihr habt immer an mich geglaubt und mich niemals im Stich gelassen. Geliebte **Rasha**, Dir danke ich besonders für Deine Geduld und dafür, daß Du den Glauben an mich auch in schweren Zeiten nicht verloren hast.

Dieses Forschungsprojekt wurde von einem Marie Curie Stipendium innerhalb des 7. Rahmenprogramms der Europäischen Union unterstützt.